Dynamique hors-équilibre : Quelques exemples en physique des surfaces

Frédéric Leroy

Mémoire présenté par

Frédéric LEROY

Pour l'obtention de :

L'HABILITATION À DIRIGER DES RECHERCHES
d'Aix-Marseille Université

Dynamique hors-équilibre : Quelques exemples en physique des surfaces

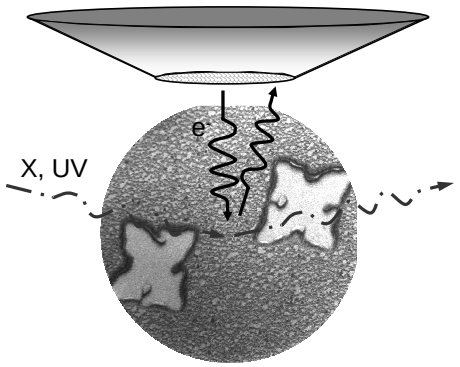

Soutenu le 27 Novembre 2013 devant le jury composé de :

Luc Barbier : Rapporteur
Nick Barrett : Examinateur
Nicolas Eustathopoulos : Membre invité
Claude Henry : Examinateur
Martin Hÿtch : Rapporteur
Jean-Marc Layet : Président
Pierre Müller : Examinateur
Sylvie Rousset : Rapporteur

REMERCIEMENTS

Je tiens tout d'abord à remercier les membres du jury de cette habilitation, en particulier Jean-Marc Layet qui a accepté d'en être le président. Je remercie également Luc Barbier pour sa lecture attentive du manuscrit et les échanges scientifiques toujours constructifs que nous avons pu avoir ainsi que Sylvie Rousset pour son regard critique et bienveillant. Martin Hÿtch n'a pas pu assister à la soutenance mais qu'il soit ici remercié pour son concours. Ce travail a aussi été examiné par Nick barrett et Claude Henry et je les en remercie. Je souhaite aussi remercier Nicolas Eustathopoulos qui a accepté de participer au jury et dont la réflexion profonde sur la dynamique du démouillage solide de films minces me sera très utile pour prolonger ma réflexion sur cette activité de recherche.

Ce mémoire est le fruit de longues années de travail au cours desquelles le partage et le plaisir de la recherche sont essentiels. Je tiens à remercier tout particulièrement Pierre Müller qui a été un collaborateur enthousiaste. La confiance qu'il m'a donnée et son implication m'ont permis de mener mes activités de recherche dans les meilleures conditions au sein du groupe Structure et Dynamique des Surfaces. Que son apport inestimable soit ici remercié. En particulier le regard, original à mon sens, qu'il porte sur nos activités de recherche, forcant la confrontation entre expérience et théorie est un atout indéniable et une exigence qui nous poussent toujours à approfondir notre réflexion scientifique. Je voudrais associer à ces remerciements

Fabien Cheynis et Stefano Curiotto qui nous ont rejoints en 2008 et 2013 et qui partagent la noble, mais parfois lourde tache de faire fonctionner le LEEM dans les meilleures conditions et toujours dans la bonne humeur. Bien sûr mes remerciements vont aussi à Thibault Passanante qui j'espère bouclera la rédaction de son manuscrit de thèse dans les meilleures conditions.

Ces études ont souvent été menées en collaboration, en particulier avec des théoriciens. Ils ont joué un rôle de premier plan dans notre compréhension de la physique des instabilités morphologiques des surfaces cristallines. Je voudrais remercier tout particulièrement Olivier Pierre-Louis et Yukio Saito pour avoir partagé l'aventure du démouillage à l'état solide des films minces qui se poursuit aujourd'hui par des études conjointes sur la dynamique de la ligne triple solide-solide-vide. Ces travaux ont aussi été l'occasion de collaborer avec Jean-Charles Barbé et ses collègues du Léti. Leur apport, en particulier dans la fabrication des substrats de Silicium sur Isolant (SOI) ou de Germanium sur Isolant (GOI) a été primordial dans ces études et je les en remercie vivement. Les théoriciens de l'IRPHE puis/et de l'IM2NP : Thomas Frisch, Jean-Marc Debierre et Mathieu Dufay ont été au coeur de l'interprétation des phénomènes d'instabilité sur les faces vicinales de Si par mise en paquets/méandrage de marches atomiques. Leur enthousiasme pour ce sujet nous a permis d'interpréter la physique de ces transitions morphologiques. Je tiens également à remercier l'équipe Agrégats et Catalyse dirigée par Claude Henry, en particulier Georges Sitja, Maxence Marsault et Séverine Le Moal pour les moments mémorables passés au synchrotron (ESRF) à étudier la croissance auto-organisée d'agrégats nanométriques de Palladium. Les expériences sur Synchrotron ont été aussi au coeur d'une collaboration avec Bernard Croset, Geoffroy Prévot ainsi qu'Alessandro Coati et Yves Garreau. La bonne humeur est toujours au rendez-vous et ce n'est pas le moindre des atouts pour tenir durant ces longues nuits à regarder défiler des spectres de diffraction X. Bien sûr ces expériences ont aussi été l'occasion de conserver des liens étroits avec mes collaborateurs de thèse, en particulier Gilles Renaud dont l'enthousiasme et l'énergie sont des valeurs sures, mais aussi Nils Blanc et Olivier Ulrich,

toujours efficaces et disponibles sur la ligne de lumière BM32.

Toute ma gratitude va à Jean-Jacques Métois qui a largement contribué à l'avancement de ce travail. Je le remercie pour les très nombreuses discussions que nous avons pu avoir autour du microscope électronique en réflexion. En particulier durant les premières années de mon recrutement son expertise sur les problèmes d'électromigration sur les faces vicinales de Silicium a été précieuse.

Un grand merci à Ezra Bussmann qui a partagé avec le groupe, pendant 18 mois de post-doc, l'arrivée du LEEM et les premiers résultats très prometteurs sur le démouillage des films minces. Son esprit critique et ses efforts pour faire fonctionner le microscope sont encore dans ma mémoire.

Merci aussi à Raymond Kern pour son soutien et son regard bienveillant sur nos activités de recherche.

Un grand merci aux équipes techniques du laboratoire, Alain Ranguis, Fred Bedu, Igor Ozerov, William Bon, Philippe Bindzi, Brice Detailleur pour leur aide sur l'instrumentation et aussi à tous ceux avec qui j'ai partagé une part de ces huit années passées au CINaM : Laurent, Lisa, Matthieu, Jean-Philippe, André, Daniela, Lukasz, Aude, Anne...

Enfin chacun des chercheurs et enseignants-chercheurs ne peut réellement s'épanouir que dans un cadre collectif qui le favorise et le stimule. Je remercie donc Slava Safarov et Claude Henry de m'avoir accueilli au sein du Centre Interdisciplinaire de Nanoscience de Marseille.

TABLE DES MATIÈRES

Introduction générale **3**

I Démouillage de films solides **7**

1. Mise en perspective **9**

2. Principaux résultats **11**

2.1 État de l'art 11

2.2 Dynamique du démouillage de films de Si sur SiO_2 (articles joints $[1, 2]$) 14

2.3 Anisotropie cristalline (article joint $[3]$) 20

2.4 Ge/SiO_2 versus Si/SiO_2 (articles joints $[4, 5]$) 23

2.5 Conclusion et perspectives 27

3. Articles sélectionnés : Démouillage de films solides **29**

3.1 Dynamique du démouillage dans le système Silicium sur isolant (SOI)
Bussmann *et al.*, New J. Phys. (2011) 29

3.2 Dynamique du démouillage de Si/SiO_2
Cheynis *et al.*, Phys. Rev. B (2011) 39

3.3 Dynamique, anisotropie et stabilité des fronts de démouillage
Leroy *et al.*, Phys. Rev. B (2012) 49

3.4 Démouillage de Ge/SiO_2 par GISAXS
Cheynis *et al.*, Appl. Phys. Lett. (2013) 56
3.5 Influence des facettes sur la dynamique des fronts de démouillage : une comparaison Ge et Si sur SiO_2
Leroy *et al.*, Phys. Rev. B (2013) 61

II Instabilités des surfaces de silicium induites par électromigration 71

1. Mise en perspective 73

2. Principaux résultats 75
2.1 État de l'art 75
2.2 Onde de densité de marches et facettage induits par électromigration (voir article joint [6]) 76
2.2.1 Onde de densité de marches 79
2.2.2 Facettage induit par électromigration 84
2.3 Transition abrupte méandrage / mise en paquet de marches atomiques (voir article joint [7]) 87
2.4 Conclusion 91

3. Articles sélectionnés : Instabilités des surfaces de silicium induites par électromigration 93
3.1 Onde de densité de marches et facettage sur les faces vicinales de silicium
Leroy *et al.*, Phys. Rev. B (2007) 93
3.2 Transition de méandrage et de mise en paquet de marches atomiques
Leroy *et al.*, Surf. Sci. (2009) 109

III Croissance auto-organisée de nanostructures 117

1. Mise en perspective 119

2. Principaux résultats **123**
2.1 État de l'art 123
2.2 Croissance de nanostructures de Pd auto-organisées sur Al_2O_3 par GISAXS (voir article joint [8]) 124

3. Articles sélectionnés : Croissance auto-organisée de nanostructures **129**
De la molecule au cristal : reactivité d'agrégats métalliques supportés
Sitja *et al.,* Nano Lett. (2013) 129

Conclusion et perspectives **145**

IV Curriculum Vitae et vie scientifique

Introduction générale

Ce mémoire décrit mes travaux de recherche réalisés depuis ma thèse en 2004. Ils sont le fruit d'une histoire qui a débuté l'année de mon DEA à Grenoble et qui se poursuit encore aujourd'hui. Cette année là, j'ai découvert la physique des surfaces, par l'intermédiaire du cours de "*Physique des Nanostructures*" de Joël Cibert et du livre de "*Physique de la croissance cristalline*" de Jacques Villain et Alberto Pimpinelli. Ils m'ont donné le goût d'observer la structure cristallographique et la dynamique d'évolution de la surface d'un cristal pour comprendre par exemple les processus de croissance d'un matériau, la mise à l'équilibre d'un cristal ou encore les fluctuations du mouvement d'une marche atomique. Pour aborder ces questions il y a aujourd'hui de multiples techniques expérimentales disponibles. Toutefois, ces processus étant le plus souvent hors-équilibre, pouvoir caractériser ces phénomènes *in situ* et avec une résolution temporelle adaptée est un atout indéniable.

Si mes travaux de thèse ont été dédiés à la caractérisation *in situ* des surfaces cristallines par diffusion des rayons X, j'ai depuis complété cette approche par des techniques de microscopie électronique et de microscopie en champ proche. En particulier, et elle sera largement présentée dans le chapitre sur le démouillage de films solides, la technique de microscopie à électrons lents (LEEM, acquise au laboratoire en 2009), permet d'étudier *in situ* avec une résolution temporelle inférieure à 0.1 s, et à hautes températures ($>1000°$ C), la dynamique d'une surface avec une résolution latérale de 10 nm et une résolution verticale atomique. C'est donc un outil très adapté aux études cinétiques des phénomènes de surfaces (voir exemple figure .1).

Le premier phénomène que j'aborde dans ce mémoire est le démouillage de films monocristallins. En effet si le démouillage des liquides a été longuement étudié, donnant lieu à des dynamiques variées, le démouillage des solides n'a suscité que récemment un intérêt. Ce phénomène a la même origine que le démouillage des liquides : une réduction de l'énergie de surface/interface par changement de forme du film. Cependant, la physique de cette instabilité morphologique est assez différente dans le cas des solides et ce pour 3 raisons : (i) le transport des atomes se fait par diffusion de surface au lieu d'un écoulement piloté par les propriétés hydrodyna-

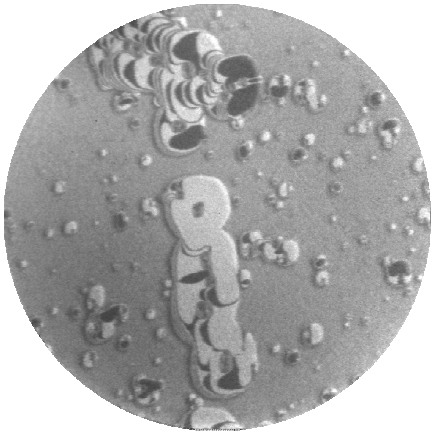

Figure .1 *– Image LEEM en champ sombre d'une surface de Si(100) partiellement oxydée. Dû à un recuit thermique, l'oxyde de surface est en cours de décomposition. Les zones blanches et noires sont des terrasses de Si planes à l'échelle atomique reconstruites respectivement* (2×1) *et* (1×2)*. Les zones grisées, sur le reste de la surface, sont formées de l'oxyde de Si. Champ de vue 10* μm*.*

miques dans le cas des liquides ; (ii) les solides sont très anisotropes ; (iii) les solides épitaxiés sont l'objet de contraintes élastiques importantes, qui peuvent modifier le bilan énergétique global.

La seconde partie traite des instabilités morphologiques des surfaces vicinales de silicium soumises à un courant électrique continu. Ce courant électrique induit une asymétrie dans le déplacement des ad-atomes par diffusion de surface. Ce phénomène est appelé électromigration. Or les déplacements de matière sur les surfaces vicinales de silicium sont aussi étroitement corrélés aux propriétés physiques des marches atomiques. Par conséquent l'électromigration est un moyen d'étude de la dynamique des marches. En particulier nous avons pu sonder les interactions mutuelles répulsives entre marches qui proviennent du champ de déformation élastique généré dans le substrat et qui tendent à contrebalancer l'effet de l'instabilité induite par le courant électrique. On s'est attaché à étudier les instabilités de mise en paquets et de méandrage des marches atomiques.

Dans la dernière partie j'aborde brièvement la question de notre capacité à piloter des déplacements de matière à l'échelle nanométrique pour fabriquer à la demande des matériaux avec des propriétés spécifiques. C'est

un défi à la fois pour la physique fondamentale et pour la physique appliquée. L'une des approches les plus ambitieuse est d'utiliser la structuration spontanée de certaines surfaces (reconstruction, facettage ...) comme gabarit pour la croissance de nano-objets. L'objectif est de réaliser des nanostructures de tailles parfaitement définies pour en contrôler les propriétés. En particulier nous avons caractérisé *in situ* par GISAXS sur la ligne de lumière BM32 de l'ESRF la croissance auto-organisée d'agrégats de Pd sur une surface nanostructurée d'Al_2O_3 sur $Ni_3Al(111)$. La réactivité des agrégats de Pd vis-à-vis de l'adsorption de CO a été ensuite systématiquement étudiée en fonction de leurs tailles. Enfin et pour terminer, j'aborde les perspectives que je donne à ce travail.

Première partie

Démouillage de films solides

MISE EN PERSPECTIVE

Le démouillage solide est un problème nouveau de physique fondamentale relevant de la morphogénèse, avec une dynamique d'évolution fortement non linéaire. Afin d'accéder à une meilleure compréhension des mécanismes de base qui entrent en jeu lors du démouillage de films minces à l'état solide, nous avons étudié la dynamique du phénomène en alliant expérience et théorie.

Sur le plan expérimental la réalisation de ces études a principalement nécessité l'utilisation d'outils de caractérisation *in situ*. La microscopie à électrons lents (Low Energy Electron Microscopy) a permis d'accéder à la dynamique du processus à des échelles spatio-temporelles adaptées (10 nm à 100 μm ; 1s à 1h) et la diffusion centrale des rayons X en incidence rasante (Grazing Incidence Small Angle X-ray Scattering) de mettre en évidence la présence de facettes sur les bourrelets de démouillage jouant un rôle prépondérant sur sa dynamique. Des moyens de caractérisation *ex situ* ont aussi permis de déterminer la morphologie locale notamment celle du bourrelet à proximité de la ligne triple et de confronter ces mesures aux modèles. Évidemment pour réaliser des études modèles de démouillage solide, des films minces de très grande qualité cristalline et homogène en épaisseur ont été nécessaire. Les substrats dit SOI (Silicon-On-Insulator) ou GOI (Germanium-On-Insulator), fabriqués par grâce au procédé SmartCut, et formés respectivement d'un film monocristallin de silicium ou de germanium sur silice amorphe, ont joué un rôle essentiel. Ces substrats, en plus

de leur caractère modèle pour la physique des surfaces, représentent un enjeu industriel très important en particulier pour la micro-électronique. Ils permettent le développement de nouveaux composants sur la base de procédés technologiques complexes. Ces matériaux sont ainsi soumis à des séries de transformations successives (gravure, reprise de croissance, oxydation, nitruration, irradiation...) incluant de nombreux cycles thermiques. Au delà des performances intrinsèques des matériaux de base, de nouveaux problèmes de fiabilité et d'endurance liés aux processus technologiques sont apparus. L'un de ces problèmes, est le démouillage des films minces à l'état solide qui se produit lors des traitements thermiques nécessaires à la fabrication des composants. En particulier les structures Xtrem SOI^{TM} (SOITEC), qui sont formées d'un film « actif » de silicium sur silice de quelques dizaines de nanomètres d'épaisseur, sont très instables sous recuit thermique. Sur la figure I.1 est reporté le démouillage d'un film de Si sur SiO_2. Il conduit au retrait d'un front instable donnant lieu à des digitations qui se fragmentent en nanocristaux de silicium détruisant du même coup les propriétés électroniques du film. Ces substrats modèles ont été au coeur de nos études sur le démouillage avec ce double intérêt fondamental et technologique.

Sur le plan théorique, les études se sont articulées autour d'une approche multi-échelles en s'appuyant sur des simulations Monte Carlo Cinétiques faites en collaboration avec O. Pierre-Louis de l'ILM (Lyon) et une analyse à partir de modèles macroscopiques développés au CINaM.

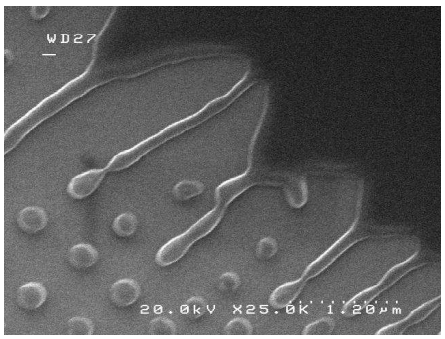

Figure I.1 *– Image MEB d'un film mince de Si ayant partiellement démouillé. (CEA-Léti).*

2. PRINCIPAUX RÉSULTATS

2.1 État de l'art

Avant d'aborder les résultats scientifiques un état de l'art s'impose. L'instabilité morphologique d'un film mince solide sur un substrat à été observée depuis longtemps [1]. Elle conduit à la transformation d'un film 2D en une assemblée de nanocristaux 3D qui par analogie avec les films liquides a été appelée démouillage solide. Ce processus d'agglomération spontanée est généralement attribué au gain d'énergie de surface et d'interface qui agit comme force motrice. Toutefois contrairement aux liquides pour lesquels la cinétique de démouillage est pilotée par ses propriétés hydrodynamiques il n'en est évidemment pas de même pour les solides. Le cadre théorique décrivant la cinétique de démouillage d'un film mince a été posé historiquement par Mullins [2]. Le transport de matière pendant le démouillage du film est assuré soit par un mécanisme de diffusion de surface ou par un mécanisme d'évaporation/condensation d'un gaz d'adatomes. Aux températures usuelles de démouillage solide (T$= 800-900°$C), le processus dominant est la diffusion de surface ($T_{fus}^{Si} = 1414°$C). Des lois d'échelle ont été prédites dans le cadre de modèles continus pour la cinétique de recul d'un front droit démouillant ($x \sim t^{\frac{2}{5}}$) [1,3] ou pour un trou de forme circulaire ($r \sim t^{\frac{1}{4}}$) [4]. Ces modèles s'appuient sur les 3 points suivants :

(i) la conservation de la matière :

$$\dot{z} \sim -\overrightarrow{\nabla}.\overrightarrow{j} \tag{2.1}$$

(ii) les principes de la thermodynamique irréversible où il est admis que la densité superficielle de courant d'ad-atomes $\overrightarrow{j}$ est une fonction linéaire (pour de petites variations) du gradient du potentiel chimique μ.

$$\overrightarrow{j} \sim -\overrightarrow{\nabla}.\mu \tag{2.2}$$

(iii) l'expression du potentiel chimique μ, fonction linéaire de la courbure κ selon l'expression de Gibbs-Thompson.

$$\mu \sim \kappa \tag{2.3}$$

Ces résultats théoriques n'ont toutefois qu'un intérêt limité dans la mesure où le démouillage solide conduit la plupart du temps à des morphologies complexes (présence de digitations) qui ne sont pas prédites par les modèles cités ci-dessus et qui manquent donc, de fait, leur objectif de décrire la cinétique d'agglomération d'un film mince. Le caractère instable de la morphologie d'un front uniforme de démouillage a été proposé par Jiran et Thompson [5, 6] et validé quelques années plus tard théoriquement par Kan et Wong [7]. La dernière avancée récente concerne les questions d'anisotropie des figures de démouillage. En effet selon l'orientation cristallographique initiale du film mince, des morphologies très distinctes sont observées (voir Fig. I.2). Contrairement aux liquides les cristaux sont caractérisés par des propriétés anisotropes. En particulier les propriétés singulières de transport de matière sur les plans denses jouent un rôle central. Les modèles continus qui s'appuient sur la description proposée par Mullins ne peuvent pas aborder ces questions. Ce n'est que récemment qu'O. Pierre-Louis et ses collaborateurs ont traité du rôle des facettes dans la dynamique de démouillage [8, 9]. De nouvelles lois d'échelle ont été prédites mais aussi et de façon plus spectaculaire il a été proposé que, contrairement aux modèles continus, certaines orientations cristallographiques de fronts sont stables morphologiquement formant un bourrelet droit (sans digitation) reculant avec une dynamique originale.

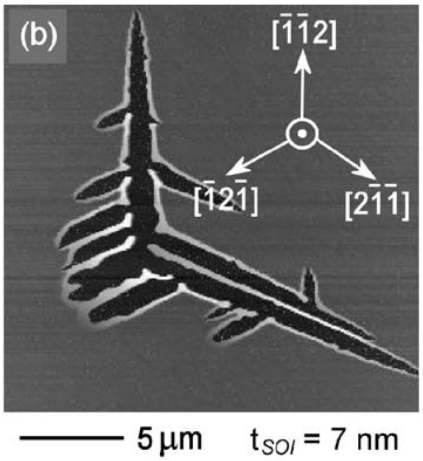

Figure I.2 *– Figure extraite de la référence [10] montrant le démouillage d'un film de Si(111) de 7 nm d'épaisseur sur SiO_2 (950° C, 10 s).*

C'est dans ce contexte que nous avons abordé expérimentalement les questions relatives au démouillage solide. En particulier il était nécessaire de combler le vide expérimental sur la dynamique du processus [11–16]. L'utilisation de matériaux modèles SOI (Silicon-On-Insulator) et GOI (Germanium-On-Insulator) obtenus par une collaboration étroite avec le CEA-Léti dans le cadre du projet ANR DEFIS (Démouillage de Films Solide) a été cruciale pour avoir des résultats quantitatifs. Nous avons effectué des mesures *in situ* par LEEM afin d'obtenir l'évolution morphologique des films minces pendant le démouillage [17]. Les lois d'évolution de la vitesse de démouillage en fonction de la température et de l'épaisseur du film ont été extraites [18]. Nous avons pu quantifier les énergies mises en jeu à la fois concernant la force motrice et aussi le mécanisme par diffusion de surface. Le rôle primordial des facettes sur la dynamique du démouillage a été étudié grâce à deux campagnes de mesures synchrotron par GISAXS sur la ligne de lumière BM32 de l'ESRF [18–20]. Enfin et pour aborder la question de l'anisotropie des vitesses de démouillage nous avons utilisé les moyens de lithographie électronique de la plate-forme de proximité C'Nano Paca "Planète" pour fabriquer des tranchées droites d'orientations contrôlées dans les films de silicium et de germanium. Les fronts de silicium orientés selon $\langle 110 \rangle$ se sont révélés stables morphologiquement met-

tant en lumière un effet spectaculaire de l'anisotropie cristalline et le rôle stabilisant des facettes $\{111\}$ et $\{113\}$ [21].

2.2 Dynamique du démouillage de films de Si sur SiO_2 (articles joints $[1, 2]$)

Les expériences de démouillage de Si sur SiO_2 ont été réalisées sur des substrats SOI orientés dans la direction $\langle 100 \rangle$ et fabriqués par le procédé Smart Cut développé initialement par le CEA Léti et aujourd'hui commercialisé par la société SOITEC. Les mesures de largeur angulaire des pics de Bragg des films de Si indiquent que ces films sont monocristallins (FWHM$< 0.01°$). Le démouillage a été étudié pour différentes épaisseurs de film (6, 11, 14 et 22 ± 2 nm) et à différentes températures. Aucune différence qualitative n'a été observée sur la morphologie des films pendant le démouillage. Les mesures de cinétique de démouillage ont été réalisées par LEEM en utilisant principalement le mode champ sombre qui consiste à sélectionner la tache de diffraction $1/2$ associée à la reconstruction de surface du Si(100)-(2×1) ou (1×2) [22,23]. Comme deux terrasses adjacentes séparées par un plan atomique ont des reconstructions orthogonales (il y a deux atomes dans la maille primitive du Si), les terrasses apparaissent blanches ou noires selon le type de reconstruction (2×1) ou (1×2), ce qui permet de distinguer nettement les marches atomiques qui les séparent avec une résolution latérale de l'ordre de 10 nm.

La microscopie optique nous a montré qu'un nombre réduit de sites de démouillage nucléent ($\sim 10^2$ site/mm^2). Nous avons caractérisé par LEEM l'évolution morphologique locale de ces zones [17]. La figure I.3 montre une succession d'images enregistrées pendant le démouillage d'un film de Si d'épaisseur 22 nm à une température de $870°$C. On distingue 4 étapes dans le processus de démouillage : (i) la nucléation d'un trou sur un défaut. (ii) L'ouverture de ce trou de forme initiale carrée. (iii) L'instabilité de forme du bourrelet qui favorise la formation de doigts et (iv) le perlage de ces doigts en nanocristaux. Notons toutefois que même si une structure en doigts se développe, la zone démouillée conserve une enveloppe de forme

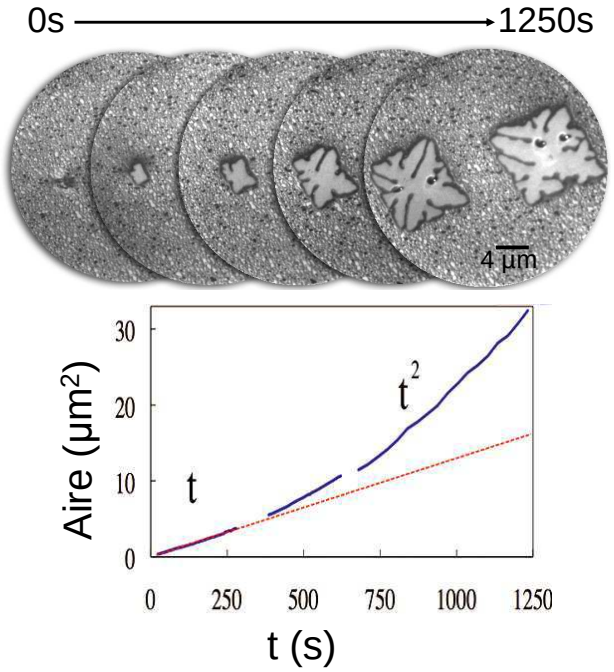

Figure I.3 *– Haut : Séquence d'images LEEM montrant les différentes étapes du démouillage d'un film de silicium depuis la nucléation d'un trou sur un défaut jusqu'au développement de grandes zones démouillées laissant apparaître des doigts qui sont instables et forment par perlage des nanocristaux. Bas : évolution de l'aire démouillée en fonction du temps. Un régime quadratique succède à un régime linéaire.*

carrée avec des côtés orientés selon la direction $\langle 110 \rangle$. Du point de vue quantitatif cette évolution morphologique conduit à deux régimes d'évolution temporelle de l'aire de démouillage. Initialement, tant que le trou est carré, on observe une croissance linéaire de l'aire. L'instabilité se développe d'abord aux coins du trou et conduit à l'apparition de doigts. On observe ensuite une croissance quadratique de l'aire démouillée indiquant que la vitesse des fronts $\langle 110 \rangle$ atteint un régime stationnaire caractéristique de la température et de l'épaisseur du film. La complexité de la morphologie des figures de démouillage a été abordée au travers de simulations Monte Carlo Cinétique en collaboration avec O. Pierre-Louis. Le principe en est simple : un film mince A est déposé sur un substrat plan B. Les "atomes" A et B sont disposés selon un réseau cubique (modèle Solid-On-Solid) et ont une interaction entre premiers voisins. La force motrice pour le dé-

mouillage est assurée par le gain énergétique $E_s = \gamma_A + \gamma_{A-B} - \gamma_B > 0$, où γ_i sont les énergies de surface et d'interface des solides en question, et la diffusion de surface est assurée par une fréquence de saut des "atomes" A selon $\nu = \nu_0 e^{(-nJ-\delta_{0i}E_s)/kT}$ (les "atomes" B sont figés). n est le nombre de voisin de "l'atome" A dans le plan, J est l'énergie associée à cette interaction et δ_{0i} est le symbole de Kronecker ($i = 0, 1, 2...$ est le numéro de la couche atomique auquel appartient l'atome). Il y a donc un excès d'énergie pour un "atome" A en contact avec B ($i = 0$). Des extraits des simulations sont reproduits sur la figure I.4. Ils montrent le même type de structures de démouillage que celles observées expérimentalement. L'accord est également quantitatif montrant une évolution temporelle de l'aire démouillée d'abord linéaire puis quadratique. Cet accord remarquable montre que les ingrédients physiques présents dans les simulations numériques sont suffisants pour expliquer l'essentiel du phénomène. Ces ingrédients sont le gain d'énergie de surface/interface qui agit comme force motrice pilotant le démouillage et la diffusion de surface qui est le mécanisme de transport de la matière.

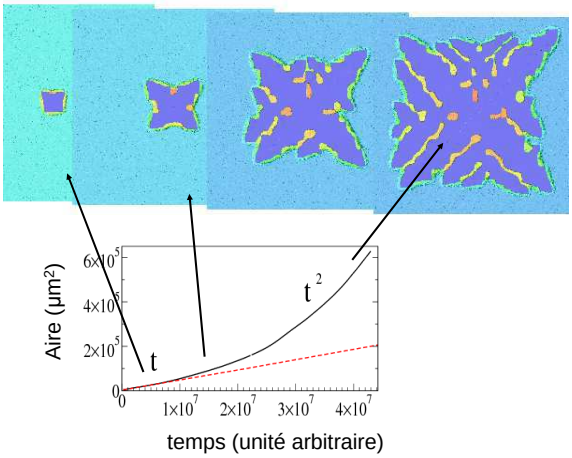

Figure I.4 *– Haut : Séquence d'images extraites d'une simulation Monte Carlo Cinétique du démouillage d'un film de 3 monocouches d'épaisseur. Les structures de démouillage obtenues ressemblent de manière frappante à celles observées expérimentalement. Bas : Sur un plan plus quantitatif l'aire démouillée suit la même évolution, i.e. une évolution initialement linéaire puis quadratique.*

Si les simulations Monte Carlo Cinétiques permettent clairement de dé-

terminer quels sont les paramètres physiques pertinents qui gouvernent le processus de démouillage d'un film solide, la complexité du phénomène reste entière et la dépendance de sa vitesse avec les paramètres élémentaires que sont la température et l'épaisseur du film reste à préciser. En nous appuyant sur nos mesures expérimentales de vitesse nous avons proposé une description qualitative du démouillage sur la base de quelques arguments physiques.

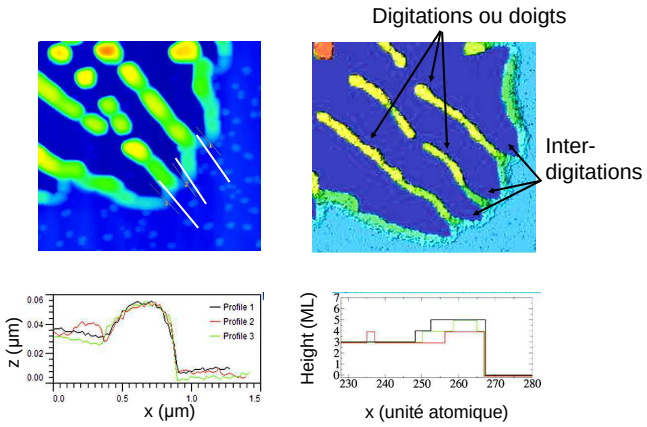

Figure I.5 – *Détails de la morphologie du front de démouillage par microscopie à force atomique et simulations Monte Carlo Cinétique. L'accord est remarquable même localement. Sont représentés aussi des profils de la surface du film. On peut voir que l'épaisseur du bourrelet est plus faible au niveau des interdigitations.*

En particulier dans le régime quadratique, l'instabilité morphologique du front de démouillage qui s'est développée conduit à une vitesse de recul du front constante. L'analyse des images LEEM montre que ce front est formé d'interdigitations qui pénètrent à l'intérieur du film mince de silicium générant sur ses côtés des doigts de silicium. Les images topographiques réalisées *ex situ* par AFM (voir Fig.I.5) indiquent que c'est à l'extrémité des interdigitations que l'épaisseur du bourrelet est la plus faible. Ceci en fait naturellement le lieu du recul du front de démouillage. En considérant que la vitesse de recul du front est égale à celle de recul d'une interdigitation (pas d'effets collectifs) et en faisant l'approximation que l'enveloppe de la partie active de ces interdigitations forme un front droit, nous avons évalué la vitesse de recul du front de démouillage [6] (voir Fig. I.6).

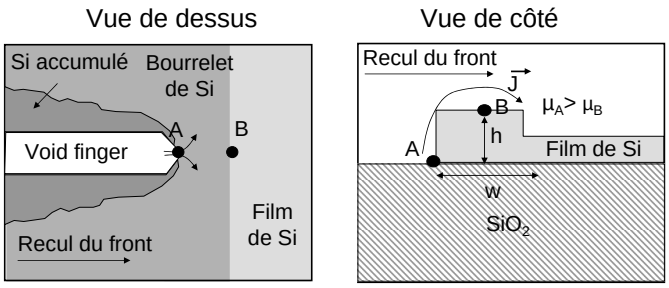

Figure I.6 *– Schéma du modèle du front de démouillage. Le bourrelet, de forme rectangulaire, est caractérisé par une hauteur h et une largeur w. Le transfert de matière est induit par le gradient de potentiel chimique pour un atome localisé à la ligne triple se déplaçant sur le bourrelet.*

Le flux d'atomes j lors du recul du front s'écrit :

$$j \sim -\nabla.\mu \tag{2.4}$$

Contrairement au cas du démouillage piloté par les effets de courbure, le gain de potentiel chimique doit inclure le bilan d'énergie de surface/interface E_s.

$$\mu = \frac{E_s}{h} \tag{2.5}$$

La largeur caractéristique du bourrelet w permet d'estimer le gradient de potentiel chimique :

$$\nabla.\mu \sim -\frac{E_s}{h} \times \frac{1}{w} \tag{2.6}$$

Comme la vitesse v de recul du front est proportionnelle au flux d'adatomes j et inversement proportionnelle à son épaisseur h, on en déduit que :

$$v \sim \frac{j}{h} \sim \frac{E_s}{h} \times \frac{1}{w} \times \frac{1}{h} \sim \frac{E_s}{h^2 w} \tag{2.7}$$

En intégrant les paramètres physiques on obtient l'expression de la vitesse de recul v donnée dans l'article [18] :

$$v = \frac{\Omega^2}{h^2 w a^2} Dc \frac{E_s}{kT} \tag{2.8}$$

où Ω et a sont des facteurs géométriques (resp. volume atomique et distance inter-atomique de surface), D est le coefficient de diffusion des adatomes et c leur concentration (fraction). La diffusion des espèces en surface et leur formation sont des processus thermiquement activés qui dépendent fortement de la température à travers respectivement l'énergie de barrière de diffusion E_{diff} et l'énergie de formation des espèces diffusantes E_{form}.

$$Dc = D_0 c_0 e^{-\frac{E_{diff}+E_{form}}{kT}} \tag{2.9}$$

où D_0 et c_0 sont des constantes.

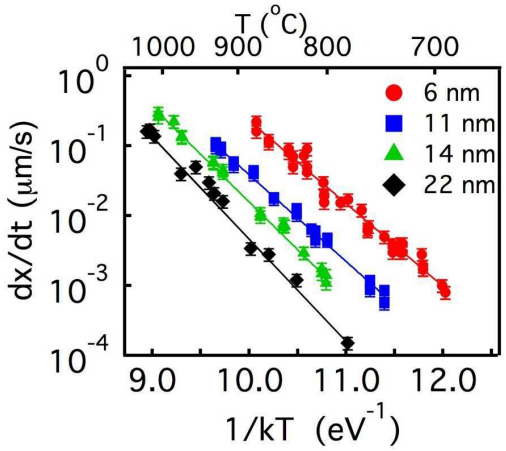

Figure I.7 – *Analyse quantitative de la vitesse de démouillage $v = dx/dt$ en fonction de la température et pour différentes épaisseurs initiales de film.*

L'étude de la vitesse de démouillage en fonction de la température et l'épaisseur h des films minces nous a permis d'estimer le domaine de validité de l'équation 2.8 et de donner une estimation de l'énergie d'activation $E_a = E_{diff} + E_{form}$. La figure I.7 montre dans un graphe d'Arrhénius des

vitesses de front de démouillage pour différentes épaisseurs de film. L'énergie d'activation est estimée à $E_a = 2.0 \pm 0.2$ eV en accord avec des mesures expérimentales de vitesse de guérissage de surface de Si(100) gravées (2.3 eV [24]).

2.3 Anisotropie cristalline (article joint [3])

L'anisotropie cristalline joue à plein dans le processus de démouillage solide de films minces monocristallins. La forme carrée des figures de démouillage des films de Si(100) observées en LEEM, la présence de facettes en particulier $\{111\}$ et $\{113\}$ mesurées en GISAXS ainsi que l'épaississement du bourrelet par nucléation/croissance de nouveaux plans atomiques sur sa facette sommitale sont toutes des manifestations du caractère anisotrope de la structure cristalline. Dans cette partie je présente une autre conséquence remarquable du caractère anisotrope de la structure cristalline, i.e. l'anisotropie des vitesses de démouillage des fronts droits de silicium et plus particulièrement le caractère singulier de la vitesse de recul du front $\langle 110 \rangle$ [21]. Pour aborder cette question de l'anisotropie des vitesses de démouillage, il faut s'affranchir du démouillage spontané induit par la nucléation hétérogène de trous sur des défauts interfaciaux. Pour contourner ce problème nous avons, dans le cadre de la thèse de Thibault Passanante, réalisé par lithographie électronique des tranchées rectilignes dans des directions bien définies dans les films de Si.

Sur la figure I.8 sont montrés le principe de fabrication des tranchées en utilisant les moyens de la plate-forme de proximité C'Nano-PACA "Planète" et quelques images des structures obtenues par microscopie optique et microscopie à force atomique. En particulier nous nous sommes attachés à réaliser des front droits dans les directions singulières $\langle 110 \rangle$ et $\langle 100 \rangle$ pour lesquelles nous pouvions attendre un comportement original compte tenu des résultats précédents concernant le démouillage spontané. La figure I.9 montre que les fronts $\langle 100 \rangle$ sont instables morphologiquement générant l'apparition de doigts de silicium perpendiculaires à la direction initiale du front. Les fronts orientés selon la direction $\langle 110 \rangle$ sont quant à eux stables morphologiquement et reculent à une vitesse beaucoup plus faible (facteur

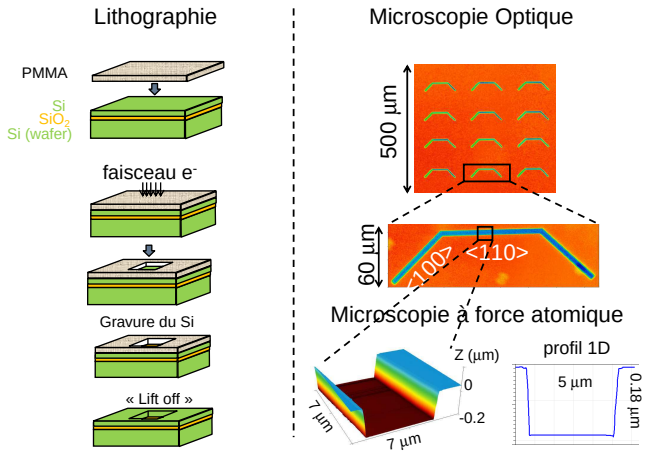

Figure I.8 *– Gauche : Principe de la fabrication des fronts de démouillage par lithographie électronique. Droite : Images de la surface gravée par microscopie optique et microscopie à force atomique.*

supérieur à 10). Cette différence spectaculaire, prédite théoriquement par O. Pierre-Louis [8,9] dans le cas de solides anisotropes, est ici observée expérimentalement.

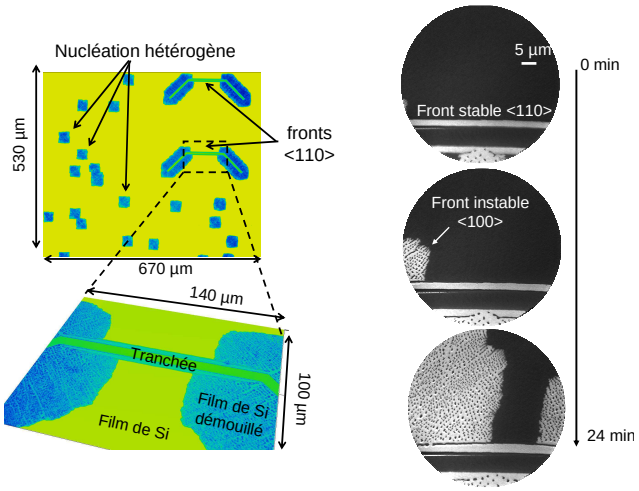

Figure I.9 *– Gauche : Images post-mortem par microscopie optique de la morphologie de zones de démouillage. On peut y voir, des zones carrées de démouillage provenant de la nucléation sur défauts et, sur les zones préalablement gravées, un démouillage préférentiel à partir des fronts orientés selon la direction* $\langle 100 \rangle$*. Droite : Séquence d'images LEEM en champ clair d'un film de Si d'épaisseur* 22 ± 2 *nm* ($T = 930°$) *montrant un front stable reculant à vitesse très réduite tandis que des fronts instables démouillant et provenant de zones éloignées envahissent la surface du film.*

Nous avons étudié la vitesse de recul du front au cours du temps. Contrai-

rement au cas de la nucléation hétérogène où le front atteint une vitesse constante dès que l'instabilité s'est suffisamment développée, la vitesse de recul du front stable n'est pas constante. Il y a un ralentissement progressif de la vitesse du front suivant une loi $x(t) = t^{\alpha}$. Expérimentalement nous avons obtenu des valeurs de $\alpha \sim 0.3 - 0.4$ (voir Fig. I.10).

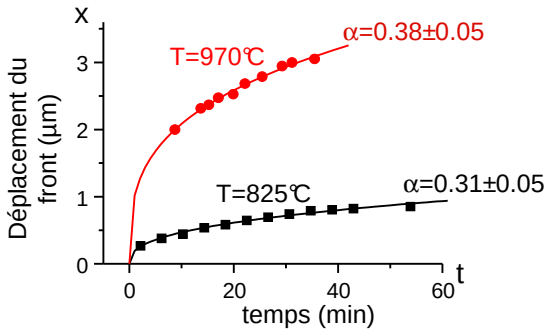

Figure I.10 – *Mesures expérimentales et ajustements des vitesses de recul à différentes températures de fronts droits orientés selon la direction* $\langle 110 \rangle$.

Le recul du front s'accompagne d'un épaississement du bourrelet que l'on mesure expérimentalement en LEEM par imagerie en champ sombre (voir figure I.11). En effet l'alternance d'un contraste noir/blanc au sommet du bourrelet signe la complétion de nouveaux plans atomiques sur la facette sommitale (001). L'épaisseur du bourrelet suit une croissance nonlinéaire de la forme $h \sim t^{\beta}$ avec $\beta \sim 0.3 - 0.4$. Ces loi d'échelle expérimentales à la fois pour le recul et l'épaississement sont à comparer aux modèles proposés dans le cadre de la théorie proposée par Mullins [2, 25], Brandon et Bradshaw [1] puis Wong [3]. Ces modèles prédisent un recul du front en $t^{2/5}$ et un épaississement en $t^{1/5}$. On observe un écart avec les données expérimentales notamment en ce qui concerne l'évolution temporelle de l'épaississement. Cet écart est attribuable probablement au processus de nucléation/complétion de nouveaux plans atomiques sur la terrasse sommitale. La dynamique de croissance spécifique d'une facette ne peut être correctement traitée dans le cadre de cette théorie. Le facettage des fronts

de démouillage a été récemment pris en compte par O. Pierre-Louis et ses collaborateurs sans toutefois permettre un accord quantitatif avec nos données expérimentales. Il semblerait que le processus de nucléation utilisé dans cette modélisation (théorie capillaire) ne soit pas applicable au silicium à ces températures (nucleus de taille très inférieure à la distance interatomique) comme nous l'avons discuté dans [21].

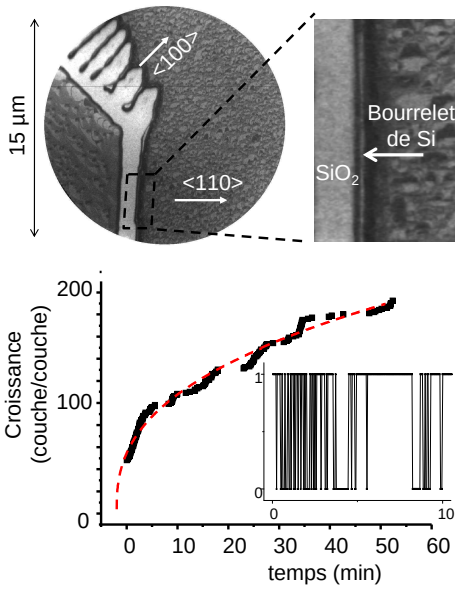

Figure I.11 – *Image LEEM du recul d'un front stable* $\langle 100 \rangle$ *et d'un front instable* $\langle 110 \rangle$*. Sur le front stable l'alternance du contraste noir/blanc au sommet du bourrelet a permis d'évaluer l'évolution temporelle de la hauteur du bourrelet en nombre de monocouches atomiques par minutes.*

Notons enfin que la planéité du sommet du bourrelet est remarquable avec des terrasses de dimensions supérieures au micron allongées dans le sens de sa longueur. On observe aussi que les petits décalages qui apparaissent sur le bord du front lors de son recul sont guéris préservant le caractère rectiligne du front de démouillage et montrant par la même que la stabilité morphologique du front est assez robuste (voir article [21]).

2.4 Ge/SiO_2 versus Si/SiO_2 (articles joints $[4, 5]$)

Si le rôle des facettes est clairement mis en évidence dans le cas du démouillage de Si/SiO_2, le démouillage de films de Ge(001) sur SiO_2 en

est une autre illustration. Le Ge(001) présente la même structure cristalline que le silicium (diamant) et des propriétés physiques voisines. On pourrait donc s'atteindre en principe à des différences faibles concernant la dynamique de démouillage de ces deux matériaux. Sur la figure I.12, une séquence d'images PEEM montre le démouillage d'un trou de Ge/SiO_2. Des structures semblables à celles observées sur le silicium apparaissent avec toutefois des différences notables. Les embranchements successifs forment une structure dendritique contrairement au cas du silicium. Les doigts formés font des angles parfaitement droits entre eux alors que dans le cas du silicium les doigts ont des orientations moyenne variable ($\pm 15°$ autour de la direction $\langle 100 \rangle$). Enfin les côtés des carrés de démouillage de Ge sont alignés dans la direction $\langle 100 \rangle$ tandis qu'ils sont alignés dans la direction $\langle 110 \rangle$ dans le cas du silicium.

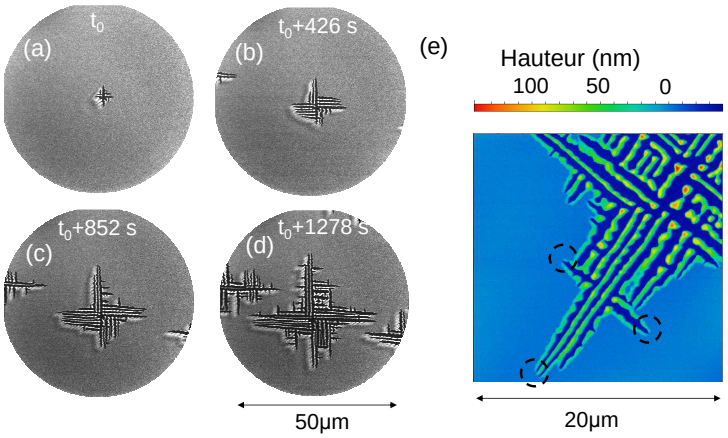

Figure I.12 *– (a)-(d) Séquence d'images PEEM montrant l'ouverture dendritique d'un trou de démouillage d'un film de Ge (épaisseur 28 nm, T=735°C). (e) Image AFM* ex situ *du même échantillon. Les zones encerclées montrent des extrémités d'interdigitations pointus.*

Pour interpréter ces différences nous avons entrepris de caractériser toutes les facettes présentes au cours du démouillage des films de Ge(100). Pour cela nous avons réalisé une campagne d'expériences à l'ESRF sur la ligne de lumière BM32. L'objectif était de mesurer *in situ* par GISAXS [26], le signal de diffusion diffuse des rayons X provenant des différentes facettes

cristallographiques. Nous avons mesuré deux jeux de données différents selon la température de démouillage (voir fig. I.13 et I.14) : (i) à basse température (∼800°C), les facettes {111}, {113} et {15 3 23} ont été mesurées. (ii) à haute température (∼890°C), seules les facettes {111}, {113} et {311} sont présentes [1].

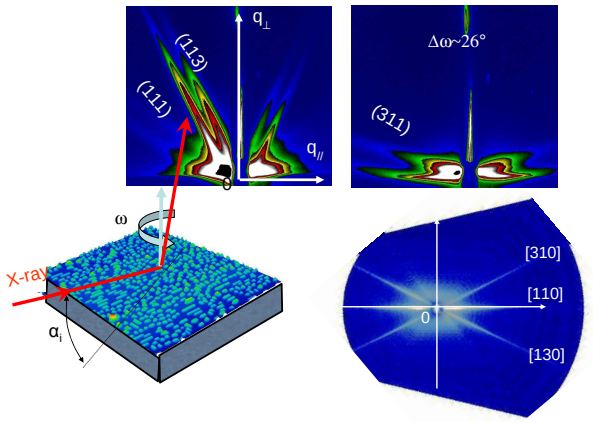

Figure I.13 *– Clichés GISAXS du démouillage à 890° C d'un film de Ge de 30 nm d'épaisseur. Le faisceau des rayons X est aligné selon les deux azimuts ⟨110⟩ et ⟨310⟩. Les facettes observées sont les facettes {111}, {113} et {311}. Carte de l'espace réciproque reconstituée au voisinage de l'origine à partir de 400 images GISAXS (30 s d'acquisition par image) enregistrées tous les 0.25°.*

La présence des facettes {15 3 23} dans le cas du démouillage du Ge est une différence importante avec le démouillage du Si durant lequel seules les facettes {111}, {113} et {311} sont présentes. Dans le cas du silicium les facettes qui limitent le processus de démouillage sont les facettes {111} et {113}. On les retrouve à la fois sur les fronts stables mais aussi à l'extrémité des interdigitations indiquant que c'est leur vitesse de recul qui est limitante [2]. Concernant le démouillage des films de germanium, les images par LEEM et AFM montrent que l'angle à l'extrémité des interdigitations est beaucoup plus aigu (voir fig. I.12e). Les facettes révélées expérimentalement par GISAXS et qui sont susceptibles de former ces angles sont du

1. les facettes {15 3 23} ont atteint leur température de transition rugueuse. Remarquons que la température de transition rugueuse de la facette {100} est également très proche : 860° C, [27]

2. Les mesures par LEEM, i.e. en vue de dessus, montrent que l'extrémité des interdigitations forme un angle droit. C'est la signature que deux facettes adjacentes sont par exemple du type $(11n)$ et $(1\bar{1}n)$

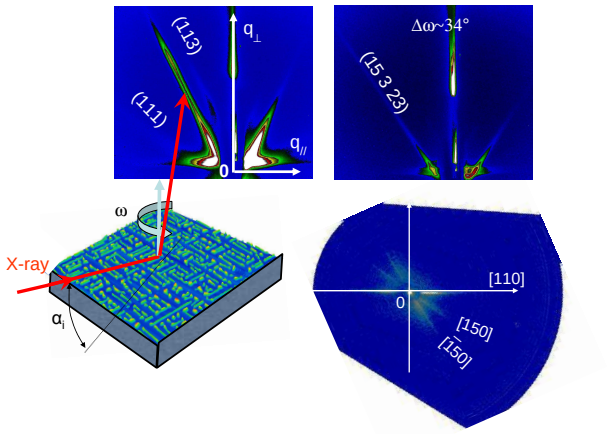

Figure I.14 *– Clichés GISAXS obtenus dans deux azimuts différents (⟨110⟩ et ⟨510⟩)du démouillage à 800° C d'un film de Ge de 33 nm d'épaisseur. Les facettes observées sont les facettes* {111}, {113} *et* {15 3 23}. *Carte de l'espace réciproque reconstituée au voisinage de l'origine à partir de 500 images GISAXS (30 s d'acquisition par image) enregistrées tous les 0.25°.*

type {15 3 23} ou {311}. Deux facettes adjacentes, e.g. (15 3 23) et (15 $\bar{3}$ 23) forment un angle projeté dans le plan de 22.6° (36.9° pour les facettes (311) et (3$\bar{1}$1)). Ces facettes limitent donc la dynamique de recul du front de Ge. Les conséquences en sont remarquables. Tout d'abord cela implique que les doigts de Ge sont alignés sur la bissectrice des deux axes de zone des facettes à l'extrémité de l'interdigitation, i.e. la direction ⟨110⟩. Comparés aux doigts de Si ils sont donc tournés de 45°. Cette orientation des doigts de Ge fait aussi qu'ils développent sur leurs bords latéraux des facettes qui ont comme axe de zone l'axe ⟨110⟩, i.e. les facettes {111}, {113} observées en GISAXS. Ces facettes confèrent aux doigts de Ge des propriétés singulières : une grande stabilité directionnelle (formation de structures à angle droit) et aussi une stabilité vis-à-vis du perlage (doigts très allongés et perlant tardivement) contrairement au Si. Ces différences conduisent finalement à une dynamique de démouillage profondément différente de celle observée pour le Si. Elle a fait l'objet d'une étude approfondie par GISAXS (voir article [19]) et par PEEM (voir article [20])

2.5 Conclusion et perspectives

La dynamique complète du démouillage de films monocristallins de silicium et de germanium d'épaisseur nanométrique a été étudiée à la fois sur le plan expérimental et sur le plan théorique. En particulier la microscopie à électrons lents, *in situ*, a permis de décrire en temps réel la dynamique d'agglomération du film [17, 18]. Quatre étapes du processus ont pu être distinguées en accord avec les travaux précédents [16] : (i) la nucléation d'un trou dans le film, (ii) la croissance de ce trou à laquelle est associée la formation d'un bourrelet facetté sur le front de démouillage, (iii) la déstabilisation de ce bourrelet qui conduit à la formation de digitations plus ou moins allongées (longues digitations dans le cas du Ge) et (iv) la fragmentation de ces digitations en nanocristaux.

Cette évolution complexe de la morphologie des films a été confrontée quantitativement et avec succès à des simulations Monte Carlo Cinétique en utilisant un jeu minimum de paramètres physiques que sont l'énergie de cohésion du film et celle d'adhésion sur le substrat ainsi que la température [17]. L'adéquation remarquable entre les expériences et les simulations numériques a permis de montrer que le démouillage solide est piloté par la réduction des énergies d'interface/surface et que le mécanisme élémentaire de déplacement de matière est la diffusion de surface, phénomène thermiquement activé. Elle nous a aussi permis de proposer un modèle analytique du phénomène de démouillage rendant compte de la vitesse de recul des fronts de démouillage en fonction de l'épaisseur du film et de la température. Pour accéder à une compréhension plus détaillée du processus de démouillage nous avons réalisé des fronts droits par lithographie électronique de façon à caractériser l'anisotropie des vitesses de démouillage en fonction de l'orientation du front [21]. Nous avons pu mettre en évidence que l'orientation cristallographique singulière $\langle 110 \rangle$ du silicium était morphologiquement stable (le front reste parfaitement droit tout en reculant) et que sa vitesse de recul était très fortement réduite par rapport aux autres orientations cristallographiques toutes instables. Les mesures *in situ* par diffusion centrale des rayons X en incidence rasante nous ont montré que ce front était probablement stabilisé par les facettes $\{111\}$ et $\{113\}$. Le

rôle des facettes a aussi été abordé dans le cas du démouillage des films de germanium. En particulier les facettes $\{15\ 3\ 23\}$ jouent un rôle déstabilisant pour le front $\langle 110 \rangle$ et conduisent à une cinétique de démouillage dendritique profondément différente de celle du silicium [19, 20]. Fort de ces avancées dans la compréhension du phénomène de démouillage nous souhaitons dans l'avenir, d'une part explorer les moyens de contrôle du démouillage, par exemple *via* l'adsorption d'une espèce étrangère qui jouerait sur la taille des facettes et sur les propriétés de diffusion de surface, et d'autre part étudier le démouillage à l'échelle plus locale notamment en nous intéressant à la dynamique de la ligne triple décrite en terme de marches atomiques.

ARTICLES SÉLECTIONNÉS : DÉMOUILLAGE DE FILMS SOLIDES

[1] : Dynamique du démouillage dans le système Silicium sur isolant (SOI)
Bussmann *et al.*, New J. Phys. (2011)

New Journal of Physics
The open-access journal for physics

Dynamics of solid thin-film dewetting in the silicon-on-insulator system

E Bussmann[1,3], F Cheynis[1], F Leroy[1], P Müller[1,4] and O Pierre-Louis[2]

[1] Centre Interdisciplinaire de Nanoscience de Marseille (CINaM) CNRS UPR 3118, Aix-Marseille Université, 13288 Marseille, France
[2] LPMCN, Université Lyon 1, 43 Bd du 11 novembre, 69622 Villeurbane, France
E-mail: muller@cinam.univ-mrs.fr

New Journal of Physics **13** (2011) 043017 (9pp)
Received 23 December 2010
Published 14 April 2011
Online at http://www.njp.org/
doi:10.1088/1367-2630/13/4/043017

Abstract. Using low-energy electron microscopy movies, we have measured the dewetting dynamics of single-crystal Si(001) thin films on SiO_2 substrates. During annealing ($T > 700\,^{\circ}C$), voids open in the Si, exposing the oxide. The voids grow, evolving Si fingers that subsequently break apart into self-organized three-dimensional (3D) Si nanocrystals. A kinetic Monte Carlo model incorporating surface and interfacial free energies reproduces all the salient features of the morphological evolution. The dewetting dynamics is described using an analytic surface-diffusion-based model. We demonstrate quantitatively that Si dewetting from SiO_2 is mediated by surface-diffusion driven by surface free-energy minimization.

S Online supplementary data available from stacks.iop.org/NJP/13/043017/mmedia

Solid thin films play a variety of vital technological roles, e.g. as catalytic membranes, and are key building-blocks of microelectronics. Numerous thin-film systems are known to be susceptible to *dewetting* instabilities, wherein the two-dimensional (2D) film spontaneously agglomerates into compact 3D nanostructures—typically during thermal annealing—which may activate mass-transport processes in or on the film [1]–[22]. From one viewpoint, dewetting is a problem that e.g. complicates the fabrication of thin-film-based devices by imposing constraints on the thermal budget during processing [1]. However, thin-film dewetting

[3] Present address: Sandia National Laboratories, Albuquerque, NM 87185, USA.
[4] Author to whom any correspondence should be addressed.

is also an innovative route for producing surface-adsorbed nanocrystals used in catalysis, vapor–liquid–solid nanowire growth and emerging nanoscale devices [2, 3].

To understand solid thin-film dewetting instabilities, a key challenge is to explore the interplay between kinetic processes and thermodynamic forces that transforms the film into 3D structures [19]–[22]. Silicon-on-insulator (SOI), an essential building-block of microelectronics, is an excellent model system to study solid-state dewetting. Our samples are single-crystal Si(001) films, elastically relaxed and dislocation-free, on amorphous SiO_2 substrates. Previous works showed, by post-mortem *ex-situ* measurements, that < 100 nm thick Si films dewet from SiO_2, producing Si nanocrystals during annealing ($T > 700^{\circ}$C) [5]–[17]. The Si nanocrystals have a relatively high Young's contact angle of 72–73 $^{\circ}$ [10, 14], implying that dewetting is favorable from a surface free-energy standpoint. It has been suggested that SOI dewetting is driven either by thermal expansion mismatch stress [7, 8], or by surface and interfacial free energies [12, 14], but neither suggestion has been justified by connecting measurements with comprehensive models.

Here, we report on a quantitative characterization of the dewetting dynamics of SOI measured *in situ* in real time using low-energy electron microscopy (LEEM). Solid-state SOI dewetting occurs in a fluid-like mode, with capillary instabilities decomposing the Si film into 3D finger structures, which in turn decompose into Si nanoislands. We show that the entire complex morphological evolution is reproduced by a kinetic Monte Carlo (KMC) model in which dewetting is driven by surface free energies and mass transport is mediated by surface diffusion. We develop a surface-diffusion-based model of the dynamics. By fitting the model to our data, we show that SOI dewetting is driven by surface free-energy minimization. Our results provide a complete physical picture of one mode of solid thin-film dewetting, definitively resolving the uncertainty about the cause of SOI dewetting.

The experiments are performed in an Elmitec LEEM III at pressures $< 10^{-9}$ Torr. The LEEM measurements are complemented by *ex-situ* non-contact atomic force microscopy (AFM; PSIA-XE 100) measurements of the surface morphology at room temperature. Our samples are *bonded* SOI (CEA-Leti, France) fabricated by the *Smart Cut*^{TM} process. Each sample is a single-crystal Si(001) film, 6, 11, 14 or 22 ± 2 nm thick, bonded to a 150-nm-thick α-SiO_2 layer on an Si(001) wafer. Prior to the experiments, the samples are cleaned by a published formula [23]. Dewetting is measured by recording a LEEM image sequence at a fixed rate (0.3–10 Hz) while annealing the sample ($T > 700^{\circ}$C). The images are acquired in a darkfield mode from electrons in a 1/2-order diffraction spot associated with either the Si(001)-2×1 or 1×2 surface reconstructions [24]. Adjacent terraces have orthogonal (2×1 versus 1×2) reconstructions, and so they appear alternately bright and dark, allowing us to see the step-terrace structure of the surface with 10 nm resolution. LEEM movies show the nanoscale motion of atomic-height steps on the surface, which is an indication of surface diffusion. We can see the larger-scale evolution of dewetting, e.g. shape and size of the 3D features, and simultaneous local processes, e.g. layer-by-layer nucleation and growth on facets of 3D features.

Figure 1(a) shows several images revealing the key features of the SOI dewetting process in which (i) voids open at defects in the Si, exposing the oxide, (ii) the voids grow, evolving a 3D Si rim, (iii) the rim undergoes a (capillary) instability to form Si fingers and (iv) the fingers break down into Si nanocrystals [12, 14]. A typical movie revealing the complete dewetting sequence (after square-void nucleation) can be found in the supplementary data, available at stacks.iop.org/NJP/13/043017/mmedia. On each sample, numerous voids open simultaneously

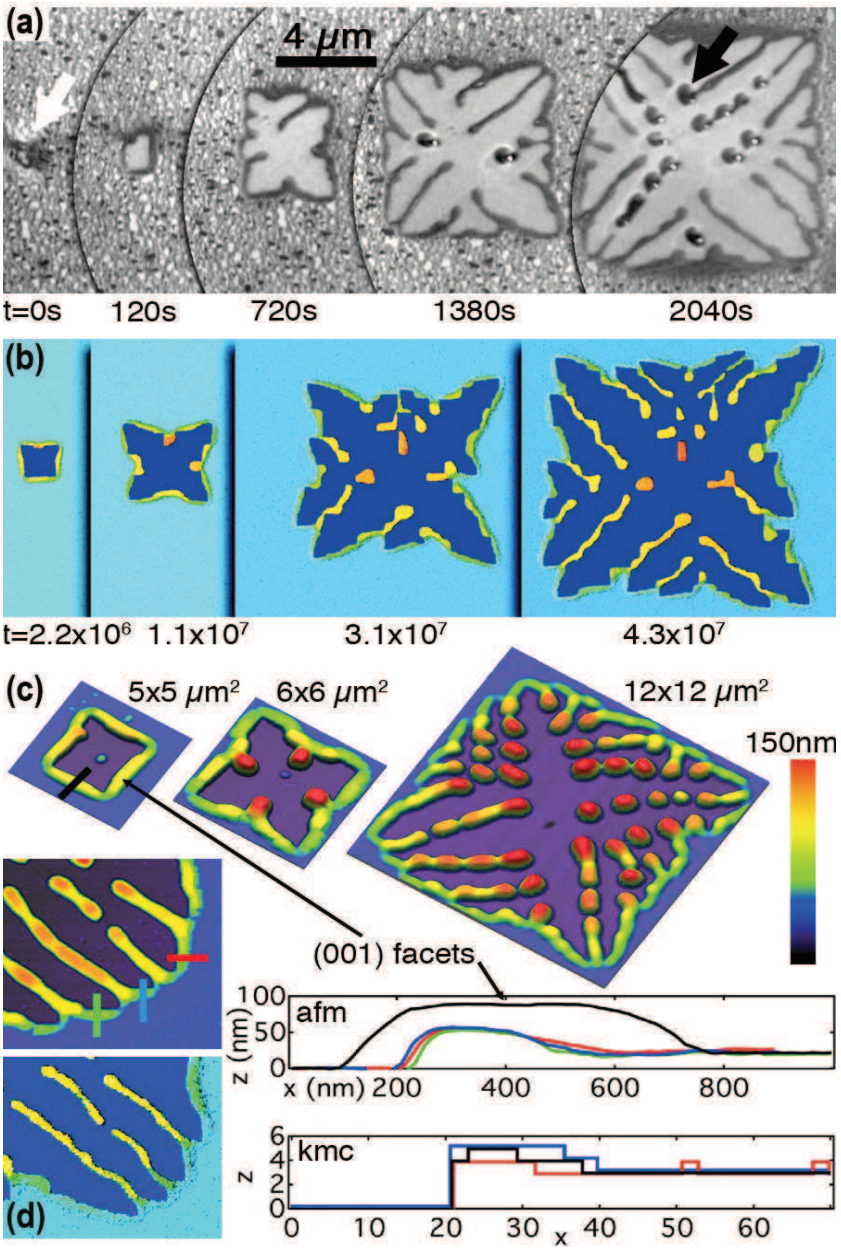

Figure 1. (a) LEEM images of SOI dewetting (SOI, 22 ± 2 nm thick, $T = 870\,^{\circ}$C, electron energy $= 7.8$ eV). Bright–dark speckling is due to the 2×1 Si surface (darkfield conditions). Dewetting voids nucleate at defects (white arrow, $t = 0$ s). Si nanocrystals (black arrow) appear distorted owing to electronic charging effects. (b) KMC simulation of dewetting ($E_s/J = 1.5$ and $k_B T/J = 0.4$, 1200×1200 lattice, initial film thickness $= 3$ layers). (c) AFM images of various stages of dewetting along with line profiles through the dewetting rim. The location of the profiles is indicated in the images. (d) Dewetting rim in the KMC model along with a few line profiles near void fingertips.

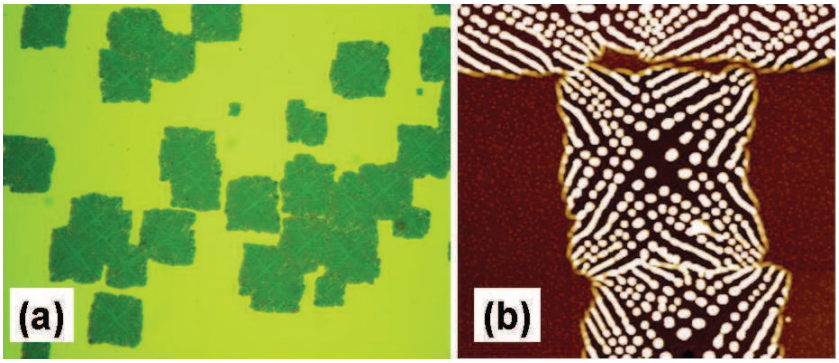

Figure 2. Large-scale images of dewetting: (a) optical image (field of view $100 \times 130\,\mu m^2$) with several similar square-shaped dewetting zones. (b) AFM image (field of view $30 \times 30\,\mu m^2$). Note that these images have been taken in the latter stages of the dewetting process where the dewetted zones start to coalesce.

at the beginning of the anneal, and undergo the same qualitative evolution exposing similar square-shaped dewetted areas (see figure 2). The qualitative features of the dewetting process are identical for 6–22 nm thick Si films, in agreement with recent experimental results [6, 9], which show that, in this thickness range, dewetting occurs via hole nucleation regardless of the thickness of the film. For thinner films (< 4 nm) hole nucleation is homogeneous, and a different arrangement of islands, with poorer order, is observed (in agreement with KMC simulations of [29]). Here we present results for 11, 14 and 22 nm thick films. Note that since the 2×1 and 1×2 surface reconstructions are visible during the whole dewetting process, this is a solid-state dewetting mechanism. This behavior is expected since (i) although the melting temperature of nanostructures is size dependent, Wautelet [25] has shown that the melting point reaches $T = 1000\,^{\circ}C$ for 3D Si particles of radius 6 nm, and (ii) there is no surface premelting of the Si(001) surface in this temperature range [26, 27].

A surface-energy-driven KMC model [28, 29] reproduces the key features of the dewetting experiments. In the KMC model, a film of material A is placed on a substrate B, which is flat and frozen. Units of A occupy a simple cubic lattice, bound by energy $-nJ$, where n is the number of in-plane nearest neighbors. Units of A in direct contact with the substrate have an additional energy E_s, which is the dewetting driving force. Under the conditions of the model, $E_s = \gamma_A + \gamma_{A-B} - \gamma_B$, where γ_A and γ_B are surface free energies, and γ_{A-B} is the interfacial free energy. $E_s > 0$ enforces dewetting. In a simulation, a hole is made in film A to mimic heterogeneous nucleation; then the system evolves by moving units of A to nearest-neighbor sites at rates $\nu = \nu_o \exp(-(nJ - \delta_{0i} E_s)/k_B T)$, where δ_{0i} is the Kronecker delta ($i = 0, 1, 2, 3, \ldots$ is the layer in which the A unit sits). There are two parameters in the model, E_s/J and $k_B T/J$. Figure 1(b) shows typical simulation results. Owing to computational time limitations, the simulation uses a film three monolayers thick[5,6]. Comparing figures 1(a) with (b), it is clear that this 'coarse' KMC simulation reproduces all the complex features of the experiments, which means that the model contains the correct ingredients

[5] Simulations with $0.5 < E_s/J < 2$ and $k_B T/J = 0.4$ yield the same features. For SOI, we estimate $0.2 < J < 1\,\text{eV atom}^{-1}$, $1 < E_s < 2\,\text{eV atom}^{-1}$ and $k_B T \sim 0.1\,\text{eV}$, so $2 < E_s/J < 7$ and $0.1 < k_B T/J < 0.5$.

[6] With only three layers, the formation of new voids must be forbidden to prevent homogeneous dewetting.

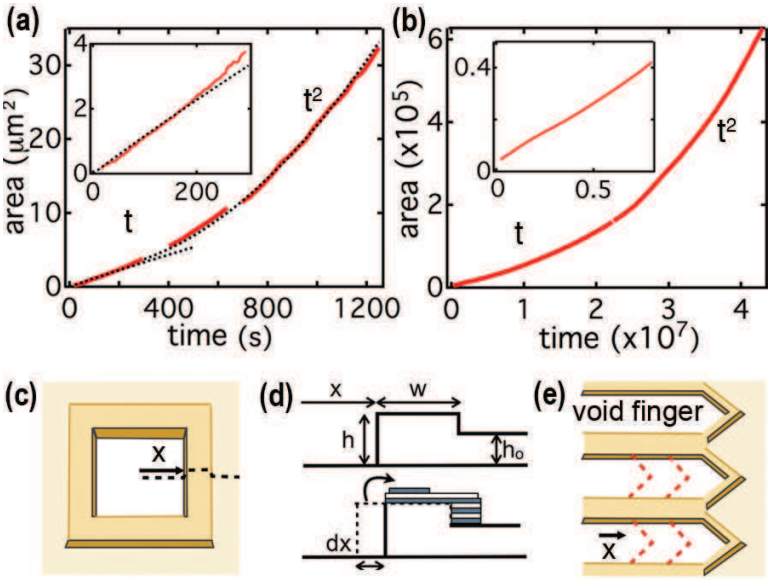

Figure 3. Dewetted area versus time in (a) the experiments and (b) the KMC model for the voids shown in figure 1. The unit of time is ν_o^{-1}, the area is in 'units of A'. Insets: early linear growth. Dotted lines: the results of our analytic model. (c–e) Schematic diagrams of the dewetting dynamics. (c) A square void and rim. (d) The rim grows, and thickens via nucleation on the top facet, as the void grows. (e) Later stages: finger growth.

(surface free energies and surface diffusion). Simulations over a range of E_s/J values yield the same qualitative features (see footnotes 5 and 6).

Let us now compare the qualitative features of the KMC simulations to the SOI dewetting experiments. Owing to the surface-free-energy cost to spontaneously form holes in the crystal surface [14], dewetting starts with void formation at preexisting extrinsic defects, such as pinholes and scratches that expose the oxide (figure 1(a)). In this early time of the dewetting, the voids evolve a square shape with ⟨110⟩-oriented sides (⟨100⟩ in the KMC model). Insets of figures 3(a) and (b) show that the void area grows linearly in time (i.e. $x \propto t^{1/2}$). The material (Si) expelled from a void is conserved in a 3D rim around the void (figure 1(c))[7]. The rim is facetted, e.g. {100} and {111} in experiments [10, 11] and {100} in the KMC model. There is a large (001) top facet on the rim (see the black AFM lineprofile in figure 1(c)). In the LEEM and the KMC model, the rim is directly observed to thicken via layer-by-layer nucleation and growth on the (001) top-facet. A schematic diagram of the void–rim evolution is shown in figures 3(c) and (d).

The shape evolution of the voids is shown in figure 4 in stroboscopic images compiled from LEEM and KMC data. Figure 4 shows that the KMC simulation captures the local dynamics of the void shape evolution observed in the experiments.

As the voids grow, their shape evolves from square to star-like (figure 4(a)). The center of the rim thickens relative to the corners (figures 1(a)–(c)). The thickened regions move outward with $x \propto t^{1/2}$, while the void corners move out at a constant velocity, i.e. $x \propto t$ (figures 4(e) and (f)).

[7] Some Si (< 2%) is lost to a reaction, $Si + SiO_2 \rightarrow 2SiO$, at the triple line. The SiO desorbs into the vacuum.

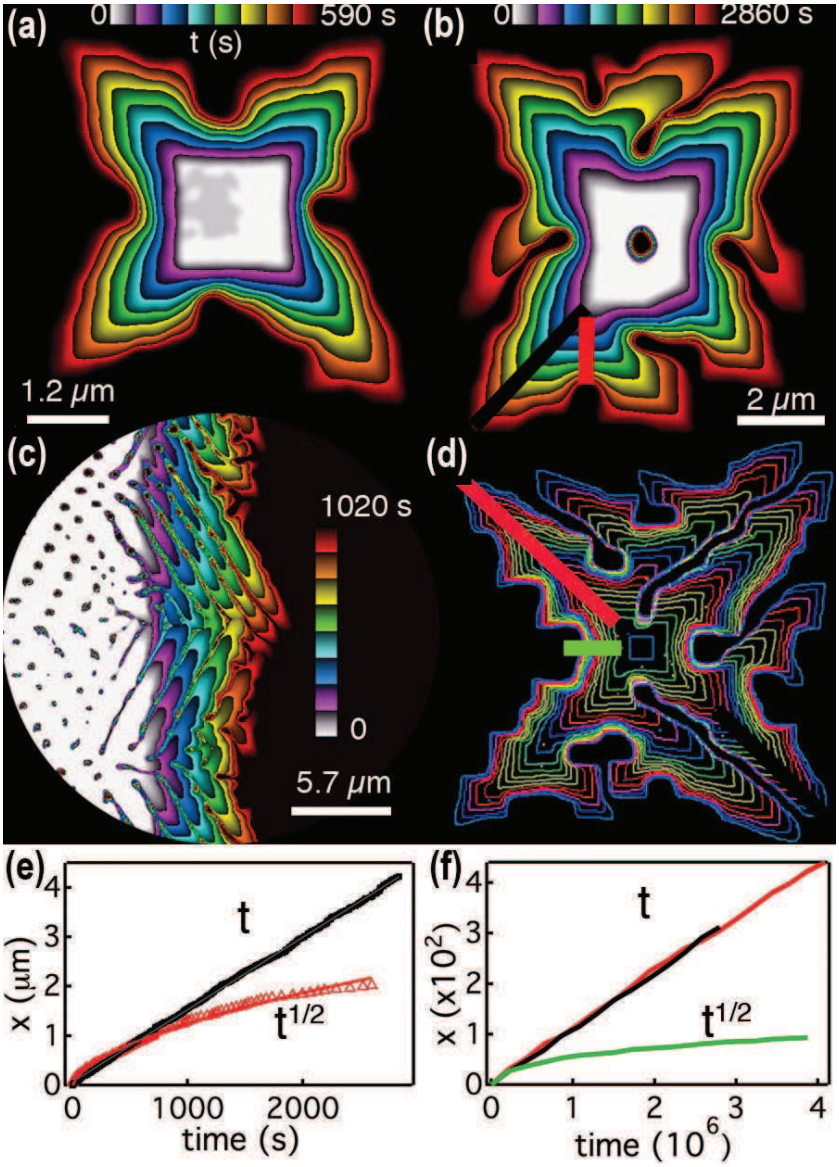

Figure 4. Stroboscopic images showing the void edge position versus time (color). (a) Early times (11 nm thick SOI, 800 °C). (b) Finger formation (14 nm SOI, 800 °C). (c) Late times (14 nm SOI, 850 °C). (d) Finger formation in the KMC model ($E_s/J = 1$, $k_BT/J = 0.4$, 1200×1200 lattice, initial thickness = 3 layers). (e, f) Position of the void-edge-versus-time along lines indicated in the upper panel in (e) experiments and (f) the KMC model. The unit of time is ν_o^{-1}; the length is in units of Å.

The thickened regions evolve into 3D Si fingers, which can grow to >10 times the initial film thickness. The finger development in the experiment and the KMC model is qualitatively similar (figures 4(b) and (d)). As the voids continue to open, periodic rim thickening seeds new fingers at a characteristic wavelength along the void edge. The periodic thickening of the rim is similar to the rim-pinching instability modeled in [30, 31]. This instability is driven by surface

free energies (reduction of the surface area at fixed volume). Compact capillary fingers are a common feature of solid and fluid thin-film dewetting systems [18, 30, 32]. The fingers are uniformly oriented with respect to the void edges. In the experiment, the fingers are oriented at 25–45 ° with respect to the ⟨110⟩-oriented dewetting edge. Previous works claim that the Si finger direction, which is quoted as ⟨130⟩ ($\sim 27°$), is determined by the presence of facets, e.g. {311}, on the sides of the fingers [10, 13, 14]. In the KMC model, the ⟨110⟩-oriented fingers are not bounded by low-free-energy facets, but rather by relatively high-free-energy {110} surfaces. Thus, the fingers in the KMC model are oriented by a balance of surface kinetic processes.

Finally, as the rim retracts, the Si fingers lengthen and then break down at a characteristic wavelength into Si nanocrystals (figure 1). The breakdown, a Plateau–Rayleigh capillary instability, is driven by surface energies (reduction of Si surface area at fixed volume). In the long-time limit (figure 4(c)), straight fingered void edges move at a constant speed set by finger growth, $x \propto t$, leaving Si islands in their wake.

To connect the void growth rate with the underlying physics, i.e. the thermodynamic driving force and the limiting mass-transport mechanism, governing dewetting, we have built an analytic 2D model. We assume that the rim position, $x(t)$, moves with a speed determined by an Einstein relation $\mathrm{d}x/\mathrm{d}t = -\mu F$, where μ is a surface-diffusion-based mobility, and F is a thermodynamic driving force [33]. In the model geometry in figures 3(c) and (d), the driving force per unit length acting to displace the rim outward a distance $\mathrm{d}x$ is $F = -E_s + 2\gamma_{\mathrm{Si}}(d)h/\mathrm{d}x$. Typically, $E_\mathrm{s} \gg 2\gamma_{\mathrm{Si}}\mathrm{d}h/\mathrm{d}x$, so the driving force is $\approx -E_\mathrm{s}$. Using Morgenstern's method [34], with the approximation that the mobility is limited by diffusion across the width, w, of the rim, we obtain [29] $\mu = \Omega^2 D_\mathrm{s} c/a^2 h^2 w k_\mathrm{B} T$, where Ω and a^2 are the volume and surface area of an atom, and $D_s c$ is the surface self-diffusivity on the rim. So $\mathrm{d}x/\mathrm{d}t = -\mu F = (\Omega^2 D_s c/a^2 h^2 w)(E_S/k_\mathrm{B}T)$.

To fit void growth, it is necessary to know how the rim grows, i.e. we need to know $h(t)$ and $w(t)$. A recent model [29] proposed that the growth of a facetted dewetting rim is controlled by *size-dependent nucleation-limited dynamics*, which governs the growth of 3D structures in some other crystalline dewetting systems, e.g. ice/Pt(100) [21]. In this regime, the growth of facetted 3D structures is limited by the rate of layer nucleation, which is typically a strong decreasing exponential function of the size of the structure. In our KMC model, the rim thickens obeying size-dependent nucleation-limited dynamics, where the nucleation rate is a strong exponentially decreasing function of the height, i.e. $\mathrm{d}h/\mathrm{d}t \propto \exp(-h/k_\mathrm{B}T)$ [29]. By contrast, in the experiments there is no distinct evidence of size-dependent nucleation-limited rim growth: new layers nucleate on the top facet at a roughly constant rate independent of its height.

To fit the void growth dynamics in the early times ($x \propto t^{1/2}$), we approximate that the rim grows with a *fixed aspect ratio*, $(h - h_\mathrm{o})/w =$ constant. The black AFM lineprofile in figure 1(c) shows that $h - h_\mathrm{o} \approx 70$ nm and $w \approx 600$ nm. With a fixed aspect ratio, $(h - h_\mathrm{o})/w = 1/9$, and mass conservation, $x h_\mathrm{o} = w(h - h_\mathrm{o})$, we numerically integrate our expression for $\mathrm{d}x/\mathrm{d}t$ to determine the void area-versus-time. The surface self-diffusivity, $D_s c = 7.4 \times 10^6\,\mathrm{nm^2\,s^{-1}}$, of Si(100) at $T = 870\,^\circ\mathrm{C}$ is taken from [35], and E_s is the fit parameter. The best fit, inset of figure 3(a), is $E_\mathrm{s} = 14\,\mathrm{eV\,nm^{-2}}$, within the range $E_\mathrm{s} \sim 7$–$15\,\mathrm{eV\,nm^{-2}}$ estimated from published values of the Si surface free-energy [36]–[38][8]. Our calculation shows that a driving force

[8] From [37]–[39]: $\gamma_\mathrm{si} \approx 5$–$9\,\mathrm{eV\,nm^{-2}}$ at $T \sim 800\,^\circ\mathrm{C}$. Anisotropy of γ_si is negligible ($\sim 10\%$) [37, 38]. From AFM data: $\theta_c \approx 50$–$80\,^\circ$. Using these numbers: $E_\mathrm{s} = \gamma_{\mathrm{Si}}(1 + \cos\theta_c) \approx 7$–$15\,\mathrm{eV\,nm^{-2}}$.

consistent with known values of the surface and interfacial free energies for the Si/SiO_2 system can cause dewetting at the rates we measure.

With this *fixed aspect-ratio* assumption, our analytic model asymptotically obeys $x \propto t^{\beta}$, where $\beta = 2/3$ in the short-time limit. The exponent β decreases with time, and for large times $\beta = 2/5$, which is consistent with the motion of a straight dewetting rim in the isotropic diffusion-limited model of Wong [39], but in disagreement with the $\beta = 1/4$ exponent predicted by Srolovitz and Safran [40]. The assumption of a rectangular cross-section with a fixed aspect ratio has two main advantages. Firstly, it accounts for the crystalline anisotropy of Si, with a wide facet on the top of the rim. Secondly, it leads to a simple analytical solution for arbitrary times, even outside the asymptotic large-time limit discussed by Wong [39].

After finger formation, void growth reaches a steady state in which the void area $\propto t^2$ (figure 3), i.e. the linear dimensions of the void increase at a constant speed set by the growth of the void fingers (figures 4(b) and (d)). That the void fingertips move outward at a constant speed implies that the rim near the fingertips propagates with a conserved volume and shape, i.e. mass is efficiently shuttled from the film into the Si fingers. In the experiment at $T = 870\,^{\circ}\mathrm{C}$ (figure 3(a)), the void fingers grow at $2.2 \pm 0.5\,\mathrm{nm\,s^{-1}}$. From our expression for $\mathrm{d}x/\mathrm{d}t$, we calculate $E_s = 10\,\mathrm{eV\,nm^{-2}}$. We have used $h = 60\,\mathrm{nm}$, $w = 250\,\mathrm{nm}$, from the AFM data in figure 1(c). In KMC simulations with $E_S/J = 1$ and $k_B T/J = 0.4$, the finger velocity is $\mathrm{d}x/\mathrm{d}t = 1.1 \times 10^{-4} v_0$, where the length unit is the lattice spacing a. Our formula for the speed, with $h_1 \approx 4$ and $w \approx 7$ observed in the simulations, gives $\mathrm{d}x/\mathrm{d}t = 0.4 \times 10^{-4} v_0$, in reasonable agreement with the simulations.

To conclude, we have presented measurements of SOI dewetting dynamics. Dewetting begins with the growth of voids surrounded by a thickening Si rim. In the early stage of dewetting, rim growth determines the dynamics and the void area grows linearly with time. In later stages, dewetting is dominated by void finger growth, and the dewetted area grows as t^2. A surface-energy-driven KMC model reproduces the dewetting morphological evolution. A simple analytic model shows that the void growth rate is consistent with a surface free-energy driving force. Our results show that SOI dewetting is mediated by surface diffusion driven by surface free energies with a driving force $E_s \sim 10$–$14\,\mathrm{eV\,nm^{-2}}$.

Acknowledgments

We thank T Passanante for sample preparation. This work was supported by ANR PNano Grant DEFIS (ANR 08-Nano-036).

References

[1] Jahan C *et al* 2005 *J. Cryst. Growth* **280** 530–8
[2] Kodambaka S V *et al* 2007 *Science* **316** 729
[3] Yuan H-C *et al* 2005 *Proc. SPIE* **5971** 597118
[4] Schrank C *et al* 2004 *Thin Solid Films* **459** 276
[5] Ono Y *et al* 1995 *Japan J. Appl. Phys.* **34** 1728
[6] Nuryadi R *et al* 2000 *Appl. Surf. Sci.* **159-160** 121
[7] Legrand B *et al* 2000 *Appl. Phys. Lett.* **76** 3271
[8] Legrand B *et al* 2002 *J. Appl. Phys.* **91** 106
[9] Nuryadi R *et al* 2002 *J. Vac. Sci. Technol.* B **20** 167

[10] Yang B *et al* 2005 *Phys. Rev.* B **72** 235413
[11] Sutter P *et al* 2006 *Appl. Phys. Lett.* **88** 141924
[12] Danielson D T *et al* 2006 *J. Appl. Phys.* **100** 083507
[13] Dornel E *et al* 2006 *Phys. Rev.* B **73** 115427
[14] Danielson D T 2008 *PhD Thesis* MIT, Boston, MA
[15] Dornell E 2007 *PhD Thesis* Grenoble
[16] Fan Y *et al* 2008 *Japan J. Appl. Phys.* **47** 1461
[17] Burhanudin Z A *et al* 2005 *Appl. Phys. Lett.* **87** 121905
[18] Jiran E and Thompson C V 1990 *J. Electron. Mat.* **19** 1153
[19] Thurmer K *et al* 2003 *Phys. Rev.* B **68** 155423
[20] Ling W L *et al* 2004 *Surf. Sci.* **570** L297
[21] Thurmer K and Bartelt N C 2008 *Phys. Rev. Lett.* **100** 186101
[22] McCarty K F *et al* 2009 *New J. Phys.* **11** 043001
[23] Bussmann E, Cheynis F, Leroy F and Müller P 2010 *IOP Conf. Ser.: Mater. Sci. Eng.* **12** 012016
[24] Bauer E 1994 *Rep. Prog. Phys.* **57** 895
[25] Wautelet M 1991 *J. Phys. D: Appl. Phys.* **24** 343
[26] Müller P and Kern R 2003 *Surf. Sci.* **529** 59
[27] Fraxedas J, Ferrer S and Cousin F 1994 *Europhys. Lett.* **25** 119
[28] Pierre-Louis O, Chame A and Saito Y 2007 *Phys. Rev. Lett.* **99** 136101
[29] Pierre-Louis O, Chame A and Saito Y 2009 *Phys. Rev. Lett.* **103** 195501
[30] Kan W and Wong H 2005 *J. Appl. Phys.* **97** 043515
[31] Dufay M and Pierre-Louis O 2011 *Phys. Rev. Lett.* **106** 105506
[32] Karthaus O *et al* 1999 *Chaos* **9** 308
[33] Schmid A K *et al* 2000 *Science* **290** 1561
[34] Morgenstern K *et al* 1995 *Phys. Rev. Lett.* **74** 2058
[35] Keefe M E *et al* 1994 *J. Phys. Chem. Solids* **55** 965
[36] Jaccodine R 1963 *J. Electrochem. Soc.* **110** 524
[37] Eaglesham D J *et al* 1993 *Phys. Rev. Lett.* **70** 1643
[38] Métois J-J and Müller P 2004 *Surf. Sci.* **548** 13
[39] Wong H *et al* 2000 *Acta Mater.* **48** 1719
[40] Srolovitz D J and Safran S A 1986 *J. Appl. Phys.* **60** 247

[2] : Dynamique du démouillage de Si/SiO_2

Cheynis *et al.*, Phys. Rev. B (2011)

PHYSICAL REVIEW B **84**, 245439 (2011)

Dewetting dynamics of silicon-on-insulator thin films

F. Cheynis,* E. Bussmann,† F. Leroy, T. Passanante, and P. Müller
Centre Interdisciplinaire de Nanoscience de Marseille (CINaM), UPR CNRS 3118, Aix-Marseille Université, Case 913, Campus de Luminy, FR-13288 Marseille Cedex, France
(Received 3 November 2011; published 20 December 2011)

Using low-energy electron microscopy (LEEM), we have measured, in real time, the dewetting of single-crystal Si(001) thin films on amorphous silicon dioxide substrates, which transforms the two-dimensional (2D) thin film into three-dimensional (3D) compact Si nanocrystals. The dewetting scenario has been reported by Bussmann *et al.* [New J. Phys. **13**, 043017 (2011)]. Analytic 2D and 3D models based on simple approximate geometries of the dewetting front have been developed to analyze LEEM measurements. They enable us to estimate the driving force for dewetting $E_s \sim 14$ eV/nm^2. Starting from a Si-film thickness dependent *effective* dewetting activation barrier, a single Si(001) surface self-diffusion energy of $E_a = 2.0 \pm 0.2$ eV is derived. First nanoisland-formation dynamics measurements are discussed. Finally, grazing incidence small-angle x-ray scattering (GISAXS) is used to characterize the structure and the morphology of the Si nanocrystals created by the dewetting process.

DOI: 10.1103/PhysRevB.84.245439 PACS number(s): 68.35.Fx, 68.35.Md, 68.37.Nq

I. INTRODUCTION

Solid thin films with thickness of a few nanometers are crucial elements in numerous technologies, e.g., microelectronics and catalysis. In many systems, the flat two-dimensional (2D) film is a nonequilibrium configuration, so that the film may *dewet* upon thermal treatments to form compact three-dimensional (3D) structures.[1–5] Silicon-on-insulator (SOI) is an example of a metastable film that undergoes a dewetting instability when annealed.[6–11] This key building block for the next generation CMOS microelectronics consists of a single-crystalline Si thin film, in our case Si(001), on an amorphous silicon dioxide substrate.

Although many *ex situ* analyses of the morphology of dewetted SOI films are already available,[6–18] a detailed *in situ* characterization of the dynamic evolution of the SOI dewetting process has only been reported recently.[19] For this purpose, we have used low-energy electron microscopy (LEEM). This technique gives simultaneously access, in *real time*, to the micrometric lateral scale of the dewetting area and the atomic vertical scale. In our previous work, we have confirmed the following dewetting scenario: (i) the heterogeneous nucleation at randomly distributed defects and growth of voids surrounded by (ii) a thickening rim, (iii) the formation of Si fingers, and (iv) the breakdown of Si fingers into 3D nanoislands. This paper also shows that Si dewetting from a SiO_2 substrate is mediated by surface diffusion and driven by surface-free-energy minimization.

This paper extends our previous paper[19] in many respects. In Sec. II, we clearly show the effect of the surface preparation on the dewetting morphologies, possibly explaining the different void-growth behaviors reported in the literature. The different dewetting stages are then reviewed and new analysis is brought forward: the 2D analytic model for the thickening rim velocity given in Ref. 19 is described in more detail and further analytic solutions are discussed relative to existing theoretical predictions (Sec. III B). Section IV compares the observed rim instability with Ref. 20, which interpreted this phenomenon in terms of a Rayleigh-Plateau instability. In Sec. V, a 3D model for the Si finger formation is introduced, enabling us to determine a geometry-independent activation energy of 2.0 ± 0.2 eV, in quantitative agreement with the value of 2.3 ± 0.1 eV for Si(001) surface diffusion obtained in Ref. 21. First, experimental results on the nanoisland formation dynamics using both LEEM and grazing incidence small-angle x-ray scattering (GISAXS) are described in Sec. VI. Finally, in Sec. VII, we discuss several potential additional effects that could play a role in dewetting.

II. EXPERIMENT

A. Methods and materials

Experimental investigations were done on silicon-on-insulator (SOI) thin films fabricated by means of the Smart Cut© process at CEA-LETI (Grenoble, France). SOI samples are a single-crystal Si(001) film bonded onto a ∼140-nm-thick oxide layer on a Si(001) substrate.

The experiments are performed with an ELMITEC LEEM III microscope at pressures $<10^{-9}$ Torr (base pressure $<2 \times 10^{-10}$ Torr). SOI samples with different Si thicknesses (6, 11, 14, and 22 ± 2 nm) are first prepared *ex situ* by repeated cycles of chemical oxidation (H_2SO_4:H_2O_2, 3:1 by volume), and stripping of the oxide with HF acid. In the final step, a protective oxide layer (∼1–2 nm thick) is formed in a HCl:H_2O_2:H_2O (3:1:1 by volume) solution. After introduction in the ultrahigh vacuum (UHV) setup, samples are degassed overnight at 500 °C. Prior to dewetting, the oxide layer is desorbed by annealing at ∼700 °C. The reaction $Si + SiO_2 \rightarrow 2SiO$ with SiO molecules desorbing into vacuum is indeed active at temperatures >700 °C.[22] Subsequent low-energy electron diffraction (LEED) measurements [Fig. 1(a)] show that the surface has 1/2-order spots associated with the (2×1) and (1×2) reconstructions characteristic of a clean Si(001) surface under UHV conditions.

In dewetting experiments, the sample is annealed at a fixed temperature ($T > 700$ °C), while a sequence of LEEM images is recorded at a fixed rate to create a movie of the dewetting process. The images are typically recorded in dark-field mode using electrons from one of the 1/2-order LEED spots associated with the surface reconstruction. Adjacent Si(001) terraces have orthogonal reconstructions [(2×1)

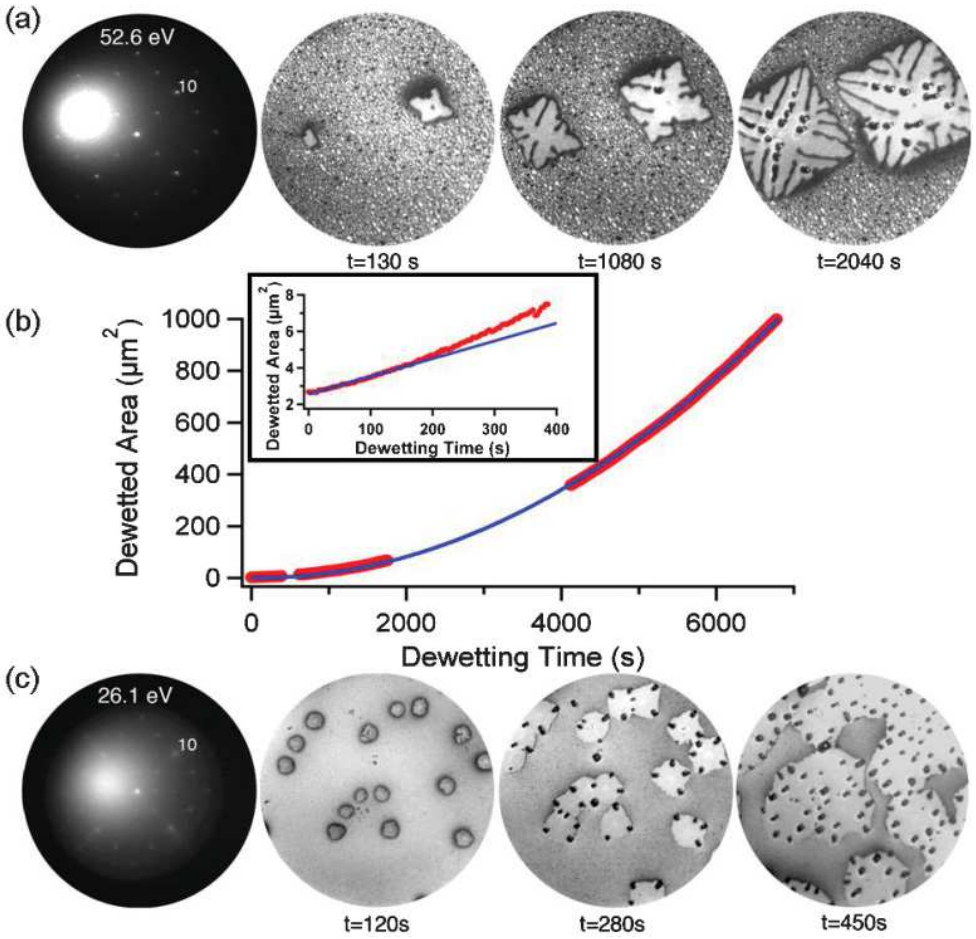

FIG. 1. (Color online) (a) LEEM images of SOI dewetting (SOI 22 ± 2 nm thick, $T = 870$ °C, $E_{e^-} = 7.8$ eV) of a clean surface showing strong 1/2-order LEED spots. Bright-dark speckling is due to the 2×1 Si surface (dark-field conditions). Void nucleation starts on morphological defects at $t = 0$ s. The images have been taken at $t = 130$ s (square-void opening), then $t = 1080$ s (instability of the side of the square voids), and $t = 2040$ s (finger growth and nanoisland formation in organized rows). (b) Typical time evolution of a given dewetting void imaged in (a). Blue solid lines show the linear (inset) and quadratic time evolution of a dewetted area. (c) LEEM sequence of a surface prepared inadequately [i.e., not showing strong (2×1) and (1×2) LEED spots]. Images have been obtained, respectively, at $t = 120$, 280, and 450 s. For all images, field of view (FOV) is 25 μm.

versus (1×2)] so that they appear alternately bright and dark according to the reconstruction orientation [Fig. 1(a)]. This contrast gives us direct access to the local vertical atomic-scale structure of the surface, so that we can observe in *real time* the motion of individual steps. The contrast also gives direct insight into nucleation processes on facetted 3D structures during dewetting. In addition to LEEM measurements, *ex situ* noncontact atomic force microscopy (AFM) is used to characterize the sample topography (PSIA-XE 100).

B. Dewetting sequence and surface preparation

Figure 1(a) shows a LEEM image sequence of the dewetting of a SOI thin film. The dewetting process is qualitatively identical for Si films 6 to 22 nm thick: (i) square crystallographically oriented voids nucleate heterogeneously at defects in the Si layer, exposing the oxide (which appears bright due to charging effects), (ii) the voids grow spontaneously and give rise to a Si rim at the edge, (iii) the rim undergoes a shape instability to form Si fingers, and (iv) the fingers break apart into Si nanocrystals.[13,15] This dewetting pathway is characteristic of a clean Si(001) surface exhibiting strong (2×1) and (1×2) LEED spots

We observe a different dewetting pathway [Fig. 1(c)] for samples that have been either simply loaded directly in the UHV system, without preparation, or prepared inadequately, e.g., kept in vacuum a long time (>10 h) after decomposition of the chemical oxide prior to dewetting. The sample surfaces show a $c(4 \times 4)$ reconstruction characteristic of a residual C contamination.[23] Figure 1(c) shows a LEEM image sequence of the dewetting of such a contaminated sample in which (i) round voids open heterogeneously in the Si film, (ii) the voids grow without the formation of a 3D Si rim, (iii) the void edges do not exhibit elongated fingers, but facetted compact 3D Si nanocrystals, and (iv) the film edge retracts, leaving isolated nanocrystals on the oxide. The resulting islands are relatively disorganized, compared to those obtained from a clean Si(001) surface. In the literature, results corresponding to both pathways can be found.[8,24]

III. INITIAL STAGES OF DEWETTING

A. Square-void and rim formations

SOI dewetting begins with heterogeneous nucleation of voids with ⟨110⟩-oriented sides. From the LEEM image sequences, it is possible to follow the dewetting phenomenon at the micron scale by measuring the time evolution of individual void areas [Fig. 1(b)]. In the initial stage (i.e., as long as the voids remain square shaped), the dewetted area increases approximately linearly in time. The material (Si) expelled from the void is transferred to a 3D rim.[19] This rim is facetted and a {001} top facet is observed in atomic force microscopy [Fig. 2(b)] and LEEM measurements. In dark-field imaging, rim summits exhibit a dark or bright contrast [Fig. 2(a)]. Additional lateral facets are also expected [e.g., {111} (Refs. 11 and 12)].

In LEEM movies, successive atomic layers added to the rim top facet appear alternately bright and dark, owing to their orthogonal surface reconstructions. As the void grows, the rim thickens *via* the nucleation of new layers on the top {001} facet.

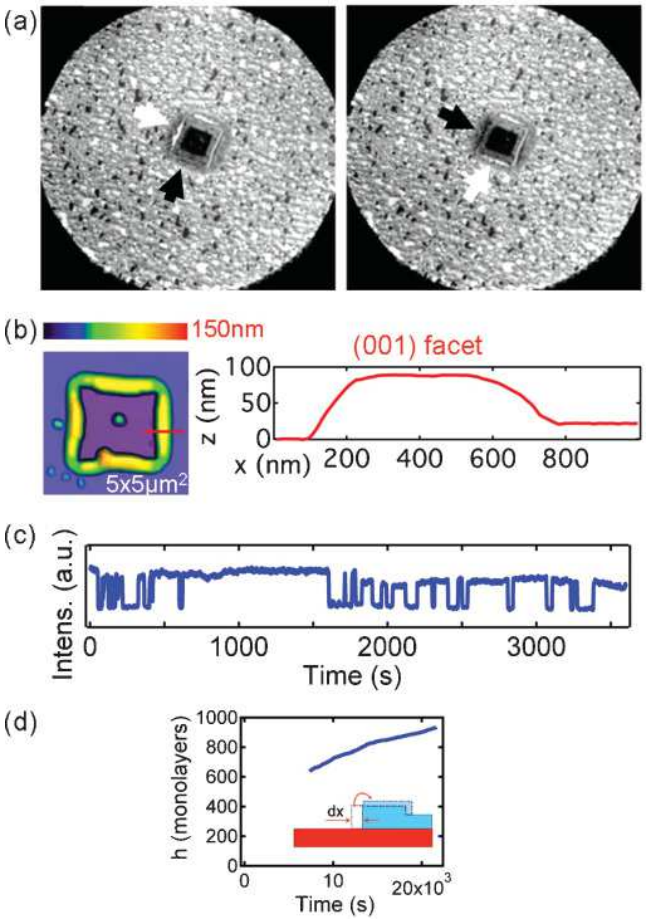

FIG. 2. (Color online) (a) Dark-field LEEM images illustrating the contrast inversion of the two {001} top facets (cf. arrows) due to the nucleation and completion of a new monolayer on each top facet (SOI 22 ± 2 nm thick, $T = 766$ °C, $E_{e^-} = 3.8$ eV, FOV $= 25$ μm). (b) AFM image and profile of a dewetting void and rim. (c) Time evolution of the contrast of a {001} top facet. (d) Average height of the rim versus time.

Figure 2(b) illustrates the contrast change of the {001} top facet during void growth. By recording on each facet the LEEM intensity as a function of time [Fig. 2(c)], the height of the rim as well as the nucleation and growth kinetics are monitored in real time. The rim height versus time is obtained by counting the new layers on the top facet of the rim [Fig. 2(d)]. The height evolution of the rim is limited by the nucleation rate rather than by the layer completion. Once a new layer has nucleated, it spreads and covers the facet much faster than the time between nucleation events. From our measurements, no clear evidence of a height-dependent nucleation barrier, as predicted by Ref. 25, can be found. A detailed study of the nucleation properties on the top facet will be published in a forthcoming paper.

B. Modeling of the rim velocity and determination of the driving force

To model the dewetting dynamics of the Si layer, we have developed a 2D approach describing the experiments shown in Fig. 1(a) and the kinetic Monte Carlo (KMC) simulations reported in Ref. 19. In this analytic model, depicted in Fig. 3, a facetted rim recedes by surface-diffusion-mediated mass transfer from the base of the rim to the top of the rim. The growth and thickening of the rim *via* nucleation on the top facet are also accounted for.

We assume that the rim position $x(t)$ moves with a velocity determined by an Einstein relation $v_{\text{rim}} = -MF$, where M is an effective surface-diffusion-based mobility, and F is a thermodynamic driving force.[26] In the model geometry, the driving force per unit length of dewetting front when displaced by a distance δx is $F = -(\gamma_{\text{Si}} + \gamma_{\text{int}} - \gamma_{\text{Ox}}) + 2\gamma_{\text{Si}}\delta h/\delta x$. The first term $E_s = \gamma_{\text{Si}} + \gamma_{\text{int}} - \gamma_{\text{Ox}}$ is associated with the decrease of surface and interface free energies due to the void growth and $2\gamma_{\text{Si}}\delta h/\delta x$ is associated with the change of height. Since the rim is wide, $E_s \gg 2\gamma_{\text{Si}}\delta h/\delta x$ and the driving force per unit length is $\approx -E_s$. Using Morgenstern's method,[27] we determine the mobility of the rim assuming that surface diffusion, across the width w of the rim, is limiting. The number of atoms involved during the rim displacement δx is proportional to the square root of the number of atoms diffusing on the surface of the rim during time t: $N \sim hL\delta x/\Omega \sim \sqrt{n_o t/\tau}$, where L is the (arbitrary) length of the rim, Ω is an atomic volume, and n_o the number of adspecies on the surface. In a diffusion-limited regime, the average time to cross the rim of width w is $\tau \sim w^2/D_s$, where D_s is the diffusion coefficient for adspecies. The number of adspecies on the surface is $n_o \sim wLc/a^2$ with c the adspecies surface fraction and a an atomic distance. We obtain $\delta x^2 = D_{\text{eff}} \times t$, where D_{eff} is an effective diffusion coefficient ($D_{\text{eff}} = M \times k_B T$). Putting all together, we obtain $M = \Omega^2 D_s c/(a^2 Lh^2 w k_B T)$ and $v_{\text{rim}} =$

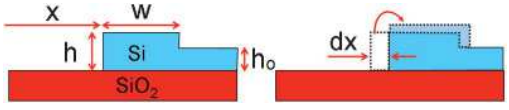

FIG. 3. (Color online) Geometry used to model a 2D rim receding *via* thickening. Owing to thickening, the rim slows down as it moves outward.

TABLE I. Analytic expressions obtained by integration of Eq. (1) for two asymptotic conditions assuming mass conservation ($xh_0 = w\Delta h$). $K = \frac{\Omega^2}{a^2}\frac{D_{s,o}c_0}{k_BT}E_s e^{-E_a/k_BT}$, where h_0 is the initial thickness of the film, h the actual rim thickness, and $\Delta h = h - h_0$ the height excess at the rim.

Geometry assumption	$h = Cst$	$\alpha = \Delta h/w = Cst$
$x(t)$	$x^2 = 2K\frac{\Delta h}{h_0 h^2}t$	$\left(\frac{2}{3}h_0^2x^{3/2} + \frac{h_0^{3/2}}{\alpha^{1/3}}x^2 + \frac{2}{5}\frac{h_0}{\alpha}x^{5/2}\right) = K\left(\frac{\alpha}{h_0}\right)^{1/2}t$

$-MF = (\Omega^2 D_s c/a^2h^2w)(E_s/k_BT)$ similar to Ref. 25. In the following, we write

$$v_{\text{rim}} = \left(\frac{\Omega^2}{h^2wa^2}\right)D_{s,o}c_o e^{-E_a/k_BT}\left(\frac{E_s}{k_BT}\right), \qquad (1)$$

where $D_{s,o}$ and c_o are the diffusion and the adspecies surface fraction prefactors and $E_a = E_{\text{diff}} + E_{\text{form}}$ is an activation energy that can be written as the sum of the formation energy (E_{form}) and the diffusion barrier (E_{diff}) of the diffusing species. Note that the front velocity [Eq. (1)] can be written as a function of the chemical potential at the facetted rim $\mu = E_s/h$ (Ref. 28):

$$v_{\text{rim}} = (\Omega/a)^2\, D_{s,o}c_o\frac{e^{-E_a/k_BT}}{hw}\left(\frac{\mu}{k_BT}\right). \qquad (2)$$

In general, $h(t)$ and $w(t)$ are required to calculate the velocity of the dewetting front [Eq. (1)]. However, in a few special cases, expressions of $x(t)$ can be obtained by integration of Eq. (1), leading to an area variation $A(t) \propto t^{\chi}$ with, $\chi = 1$ or $4/5$ for, respectively, a constant rim height h and a constant rim aspect ratio $\alpha = (h - h_0)/w$ (Table I). Note that the exponent $4/5$ found at constant α in the long-time limit is consistent with the exponent found in Refs. 29 and 30, respectively, for a 3D opening void with a contact angle of 90° and for the motion of a straight dewetting front. Both reports use an isotropic diffusion-limited model. To be thorough, Srolovitz and Safran numerically found $\chi = 1/2$ when considering a continuous 2D model[31] and Jiran and Thompson predict a constant edge velocity (i.e., $\chi = 2$) for a dewetting front exhibiting fingers.[1]

From our expression of the rim velocity v_{rim}, the SOI dewetting driving force can be determined. Using the measured evolution $h(t)$ [Fig. 2(f)] and assuming mass conservation [$xh_o = w(h - h_o)$], we numerically integrate our expression of v_{rim} and fit it to the void area versus time experiments

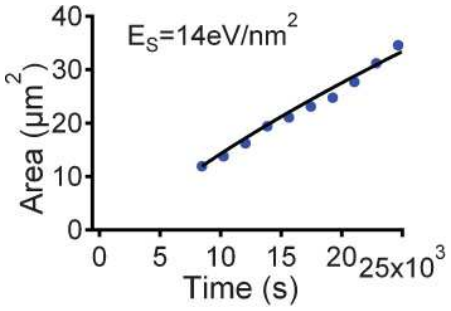

FIG. 4. (Color online) Area versus time measurements (dots) for a dewetting void at $T = 780\,^{\circ}$C in the initial regime where $A \propto t$. The solid line shows the best-fit solution obtained for a value of 14 eV/nm^2.

using E_s as the only fit parameter. The value of the surface self-diffusivity, $D_s c = D_{s,o}c_o e^{-E_a/k_BT}$ at $T \sim 800\,^{\circ}$C is 10^6 nm^2/s.[21] The best fit is obtained for $E_s \sim 14$ eV/nm^2 (~ 2.3 J/m^2) (Fig. 4). For comparison, the value of E_s can be estimated from the literature and our AFM data [$E_s = \gamma_{\text{Si}} + \gamma_{\text{Si-SiO}_2} - \gamma_{\text{SiO}_2} = \gamma_{\text{Si}}(1 + \cos\theta_c)$ where θ_c is the Si-SiO$_2$ equilibrium contact angle]. From Refs. 32–34, $\gamma_{\text{Si}} \sim 5$–$9$ eV/nm^2 at $T = 830\,^{\circ}$C. Anisotropy of γ_{Si} is negligible ($\sim 10\%$).[35] From AFM data, we estimate $\theta_c \sim 50^{\circ}$–80°. Using these numbers, we estimate that E_s is in the range 7–15 eV/nm^2, which is comparable with the value we find by fitting the experiments. It can thus be concluded that surface free energies provide a sufficient driving force to cause dewetting *via* Si(001) surface diffusion.

IV. RIM INSTABILITY AND SI FINGER FORMATION

As dewetting proceeds, square-shaped voids evolve and exhibit in turn a starlike shape as evidenced in Fig. 1(a). The time evolution of a given dewetting void area transits from a linear to a quadratic behavior [Fig. 1(b)]. This implies that the edges of the dewetting areas move on the average at a constant speed (i.e., $x \propto t$). The void edges, however, do not retract uniformly. Stroboscopic visualization (Fig. 5) illustrates the local variations of the void edge receding motion. Typically, two behaviors are observed. The dewetting front can locally slow down ($x \propto t^{1/2}$). At later times, these regions generate 3D structures, called in the following Si fingers, where mass is transferred and accumulated. Other regions of the dewetting front, called in the following void fingers (i.e., areas between two adjacent Si fingers), are characterized by a $x \propto t$ behavior. We refer to this as the steady-state regime where front moves at a constant average speed. The void fingers are responsible for the overall quadratic time evolution in time of the dewetted area, which is then characterized by the formation of periodic compact Si fingers interleaved with void fingers. The void fingers propagate most rapidly along ⟨100⟩ directions. As shown in Fig. 5 (white set squares), most void fingers exhibit a 90°-arrow end, suggesting that void fingers are terminated by {111} planes that intersect the {001} base plane along ⟨110⟩ directions. The void finger propagation, however, is constrained by impingement and nucleation of void fingers. This results in orientation of the Si fingers preferentially along ⟨100⟩ directions. {131} and {151} facets of Si fingers, however, may induce local bifurcations resulting in Si fingers oriented along ⟨130⟩ and ⟨150⟩ directions, which are the intersections of {131} and {151} planes with the {001} base plane (Fig. 9).

The 3D instability of the dewetting front has been theoretically studied by Kan and Wong in Ref. 20. The authors performed a 3D linear stability analysis of the dewetting front in the small-slope limit under a lateral x perturbation.

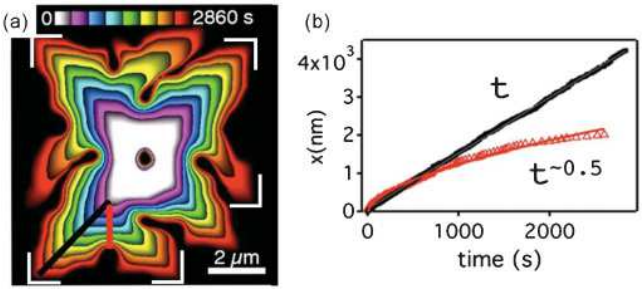

FIG. 5. (Color online) (a) Stroboscopic image of a dewetting area showing the local variations associated with the formation of Si and void fingers (SOI 14 ± 2 nm thick, $T = 800$ °C). The white set squares indicate the 90°-arrow termination of the void fingers. (b) Time evolution of the dewetting edge position along the two directions marked in (a) using lines with the corresponding color. Solid lines are least-squares fits to the data.

Numerical results show that (i) there is a coupling between the lateral x and vertical y instabilities. (ii) Fourier modes of the front response are characterized by a wave number k and a growth rate σ. The latter reaches a maximum for a critical wave number value, which is likely to correspond to the inter-Si finger distance observed in the steady-state dewetting regime (Fig. 9).

Figure 6 summarizes the temperature dependence of the experimental average inter-Si finger distance (λ_{fin}) and the wavelength characterized by the highest growth rate. The latter quantity is obtained from Ref. 20 using experimental front velocities as input for the $\sigma_m(b)$ curve, where b is proportional to the front velocity. Although developed in a small-slope approximation, Kan and Wong's model and the experimental data are in good qualitative agreement. A recent work[36] has raised a debate as to whether the observed 3D instability of the dewetting front should be attributed to a standard Rayleigh-Plateau instability or a diffusive kinetic instability. In the experiments, we have not been able to find evidence of a time dependence of the mode of largest amplitude nor the coarsening of the rim as predicted in Ref. 36.

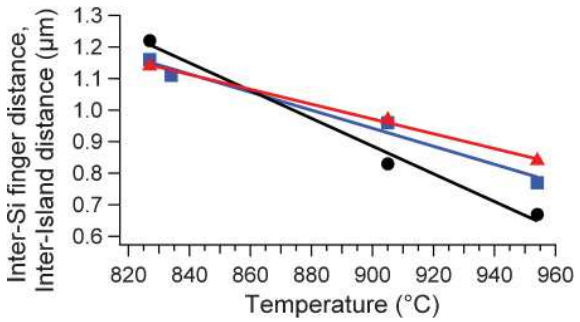

FIG. 6. (Color online) Temperature dependence of the interfinger distance (λ_{fin}) (black solid circles), the interfinger distance determined from Ref. 20 (red solid triangles), and the interisland distance (λ_{isl}) (blue solid squares). All quantities have been measured for 22-nm-thick films. Solid lines show the linear temperature dependence of λ_{fin} and λ_{isl}.

V. SI FINGERS AND DEWETTING ACTIVATION ENERGY

As described in the preceding section, once a dewetting front exhibits Si and void fingers, the void area evolves quadratically in time. In other words, the occurrence of fingers plays a major role in the overall dynamics.

To account for the 3D structure of the dewetting front exhibiting void fingers and Si fingers, we modify our 2D model described in Sec. III B. The simplified geometry of dewetting fronts with void fingers is defined in Fig. 7. In this approach, the thermodynamic driving force on the receding rim is only due to the *active* part of the rim, defined by the volume of effective length ζ and height h_m. The effective driving force acting on the length ζ reads as $F = -E_s\zeta$, and the mobility of a void finger characterized by a period λ_{fin} is $M = \Omega^2 D_s c/a^2 \lambda_{\text{fin}} h_m^2 w k_B T$. We thus obtain $v_{\text{front}} \approx v_{\text{rim}} \frac{\zeta}{\lambda_{\text{fin}}}$ with $h = h_m$. Assuming that the front velocity is thermally activated with an *effective* activation barrier E_{eff} (i.e., $v_{\text{front}} = Ce^{-E_{\text{eff}}/k_B T}$, where C is a constant term), we obtain a geometry-dependent activation barrier

$$E_{\text{eff}} = E_a + k_B T\,(\ln k_B T) + k_B T \ln\left(h_m^2 w \lambda_{\text{fin}}/\zeta\right), \quad (3)$$

where all quantities have been defined previously.

To confirm this approach, real-time LEEM measurements of the velocity of dewetting fronts exhibiting Si and void fingers have been done at different sample temperatures and for several initial film thicknesses [Fig. 8(a)]. Table II shows that the measured *effective* activation barrier (E_{eff}) depends on the initial Si-film thickness. Equation (3) also requires knowledge of the temperature evolution of the different geometrical parameters: λ_{fin}, h_m, w, and ζ. Figure 8(b) shows the temperature evolution of λ_{fin}, the only parameter that can be experimentally monitored.

Assuming that the temperature dependence of all the characteristic lengths (h_m, w, and ζ) scale as $\lambda_{\text{fin}}(T)$, we can estimate E_a by fitting numerically the curves shown in Fig. 8(a). In this numerical calculation, E_a and C are the only fit parameters as $\lambda_{\text{fin}}(T)$ is known [Fig. 8(b)]. The so-obtained fit curves are plotted as solid lines in Fig. 8(a) and numerical values of E_a are reported in Table II. For the different initial

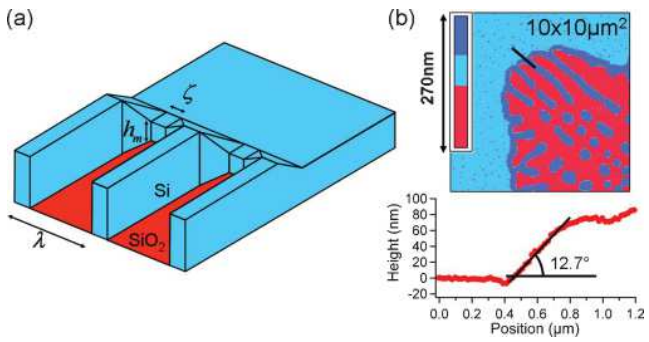

FIG. 7. (Color online) (a) Schematic of a receding front exhibiting fingers. Parameters ζ and h_m characterize the *active* part of the receding front. (b) AFM image of a dewetting area and the corresponding line profile illustrating the small-slope descending extremity of a Si finger (SOI 22 ± 2 nm thick, $T = 835$ °C).

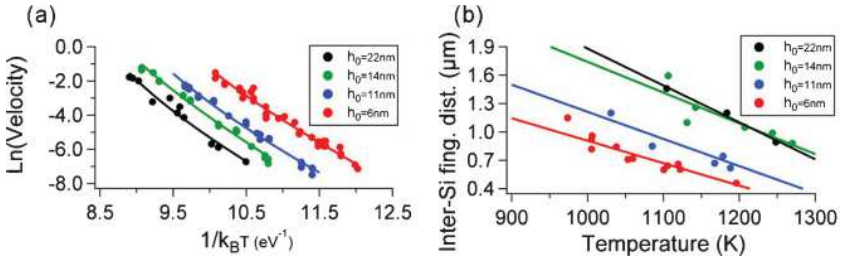

FIG. 8. (Color online) Temperature dependence (a) of the void growth velocity shown as an Arrhenius plot and (b) of the inter-Si finger distance measured for SOI films of various initial thicknesses. Solid lines are (a) corrected-Arrhenius fits (see text for details) and (b) linear fits.

Si thicknesses, a common value of the activation energy is found, $E_a = 2.0 \pm 0.2$ eV. This value is in good agreement with results reported in Ref. 21. In this study, the authors used optical methods to monitor, upon UHV annealing, the decay of a periodic structure patterned on a Si(001) surface and found an activation energy [identified to Si(001) surface self-diffusion] of $E_a = 2.3 \pm 0.1\,eV$. In both cases, despite the fact that different driving forces are at work (curvature-induced surface healing or dewetting), we expect Si diffusion to be kinetically limiting where mass is mainly agglomerated: in this study, at the descending extremity of the Si fingers shown in Fig. 7(b) (Si thin-film side). This small-slope region exhibits a high density of {001} terraces and should therefore favor Si accumulation by step flow. This result confirms *a posteriori* our scaling assumption as we obtain a common value of E_a despite initially a nonsimple Arrhenius law [$E_{\text{eff}}(h_0, T)$].

VI. NANOISLAND FORMATION

In the steady-state regime, the void fingers govern the overall dynamics by shuttling mass from the triple line to the Si fingers, which lengthen and eventually break down into Si nanocrystals (Fig. 9). It has been widely reported that elongated solid structures, such as Si fingers, can agglomerate according to Rayleigh-Plateau instability.[15,16,37–39] Using surface-diffusion models, two quantities characterizing the island formation are derived. The interisland distance λ_{isl} results from energetics considerations: $\lambda_{\text{isl}} \propto h_{\text{Si}}$, from dimensional analysis. Considering a solid cylinder in the absence of a substrate, Nichols and Mullins[37] found $\lambda_{\text{isl}} = 2^{3/2}\pi r_0$, where r_0 is the cross-sectional radius. Including the contact angle θ_c between the elongated structure and the substrate, McCallum *et al.*[39] established $\lambda_{\text{isl}} = 2^{3/2}\pi r \sqrt{\frac{\theta_c - \sin\theta_c \cos\theta_c}{\theta_c \sin^2\theta_c}}$, where r is the projected half-width of the elongated structure ($r_0 = r/\sin\theta_c$). The characteristic time required between two island formation events in the case of a cylinder is $\tau_{\text{gen}} \propto r_0^4/B$, where B is the generalized diffusion coefficient introduced by Mullins.[40]

TABLE II. Effective activation energies E_{eff} calculated when assuming an Arrhenius behavior of the receding velocity of a dewetting front and estimated values of the activation energy E_a when using our expression of v_{fin} with the additional assumption that all the characteristic lengths scale as $\lambda_{\text{fin}}(T)$.

h_o (nm)	6 ± 2	11 ± 2	14 ± 2	22 ± 2
E_{eff} (eV)	2.7 ± 0.2	2.9 ± 0.2	3.1 ± 0.2	3.4 ± 0.2
E_a (eV)	1.9 ± 0.2	1.9 ± 0.2	2.2 ± 0.2	1.9 ± 0.2

Similarly, the growth rate of an instability of wavelength λ reads as $\sigma \propto B/r_0^4$.

Figure 10 compares our experimental results with preexisting theoretical predictions. Expressions for λ_{isl} found in Refs. 37 and 39 do not depend explicitly on temperature. However, as described in Sec. IV, the inter-Si finger distance decreases as the dewetting temperature is increased. Due to mass conservation, the geometrical parameter r (or r_0) is expected to behave as λ_{fin}. LEEM measurements show that $\lambda_{\text{isl}} \sim 6r$ while $2^{3/2}\pi \simeq 8.9$ and $2^{3/2}\pi\sqrt{\frac{\theta_c - \sin\theta_c\cos\theta_c}{\theta_c \sin^2\theta_c}} \simeq 8.2$ for $\theta_c = 73°$. Models based on Mullins approach for unsupported cylinders or elongated structures on a substrate seem to overestimate the interisland distance.

Using real-time LEEM measurements, we have been able to determine the average time between the generation of two subsequent Si nanocrystals from the same Si finger. The evolution of this characteristic time as a function of $1/B$ is shown in Fig. 10(b). The generalized surface-diffusion coefficient $B = \frac{D_s c \gamma_0 \Omega^2}{k_B T}$ (Ref. 40) has been calculated using the following values: Si surface-diffusion coefficient $D_s c = 10^{17}\, e^{\frac{-2.3eV}{k_b T}}$ nm^2/s,[21] Si surface energy density $\gamma_0 \sim 7$eV/nm^2, Si atomic volume $\Omega = \frac{1}{8}(0.5431)^3$ nm^3. From the slope of the $\tau_{\text{gen}}(1/B)$ curve and using a standard experimental value for r_0, we obtain $\tau_{\text{gen}} \sim 0.1\, r_0^4/B$. These results can be compared to numerical simulations obtained by McCallum *et al.*[39] and Dornel.[16] In the case of an infinite unsupported cylinder, Dornel showed that $(\tau_{\text{gen}})_{\text{inf}} \sim 30\, r_0^4/B$. McCallum *et al.*

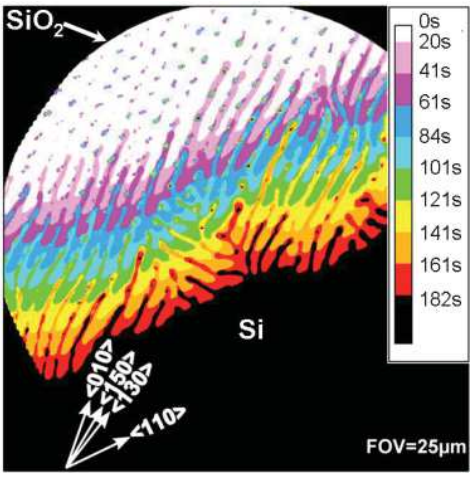

FIG. 9. (Color online) Stroboscopic image of the growth of a dewetting void showing the propagation of void fingers, a constant velocity, and the decomposition of Si fingers into Si nanoislands (SOI 22 ± 2 nm thick, $T = 975$ °C).

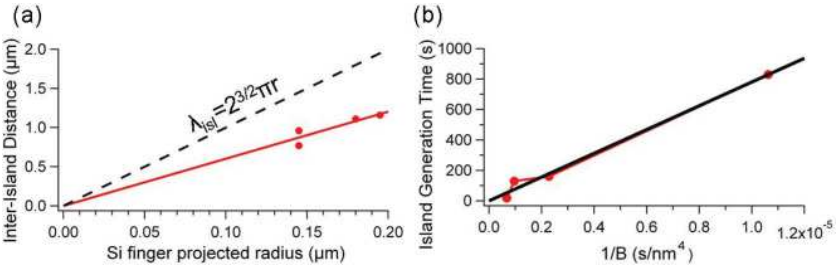

FIG. 10. (Color online) (a) Interisland distance λ_{isl} as a function the corresponding Si-finger projected half-width (r). (b) Average time between the generation of two adjacent Si nanocrystals from the same Si finger (τ_{gen}) as a function of $1/B$, where B is the generalized surface-diffusion coefficient introduced by Mullins (Ref. 40). Solid lines are linear fits.

included the contact angle between the unstable elongated structure and the substrate. By using the appropriate value of θ_c (in our case $\theta_c \sim 73°$), one can then determine that $(\tau_{gen})_{inf} \sim 24 r_0^4/B$. To the best of our knowledge, Ref. 16 is the only work to simulate the generation of individual Si nanostructures from the extremity of semi-infinite cylinders, as observed in experiments. In this study, Dornel obtained that for unsupported structures, $(\tau_{gen})_{semi} \sim 4.7\, r_0^4/B$. From these complementary results, it turns out that the effects of the substrate and an extremity accelerate the onset of instabilities. Again, standard models based on the Mullins approach, even when including the effect of the substrate, seem to underestimate the dynamic of the dewetting. Simulations of systems of finite size in contact with the substrate might be of high interest. One might also include the excess energy E_s in the local chemical potential as in our 2D model instead of considering only the local surface curvature.[19,36]

The structural properties of the Si nanoislands have been characterized during and after the completion of the dewetting process by grazing incidence x-ray diffraction (GIXD) and GISAXS (for a review, see Ref. 41).

Concerning the structure, we find that the Si-film crystallographic orientation is strictly preserved during the dewetting of the film [Fig. 11(a)] since no rotation of the Si nanoislands has been detected (in the limit of $\pm 0.5°$). All Si nanoislands exhibit the same facet orientation as confirmed by GISAXS. The GISAXS intensity scattered by the nanoislands has been measured over a three-dimensional volume of the reciprocal space. GISAXS patterns have been recorded at different azimuths, by rotating the sample by steps of 1° over a large angular range (100°). This complete set of GISAXS patterns shows 20 distinct scattering rods [Fig. 11(b)] arising from the facets of Si nanoislands. The largest are {113} and {111} facets and the smallest are {001} and {311}. They all belong to the Si equilibrium shape.[42] The occurrence of the {001} top facet is known from AFM data but is not measured accurately by GISAXS due to the predominance of the specular rod of the SiO_2 surface in the same region of reciprocal space. From these results, the facet size can be estimated from the full width at half maximum of the scattering rods. A schematic shape of Si nanoislands leading to the recorded GISAXS pattern is proposed in Fig. 11(c). Notice that for algorithmic reasons the reconstructed shape is assumed to be polyhedric, however, we can not exclude the existence of rounded parts as reported by Ref. 16.

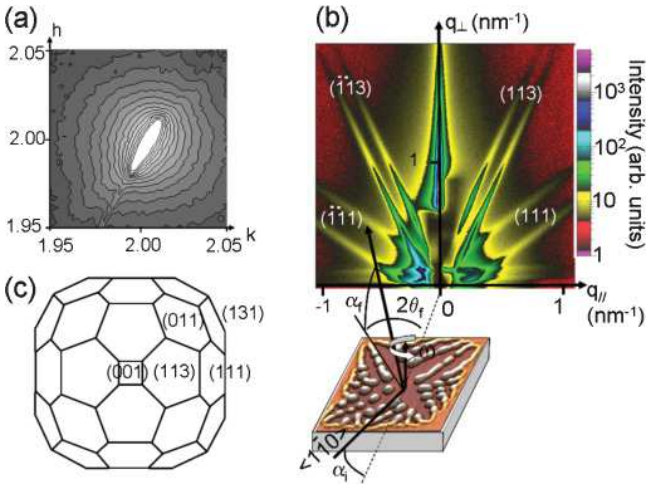

FIG. 11. (Color online) GIXD and GISAXS measurements after complete dewetting of a 22-nm-thick SOI film. (a) In-plane map of reciprocal space around (220) Bragg peak measured by GIXD. (b) Sketch of the GISAXS geometry and pattern measured with the incident beam aligned in the ⟨1-10⟩ direction. Extended scattering rods from {113} and {111} facets are observed. (c) Mean shape of Si nanoislands extracted from the analysis of GISAXS patterns.

VII. POTENTIAL ADDITIONAL EFFECTS

As shown in this paper and in Ref. 19, SOI dewetting is mainly driven by surface-free-energy minimization and mediated by surface diffusion. However, some other phenomena could also influence SOI dewetting such as Si-SiO_2 chemical reaction, stress, and shape effects.

(1) *Chemical reaction effect on the dewetting rate.* In our experimental conditions ($P < 10^{-9}$ Torr and $T < 1000$ °C), the silicon and the buried oxide react.[43] As the SiO_2 is exposed, the SiO_2+2Si→2SiO reaction occurs. From an estimation of the oxide decomposition rates reported in Ref. 22, the activation energy for oxide decomposition is around 4.1 eV while we measure a dewetting activation energy $\simeq 2.0 \pm 0.2$ eV (Sec. V). The chemical reaction thus does not consume a significant amount of Si during dewetting. More precisely, we estimate that in our experimental conditions, ∼1% of the Si film is lost during the chemical reaction, which is consistent with the depth of the grooves observed in the remaining SiO_2 after Si agglomeration.

(2) *Stress effects.* The process of fabrication of our sample (Smart Cut© process) leads to single-crystalline Si films without any grain boundaries that could cause local stresses. Furthermore, thanks to its lateral dimensions as well as its thickness, intrinsic surface-stress can not induce any bulk stress in the film.[44,45] We have checked by x-ray

diffraction at the European Synchrotron Radiation Facility (ESRF) that the samples are strain free. However, from a more general point of view, we can wonder about stress effects on the SOI dewetting process. For this purpose, we have measured the dewetting rates of SOI films biaxially strained (1% of strain). The dewetting rates we found are the same (within experimental uncertainties) for both strained and unstrained materials. This is expected since the driving force for SOI dewetting ($E_s \sim 14\text{eV/nm}^2$) is very large compared to the elastic energy, which for a strain of 1% is only $\sim 0.1 E_s$.[46]

(3) *Shape effects.* Our geometrical assumptions for the rim shape enable us to give simple analytic expressions of the dewetting velocities based on surface diffusion on the {001} facet of the rim. However, in the experiments, the rim exhibits additional facets (e.g., {311}, {111} facets) that may play a role in the Si diffusion *via*, for instance, their surface energies and/or surface-diffusion properties. In our temperature range, the surface energy anisotropy is less than 10%,[35,42] so that its influence on the amplitude of the dewetting driving force ($\sim E_s$) is not expected to be significant. Also, Watanabe *et al.*[47] have pointed out that the self-diffusion on {110} and {111} facets are all similar to that of the Si(001) surface. This implies that the occurrence of additional facets should not influence the mobility (M) of the dewetting front. Finally, our expression of the driving force neglects the contribution of the shape change. Whatever the true shape of the profile is, the driving force can always be divided into a contribution due to the shift of the rim at constant shape ($\sim E_s$) and a contribution due to the shape modification of the rim at constant position. This second contribution can be neglected because of the high value of E_s we find for the SOI system. We could imagine opposite situations for which the driving force essentially originates from the shape modification of the rim. This may be the case for systems in which the dewetting is not driven by surface energy, but only by elastic relaxation.[46]

VIII. SUMMARY

Using the LEEM microscopy technique as a powerful method for studying *in situ* and in *real-time* the surface dynamics of SOI dewetting, we conclude that (i) the dewetting dynamics as well as the dewetted morphologies are extremely sensitive to the sample preparation. (ii) The early-stage void opening (Area $\propto t$) is accompanied by a layer-by-layer rim thickening. A 2D analytic model, described and discussed with respect to the previous reports, is used to determine a SOI dewetting driving force of $E_s \sim 14$ eV. (iii) The observed 3D rim instability is not inconsistent with a standard Rayleigh-Plateau interpretation. (iv) In the long-time limit (Area $\propto t^2$), a Si(001) surface self-diffusion energy $E_a = 2.0 \pm 0.2$ eV is determined, using a 3D analytic model, in good agreement with the values obtained from the literature. This suggests that the dewetting is kinetically limited by Si diffusion where mass is mainly accumulated: at the descending extremity of the Si fingers resulting from the 3D rim instability. (v) The Si fingers create individual Si islands. The measured dynamics can not solely be explained by standard stability analysis; based on Mullins diffusion equation, finite-size effects are expected to play a significant role. (vi) The resulting nanoislands exhibit {113}, {111}, {011}, and {311} facets, expected for the Si equilibrium shape.

ACKNOWLEDGMENTS

This work was supported by ANR grant PNANO DéFIS (Grant No. ANR 08-nano-036) and by APO grant delivered by Provence Alpes Côte d'Azur Region Council. The authors would like to thank J. Eymery and N. Blanc for fruitful discussions and their help during our beamtime access at the ESRF. Beamline BM32 staff are also acknowledged. The authors thank A. Locatelli for allowing preliminary studies on the beamline *nanospectroscopy* at the synchrotron *Elettra* (Trieste, Italy).

*cheynis@cinam.univ-mrs.fr
†Permanent address: Photonic Microsystem Technologies, Sandia National Labs, PO Box 5800, Albuquerque, NM.

[1] E. Jiran and C. V. Thompson, J. Electron. Mater. **19**, 1153 (1990).
[2] C. Schrank, C. Eisenmenger-Sittner, E. Neubauer, H. Bangert, and A. Bergauer, Thin Solid Films **459**, 276 (2004).
[3] K. Thurmer and N. C. Bartelt, Phys. Rev. Lett. **100**, 186101 (2008).
[4] K. F. McCarty, J. C. Hamilton, Y. Sato, A. Saá, R. Stumpf, J. de la Figuera, K. Thurmer, F. Jones, A. K. Schmid, A. A. Talin, and N. C. Bartelt, New J. Phys. **11**, 043001 (2009).
[5] J. Ye and C. V. Thompson, Appl. Phys. Lett. **97**, 071904 (2010).
[6] Y. Ono, M. Nagase, M. Tabe, and Y. Takahashi, Jpn. J. Appl. Phys. **34**, 1728 (1995).
[7] R. Nuryadi, Y. Ishikawa, and M. Tabe, Appl. Surf. Sci. **159-160**, 121 (2000).
[8] B. Legrand, V. Agache, J. P. Nys, V. Senez, and D. Stiévenard, Appl. Phys. Lett. **76**, 3271 (2000).
[9] B. Legrand, V. Agache, T. Mélin, J. P. Nys, V. Senez, and D. Stiévenard, J. Appl. Phys. **91**, 106 (2002).
[10] R. Nuryadi, Y. Ishikawa, Y. Ono, and M. Tabe, J. Vac. Sci. Technol. B **20**, 167 (2002).
[11] B. Yang, P. Zhang, D. E. Savage, M. G. Lagally, G. H. Lu, M. Huang, and F. Liu, Phys. Rev. B **72**, 235413 (2005).
[12] E. Sutter and P. Sutter, Nanotechnology **17**, 3724 (2006).
[13] D. T. Danielson, D. K. Sparacin, J. Michel, and L. C. Kimerling, J. Appl. Phys. **100**, 083507 (2006).
[14] E. Dornel, J.-C. Barbé, F. de Crécy, G. Lacolle, and J. Eymery, Phys. Rev. B **73**, 115427 (2006).
[15] D. T. Danielson, Ph.D. thesis, MIT, 2008.
[16] E. Dornell, Ph.D. thesis, UJF, Grenoble, 2007.
[17] Y. Fan, R. Nuryadi, Z. A. Burhanudin, and M. Tabe, Jpn. J. Appl. Phys. **47**, 1461 (2008).
[18] Z. A. Burhanudin, R. Nuryadi, Y. Ishikawa, M. Tabe, and Y. Ono, Appl. Phys. Lett. **87**, 121905 (2005).
[19] E. Bussmann, F. Cheynis, F. Leroy, P. Müller, and O. Pierre-Louis, New J. Phys. **13**, 043017 (2011).

[20]W. Kan and H. Wong, J. Appl. Phys. **97**, 043515 (2005).
[21]M. E. Keefe, C. C. Umbach, and J. M. Blakely, J. Phys. Chem. Solids **55**, 965 (1994).
[22]H. Hibino, M. Uematsu, and Y. Watanabe, J. Appl. Phys. **100**, 113519 (2006).
[23]R. Miotto and A. Ferraz, Surf. Sci. **603**, 1229 (2009).
[24]G. Capellini, G. Giasca, M. de Seta, A. Notargiamoco, F. Evangestelli, and M. Nardonne, J. Appl. Phys. **105**, 093525 (2009).
[25]O. Pierre-Louis, A. Chame, and Y. Saito, Phys. Rev. Lett. **103**, 195501 (2009).
[26]A. K. Schmid, N. C. Bartelt, and R. Q. Hwang, Science **290**, 1561 (2000).
[27]K. Morgenstern, G. Rosenfeld, B. Poelsema, and G. Comsa, Phys. Rev. Lett. **74**, 2058 (1995).
[28]O. Pierre-Louis, A. Chame, and M. Dufay, Eur. Phys. J. B **77**, 57 (2010).
[29]R. Brandon and F. J. Bradshaw, Royal Aircraft Establishment Report No. 66095.
[30]H. Wong, P. Voorhees, M. Miksis, and S. Davis, Acta Mater. **48**, 1719 (2000).
[31]D. J. Srolovitz and S. Safran, J. Appl. Phys. **60**, 255 (1986).
[32]R. Jaccodine, J. Electrochem. Soc. **110**, 524 (1963).
[33]D. J. Eaglesham, A. E. White, L. C. Feldman, N. Moriya, and D. C. Jacobson, Phys. Rev. Lett. **70**, 1643 (1993).
[34]J.-J. Métois and P. Müller, Surf. Sci. **548**, 13 (2004).
[35]P. Müller and J.-J. Métois, Thin Solid Films **517**, 65 (2008).
[36]M. Dufay and O. Pierre-Louis, Phys. Rev. Lett. **106**, 105506 (2011).
[37]F. A. Nichols and W. W. Mullins, Trans. AIME **233**, 1840 (1965).
[38]D. J. Srolovitz and C. V. Thompson, Thin Solid Films **139**, 133 (1986).
[39]M. McCallum, P. Voorhees, M. Miksis, S. Davis, and H. Wong, J. Appl. Phys. **79**, 7604 (1996).
[40]W. W. Mullins, J. Appl. Phys. **28**, 333 (1957).
[41]G. Renaud, R. Lazzari, and F. Leroy, Surf. Sci. Rep. **64**, 255 (2009).
[42]J.-M. Bermond, J.-J. Métois, X. Egea, and F. Floret, Surf. Sci. **330**, 48 (1993).
[43]K. Sudoh and M. Naito, J. Appl. Phys. **108**, 083520 (2010).
[44]R. Kern and P. Müller, Surf. Sci. **392**, 103 (1997).
[45]P. Müller, P. Turban, L. Lapena, and S. Andrieu, Surf. Sci. **488**, 52 (2001).
[46]F. Cheynis, E. Bussmann, F. Leroy, T. Passanante, and P. Müller, Int. J. Nanotechnol. **8** (2011), (in press).
[47]F. Watanabe, S. Kodambaka, W. Swiech, J. Greene, and D. Cahill, Surf. Sci. **572**, 425 (2004).

[3] : Dynamique, anisotropie et stabilité des fronts de démouillage
Leroy *et al.*, Phys. Rev. B (2012)

PHYSICAL REVIEW B **85**, 195414 (2012)

Dynamics, anisotropy, and stability of silicon-on-insulator dewetting fronts

F. Leroy, F. Cheynis, T. Passanante, and P. Müller
Centre Interdisciplinaire de Nanoscience de Marseille (CINaM) CNRS UMR 7325, Aix-Marseille Université, Case 913 Campus de Luminy, 13288 Marseille Cedex 9, France
(Received 1 March 2012; published 8 May 2012; corrected 29 May 2012)

We report on the anisotropy of solid state dewetting of straight fronts of Si(001)/SiO_2 obtained by electron beam lithography. The ⟨110⟩ front is stable. It recedes with formation of a faceted rim that thickens in a layer-by-layer mode kinetically limited by 2D nucleation on the top facet of the rim. The front position and the height of the rim respectively obey $\sim t^{0.37\pm0.03}$ and $\sim t^{0.38\pm0.02}$ power laws. The ⟨100⟩ front is unstable. It breaks down then recedes at constant velocity. The ⟨100⟩ front instability is characterized by the formation of void fingers whose tips retract at constant shape with a kinetics limited by the mass transfer from the void tip to the Si fingers. The conditions of stability of a straight front are discussed in the light of recent theoretical models. New perspectives for controlling solid dewetting are opened.

DOI: 10.1103/PhysRevB.85.195414 PACS number(s): 68.55.−a, 68.35.Md, 68.37.Nq, 68.60.Dv

I. INTRODUCTION

Metastable thin solid films, when annealed, can agglomerate into an assembly of nanocrystals. This dewetting process is a limit for the fabrication of advanced devices.[1] Conversely, it is also a common method to produce self-organized nanocrystals used in several nanoscale processes.[2,3] As such, a fundamental understanding of the mechanisms governing solid state dewetting is of particular relevance. In recent years, ultrathin crystalline silicon-on-insulator (SOI) film has been recognized as a model system for studying solid state dewetting.[4–7] Spontaneous dewetting of single-crystalline SOI thin film is generally initiated by heterogeneous nucleation of voids at randomly distributed defects followed by their growth. These voids are surrounded by a thickening rim at the origin of a fingering instability. At last the fingers break down into 3D nanoislands self-organized into a regular array.[4,8–19] Most of the experiments on solid state dewetting concern such spontaneous dewetting of continuous thin films except for two studies on line-shaped[20] or square-shaped[21] nanostructures. All these experiments show a strong anisotropy of the SOI dewetting leading to the formation of ⟨110⟩-sided voids as well as to the line-up of Si islands in the dewetted state. The origin of this anisotropy has been discussed on the basis of *ex situ* examination of the final dewetted state (see for instance Refs. 12 and 15) but also on the basis of preliminary real-time observations (see for instance Refs. 7 and 13) for heterogeneous nucleation and SOI nanopatterns.[20,21] However, heterogeneous nucleation is not controlled *by definition,*and the dewetting of nanopatterns appears to be influenced by the pattern shape and by the amount of Si available in such small SOI structures.[20,21] It is thus necessary to go beyond these first approaches by studying the dewetting of true 2D films initiated at straight edges whose crystallographic orientation is perfectly controlled. It is all the more important that theoretical predictions[17,22–25] concern simple geometry as the dewetting from straight fronts. Moreover, contrary to classical theoretical investigations based on the isotropic continuum surface-diffusion model of Mullins,[26] the most recent models highlight several crystallinity effects such as the anisotropy of dewetting velocity and the role of 2D nucleation on the rim thickening[22–24] that cannot be accurately studied through heterogeneous dewetting or dewetting of nanopatterns.

In this paper, we present the first real-time observation of the dewetting of SOI films from artificial well-oriented edges obtained by lithography. Using various edge orientations, we have been able to investigate the anisotropy of the instability of solid dewetting straight fronts with a peculiar emphasis on kinetics. We show that (i) the ⟨110⟩-oriented edge retracts as $x \sim t^{0.37\pm0.03}$ accompanied by a rim-thickening $h \sim t^{0.38\pm0.02}$ (t being time) and (ii) the ⟨100⟩ edges are highly unstable against the formation of perpendicular elongated Si structures called in the following Si fingers, separated by void fingers. The void tips propagate at constant shape with $x \sim t$ and $dh/dt = 0$. For stable ⟨110⟩ orientations the kinetics is governed by the 2D nucleation on top of the rim. For unstable ⟨100⟩ orientations, kinetics is governed by the mass transfer from the void-finger tip to the Si fingers. At last we show how a stable ⟨110⟩ front may be destabilized by local defects.

II. EXPERIMENT

The experiments have been performed with a low-energy electron microscope (Elmitec LEEM III) at pressures $< 10^{-9}$ Torr. The samples are bonded SOI (CEA-Leti, France) composed of stress-free single-crystal Si(001) films (22 ± 2 nm thick) on a 150-nm-thick amorphous SiO_2 film.[16] The samples are cleaned according to a published recipe.[27] We measure dewetting by LEEM in bright field, dark field, and tilted bright imaging modes.[28] In these modes images are formed either from a reflected spot, 1/2-order diffraction beam associated with the Si(100)-2×1 surface reconstruction or from a tilted incident beam. As adjacent terraces have orthogonal surface reconstructions dark field and tilted bright field modes give rise to a bright-dark contrast that reveals the step organization at the surface. LEEM image sequences are recorded at a fixed rate (0.3–10 Hz) to form a movie of the dewetting process. The LEEM measurements show simultaneously the micrometer-scale structure of the dewetting front, the nanoscale motion of surface atomic steps, and 2D nucleation events. The motion of steps during the dewetting process is a clear indication of a surface diffusion mediated process and allows us to draw

connections between macroscopic evolution and atomistic processes. Well-oriented trenches have been fabricated by electron beam lithography. For this purpose we use a PPMA-950K electrosensitive positive resin deposited by spin coating and insolated on predefined regions by a 20 keV electron gun. The insolated resin is then dissolved by the MIBK:IPA (1:3) chemical solvent. Finally, trenches are dug by reactive ion etching by means of a radio frequency source (15 W) which generates a plasma in the SF6 low-pressure gas suitable for the silicon etching. The depth of the trenches allows us to reach the underlying SiO_2 substrate.

III. STRUCTURE AND DYNAMICS OF THE DEWETTING FROM STRAIGHT FRONTS

A. Dewetting phenomenon

Let us first describe qualitatively the morphology of fronts dewetting for various orientations of in-plane trenches. Whereas for continuous SOI film annealed at $T > 750\,^{\circ}$C the dewetting starts at morphological defects,[4,8–19,29] the dewetting of the patterned films starts at the edges of the artificial trenches. Due to the fourfold symmetry of the Si(001) surface, in-plane trench orientations between 0° and 45° with respect to the ⟨110⟩ direction have been studied. According to the orientation of the front edges, we observe two different dewetting mechanisms (Fig. 1 and Fig. 2). If the film edge is aligned along the ⟨110⟩ direction, the dewetting occurs by the retraction of a straight front [Figs. 2(a) to 2(d)]. For other crystallographic directions, a breakdown of the trench edge is observed and the dewetting proceeds via the formation of void fingers separated by Si fingers (see Fig. 1 for fronts oriented at 10°, 20°, 30°, and 45° with respect to the ⟨110⟩ direction). In the following ⟨110⟩ straight fronts will be called stable fronts while fingered fronts will be called unstable fronts. This is illustrated in Fig. 2 where are reported a LEEM

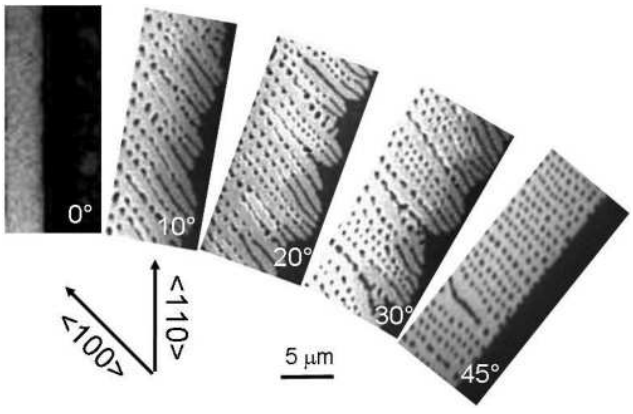

FIG. 1. LEEM images (bright field) of UHV-annealed SOI artificial fronts having different edge orientation with respect to the ⟨110⟩ direction. The Si material is dark and the SiO_2 substrate is bright. The dewetting fronts form ⟨100⟩-oriented Si fingers whatever the initial orientation of the dewetting fronts. The breakdown of the Si fingers, separated by $\lambda \approx 0.8\ \mu$m, forms 3D nanoislands (dots) aligned in the ⟨100⟩ direction. Notice that the nanoisland distribution is more narrow when the Si fingers are perpendicular to the front edge (Si thickness: 22 nm, temperature: 825 °C).

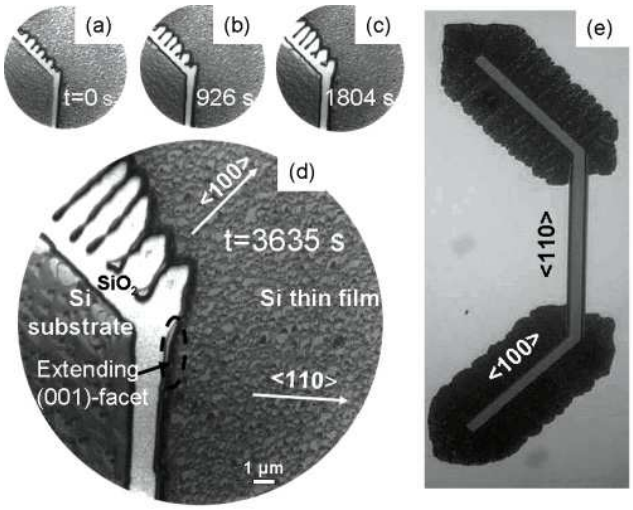

FIG. 2. (a) to (d): LEEM sequence (dark field mode, same field of view of 15 μm) obtained during dewetting of an artificial trench formed by ⟨110⟩- and ⟨100⟩-oriented branches: The ⟨110⟩ edge remains straight while the ⟨100⟩ edge recedes by formation of perpendicular Si fingers separated by void fingers. (e) Macroscopic picture (obtained by optical micrograph) of the partial dewetting at 825 °C of an artificial trench with one ⟨110⟩- and two ⟨100⟩-oriented branches dug by lithography (trench width: 2 μm, total length: 75 μm, Si thickness: 22 nm).

sequence of a dewetting trench constituted by ⟨110⟩ and ⟨100⟩ segments [Figs. 2(a) to 2(d)] and a macroscopic view of a partially dewetted trench [Fig. 2(e)]. The dewetted zones essentially develop from the ⟨100⟩ segments which illustrates the strong anisotropy of the dewetting velocity $V_{\langle 100\rangle} \gg V_{\langle 110\rangle}$. Notice that the Si fingers periodically shed mass, forming 3D nanoislands (dots in Fig. 1 and 5).

In the following we focus on the kinetics of the stable ⟨110⟩ and unstable ⟨100⟩ fronts. We will focus on the stationary state in which both stable and unstable fronts recede at constant morphology. In both cases we have measured, *in situ*and in real time, the kinetics of edge retraction as well as the kinetics of the local rim thickening at $T = 825\,^{\circ}$C for a 22-nm-thick SOI film.

B. Kinetics of stable receding fronts

Let us study the retraction of ⟨110⟩-oriented edges. Figure 2 reveals the key feature of the process: The ⟨110⟩-oriented edge is stable and remains straight during the dewetting process. During dewetting, the silicon expelled from the trench edge is transferred to a 3D rim (see AFM profile in Fig. 3). LEEM movies show that this rim is topped by a (001) atomic 1×2 or 2×1 reconstructed flat facet. Indeed, in dark field conditions, the top facet appears either dark or bright according to the diffraction spot—(1/2,0) or (0,1/2)—selected for imaging (Fig. 3). The flatness of the top facet of the rim is confirmed by AFM (Fig. 3). The stabilization of the ⟨110⟩ front edge orientation is highlighted by the progressive lateral extension of the (001) top facet along the front edge direction (Fig. 2).

As the rim recedes, its top facet alternatively flashes from bright to dark (inset of Fig. 4), which means that the rim thickens in a layer-by-layer growth mode with alternatively

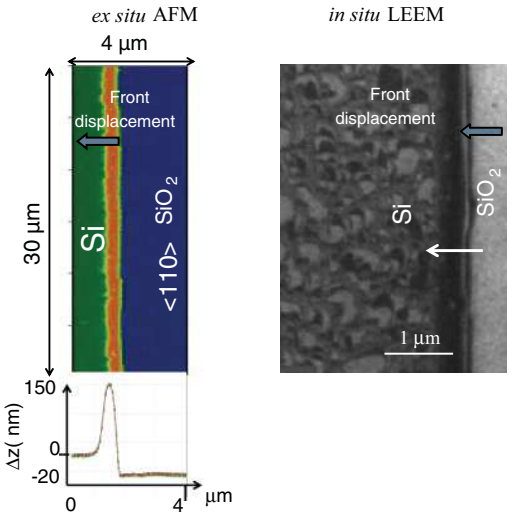

FIG. 3. (Color online) AFM and LEEM (dark field conditions) pictures of a stable ⟨110⟩ front. Notice in LEEM the bright contrast of the top of the rim characteristic of an atomically flat surface exhibiting a (1 × 2) reconstruction. AFM profile shows the 3D rim with its flat top facet.

1×2 then 2×1 surface reconstructions. The time dependence of the front position $x(t)$, as well as the time dependence of the rim thickening $h(t)$ (obtained by counting the number of flash events), is reported in Fig. 4. It is observed that the rim retracts as $\Delta x_{\rm exp}(t) = (190 \pm 20)t^{0.37\pm0.03}$ while simultaneously the global thickening behavior exhibits a $\Delta h_{\rm exp}(t) = (6 \pm 2)t^{0.38\pm0.02}$ behavior (with lengths expressed in nanometers and time in minutes). These results partially differ from numerical predictions obtained with continuous models[22] that predict $h(t) \sim t^{1/5}$ and $x(t) \sim t^{2/5}$. In Refs. 7 and 19 we have developed a 1D analytical model in which we assume that the velocity of a front edge is equal to the thermodynamic driving force times a surface-diffusion-based mobility. More precisely, our analytical expression reads $dx/dt = K\,(\mu/k_BT)$ with $K = (D_s c_{eq}\Omega^2/hwa^2)$ where Ω and a^2 respectively are the

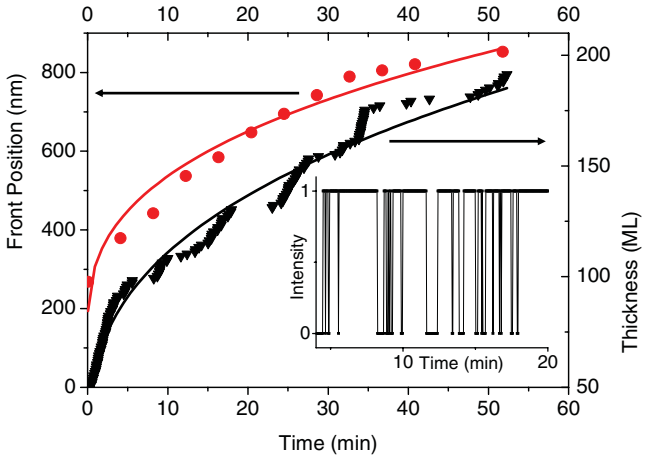

FIG. 4. (Color online) Front position (red circles) and rim height (black triangles) versus time (dots: experimental data, continuous curve: best fits). Inset: LEEM intensity versus time, recorded on the top facet of the rim, illustrating its layer-by-layer thickening.

TABLE I. Theoretical prediction and asymptotic behaviors. All the results have been obtained by considering mass conservation.

Box-shaped rim model (Refs. 7 and 19)
$dx/dt = D_s c_{eq}\Omega^2/wa^2h^2$
If $w = C^{te}$: $x \sim t^{1/3}$, $h \sim t^{1/3}$
If $w/h = C^{te}$: $x \sim t^{0.4}$, $h \sim t^{0.2}$
If $h = C^{te}$: $x \sim t^{1/2}$
If h and $w = C^{te}$: $x \sim t$

volume and surface area of an atom, D_s the diffusion constant, c_{eq} the surface adatom fraction at equilibrium, and h and w the height and the width of the rim. The quantity $\mu = E_s/h$ is the local chemical potential per unit volume at the edge of the rim[30] with $E_s = \gamma_{Si} + \gamma_{int} - \gamma_{Ox}$ a parameter that controls the wetting properties of the film (surface energy γ_{Si}) on the substrate (surface energy γ_{Ox}) with γ_{int} the interfacial energy.[7] The velocity expression dx/dt can be analytically integrated in a few asymptotic situations reported in Table I.

Comparison of experimental data and asymptotic power laws reported in Table I suggests that the rim recedes at constant width. More precisely, using all available material data, $E_s = 14$ eV nm^{-2} from Ref. 19, $D_s c_{eq} = 7 \times 10^6$ nm^2 s^{-1} valid at $T = 825\,^\circ$C,[19,31] initial film thickness $h_0 = 22$ nm, a rim width $w \approx 400$ nm (measured by AFM), $\Omega = a_0^3$, $a = a_0\sqrt{2}/2$ valid for Si(001) surface with $a_0 = 0.543$ nm the Si crystallographic parameter, we obtain $x(t) \approx 190\,t^{1/3}$ and $h(t) \approx 10\,t^{1/3}$ in quite nice agreement with the experimental behaviors: $\Delta x_{\rm exp}(t) \approx 190t^{0.37\pm0.03}$ and $\Delta h_{\rm exp}(t) \approx 6t^{0.38\pm0.02}$.

However, LEEM experiments give further information on the thickening mechanism. Indeed when analyzing the bright-to-dark blinking (see inset of Fig. 4) it can be noticed that the residence time $\tau_{\rm res}$ in the dark or bright state, which corresponds to the time needed to nucleate a 2D nucleus, is longer than the completion time of a new terrace. In other words LEEM data show that the rim thickening proceeds via nucleation of 2D islands followed by island growth that quickly invades the whole facet. The same thickening mechanism is at the origin of 3D island thickening induced by dewetting in various other systems.[5,32–34] In this context we could expect to obtain a better fit considering that the limiting step is the two-dimensional nucleation on top of the rim facet. However, in our system, the classical capillary theory of nucleation cannot be applied. Indeed, though the Si(001) surface contains two types of steps having two different free energies, at 825 °C one can use the mean step energy $\beta = 6$ meV/Å[35] so that assuming circular nucleating islands, the critical nucleus radius $(\beta/a\mu)$ deduced from the classical capillary theory is too small (roughly a dimer) and thus out of its domain of validity. The growth rate of the rim thus should be closer to a Hertz-Knudsen type law[36,37] $dh/dt \propto \mu/k_BT$, which is the form of the analytical expression given in Table I. Finally, notice that we measure $\tau_{\rm res}^{1\times2}/\tau_{\rm res}^{2\times1} = 1.50 \pm 0.02$ irrespective of the film thickness which means independently of the slowing down of the rim thickening (Fig. 4). This asymmetry is due to the diffusion anisotropy on 1×2 and 2×1 surfaces since, using the nucleation theory, there comes $\tau_{\rm res}^{1\times2}/\tau_{\rm res}^{2\times1} = D^{2\times1}/D^{1\times2}$

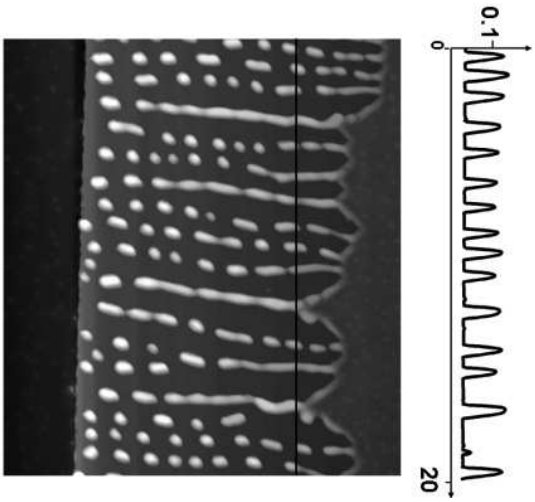

FIG. 5. AFM picture (right) and height profile (left) of an unstable ⟨100⟩ front. The AFM profile (vertical and horizontal units are μm) shows that the finger instability is associated with a local height instability. Notice that the fingers locally form bunches. The wider the finger width inside a bunch, the smaller the bunch velocity.

where D^i are the diffusion coefficients for adatoms on the terrace $i = 1 \times 2$ or $i = 2 \times 1$. Thanks to the layer-by-layer growth mode of the rim, the adatom flux leaving the front is thus alternatively oriented along or perpendicular to the dimers of the reconstructed top facet. The 2D nucleation rate is thus influenced by the dimer orientation with respect to the flux of diffusing adatoms.

C. Kinetics of unstable receding fronts

Let us now consider the case of ⟨100⟩-oriented fronts. Figure 2 shows sequential images from the retraction of a 22-nm-thick SOI film with ⟨100⟩-oriented edge. The ⟨100⟩ front is unstable; it locally slows down and forms elongated structures called Si fingers into which the mass of the film is efficiently transferred (Fig. 5). Other regions of the dewetting fronts recede at constant velocity $[x(t) \sim t]$ and govern the velocity of the mean front. This steady state regime is characterized by a constant shape of the void finger tip. From AFM and LEEM we can infer that the void finger tip is the intersection of two adjacent {111} and/or {113} facets. It is observed that the rim at the void finger tip recedes with a constant height ($\sim$ 30 nm) smaller than the height of the surrounding Si fingers. This confirms, in agreement with predictions of Table I, that void fingers receding at constant shape (constant height h and constant width w) have a constant velocity: $x(t) \sim t$. Obviously in this case there is no more local mass conservation but only a global mass conservation where the Si expelled from the void tip feeds the Si fingers leading to a periodic height variation of the receding front (Fig. 5). At a constant temperature, the period λ of the Si fingers remains constant during the whole dewetting process. We also find that the velocity of the front depends on the void-finger density: $V_{\text{fing}} \sim \lambda^{-1}$. This means that the evolution of an unstable front can be mainly captured by simply considering the local behavior of a void tip. At first sight, the dewetting dynamics is thus simply limited by the mass transfer from each void tip to its neighboring Si fingers (for a discussion see Ref. 7).

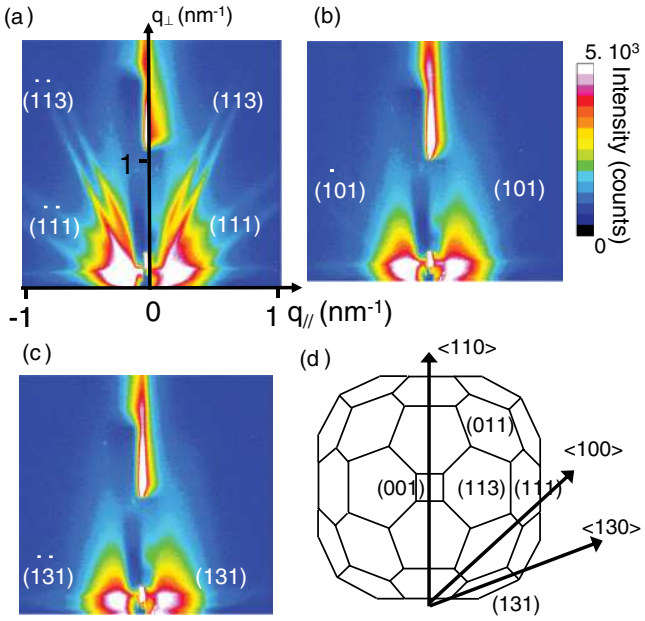

FIG. 6. (Color online) GISAXS patterns recorded with incident beam parallel to ⟨110⟩ (a), ⟨100⟩ (b), and ⟨130⟩ (c) directions. In (d) is sketched the Si equilibrium shape with its characteristic {011}, {001}, {113}, and {111} microfacets as well as the directions of the fronts described in the text.

However collective behaviors involving neighbored fingers exist. It results that Si fingers may form bunches of 2–5 fingers (Fig. 2 and Fig. 5) of local velocity $V_{\text{bunch}} \sim \lambda_{\text{loc}}^{-1}$ where λ_{loc} is the interfinger distance inside the bunch.

IV. STABILITY CONDITIONS AND SURFACE FACETING

The presence of facets on the dewetting fronts has been characterized by grazing incidence small angle x-ray scattering (GISAXS) at the European Synchrotron Facility in Grenoble, France. We report in Figs. 6(a) to 6(c) the GISAXS patterns recorded with incident beam respectively parallel to the ⟨110⟩, ⟨100⟩, and ⟨130⟩ directions. In the case of the ⟨110⟩ direction, we observe scattering rods (with respect to the surface normal)

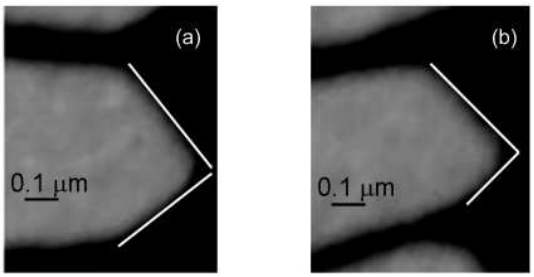

FIG. 7. Void-tip structure (bright field mode; dark: Si material, bright SiO_2 substrate). (a) Symmetric void tip formed by two symmetric microfronts oriented along {110} directions (bright lines) characteristic of a perfectly ⟨100⟩-oriented dewetting front. (b) Asymmetric void-tip characteristic of a dewetting front slightly misoriented from the ⟨100⟩ direction, with two asymmetric microfronts oriented along {110} directions (bright lines) at the origin of local deviation of the Si finger orientation.

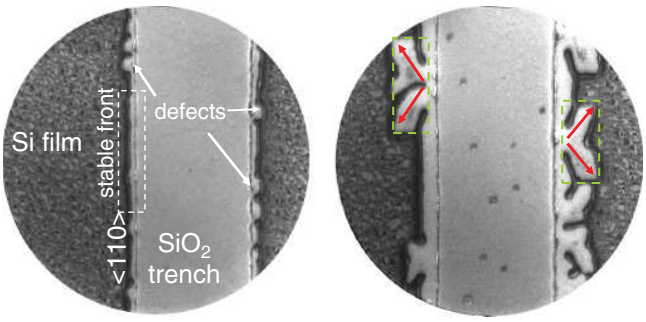

FIG. 8. (Color online) Instability of a ⟨110⟩-oriented front initiated by the formation of squared defects whose corners are at the origin of the formation of ⟨100⟩- and ⟨010⟩-oriented fingers (red arrows).

associated with the presence of well-developed {111} and {113} facets. These facets belong to the Si equilibrium shape[7,38,39] and have for common zone axis the ⟨110⟩ front direction. For the ⟨100⟩ direction, the only facet is a small {011} facet. The strong stability of the ⟨110⟩ front with respect to the ⟨100⟩ front is thus clearly associated with the presence of facets parallel to the front edge leading to a fully faceted ⟨110⟩ front. Since {111} and {113} facets stabilize the ⟨110⟩ front we could expect that other directions, such as ⟨310⟩ fronts, could be stabilized by {311} facets. However, as already reported by Danielson,[16] this is not the case. This is mainly due to the small size of these facets [Fig. 6(c)].

The sketch of the Si equilibrium shape reported in Fig. 6 illustrates the strong stability of the ⟨110⟩ front with respect to the ⟨100⟩ front. The {111} and {113} facets that stabilize the ⟨110⟩ front favor a decomposition of the ⟨100⟩ front into two microfronts oriented along the ⟨110⟩ directions. These microfronts are the sides of the tip of the void fingers formed by the unstable front in experiments as reported in Fig. 7(a). Notice that if a local deviation of the front orientation occurs, the corresponding void tips are no more formed by two symmetric microfronts but a local asymmetry appears and leads to local deviations of the finger orientation [Fig. 7(b)].

All these experimental observations are in agreement with recent models of solid dewetting mechanisms where, on the basis of diffusion-limited mass transport and 2D nucleation on the rim facet, it has been predicted that front instability emerges for rough front orientations, while fronts along faceted orientations remain stable.[24]

Finally, the results reported in Fig. 8 allow us to understand how a ⟨110⟩ stable front may be destabilized by defects. In most cases, small defects which locally modify the front velocity are spontaneously healed. However, in a few cases, the pinning leads to the formation of square-shaped defects (Fig. 8) limited by ⟨110⟩ stable sides. The corners of these squared defects behave as precursors of ⟨100⟩-oriented void fingers limited by ⟨110⟩ microfronts. Thus a defective ⟨110⟩ front may be destabilized, forming after a long enough time an assembly of ⟨100⟩- and ⟨010⟩-oriented Si fingers separated by periodic void fingers [see for instance Fig. 4(c) in Ref. 19]. Notice that such a local destabilization of ⟨110⟩ fronts naturally occurs in the case of heterogeneous dewetting on defected zones, where the ⟨110⟩-oriented sides of the opening voids are at the origin of finger formation.[7] As shown in Fig. 7 local deviations of the side orientation lead to local deviations of the finger orientation. This is the reason heterogeneous dewetting leads to a majority of ⟨100⟩-oriented fingers but also other possible orientations, among which is ⟨130⟩-oriented fingers locally stabilized by the presence of {131} facets along the fingers.[15,32]

V. CONCLUSION

In conclusion, SOI dewetting exhibits a strong anisotropy. The ⟨110⟩ fronts are stable. They recede by forming a faceted rim that thickens in a layer-by-layer mode. While classical theories based on isotropic continuum surface diffusion correctly capture the main tendencies ($x \sim t^{\alpha}$, $h \sim t^{\beta}$), they fail to find the accurate value of the exponent which is driven by the 2D nucleation mechanism on top of the faceted rim. The ⟨100⟩ fronts are highly unstable. Again, classical theories fail to predict the correct behavior while our analytical expression reported in Refs. 7 and 19 agrees with most of the experimental results. The model could be improved by taking into account the 2D nucleation on top of the rim facet but beyond the usual capillary approximation. The stability condition is governed by the presence of crystallographic atomically flat facets having the front direction as a common zone axis. In the absence of such facets the front is unstable and forms ⟨100⟩-oriented fingers the period of which is kinetically selected since the interfinger distance has been shown[7] to correspond to the most unstable mode predicted by the classical linear analysis stability based on the surface diffusion model.[22,26] Finally, this study opens new perspectives since the dewetting may be delayed or the Si nanoisland formation may be controlled by selecting the front orientation. Indeed, unless defective, ⟨110⟩ fronts limit dewetting while ⟨100⟩ fronts dewet with formation of well-ordered Si nanoislands.

ACKNOWLEDGMENTS

We thank E. Bussmann and O. Pierre-Louis for fruitful discussions. We also acknowledge J. C. Barbé and co-workers from CEA LETI for SOI fabrication, Frederic Bedu and Igor Ozerov from CINaM-Planete for lithography support, as well as J. Eymery and N. Blanc for their help during our beam time access at the ESRF. This work is supported by ANR PNano Grant DEFIS (ANR 08-Nano-036) and PACA Grant Nanosurf.

[1]C. Jahan, O. Faynot, L. Tosti, and J. Hartmann, J. Cryst. Growth **280**, 530 (2005).
[2]S. V. Kodambaka, J. Tersoff, and F. Ross, Science **316**, 729 (2007).
[3]H.-C. Yuan, B. Yang, J. Simmons, M. Marcus, Z. Ma, and M. Eriksson, Proc. SPIE **5971**, 597118 (2005).
[4]D. T. Danielson, D. Sparacin, J. Michel, and L. Kimerling, J. Appl. Phys. **100**, 083507 (2006).
[5]K. Thurmer and N. C. Bartelt, Phys. Rev. Lett. **100**, 186101 (2008).
[6]G. Capellini, G. Ciasca, M. de Seta, A. Notargiacomo, F. Evangeslisy, and M. Nardone, J. Appl. Phys. **105**, 093525 (2009).

[7]F. Cheynis, E. Bussmann, F. Leroy, T. Passanante, and P. Müller, Phys. Rev. B **84**, 245439 (2011).
[8]Y. Ono, M. Nagase, M. Tabe, and Y. Takahashi, Jpn. J. Appl. Phys. **34**, 1728 (1995).
[9]R. Nuryadi, Y. Ishikawa, and M. Tabe, Appl. Surf. Sci. **159**, 121 (2000); **160**, 121 (2000).
[10]B. Legrand, V. Agache, J. Nys, V. Senez, and D. Stievenard, Appl. Phys. Lett. **76**, 3271 (2000).
[11]B. Legrand, V. Agache, T. Melin, J. Nys, V. Senez, and D. Stievenard, J. Appl. Phys. **91**, 106 (2002).
[12]R. Nuryadi, Y. Ishikawa, Y. Ono, and M. Tabe, J. Vac. Sci. Technol. B **20**, 167 (2002).
[13]B. Yang, P. Zhang, D. E. Savage, M. G. Lagally, G. H. Lu, M. Huang, and F. Liu, Phys. Rev. B **72**, 235413 (2005).
[14]P. Sutter, W. Ernst, Y. Choi, and E. Sutter, Appl. Phys. Lett. **88**, 141924 (2006).
[15]E. Dornel, J. C. Barbé, F. de Crecy, G. Lacolle, and J. Eymery, Phys. Rev. B **73**, 115427 (2006).
[16]D. T. Danielson, Ph.D. thesis, University of California, Berkeley, 2008.
[17]E. Dornell, Ph.D. thesis, Université de Grenoble, 2007.
[18]Y. Fan, R. Nuryady, Z. Burhadunin, and M. Tabe, Jpn. J. Appl. Phys. **47**, 1461 (2008).
[19]E. Bussmann, F. Cheynis, F. Leroy, P. Müller, and O. Pierre-Louis, New J. Phys. **13**, 043017 (2011).
[20]Y. Ishikawa, Y. Imai, H. Ikeda, and M. Tabe, Appl. Phys. Lett. **83**, 3162 (2003).
[21]Y. Ishikawa, M. Kumezawa, R. Nuryadi, and M. Tabe, Appl. Surf. Sci. **190**, 11 (2002).
[22]W. Kan and H. Wong, J. Appl. Phys. **97**, 43515 (2005).
[23]O. Pierre-Louis, A. Chame, and Y. Saito, Phys. Rev. Lett. **103**, 195501 (2009).
[24]M. Dufay and O. Pierre-Louis, Phys. Rev. Lett. **106**, 105506 (2011).
[25]J. Ye and C. V. Thompson, Phys. Rev. B **82**, 193408 (2010).
[26]W. Mullins, J. Appl. Phys. **28**, 333 (1957).
[27]E. Bussmann, F. Cheynis, F. Leroy, and P. Müller, IOP Conf. Ser.: Mater. Sci. Eng. **12**, 012016 (2010).
[28]E. Bauer, Rep. Prog. Phys. **57**, 895 (1994).
[29]Z. Burhanudin, R. Nuryadi, Y. Ishikawa, M. Tabe, and Y. Ono, Appl. Phys. Lett. **87**, 121905 (2005).
[30]O. Pierre-Louis, A. Chame, and M. Dufay, Eur. Phys. J. B **77**, 5763 (2010).
[31]M. E. Keefe, C. C. Umbach, and J. M. Blakely, J. Phys. Chem. Solids. **55**, 965 (1994).
[32]K. Thurmer, E. D. Williams, and J. E. Reutt-Robey, Phys. Rev. B **68**, 155423 (2003).
[33]K. Man, Q. Guo, and M. Altman, Surf. Sci. **600**, 1080 (2006).
[34]E. J. Luber, B. C. Olsen, C. Ophus, and D. Mitlin, Phys. Rev. B **82**, 085407 (2010).
[35]N. C. Bartelt, R. M. Tromp, and E. D. Williams, Phys. Rev. Lett. **73**, 1656 (1994).
[36]H. Hertz, Ann. Phys. (Berlin) **17**, 193 (1882).
[37]M. Knudsen, Ann. Phys. (Berlin) **47**, 697 (1915).
[38]J. Bermond, J. Métois, X. Egea, and F. Floret, Surf. Sci. **330**, 48 (1995).
[39]P. Müller and J.-J. Métois, Thin Solid Films **517**, 65 (2008).

[4] : Démouillage de Ge/SiO_2 par GISAXS

Cheynis *et al.*, Appl. Phys. Lett. (2013)

Agglomeration dynamics of germanium islands on a silicon oxide substrate: A grazing incidence small-angle x-ray scattering study

F. Cheynis,[a] F. Leroy, T. Passanante, and P. Müller
Aix-Marseille Université, CNRS, CINaM UMR 7325, 13288 Marseille, France

(Received 8 March 2013; accepted 9 April 2013; published online 23 April 2013)

Grazing-incidence small-angle X-ray scattering (GISAXS) and grazing-incidence X-ray diffraction techniques are used to characterise the thermally induced solid-state dewetting of Ge(001) thin films leading to the formation of 3D Ge islands. A quantitative analysis based on the Kolmogorov-Johnson-Mehl-Avrami model is derived. The main physical parameters controlling the dewetting (activation energy and kinetic pre-factors) are determined. Assuming that the dewetting is driven by surface/interface minimisation and limited by surface diffusion, the Ge surface self-diffusion reads as $D_{s,0}c_0\, e^{-E_a/(k_BT)} \sim 3 \times 10^{18}\, e^{-2.6\pm0.3\,\mathrm{eV}/(k_BT)}\,\mathrm{nm}^2/\mathrm{s}$. GISAXS technique enables to reconstruct the mean Ge-island shape, including facets. © *2013 AIP Publishing LLC*
[http://dx.doi.org/10.1063/1.4802843]

When metastable solid thin films are heated up to a sufficiently high temperature, a morphological transition occurs from a 2D configuration to an assembly of agglomerated 3D islands. This solid-state dewetting may become a simple method to produce well-ordered structures used, for instance, as precursors for nanowires growth.[1] *Ex situ* analysis of the morphology evolution of solid-state thin films has been available in the literature for almost fifty years.[2,3] In the last decade, *in situ* studies of their dynamic evolution have been reported mostly using Low-Energy Electron Microscopy (LEEM)[4–10] or resistive measurements.[11,12] However these techniques do not give access *in situ* to structural features such as lateral facets. The first studies to describe qualitatively the solid-state dewetting using reciprocal-space techniques such as grazing-incidence small-angle X-ray scattering (GISAXS)[13] along with grazing-incidence X-ray diffraction (GIXD) are reported in Refs. 14 and 15.

In this paper, we demonstrate that using these techniques allows to determine accurately the main physical parameters (activation energy and kinetic pre-factors) that govern the dewetting dynamics of Ge(001) solid-state thin films on amorphous SiO_2 substrate. To do so, an adequate analytical model is required. We use the Kolmogorov-Johnson-Mehl-Avrami model (or KJMA model) to interpret our experimental data.[16] In addition to real-space imaging techniques, GISAXS gives access to the mean shape of the agglomerated 3D island, including facets. Here, we focus on the dewetting properties of Ge(001) layers on amorphous SiO_2 substrate as a function of the Ge(001)-layer thickness and the dewetting temperature. These so-called Germanium-on-Insulator (GeOI or GOI) substrates are of high technological interest in the field of microelectronics.[17]

The samples under study have been obtained from GeOI wafers, fabricated by means of the Smart Cut™ process at CEA-Léti, France[17] and characterised at the European Synchrotron Radiation Facility (ESRF, beamline BM32, France). We have used an X-ray wavelength of 0.11697 nm and an incident angle close to the critical angle for total reflection on Ge ($\alpha_c = 0.23°$ at this wavelength). The GISAXS patterns have been recorded using a 2D detector (X-ray Image Star 9000, Photonic Science). The in-plane (resp. out-of-plane) exit angle range was $[-1.5°; 1.1°]$ (resp. $[0°; 2.5°]$). The initial thickness of the Ge(001) films on a ~140 nm-thick amorphous SiO_2 layer was about 45 nm. A standard chemical cleaning procedure in organic solvents of the films has been used before loading the samples into ultra-high vacuum conditions (chamber base pressure $P \lesssim 5.10^{-11}$ Torr). The ~45 nm-thick samples have been outgassed at 800°C for several hours. This thickness is sufficient to keep the Ge(001) layer in a kinetically stable state and prevent any dewetting as checked by GISAXS. The *in situ* treatment consists in a Ar-ion bombardment at room temperature under a partial pressure $P_{Ar} \sim 5.10^{-6}$ Torr and a bombardment voltage of $V = 1\,\mathrm{kV}$ ($I_{sample} \sim 6\,\mu A$). The thickness reduction of the Ge(001) film during the ion bombardment has been monitored *in situ* by GIXD by measuring the periodicity of the Pendellösung interference fringes of the (02L) crystal truncation rod. After ion bombardment, the sample is annealed at 400–600 °C for ~1 h to heal the defects induced by the ion bombardment and thus to reach a perfect crystalline state as controlled by the width of the Ge diffraction peak. Fig. 1 shows a typical sequence of the Pendellösung interference fringe evolution upon ion etching. The increase of the fringe period indicates that the Ge(001)-film thickness is being reduced. Note that the annealing at 400–600 °C after the ion etching induces an increase of the thickness of the Ge(001) layer of typically 3 nm due to the improvement of the Ge crystalline order close to the surface. Ge(001)-layer thicknesses in the range of 10–40 nm and dewetting temperatures in the range of 800–900 °C have been explored.

The morphology evolution of the Ge film during its dewetting has been studied using *in situ* GISAXS. A typical sequence of the GISAXS pattern evolution is reported in Fig. 2. In this measurement, the incident beam is parallel to the ⟨110⟩ azimuth, the dewetting temperature is close to 800 °C,

[a]Electronic mail: cheynis@cinam.univ-mrs.fr

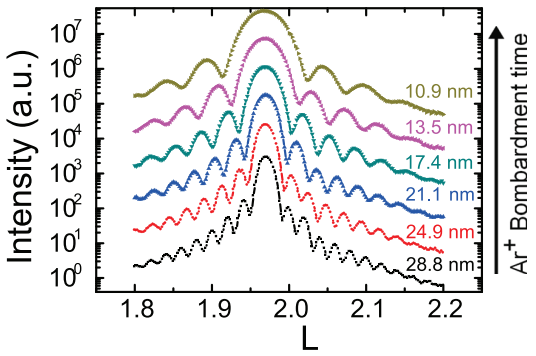

FIG. 1. Time evolution of the Pendellösung interference fringes close to the (022) Bragg peak upon ion etching at room temperature. The thickness of the Ge(001) layer is reduced from 45 nm down to 10.1 nm in about 3 h.

and the acquisition time per GISAXS pattern is 1 min. Before dewetting the diffusion pattern is characteristic of a flat surface [Fig. 2(a)]. As the dewetting proceeds, additional diffuse scattering rods (DSRs) appear. This indicates that the Ge film agglomerates into oriented Ge islands exhibiting facets. A complete analysis of the GISAXS patterns obtained for various azimuthal angles gives access to the mean shape of the 3D Ge islands [Fig. 2(e)]. The size of the facets of the reconstructed mean island shape qualitatively reproduces the facet DSR signals. The mean island shape has been elongated to mimic the typical post-mortem optical micrograph shown in Fig. 2(f). The main facets are {113}, {15 3 23}, and {111} facets. Notice that all these facets have been already observed on Ge islands[18] and have been shown to be stable surfaces.[19]

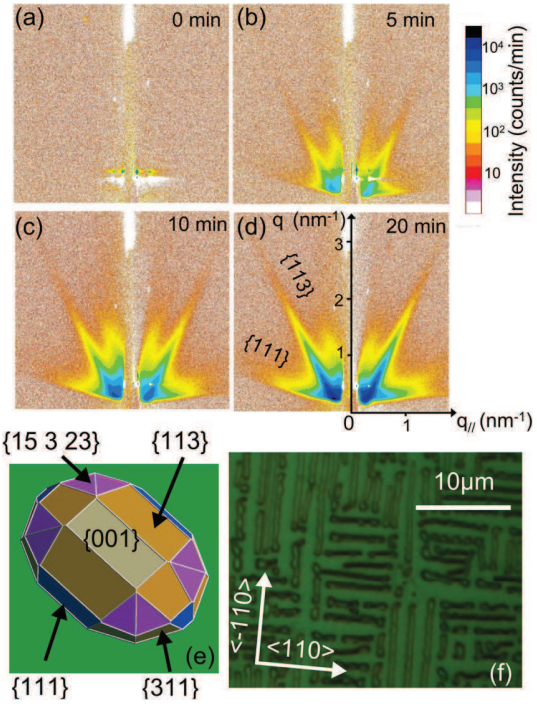

FIG. 2. (a)-(d) Time evolution of the GISAXS pattern along the ⟨110⟩ azimuth upon dewetting at 794 °C of a 33 nm-thick GeOI sample. (e) Illustrative mean Ge-island shape obtained from in-plane GISAXS scans. (f) Post-mortem optical micrographs of a 19 nm-thick GeOI sample dewetted at 794 °C.

In our measurements, the most intense signal comes from the {113} DSRs, meaning that the mean shape of the Ge islands exhibits large {113} facets. Using this signal it is thus possible to follow in real-time the dewetting dynamics of the Ge(001) layer. More specifically, we have used the intensity of the {113} facet integrated over a given region of the reciprocal space along a {113} DSR. For each sample, the data have been then background-corrected and normalized with respect to the most intense {113} DSR measured as a function of the dewetting time. With this method, we obtain normalized sigmoids (Fig. 3) that represent the evolution of the surface fraction of the dewetted area. These curves can be fitted using an adequate analytical model. In our case, the fractional dewetted area can be described within the framework of the KJMA model whose general comprehensive expressions can be found in Ref. 16. This model has been first developed to describe the crystal growth of 2D or 3D islands from nucleation to coalescence. Here, it is applied to our system, considering that the solid-state dewetting can be regarded as a growth of 2D *void islands*. Assuming that the square-shaped voids are characterised by a constant density, N_0, a mean area $2R \times 2R = 2vt \times 2vt$ (where v is the void-edge velocity, supposed to be constant) and a simultaneous initial void-island nucleation, the KJMA model evaluates the surface void-island coverage time evolution, $\theta(t)$, to be

$$\theta(t) = 1 - \exp(-4N_0 v^2 t^2). \quad (1)$$

For the following data analysis, we have used $N_0 = 1/L^2$ (with $125\,\mu m \leq L \leq 175\,\mu m$), which are reasonable void densities considering the post-mortem optical micrographs of the dewetted samples.

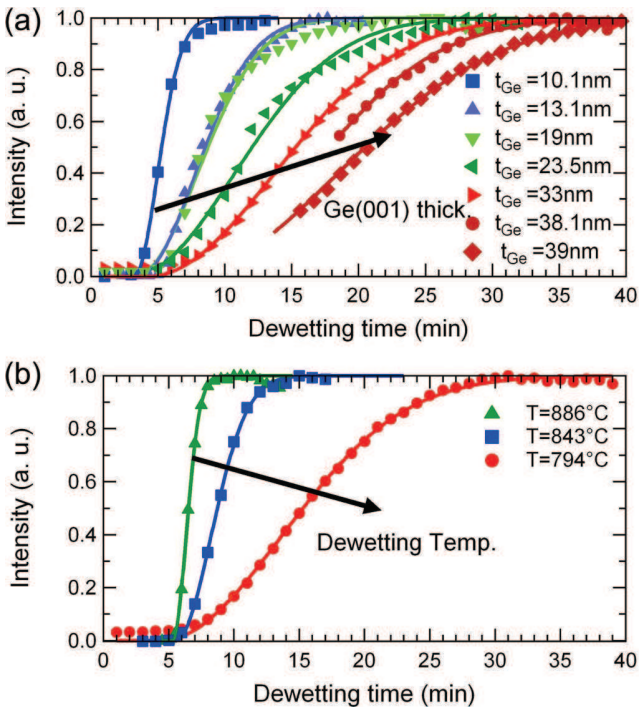

FIG. 3. Time evolution of the GISAXS intensity of the {113} facets upon dewetting (a) for different Ge(001) thicknesses at 794 °C and (b) at different temperatures for a Ge(001) thickness of ≃33 nm.

The normalized GISAXS intensity variation of {113} facets as a function of the dewetting time are summarised in Fig. 3. Fig. 3(a) shows this evolution for different Ge(001)-layer thicknesses at a given temperature (T $\simeq$ 794 °C) while in Fig. 3(b) the role of the annealing temperature for a given Ge(001)-layer thickness ($h_{Ge(001)} \simeq 33$ nm) is evidenced. Data shown in Fig. 3 fitted with Eq. (1) allow us to determine the mean void-growth velocity for our different samples (Fig. 4).

In our previous works,[7,9] we have derived an expression for the 1D velocity of the thickening void edge assuming that this displacement is driven by surface/interface energy minimisation and limited by surface diffusion on the so-called *rim*. It reads as

$$v_{rim} = \left(\frac{2\Omega^2}{\pi h_0^3 a^2}\right) D_{s,0}c_0 e^{-E_a/k_BT}\left(\frac{E_s}{k_BT}\right), \qquad (2)$$

where Ω is the Ge atomic volume, h_0 is the initial Ge-layer thickness, a is the in-plane atomic distance, $D_s c = D_{s,0}c_0 e^{-E_a/k_BT}$ is the Ge surface self-diffusion, and $E_s = \gamma_{Ge} + \gamma_{Ge/SiO_2} - \gamma_{SiO_2}$ is the surface/interface energy balance gained upon dewetting. In this case, we have assumed that the rim height is simply h_0 and, as in Refs. 3 and 20, the rim width is approximated by $\pi h_0/2$. Fig. 4 shows the evolution of the dewetting velocity as a function of the tunable experimental parameters and the corresponding non-linear fits obtained with Eq. (2). The film-thickness dependence of the void-edge velocity is compatible with a h_0^{-3} power law [Fig. 4(a)]. From the Arrhenius plot in Fig. 4(b), we obtain the dewetting activation energy: $E_a = 2.6 \pm 0.3$ eV. This value is in quantitative agreements with independent LEEM measurements yielding $E_a = 2.7 \pm 0.2$ eV.[21] Using Eq. (2) and Fig. 4 pre-factors, we have now two approaches to derive the value of $D_{s,0}c_0 E_s$. From the thickness and the dewetting temperature dependences of the velocity, we obtain, respectively, at 843 °C the following mean values: $D_{s,0}c_0 E_s = 2.5 \times 10^{19}$ eV/s and $D_{s,0}c_0 E_s = 4.2 \times 10^{19}$ eV/s. Taking into account the wide range of feasible void densities broadens the interval of accessible values for $D_{s,0}c_0 E_s$: $D_{s,0}c_0 E_s \in [2.5 \times 10^{18}\,\text{eV/s}; 7.3 \times 10^{20}\,\text{eV/s}]$ and $D_{s,0}c_0 E_s \in [1.0 \times 10^{18}\,\text{eV/s}; 6.2 \times 10^{20}\,\text{eV/s}]$, respectively. Using surface/interface energy values available in the literature, it is possible to estimate the coefficient $D_{s,0}c_0$. Typical values are $\gamma_{Ge} \simeq 5\,\text{eV/nm}^2$ [Refs. 22 and 23], $\gamma_{Ge/SiO_2} \simeq 10\,\text{eV/nm}^2$ [Refs. 24 and 25], and $\gamma_{SiO_2} \simeq 4\,\text{eV/nm}^2$ [Refs. 25 and 26]. This gives $E_s \simeq 11\,\text{eV/nm}^2$ and then $D_{s,0}c_0 \simeq 3 \times 10^{18}\,\text{nm}^2/\text{s}$ with $D_{s,0}c_0 \in [2.3 \times 10^{17}\,\text{nm}^2/\text{s}; 5.7 \times 10^{20}\,\text{nm}^2/\text{s}]$. The Ge self-diffusion becomes $D_{s,0}c_0 e^{-E_a/(k_BT)} \sim 3.6 \times 10^6\,\text{nm}^2/\text{s}$ at ~840 °C. This value is in fair agreement with the value of $\simeq 4 \times 10^6\,\text{nm}^2/\text{s}$ reported for Si by Keeffe *et al.* in Ref. 27 for a similar temperature range.

To conclude, we have shown that using X-ray scattering (GISAXS and GIXD) allows us to study quantitatively the dewetting dynamics of a solid thin film. Assuming that the dewetting is driven by surface/interface minimisation and limited by surface diffusion, we have found that the Ge surface self-diffusion reads as $D_{s,0}c_0\, e^{-E_a/(k_BT)} \sim 3 \times 10^{18}\, e^{-2.6 \pm 0.3\,\text{eV}/(k_BT)}\,\text{nm}^2/\text{s}$, in good agreement with values available for Si self-diffusion.

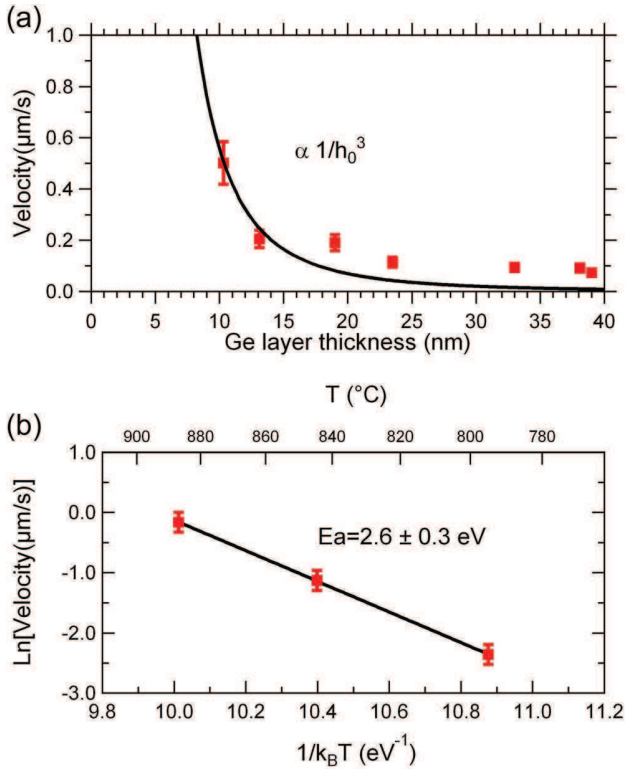

FIG. 4. (a) Thickness evolution of the dewetting velocity at 794 °C. (b) Arrhenius plot of the dewetting velocity for a Ge(001)-film thickness of 33 nm.

This work was supported by ANR grant PNANO DéFIS (Grant No. ANR 08-nano-036) and by APO grant delivered by Provence Alpes Côte d'Azur Region Council. The authors would like to thank E. Augendre (CEA-Léti) for GeOI preparation, N. Blanc and Beamline BM32 staff for their help during our beamtime access at the ESRF, and J.-C. Barbé (CEA-Léti) and S. Curiotto (CINaM) for fruitful discussions.

[1]D. Kwak, H. Cho, and W.-C. Yang, Physica E **37**, 153 (2007).
[2]R. Brandon and F. J. Bradshaw, Royal Aircraft Establishment, Report No. 66095, 1966.
[3]E. Jiran and C. V. Thompson, J. Electron. Mater. **19**, 1153 (1990).
[4]W. L. Ling, T. Giessel, K. Thurmer, R. Q. Hwang, N. C. Bartelt, and K. F. McCarty, Surf. Sci. **570**, L297 (2004).
[5]K. F. McCarty, Nano Lett. **6**, 858 (2006).
[6]E. Bussmann, F. Cheynis, F. Leroy, and P. Müller, IOP Conf. Ser.: Mater. Sci. Eng. **12**, 012016 (2010).
[7]E. Bussmann, F. Cheynis, F. Leroy, P. Müller, and O. Pierre-Louis, New J. Phys. **13**, 043017 (2011).
[8]F. Cheynis, E. Bussmann, F. Leroy, T. Passanante, and P. Müller, Int. J. Nanotechnol. **9**, 396 (2012).
[9]F. Cheynis, E. Bussmann, F. Leroy, T. Passanante, and P. Müller, Phys. Rev. B **84**, 245439 (2011).
[10]F. Leroy, F. Cheynis, T. Passanante, and P. Müller, Phys. Rev. B **85**, 195414 (2012).
[11]R. Saxena, M. J. Frederick, G. Ramanath, W. N. Gill, and J. L. Plawsky, Phys. Rev. B **72**, 115425 (2005).
[12]J. Petersen and S. G. Mayr, J. Appl. Phys. **103**, 023520 (2008).
[13]G. Renaud, R. Lazzari, and F. Leroy, Surf. Sci. Rep. **64**, 255 (2009).
[14]R. Felici, N. Jeutter, V. Mussi, F. B. de Mongeot, C. Boragno, U. Valbusa, A. Toma, Y. W. Zhang, C. Rau, and I. Robinson, Surf. Sci. **601**, 4526 (2007).
[15]R. Daudin, C. Revenant, G. Davi, and G. Renaud, Physica E **44**, 1905 (2012).

[16]M. Fanfoni and M. Tomellini, J. Phys.: Condens. Matter **17**, R571 (2005).
[17]E. Augendre, L. Sanchez, L. Benaissa, T. Signamarcheix, J.-M. Hartmann, C. Le Royer, M. Vinet, W. Van Den Daele, J.-F. Damlencourt, K. Romanjek, A. Pouydebasque, P. Batude, C. Tabone, F. Mazen, A. Tauzin, N. Blanc, M. Pellat, J. Dechamp, M. Zussy, P. Scheiblin, M.-A. Jaud, C. Drazek, C. Maurois, M. Piccin, A. Abbadie, F. Lallement, N. Daval, E. Guiot, A. Rigny, B. Ghyselen, K. Bourdelle, F. Boulanger, S. Cristoloveanu, T. Billon, O. Faynot, C. Deguet, and L. Clavelier, ECS Trans. **25**, 351 (2009).
[18]F. M. Ross, R. M. Tromp, and M. C. Reuter, Science **286**, 1931 (1999).
[19]A. A. Stekolnikov and F. Bechstedt, Phys. Rev. B **72**, 125326 (2005).
[20]D. T. Danielson, D. K. Sparacin, J. Michel, and L. C. Kimerling, J. Appl. Phys. **100**, 083507 (2006).
[21]F. Leroy, F. Cheynis, T. Passanante, and P. Müller, "Influence of facetted fronts on solid-state dewetting: a comparison between Ge and Si on SiO_2" (unpublished).
[22]W. Tyson and W. Miller, Surf. Sci. **62**, 267 (1977).
[23]R. Kern, G. Le Lay, and J. J. Métois, Curr. Top. Mater. Sci. **3**, 135 (1979).
[24]J. Du and P. Kroll, in *12th International Conference on the Physics of Non-Crystalline Solids (PNCS 12)* [J. Non-Cryst. Solids **356**, 2448 (2010)].
[25]C. Y. Chuang, Q. Li, D. Leonhardt, S. M. Han, and T. Sinno, Surf. Sci. **609**, 221 (2013).
[26]Z. Niu, K. Mukai, Y. Shiraishi, T. Hibiya, K. Kakimoto, and M. Koyama, in *Proceedings of 2nd International Conference on High Temperature Capillarity*, 1998, edited by N. Eustathopoulos and N. Sobczak, p. 175.
[27]M. E. Keeffe, C. C. Umbach, and J. M. Blakely, J. Phys. Chem. Solids **55**, 965 (1994).

[5] : Influence des facettes sur la dynamique des fronts de démouillage : une comparaison Ge et Si sur SiO_2
Leroy *et al.*, Phys. Rev. B (2013)

Influence of facets on solid state dewetting mechanisms: Comparison between Ge and Si on SiO_2

F. Leroy,* F. Cheynis,† T. Passanante, and P. Müller‡
CINaM, UMR CNRS 7325, Campus de Luminy, Aix-Marseille University, 13288 Marseille Cedex, France
(Received 7 May 2013; published 15 July 2013)

The dewetting properties of Ge/SiO_2 have been studied by low-energy electron microscopy and grazing incidence small-angle x-ray scattering in two temperature ranges characterized by the presence or the absence of {15 3 23} facets on the dewetting fronts. Thanks to a comparison with the Si/SiO_2 system, we show that the {15 3 23} facets: (i) play a role in the stabilization properties of Ge dewetting fronts, (ii) lead to a rotation of 45° of the Ge fingers with respect to the Si fingers, and (iii) increase the Ge fingers' stability delaying the formation of a three-dimensional Ge islands with respect to Si for the benefit of the formation of Ge nanowires. Studying the dewetting kinetics enables estimating the activation energy for Ge dewetting to 2.7 ± 0.2 eV. The weak energetics differences between Si and Ge systems are sufficient to change the dewetting morphologies from a squared-void opening for Si/SiO_2 to multibranch dendrites for Ge with specific consequences on the relative dewetting velocities of the Si/SiO_2 and Ge/SiO_2 systems.

DOI: 10.1103/PhysRevB.88.035306 PACS number(s): 68.35.Md, 68.37.−d, 68.60.Dv, 68.55.J−

I. INTRODUCTION

Solid state dewetting of thin films is a process by which a metastable film uncovers its substrate and agglomerates into an assembly of three-dimensional (3D) islands. Solid state dewetting is, thus, a common 2D → 3D transformation (where 2D represents two-dimensional). Continuous models based on surface diffusion[1–3] predict that, during dewetting, the film material removed from the substrate accumulates into a rim followed by a depression. During dewetting, the rim thickens, and the depression deepens so that, when the depression reaches the substrate, the film breaks and leaves a crystalline one-dimensional (1D) island in front of a new dewetting front. This repeated pinch-off mechanism is at the origin of a periodic mass shedding process.[4,5] However, continuous models based on the standard concept of curvature-driven surface diffusion cannot be directly applied to anisotropic materials. In particular, for anisotropic materials, the stability conditions of a dewetting front as well as its receding velocity are governed by the presence or the absence of atomically flat facets along the receding front edge as illustrated by experimental studies of dewetting fronts[6] or anisotropic edge retraction velocities.[7] More precisely, the concept of curvature-driven surface diffusion must be replaced by a new description[3,6,8] in which enter: (i) the driving force for dewetting expressed in terms of the local thickness of the dewetting front[5,9] and (ii) the local morphology of the receding front.[6] The importance of this latter ingredient has been particularly well illustrated in the case of Si(001) thin films on an amorphous SiO_2 substrate [$Si(001)/a SiO_2$].[6,10,11] Indeed, for $Si(001)/a SiO_2$, ⟨110⟩-oriented dewetting fronts are stabilized by {111} and {113} facets and, thus, recede keeping their initial straight shapes, whereas, ⟨100⟩-oriented fronts are destabilized and, thus, recede by forming periodic Si fingers separated by void fingers.[6,11] It results in a strong kinetics anisotropy since the ⟨100⟩ front velocity is about 10 times the ⟨110⟩ front velocity.[6]

This paper specially concerns the effects of facets on the dewetting properties of an anisotropic material. Our goal was to select a material for which stability conditions and the anisotropy retraction of a dewetting front can be controlled by tuning the facet formation. For this purpose, we have selected the $Ge(001)/a SiO_2$ system. Indeed, we will show that Ge exhibits {15 3 23} facets that can be "switched off" or can be "switched on" by varying the temperature.

The paper is set in five parts. In Sec. II, we describe the experiments. Section III is devoted to a study of the crystallographic facet characteristics of the Ge dewetted state. A coupled low-energy electron microscopy- (LEEM-) atomic force microscopy (AFM) study of the dewetting morphology as well as a study of the dewetting kinetics are reported in Sec. IV. Since $Si(001)/a SiO_2$ and $Ge(001)/a SiO_2$ systems can be considered as "brother systems" (they have five common stable facets and similar energetics since Ge bonds are simply around 20% weaker than Si bonds[12]), Sec. V is devoted to a comparison between $Ge(001)/a SiO_2$ and $Si(001)/a SiO_2$ systems. Finally, conclusions are given in Sec. VI.

II. EXPERIMENT

The dewetting experiments have been performed with low-energy electron microscope-photoemission electron microscope (LEEM-PEEM) (Elmitec LEEM-PEEM III) at high temperatures (typically, 800 °C) under pressures below 10^{-9} Torr. The samples are bonded germanium on insulator (GOI) and silicon on insulator (SOI) obtained from CEA-Leti, France.[13,14] They are composed of stress-free single-crystal Si(001) films (22 ± 2-nm thick) or Ge(001) (55 ± 2-nm thick) on an ∼150-nm-thick amorphous SiO_2 film. The SOI samples are cleaned by using a published recipe,[15] whereas, GOI samples are prepared by *in situ* outgassing at 600 °C for several hours (typically, 12 h) followed by 1-h cycles of Ar^+-ion sputtering at normal incidence at room temperature under a partial pressure of $P \sim 5.10^{-6}$ Torr and a bombardment voltage of $V = 1$ keV ($I_{sample} \sim 6\ \mu$A). After ion bombardment, the sample is annealed at 500–600 °C to heal the defects induced by the ion bombardment. The thickness reduction during the ion bombardment allows us to obtain several film thicknesses varying between 18 and 32 nm. The final Ge thickness has been measured *ex situ* by atomic force microscopy after partial dewetting of the film and by independent x-ray diffraction

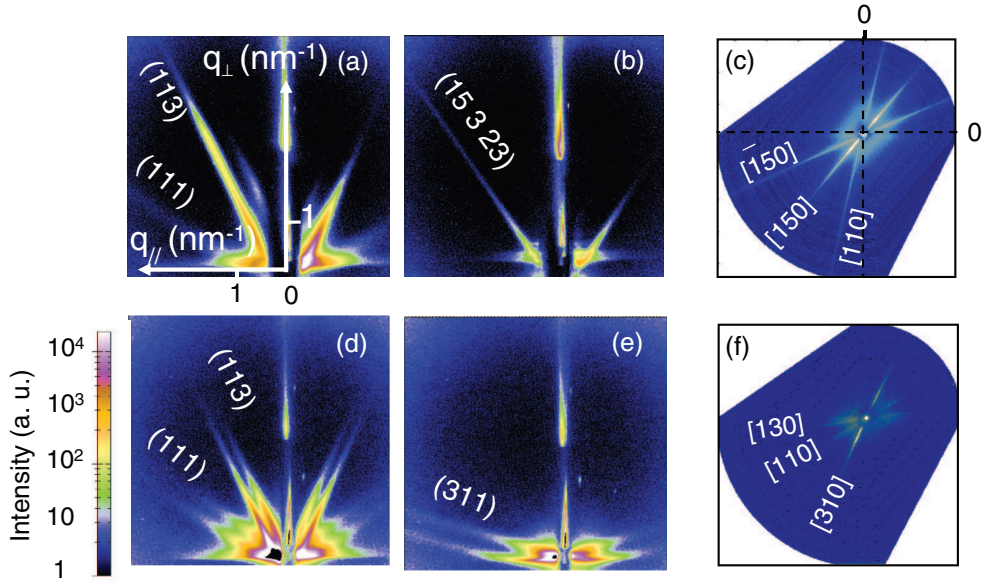

FIG. 1. (Color online) GISAXS measurements of the GOI film at $T = 800\,^{\circ}$C (on top) and $T = 890\,^{\circ}$C (bottom). Extended scattering rods from (113) and (111) facets are observed at (a) $T = 800\,^{\circ}$C and at (d) $T = 890\,^{\circ}$C when the incident beam is aligned in the $\langle 1\bar{1}0\rangle$ direction. Rotating the sample by 34°, (15 3 23) facets are observed at (b) $T = 800\,^{\circ}$C, whereas, (311) facets are observed at (e) $T = 890\,^{\circ}$C. Planar projections of the GISAXS intensities are reported in (c) and (f).

measurements.[16] Most of the dewetting experiments have been recorded *in situ* by PEEM or by LEEM. PEEM and LEEM image sequences are recorded at a fixed rate (0.3–1 Hz) to form a movie of the dewetting process. In LEEM, we have used bright-field, dark-field, and tilted bright-field imaging modes in which images are formed either from a reflected spot, 1/2-order diffraction beam associated with the $X(100)$-2 × 1 and $X(100)$-1 × 2 (X = Ge,Si) surface reconstructions or from a tilted incident beam. As adjacent terraces have orthogonal surface reconstructions, dark-field and tilted bright-field modes give rise to a bright/dark contrast that reveals the steps' organization at the surface. The LEEM measurements simultaneously show the micrometer-scale structure of the dewetting front, the nanoscale motion of surface atomic steps, and 2D nucleation events.

The facets involved in the dewetting process have been studied by *in situ* grazing incidence small-angle x-ray scattering (GISAXS) performed at the European Synchrotron Radiation Facility (ESRF BM 32 beamline, Grenoble, France). For this purpose, we have used an x-ray wavelength of 0.1169 nm and an incident angle close to the critical angle for the total external reflection of Ge ($\alpha_c = 0.23°$). The GISAXS technique and experimental considerations as the description of the 2D detector (X-ray Image Star 9000, Photonic Science) and of the slits used to avoid background scattering are described in Ref. 17.

III. GE FACETS VERSUS TEMPERATURE: A GISAXS STUDY

The GISAXS intensities scattered by the dewetting film are measured over the reciprocal space. GISAXS patterns have been recorded at different azimuths by rotating the sample by steps of 1° over a large angular range (> 90°). The GISAXS patterns show diffuse scattering rods arising from the facets of the dewetting front and the facets of the agglomerated islands. All (hkl) facets observed in GISAXS at $T = 800\,^{\circ}$C and $T = 890\,^{\circ}$C (Fig. 1) are reported in Table I. For the sake of simplicity, in the following text, we will regroup the facets by family using an *ad hoc* $\{hkl\}$ notation as reported in the first line of Table I. (For instance, the $\{113\}$ notation is, thus, not equivalent to the $\{311\}$ notation).

Figures 1(c) and 1(f) show planar projections of the recorded GISAXS intensities. At $T = 800\,^{\circ}$C [Fig. 1(c)], the $[\bar{1}50]$ and [150] directions that are the projections of the $(\bar{3}\,15\,23)$ and (3 15 23) facets, respectively, as well as the [110] direction that corresponds to the projection of (113) and (111) facets are observed. At $T = 890\,^{\circ}$C, Fig. 1(f) shows the [130] and [310] directions that are the projections of the (131) and (311) facets, respectively, as well as the [110] direction that is the projection of the (113) and (111) facets. The sharp in-plane scattering observed in the GISAXS projection is due to the similar orientation of all the dewetting zones as we will discuss later on in Sec. IV A.

These results confirm the high stability of $\{113\}$, $\{111\}$, and $\{15\,3\,23\}$ facets reported by Gai and co-workers,[18–20] who have shown that Ge material has six major stable surfaces. Five of them, the (113), (001), (101), (313), and (111) stable surfaces are common to Ge and Si materials. The $\{15\,3\,23\}$, specific to Ge, also is a stable orientation since (i) it cannot be resolved into nanofacets of any other orientation and (ii) annealing vicinals of $\{15\,3\,23\}$ surfaces leads to $\{15\,3\,23\}$ microfacets.[18–20] These results are also in agreement with scarce available data on the equilibrium shape of Ge. Indeed, Ross *et al.*,[21] studying Ge islands deposited on Si(001) substrates around $T = 700\,^{\circ}$C, found that the Ge equilibrium shape is formed by $\{113\}$ and $\{15\,3\,23\}$ facets smoothly connected by rounded parts. As reported by Stekolnikov and

TABLE I. Facets observed in GISAXS.

Family	{15 3 23}	{111}	{113}	{311}
	$(15\,3\,23)(15\,\bar{3}\,23)(3\,15\,23)(\bar{3}\,15\,23)$	$(111)(\bar{1}11)$	$(113)(\bar{1}13)$	$(311)(\bar{3}11)(131)(\bar{1}31)$
	$(\bar{1}5\,\bar{3}\,23)(\bar{1}5\,3\,23)(\bar{3}\,\bar{1}5\,23)(3\,\bar{1}5\,23)$	$(1\bar{1}1)(\bar{1}\bar{1}1)$	$(1\bar{1}3)(\bar{1}\bar{1}3)$	$(3\bar{1}1)(\bar{3}\bar{1}1)(1\bar{3}1)(\bar{1}\bar{3}1)$
Observed at 800 °C	*Yes*	*Yes*	*Yes*	*No*
Observed at 890 °C	*No*	*Yes*	*Yes*	*Yes*

Bechstedt,[22] the {15 3 23} surface could actually be stabilized by surface strain.

Since {15 3 23} facets do not exist at $T = 890\,^{\circ}$C (see Fig. 1) but exist at $T = 800\,^{\circ}$C, we can infer that the roughening transition of the {15 3 23} facet occurs around $T_R \approx 850\,^{\circ}$C. This temperature is close to the Ge(001) roughening temperature [$\approx 860\,^{\circ}$C (Ref. 23)]. Increasing the temperature close to equilibrium conditions at $T > T_R$, thus, makes the {15 3 23} facets disappear on the Ge equilibrium shape at the expense of a rounded part.

IV. DEWETTING MORPHOLOGY AND KINETICS: A COUPLED LEEM-PEEM/AFM STUDY

A. Dewetting morphologies

In the low-temperature regime ($T < T_R$), the dewetting of Ge(001)/aSiO$_2$ is initiated by the heterogeneous nucleation of voids (Figs. 2 and 3). The voids grow spontaneously with a large anisotropy of velocity. They, thus, form crosslike shapes with four void branches aligned along the ⟨110⟩ directions (Fig. 2). As shown by AFM, the voids are surrounded by a rim, characterized by a nonconstant height [Fig. 2(d)]. More precisely, the rim height varies along a branch with a decreasing amplitude away from the center of the void. In the dark-field LEEM image, recorded from a 1/2 diffracted spot, the rim summits appear dark or bright [Figs. 2(a) and 2(b)]. It means that the rim is locally faceted with a top (001) facet. Furthermore, in LEEM movies, the top facets alternatively blink from bright to dark during the dewetting, proving that the upper parts of the rim grow in a layer-by-layer mode. It is, thus, possible to measure the local rim thickening by counting the number of additive layers [Fig. 2(c)]. For initial stages, we find a linear $h(x,t) \propto t$ behavior. For completeness, notice that the flash events can only be formally observed at $T \sim 700\,^{\circ}$C (see Fig. 2) since increasing the Ge temperature promotes a reversible surface disorder with the progressive disappearance of the (1×2) and (2×1) surface reconstructions of the Ge(001) top facet.[24]

For longer times, the void branches invariably turn out to be unstable, leading to perpendicular secondary branches and then to a dendritic shape evolution (Fig. 3). Since the lower the local thickness h, the greater the local velocity,[6,9] these second branches born and develop from the thinnest parts of the rim. Thus, as predicted by Kan and Wong,[25] the lateral instability is driven by the height instability of the rim. Obviously, for kinetics reasons, the less developed secondary branches, since "younger," are close to the principal void tip. However, we

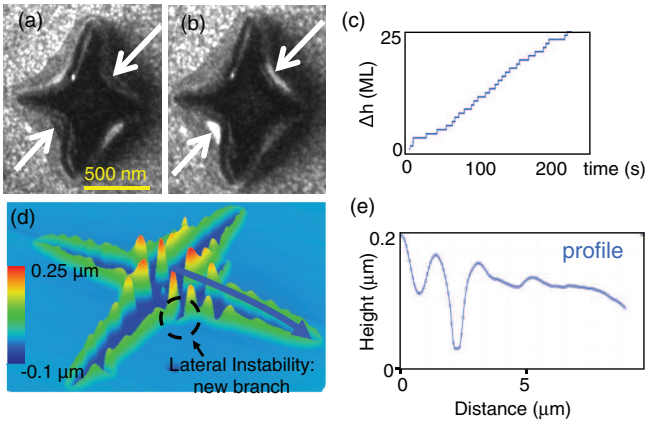

FIG. 2. (Color online) Low-temperature regime ($T \sim 700\,^{\circ}$C): (a) and (b) dark-field LEEM images recorded at t and $t + 10$ s illustrating the cross shape of the opening hole and the contrast inversion of the summit of the rim (see white arrows). From this, one can record the (c) local rim thickening expressed in monolayers (MLs) versus time. In the LEEM image, the bottom of the opening hole (the SiO$_2$ surface) is dark, the Ge surface is speckled due to the coexistence of 1×2 and 2×1 domains (area ~ 100 nm^2). The rim is "shadowed" due to its 3D structure. (d) AFM 3D view of an opening void (at a longer time) illustrating (e) the height variation in the rim along a void branch.

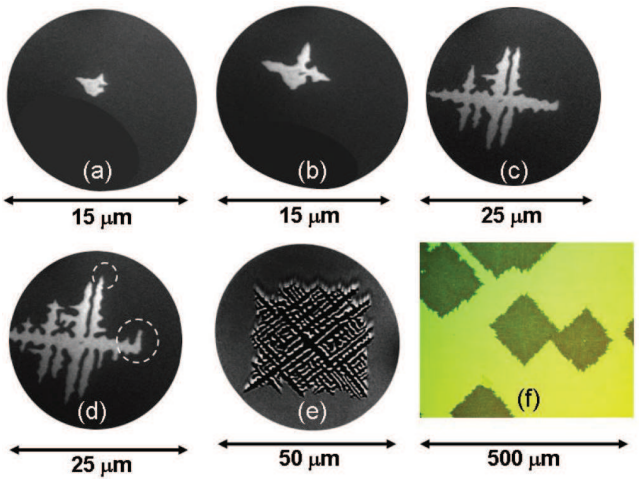

FIG. 3. (Color online) PEEM images of GeOI dewetting (40 ± 2-nm thick, $T = 800\,^{\circ}$C). The images have been taken at (a) $t = t_0$: opening void on a defect; (b) $t_0 + 1$ mn: cross-shaped formation; (c) $t_0 + 3.5$ mn: void branches with the appearance of secondary branches; (d) $t_0 + 5$ mn: branches development; (e) $t_0 + 15$ mn: square envelope limited by ⟨100⟩ edges. (f) is an optical large-scale image of dewetting that reveals several similar square-shaped dewetting areas.

cannot exclude an additional dependence of the exponential amplification coefficient of the Kan and Wong instability on the local in-plane curvature of the dewetting front as for parabolic crystals, formed by diffusion-limited growth.[26,27] Notice that the in-cascade formation of additional void branches develops a negative dendritic shape inside a square envelope limited by ⟨100⟩ edges [Fig. 3(e)]. In a few cases, a void tip encounters a defect that prevents its propagation. In this case, the void tip deviates forming a secondary orthogonal branch at its extremity [large circle in Fig. 3(d)]. The void tips are rounded and do not exhibit precise facets contrary to Si(001)/aSiO$_2$ where the void tips have been found to decompose into two microfronts oriented along the {110} directions.[6]

Finally, a large-scale optical image, that reveals several dewetting zones that have grown from different nucleation sites, is reported in Fig. 3(f). All the square-shaped zones have their sides parallel to the Ge⟨100⟩ directions. Since the nucleation events are uncorrelated,[16] this alignment of the dewetting zones is simply due to the perfect single crystallinity of the Ge(001) film, which thus, predefines the orientation of the growing dendrites. Notice that the orientation of the film is preserved during the whole dewetting process giving rise to single-crystalline nanowires and nanoislands. This common orientation is also illustrated in the sharp in-plane scattering reported in GISAXS experiments (see Fig. 1).

In the high-temperature regime ($T > T_R$), the dewetting mechanism and the dewetted morphology are similar to the low-temperature case. However, the branch density increases with the sample temperature. This is in fair agreement with classical predictions on the influence of the driving force $\Delta\mu/k_BT$ on the large-scale morphology of dendritic structures.[28]

B. Three-dimensional island formation

During dewetting, the Ge expelled from the growing void branches forms elongated structures in the ⟨110⟩ direction (see Fig. 4). The perpendicular void branches, formed by the lateral instabilities of the previous branches, intersect these elongated structures and leave Ge nanowires as seen in Figs. 4(a) and 4(b) and sketched in Fig. 4(d). These nanowires do not remain straight, but their edges mainly start to facet locally in the ⟨310⟩ and/or ⟨510⟩ directions [see Fig. 4(c)]. These directions can be associated with the presence of {311} and {15 3 23} facets and are at the origin of nanowires breaking into 3D nanoislands according to a Rayleigh-Plateau-type transition. We have noticed that the number of ⟨310⟩-oriented edges increases as a function of temperature with respect to the ⟨510⟩-oriented edges. We associate this change with the disappearance of the {15 3 23} facets due to the roughening transition.

It is observed (Fig. 4) that the number of nanowires increases with the density of side branches, whereas, a higher branch density implies shorter nanowires. It can be easily understood since the initial nanowire size (width and length) is nothing else than the interbranch distance [Fig. 4(d)]. In other words, for low branch density, nanowires are formed and give birth to 3D islands by a Rayleigh-Plateau-type instability. For higher void-branch density, 3D islands are directly let behind the branches crossover without the help of any Rayleigh-Plateau-type instability.

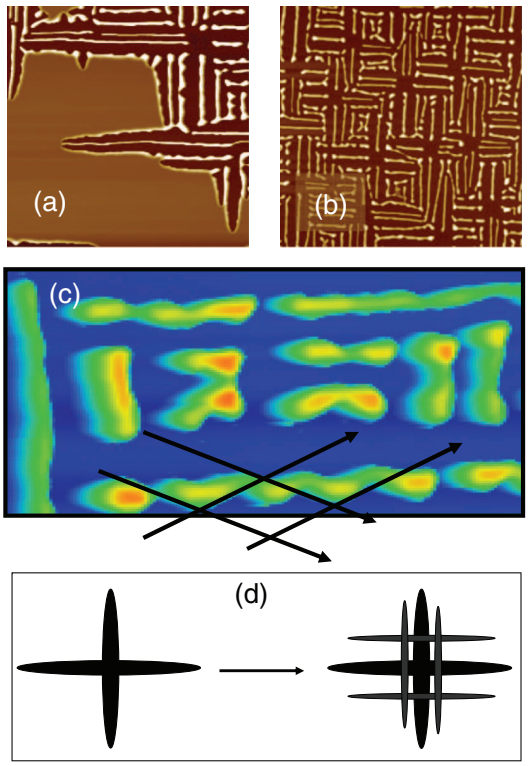

FIG. 4. (Color online) Nanowire formation. (a) AFM images of the nanowire formation (30×30 μm^2, the Ge material appears in white), (b) AFM image (50×50 μm^2) of the dewetted state exhibiting a collection of nanowires, (c) details of the nanowire's structure (10×6 μm^2), and (d) sketch of the nanowire formation by the crossing of principal and secondary void branches (dark).

C. Kinetics and activation energy for dewetting

The dewetted area versus time is reported in Fig. 5. In the early stages of dewetting (when the dewetted area is star shaped), the dewetted area grows linearly with time (red line in Fig. 5). For longer times, multibranches develop

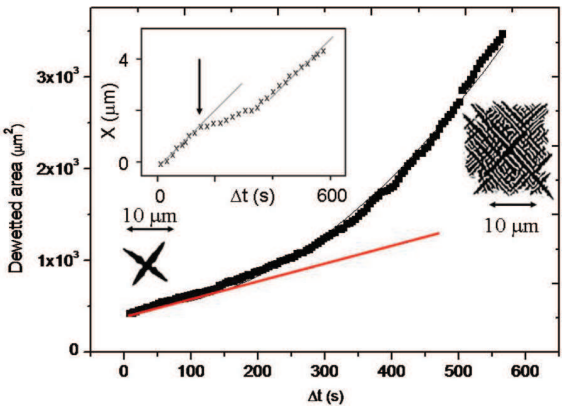

FIG. 5. (Color online) Dewetting area versus time from the star-shaped regime towards the multibranch configuration. The velocity of a typical void tip is given in the inset. The black arrow corresponds to the apparition of a secondary tip. The LEEM images, obtained at the beginning and at the end of the process, are also reported as binary images (the Ge matter in white, the opening void in black).

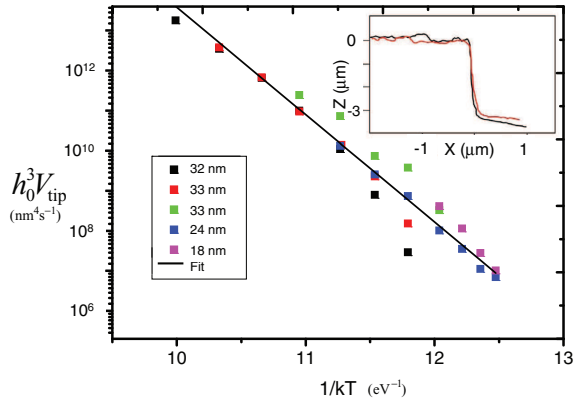

FIG. 6. (Color online) $\ln(h_0^3 V_{tip})$ versus $1/k_B T$ recorded for various thicknesses. The continuous line is the best fit obtained from Eq. (1). Inset: typical tip profiles measured by AFM.

inside a square-shaped envelope, and the dewetting area varies quadratically with time. In this regime, a focus on a typical void-tip velocity is reported in the inset of Fig. 5. It grows linearly with time but temporarily slows down each time that a secondary perpendicular branch nucleates then quickly recovers its initial velocity. Two height profiles, measured by AFM in the direction perpendicular to two typical void tips, are reported in the inset of Fig. 6. It can be seen that the void tips have no rim. In other words, the local thickness of the film simply is the initial film thickness h_0.

Since there is no experimental evidence for the occurrence of a rim at the void tips, we can write the void-tip velocity as[9,11]

$$V_{tip} = \frac{D_0 c}{k_B T} \frac{\Omega^2}{\pi a^2} \frac{2E_s}{h_0^3} e^{-E^{diff}/k_B T}, \qquad (1)$$

where $c = c_0 e^{-E^{form}/k_B T}$ is the fraction of diffusing species with E^{form} as the formation energy of the diffusing species, $D_s = D_0 e^{-E^{diff}/k_B T}$ is the surface diffusion constant, E^{diff} is the diffusion energy, and $E_s = \gamma_{Si} + \gamma_{Si/SiO_2} - \gamma_{SiO_2}$ is the surface/interface energy balance, where γ_i is the surface energy of material $i = Si, SiO_2$ and $\gamma_{i/j}$ is their interfacial energy. The other geometric quantities are Ω, the atomic volume, a, the in-plane atomic distance, and h_0, the local thickness of the film. Equation (1) has been obtained by using the expressions of Refs. 9 and 11, valid for a receding rim of local height h and local width w with $h = h_0$ and $w = \pi h_0/2$ when assuming the tip edge to be a part of a circle. Notice that Eq. (1) has also been written by Jiran and Thompson[29] but with γ_{Si} in place of E_s.

Experimental values of V_{tip} have also been recorded in the stationary regime where the density of branches is high enough to ensure a meaningful measurement of the mean velocity of a significant ensemble of tips. In order to compare samples with different initial Ge thicknesses, in Fig. 6, we have plotted $\ln(h_0^3 V_{tip})$ as a function of $1/k_B T$. Since Eq. (1) is not a simple Arrhenius equation, experimental results have been fitted with $\ln(B/k_B T) - E/k_B T$. This fit is in clear agreement with the experimental data (see Fig. 6). It enables us to extract the activation energy $E = E^{form} + E^{diff} = 2.7 \pm 0.2$ eV as well as the prefactor $\ln(B) = \ln(\frac{2\Omega^2}{\pi a^2} D_0 c_0 E_s) = 42.9 \pm 1.6$.

TABLE II. Literature data: Activation energies for the formation of Ge monomers and Ge dimers. Notice that the formation energy of the Ge monomer (E_{mo}^{form}) has been evaluated by adding the energy necessary to break a dimer 0.33 eV (Ref. 24) to the energy E_{di}^{form} necessary to form a dimer. Thus, it is likely overestimated.

	E^{form} (eV)	E^{diff} (eV)
Monomers	$\sim 1.8 \pm 0.2$	0.37 (Ref. 30)
Dimers	1.5 ± 0.2 (Refs. 31 and 32)	0.86 ± 0.3 (Ref. 33)

The activation energy we found here is in fair agreement with the value of 2.6 ± 0.3 eV found from independent GISAXS measurements of the Ge/aSiO$_2$ agglomeration kinetics.[16] From literature data (see Table II), the activation value that we find ($E = 2.7 \pm 0.2$ eV) seems compatible with the diffusion of dimers, even if, accounting for the error bars, it is quite difficult to conclude on the nature of the diffusing species. However, a dimer diffusion is surprising since, in the temperature range under study, monomers' activation is expected.[23] Thus, we believe that the diffusion energy we have determined here does not correspond to the simple diffusion on the top (001) surface of the film. Actually, the derived diffusion energy is probably a mean-activation energy corresponding to the diffusion on the whole edge profile, meaning from the triple line towards the Ge(001) surface.

The value of $\ln(B)$ enables us to estimate that 8.6×10^{17} eV s^{-1} $< D_o c_0 E_s <$ 2.2×10^{19} eV s^{-1} when using, for Ge(001), $a = a_0/\sqrt{2}$ with the Ge crystallographic parameter $a_0 = 0.566$ nm. It results in 3×10^5 nm^2 s^{-1} $< DcE_s <$ 7×10^6 nm^2 s^{-1} at 840 °C. This value is in fair agreement with the mean value $DcE_s \approx 4 \times 10^6$ nm^2 s^{-1}, obtained from independent experiments.[16] It is also comparable to the value of 4×10^6 nm^2 s^{-1}, reported for Si by Keeffe *et al.*[34] in the same temperature range. The value of E_s can be estimated from Table III where the data available in literature are reported. For γ_{SiO_2}, we have used the value calculated in Ref. 35 that is in fair agreement with the experimental value estimated from the surface tension of silica of 300 mJ m^{-2}, measured at 1700 °C and corrected from a mean-temperature coefficient of -0.15 mJ m^{-2} K^{-1} given in Ref. 36. For Si and Ge, we have reported experimental values. Within the uncertainties, we can, thus, estimate $E_s \approx 10 \pm 2$ eV nm^{-2}. This value is quite similar to the value calculated for Si(001)/aSiO$_2$ that is within the range of $E_s \sim 7$–15 eV nm^{-2}.[9]

TABLE III. Literature data for surface energies (γ_i) and interfacial energies (γ_{i/SiO_2}). These values lead to E_s on the order of 1600 mJ m^{-2} that means $E_s \approx 10 \pm 2$ eV/nm^2 since uncertainties are estimated to 20%.

i	γ_i (mJ m^{-2})	γ_{i/SiO_2} (mJ m^{-2})
Si	1240 (Ref. 37)	1280 (Ref. 38)
Ge	1100 (Ref. 37)	1000 (Ref. 39)
SiO$_2$	430 (Ref. 35)	

TABLE IV. Synthesis of experimental results. For Si, all the results originate from Refs. 9, 11, and 6.

	Ge at $T = 800\,^{\circ}$C	Ge at $T = 890\,^{\circ}$C	Si at $T = 825\,^{\circ}$C
Main morphology	Cross then sparse dendrites	Cross then dense dendrites	Square voids
Facets seen in GISAXS	{15 3 23}{133}{111}	{133}{111}	{133}{111}
Void-tip shape	Along ⟨100⟩ faceted	Along ⟨100⟩ rounded	Along ⟨110⟩
Nanowires faceting along:	Principal ⟨510⟩, secondary ⟨310⟩	Principal ⟨310⟩, secondary ⟨510⟩	⟨110⟩
Velocity anisotropy	$V_{110} > V_{100}$	$V_{110} > V_{100}$	$V_{110} < V_{100}$
Stable fronts	No stable front	No stable front	⟨110⟩

V. STABILITY AND ANISOTROPY OF DEWETTING: COMPARISON WITH SOI

As mentioned in the Introduction, a comparison with Si(001)/aSiO$_2$ results, described in Refs. 9, 11, and 6, should help to understand the stability conditions and the velocity anisotropy. For this purpose, our main results are summarized in Table IV. Notice that the stability properties of the dewetting fronts reported in the last line of Table IV result from the real-time observation of the dewetting fronts from artificial well-oriented edges obtained by electronic lithography as described in Ref. 6.

Stereographic projections of the facets detected by GISAXS experiments for both Si/aSiO$_2$ and Ge/aSiO$_2$ systems are reported in Fig. 7. The so-observed facets belong to the shaded disk in Fig. 7, whereas, the outer disk contains all the possible facets of the free equilibrium shape. The two circles do not coincide because, due to its adhesion on SiO$_2$, only a part of the free equilibrium shape emerges above the substrate defining an emerging height H.[40] The ratio between both circles is about 0.8. Notice that, for Ge, the aspect ratio measured on 3D islands by AFM is greater at high temperatures (0.75 ± 0.05) than at low temperatures (0.55 ± 0.05). It is consistent with GISAXS data since the {311} facets can only be seen on the most emerging shapes (Fig. 7).

The [110] front is the zone axis of the (113) and (111) facets. These facets stabilize the [110] front which, as a consequence, recedes keeping its straight shape.[6] On the contrary, Si-[100] fronts are destabilized by the presence of (311) and (111) facets and, thus, recede by the formation of Si fingers separated by void fingers faceted with (113) and (111) facets in order to

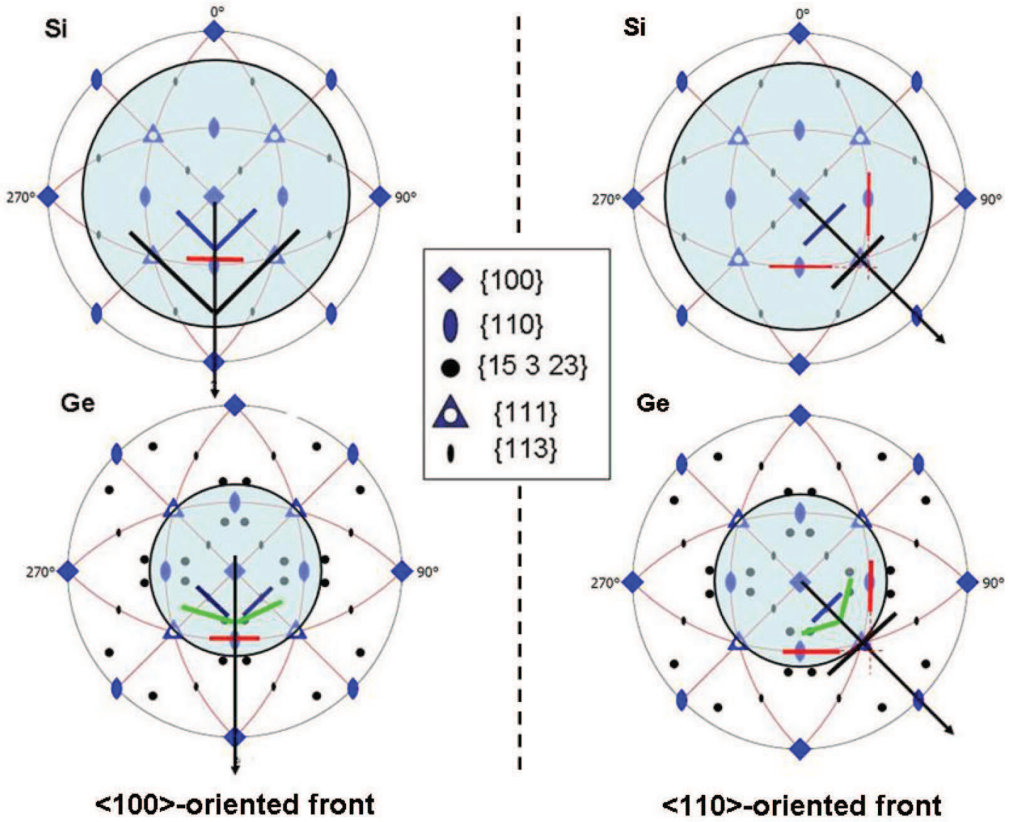

FIG. 7. (Color online) Stereographic projections of the facets detected by GISAXS for Si (top) and for Ge (bottom). The tracks of the facets are schemed in colored bars: black for {111}, red for {110}, blue for {113}, and green for {15 3 23}. The case for the [100]-directed fronts is presented on the left, whereas, the case for the [110]-oriented fronts is presented on the right.

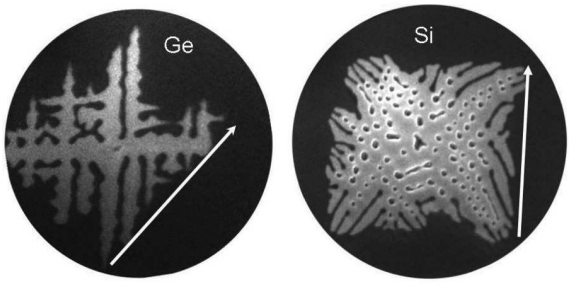

FIG. 8. LEEM images of GOI (field of view 25 μm) and SOI (field of view 25 μm) square voids. The arrow corresponds to the [100] direction for Ge but to the [110] direction for Si.

locally reform [110] stable fronts.[6] Moreover, there is $V_{110}^{\mathrm{Si}} \ll V_{100}^{\mathrm{Si}}$.[6]

For Ge at $T < T_R$, $\{15\ 3\ 23\}$ facets have extended areas, whereas, due to the low Ge emerging height, $\{111\}$ facet areas are limited. The Ge-[110] fronts and the Ge-[100] fronts are, thus, destabilized by the $\{15\ 3\ 23\}$ facets. Moreover, the orientation of the void branch and the orientation of the edges (Fig. 8) of the dewetted area show that $V_{110}^{\mathrm{Ge}} > V_{100}^{\mathrm{Ge}}$. A consequence of the absence of stable fronts is that Ge void tips do not develop facets contrary to Si void tips. For the same reason, the edges of the nanowires leaved by the crossing of the void branches are parallel to the [110] directions but tend to be destabilized by the $\{15\ 3\ 23\}$ facets giving birth to the $\langle 510\rangle$ orientations [Fig. 4(d)]. However, the $\langle 310\rangle$ directions are not excluded because of the role played by the $\{311\}$ facets.

For Ge at $T > T_R$, the $\{15\ 3\ 23\}$ facets are no longer present, and the $\{311\}$ facets are observed [Figs. 1(e) and 1(f)]. The reappearance of the $\{311\}$ facets, compared to the low-temperature case, likely has a kinetics origin since the island shapes should be closer to their equilibrium shapes at high temperatures than at low temperatures (where surface diffusion is less active). However, we cannot exclude a temperature effect on the equilibrium shape itself.[40,41]

It could be natural to think that the dewetting properties of the Ge(001)/aSiO$_2$ and Si(001)/aSiO$_2$ systems should be similar in the high-temperature regime where both systems exhibit the same facets (Table IV). However, it is not the case since, experimentally, we observe that: (i) the edge orientation of the Ge dewetting zone is rotated by 45° with respect to the Si dewetting zones (see Fig. 8), and (ii) the Ge-$\langle 110\rangle$-oriented front is unstable during dewetting, whereas, the Si-$\langle 110\rangle$-oriented front is stabilized by the $\{111\}$ and $\{113\}$ Si facets and recedes at constant shapes.[6] We believe that this discrepancy originates from the destabilization of the Ge$\langle 110\rangle$ front by the $\{15\ 3\ 23\}$ orientation, even if the $\{15\ 3\ 23\}$ facets have disappeared (above the roughening temperature). Indeed, above T_R, the $\{15\ 3\ 23\}$ facets are replaced by rounded parts, that are sufficient to prevent the [110] front from remaining straight. This is also illustrated in the shape of the Ge void tips that are more rounded at 890 °C than at lower temperatures.

Finally, we find, that Dc is of the same order for Si and Ge. It is quite surprising since, at the same temperature, the dewetting velocity is 2 orders of magnitude higher for Ge than for Si![11] The weak point, leading to this apparent paradox, is that the Si and Ge dewetting morphologies actually are different. Indeed, as shown in Fig. 9, Ge dewetting proceeds by side-branching mechanisms, whereas, Si dewetting proceeds by tip splitting. More precisely, for Si, the dewetting proceeds by the opening of square voids with an edge destabilization that leads to the collective formation of periodic fingers,[6,11] whereas, for Ge, the dewetting proceeds by the growth of quasi-independent void branches with successive side branching (Fig. 9). As described in Ref. 11, the collective behavior, valid for Si, leads to an effective thickness-dependent activation energy that, for instance, overpasses 3 eV for 20-nm-thick Si films.[11] This is not observed for the Ge/a-SiO$_2$ system. In other words, whereas, the velocity of Ge void tips can really be described by a 1D model where the tips behave independently, it is not the case of Si for which the simultaneous formation of fingers leads to 2D corrections of the expression of the velocity that is equivalent to define an effective activation energy in Eq. (1). Furthermore, the local rim of height $h > h_0$ that exists at the Si void tip also contributes to slowing down the velocity of the Si front.

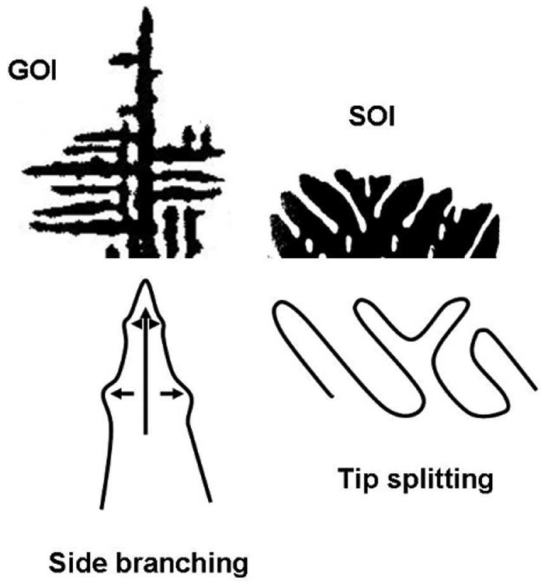

FIG. 9. Top: dewetted morphology; bottom: side-branching and tip-splitting mechanisms.

VI. CONCLUSION

The dewetting properties of Ge(001)/aSiO$_2$ have been studied above and beneath the roughening temperature $T_R \approx 850$ °C of the $\{15\ 3\ 23\}$ facet.

At $T < T_R$, the role of the facets on the dewetting properties has been confirmed. Indeed, for Si(001)/aSiO$_2$, the $\langle 110\rangle$-oriented fronts are stabilized by $\{113\}$ and $\{111\}$ facets that have a common $\langle 110\rangle$ zone axis. It is not the case for Ge(001)/aSiO$_2$ where the presence of $\{15\ 3\ 23\}$ facets associated with the small size of the $\{111\}$ facets is at the origin of the destabilization of the Ge-$\langle 110\rangle$ fronts. These $\{15\ 3\ 23\}$ facets limit the dynamics of the Ge front with three remarkable consequences: (i) The Ge fingers are aligned along the $\langle 110\rangle$ direction, which is the bisector of the (15 3 23) and (15 $\bar{3}$ 23) facets, so that the Ge fingers are 45° rotated with respect to the

Si fingers (Figs. 7 and 8), (ii) the {111} and {113} facets that develop along the Ge fingers (their ⟨110⟩ zone axis), increase the fingers' stability so that the island formation is delayed (with respect to Si) stabilizing Ge nanowires, (iii) there is an inversion of the velocity anisotropy for Ge with respect to Si: $V_{110}^{Ge} > V_{100}^{Ge}$, whereas, $V_{110}^{Si} < V_{100}^{Si}$.

At $T > T_R$, the {15 3 23} facets disappear, and the {311} facets re-introduce. However, it is not enough to restabilize the Ge-⟨110⟩ front because the sizes of the {113} and {111} facets are too small and because of the perturbation due to the rounded part originating from the roughening transition of the {15 3 23} facets. For Si(001)/aSiO$_2$, the {113} and {111} facets are sufficient to stabilize the Si-⟨110⟩ front.[6]

Experimental data enable us to extract the activation energy for the Ge dewetting velocity at 2.7 ± 0.2 eV. Finally, the weak energetics differences between Si and Ge are sufficient to change the dewetting morphology from squared-void dewetting for Si to more dendritic-like dewetting for Ge. These morphological differences are at the origin of the difference between the dewetting velocities of Si and Ge despite quite similar diffusivity and driving force values.

ACKNOWLEDGMENTS

This work was supported by an APO grant delivered by the PACA Region Council and by an ANR grant in the framework of the LOTUS project. The authors would like to thank the beamline BM32 staff from help during beam access at the synchrotron facility ESRF in Grenoble. The authors also acknowledge S. Curiotto for fruitful discussions.

*leroy@cinam.univ-mrs.fr
†cheynis@cinam.univ-mrs.fr
‡muller@cinam.univ-mrs.fr

[1] D. J. Srolovitz and S. A. Safran, J. Appl. Phys. **60**, 247 (1986).
[2] D. J. Srolovitz and S. A. Safran, J. Appl. Phys. **60**, 255 (1986).
[3] F. Cheynis, F. Leroy, and P. Müller, C. R. Phys. (to be published).
[4] H. Wong, P. Voorhees, M. Miksis, and S. Davis, Acta Mater. **48**, 1719 (2000).
[5] E. Dornel, J.-C. Barbé, F. de Crécy, G. Lacolle, and J. Eymery, Phys. Rev. B **73**, 115427 (2006).
[6] F. Leroy, F. Cheynis, T. Passanante, and P. Müller, Phys. Rev. B **85**, 195414 (2012).
[7] J. Ye and C. Thompson, Acta Mater. **59**, 582 (2011).
[8] M. Dufay and O. Pierre-Louis, Phys. Rev. Lett. **106**, 105506 (2011).
[9] E. Bussmann, F. Cheynis, F. Leroy, P. Müller, and O. Pierre-Louis, New J. Phys. **13**, 043017 (2011).
[10] D. T. Danielson, D. Sparacin, J. Michel, and L. Kimerling, J. Appl. Phys. **100**, 083507 (2006).
[11] F. Cheynis, E. Bussmann, F. Leroy, T. Passanante, and P. Müller, Phys. Rev. B **84**, 245439 (2011).
[12] J. Margrave, *The Characteristics of High Temperature Vapors* (Wiley, New York, 1967).
[13] B. Ghyselen, J. Hartmann, T. Ernst, C. Aulnette, B. Osternaud, Y. Bogumilowicz, A. Abbadie, P. Besson, O. Rayssac, A. Tiberj, N. Daval, I. Cayrefourq, F. Fournel, H. Moriceau, C. Dinardo, F. Andrieu, V. Paillard, M. Cabie, L. Vincent, E. Snoeck, F. Cristiano, A. Rocher, A. Ponchet, A. Claverie, P. Boucaud, M. Semeria, D. Bensahel, N. Kervenez, and C. Mazure, Solid-State Electron. **48**, 1285 (2004).
[14] E. Augendre, L. Sanchez, L. Benaissa, T. Signamarcheix, J. Hartmann, C. L. Royer, M. Viner, W. V. den Daele, J. Damlencourt, K. Romanjek, A. Poydebasque, P. Batude, C. Tabone, F. Mazen, A. Tauzin, N. Blanc, M. Pellat, J. Dechamp, M. Zussy, P. Scheiblin, M. Jaud, C. Drazek, C. Maurois, M. Piccin, A. Abbadie, F. Lallement, N. Daval, E. Guiot, A. Rigny, G. Ghyselen, K. Bourdelle, F. Boulanger, S. Cristoloveanu, T. Billon, O. Faynot, C. Degeut, and L. Clavelier, ECS Trans. **25**, 351 (2009).
[15] E. Bussmann, F. Cheynis, F. Leroy, and P. Müller, IOP Conf. Ser.: Mater. Sci. Eng. **12**, 012016 (2010).
[16] F. Cheynis, F. Leroy, T. Passanante, and P. Müller, Appl. Phys. Lett. **102**, 161603 (2013).
[17] G. Renaud, R. Lazzari, and F. Leroy, Surf. Sci. Rep. **64**, 255 (2009).
[18] Z. Gai, X. Li, R. G. Zhao, and W. S. Yang, Phys. Rev. B **57**, R15060 (1998).
[19] Z. Gai, R. G. Zhao, X. Li, and W. S. Yang, Phys. Rev. B **58**, 4572 (1998).
[20] Z. Gai, W. S. Yang, R. G. Zhao, and T. Sakurai, Phys. Rev. B **59**, 15230 (1999).
[21] F. Ross, R. Tromp, and M. Reuter, Science **286**, 1931 (1999).
[22] A. Stekolnikov and F. Bechstedt, Phys. Rev. B **72**, 125326 (2005).
[23] E. van Vroonhoven, H. J. W. Zandvliet, and B. Poelsema, Phys. Rev. Lett. **91**, 116102 (2003).
[24] A. D. Johnson, C. Norris, J. W. M. Frenken, H. S. Derbyshire, J. E. MacDonald, R. G. Van Silfhout, and J. F. Van Der Veen, Phys. Rev. B **44**, 1134 (1991).
[25] W. Kan and H. Wong, J. Appl. Phys. **97**, 43515 (2005).
[26] J. S. Langer, Phys. Rev. A **36**, 3350 (1987).
[27] R. Pieters and J. Langer, Phys. Rev. Lett. **56**, 1948 (1986).
[28] O. Shochet, K. Kassner, E. Ben-Jacob, S. Lipson, and H. Muller-Krumbhaar, Physica A **187**, 37 (1992).
[29] E. Jiran and C. V. Thompson, J. Electron. Mater. **19**, 1153 (1990).
[30] L. Huang, F. Liu, and X. G. Gong, Phys. Rev. B **70**, 155320 (2004).
[31] P. Kruger and J. Pollmann, Phys. Rev. Lett. **74**, 1155 (1995).
[32] E. van Vroonhoven, H. Zandvliet, and B. Poelsema, Surf. Sci. Lett. **574**, L23 (2005).
[33] T. Afanasievia, S. Bulavenko, I. Koval, and H. Zandvielt, J. Appl. Phys. Lett. **93**, 1452 (2003).
[34] M. E. Keeffe, C. Umbach, and J. Blakely, J. Phys. Chem. Solids **55**, 965 (1994).
[35] C. Chuang, Q. Li, D. Leonhardt, S. Han, and T. Sinno, Surf. Sci. **609**, 221 (2013).
[36] K. Mills and B. Keene, Int. Mater. Rev. **32**, 1 (1987).
[37] R. Kern, G. LeLay, and J. J. Métois, in *Current Topics in Materials Science*, edited by E. Kaldis (North-Holland, Amsterdam, 1979), Vol. 3, p. 135.
[38] L. T. Kong and L. J. Lewis, Phys. Rev. B **77**, 085204 (2008).
[39] J. Du and P. Kroll, J. Non-Cryst. Solids **356**, 2448 (2010).
[40] P. Müller and R. Kern, Surf. Sci. **457**, 229 (2000).
[41] P. Müller and R. Kern, Appl. Surf. Sci. **164**, 68 (2000).

Deuxième partie

Instabilités des surfaces de silicium induites par électromigration

MISE EN PERSPECTIVE

La première des structures que l'on rencontre en abondance sur les surfaces cristallines est la marche atomique. Elle joue un rôle majeur dans les problèmes de croissance cristalline et plus généralement pour comprendre les transferts de matière sur les plans denses des cristaux que ni les modèles continus, ni les modèles atomistiques ne traitent de façon appropriée. Une connaissance approfondie de la dynamique d'une marche atomique est donc un enjeu de premier plan.

Sur le plan expérimental, les surfaces de silicium légèrement désorientées par rapport au plan dense (111) ont joué un rôle important dans notre connaissance de la dynamique des marches. Il a été observé en particulier qu'un train régulier de marches pouvait, sous certaines conditions, être instable et évoluer vers une mise en paquet locale des marches atomiques. Ce processus donne naissance à des zones de forte densité de marches atomiques et à des zones de faible densité laissant donc place à de grandes terrasses planes à l'échelle atomique. Ces instabilités peuvent avoir des origines diverses. Elles peuvent être induites par les contraintes de surfaces [28], une gravure chimique [29], un dépôt [30, 31], l'adsorption d'une espèce étrangère [32–34] ou encore l'électromigration [35]. C'est ce dernier effet qui a motivé nos études, l'électromigration étant pas ailleurs un processus néfaste qui peut conduire à une perte de conductivité électrique dans les matériaux soumis à de fortes densités de courant [36, 37]. Sur le plan théorique, le premier modèle décrivant le mouvement des marches

atomiques a été proposé par Burton, Cabrera et Frank [38] (sans avoir de preuves expérimentales que les marches existent !). Il sert encore aujourd'hui de base à l'étude de la dynamique spatio-temporelle du mouvement des marches [39]. La confrontation de ce modèle avec des données expérimentales est nécessaire pour en valider la pertinence mais aussi pour en donner les limites. Nous avons entrepris de développer une modélisation de la dynamique des marches en collaboration avec des théoriciens :

- Olivier Pierre-Louis, successivement à Oxford (Rudolf Peierls Centre for Theoretical Physics) puis à Lyon (ILM), pour l'étude des ondes de densité de marches induites par électromigration (voir article [40]).
- l'équipe de théoriciens de l'IM2NP (Marseille), avec Jean-Marc Debierre, Thomas Frisch et Mathieu Dufay, pour l'étude de la transition entre les instabilités de méandrage et de mise en paquet des marches atomiques sur le silicium (voir schéma sur la figure II.1 et article [41]).

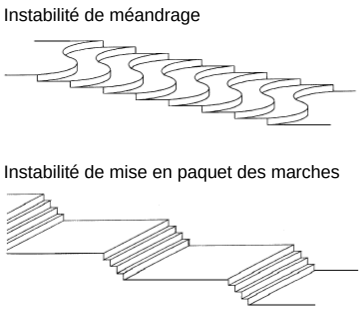

Figure II.1 *– (a) et (b) : Illustrations schématiques du méandrage et de la mise en paquets de marches atomiques (extrait de l'habilitation à diriger des recherches de Thomas Frisch [42]).*

2. PRINCIPAUX RÉSULTATS

2.1 État de l'art

Le caractère instable de la morphologie d'une surface de silicium soumise à un courant électrique perpendiculaire aux marches atomiques a été observé pour la première fois par Latyshev et ses collaborateurs en 1989 [35] sur une surface faiblement désorientée par rapport à la face (111) (voir fig. II.2). Cet effet est d'autant plus spectaculaire que cette instabilité connaît de nombreuses évolutions avec la température mais aussi parce que de nombreuses autres instabilités telles que le méandrage ont été observées, selon la valeur du champ électrique et sa direction [43–45]. Sur le plan théorique la première tentative d'interprétation de ces instabilités est due à Stoyanov [46] en adaptant le modèle continu de marches de Burton, Cabrera et Franck [38]. Il a proposé que les ad-atomes de Si, par transfert de charges avec la surface du cristal, sont partiellement chargés et subissent donc une force électrique lorsqu'un champ est appliqué. Le biais induit par cette force sur le déplacement des ad-atomes introduit une asymétrie qui peut favoriser le développement d'une instabilité par exemple de mise en paquet de marches.

Toutefois la complexité des situations observées en fonction des conditions expérimentales (T, $\vec{E}$) n'a pas permis de valider entièrement le modèle proposé. C'est dans ce cadre que nos études sur les phénomènes d'électromigration dans le silicium ont été menées, avec pour double objectif d'ap-

Figure II.2 *– Images par Reflexion Electron Microscopy du changement de morphologie d'une surface vicinale de Si(111) induite par le passage d'un courant continu (extraite de la référence [35]).*

porter des éléments expérimentaux nouveaux sur la cinétique des instabilités induites par électromigration [40, 41] mais aussi d'interpréter théoriquement les phénomènes observés en tenant compte notamment des interactions élastiques entre marches. En effet si les interactions élastiques sont souvent négligées car réputées de faible intensité, la grande portée de cette interaction répulsive joue un rôle essentiel pour les faces vicinales contrebalançant l'instabilité de mise en paquet des marches et favorisant donc la formation de structures périodiques telles que les ondes de densité de marches.

2.2 Onde de densité de marches et facettage induits par électromigration (voir article joint [6])

Les expériences d'électromigration ont été réalisées sur différentes faces vicinales de silicium (118), (223), (443) et (105). Un courant électrique continu de quelques ampères est orienté perpendiculairement aux marches dans le sens montant des marches. L'effet Joule qui résulte du passage du courant induit une augmentation de la température de l'échantillon pour atteindre dans nos expériences une température de l'ordre de 1100°C à 1250°C. Les mesures de cinétique d'électromigration ont été faites par différentes tech-

niques *in situ* et *ex situ*. En particulier nous avons enregistré *in situ* le signal de diffraction de la lumière par la surface de l'échantillon (voir figure II.3). Cette technique nous a permis de mettre en évidence qu'une structuration périodique à l'échelle du micron se développe sur la surface.

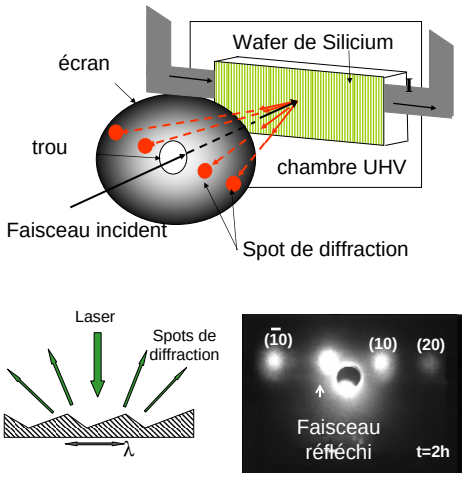

Figure II.3 *– Schéma de principe de la mesure in situ du cliché de diffraction (λ =530 nm). La surface de Si, structurée périodiquement par le phénomène d'électromigration, agit comme un réseau optique en réflexion. En bas à droite : Cliché de diffraction expérimental obtenu sur une surface de Si(105) après 2 h à 1200° C. Les taches d'intensité* (10), (20), *et* $(\bar{1}0)$ *correspondent aux différents ordres de diffraction.*

Les mesures *ex situ* par AFM révèlent les détails de l'évolution de cette morphologie (voir figure II.4(a)-(d)). Aux temps courts il apparaît sur la surface une onde de densité de marches dont la période de 4 μm est quasi-indépendante de l'orientation du cristal de silicium. L'amplitude de cette onde augmente exponentiellement au cours du temps indiquant le développement d'une instabilité (voir insert dans la figure II.4(f)). Aux temps longs la longueur d'onde et l'amplitude des oscillations convergent vers une valeur asymptotique indiquant que la surface est entièrement facettée (voir figure II.5).

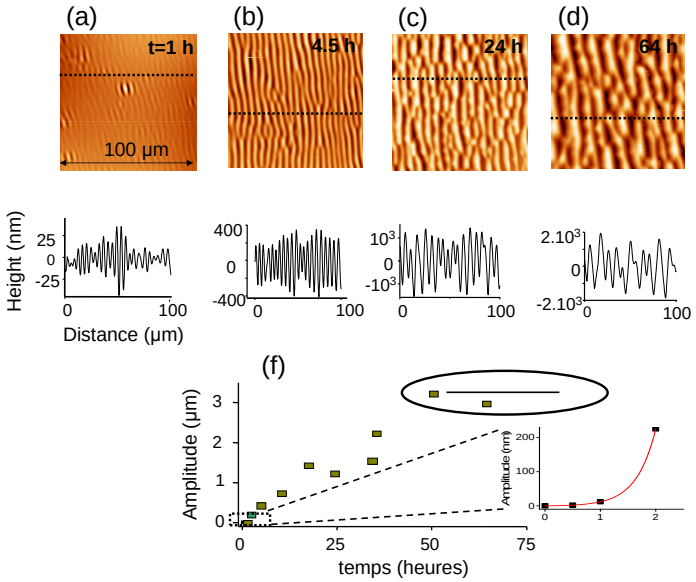

Figure II.4 *– (a)-(d) Images et profils AFM ex situ de la morphologie de la surface de Si(105) après 1, 4.5, 24, et 64 h de recuit à 1250° C sous électromigration. (f) Evolution de l'amplitude des modulations de hauteur de la surface en fonction du temps. Insert : évolution exponentielle aux temps courts.*

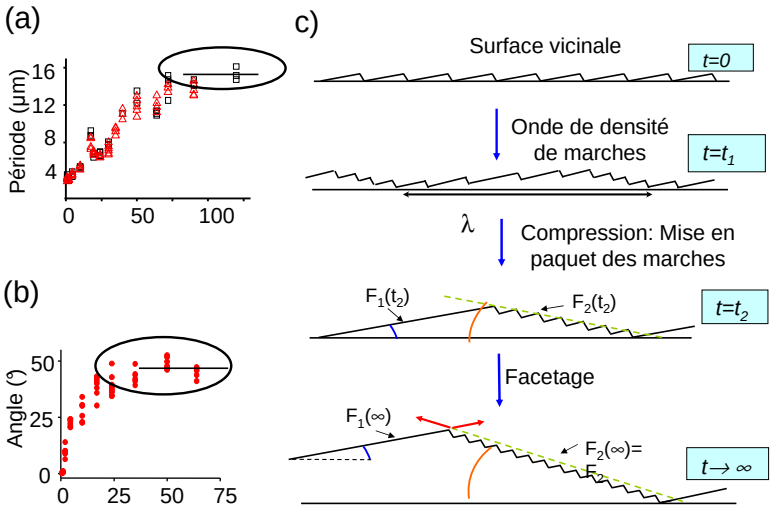

Figure II.5 *– (a) et (b), Evolution temporelle de la période et de l'angle des facettes d'une surface de Si(105) soumise à un courant continu (T= 1250° C). (c) Schéma de principe de l'évolution de la morphologie de la surface depuis l'onde de densité de marches, la compression des marches et à la fin le facettage.*

2.2.1 Onde de densité de marches

Nous allons donner ci-dessous quelques éléments d'interprétation de l'origine de cette onde de densité de marches qui se développe sur la surface du Si.

En reprenant l'argumentation développée par Misbah [45], qualitativement l'instabilité peut s'interpréter de la façon suivante (voir fig.II.6) : L'instabilité prend naissance dans la relation qu'il y a entre le déplacement d'une marche et la largeur des terrasses en présence d'un courant d'ad-atomes asymétrique induit par électromigration. Pour un faible écart à l'équilibre la force d'électromigration impose que la concentration d'ad-atomes sur les terrasses est une fonction linéaire de la position et de valeur moyenne égale à la concentration d'équilibre. Comme la vitesse d'avancée ou de recul d'une marche est proportionnelle à l'écart local à la concentration d'équilibre il s'ensuit deux situations (voir figure II.6) : dans le cas (a) où la force d'électromigration est orientée dans le sens descendant des marches la surface est instable car les grandes terrasses ont tendance à s'agrandir. Dans le cas contraire (b), les grandes terrasses ont tendances à diminuer de taille, la surface est stable.

A cette instabilité de mise en paquet des marches atomiques s'oppose le rôle stabilisant de l'interaction élastique répulsive entre les marches qui favorise un espacement régulier entre les marches. C'est le jeu entre ces deux phénomènes qui pilote le développement d'une instabilité ayant une longueur d'onde bien définie.

Pour analyser quantitativement cette instabilité construisons un modèle unidimensionnel continu de la morphologie de la surface. Les éléments de cette modélisation sont donnés dans l'article [40], ils sont ici présentés de façon simplifiée :

(i) la conservation de la matière :

$$\frac{\partial h}{\partial t} \sim -\frac{\partial j}{\partial x} \tag{2.10}$$

(ii) les principes de la thermodynamique irréversible où nous admettrons (comme pour le démouillage), que la densité superficielle de courant d'ad-atomes j est une fonction linéaire de la force motrice f (induite par le

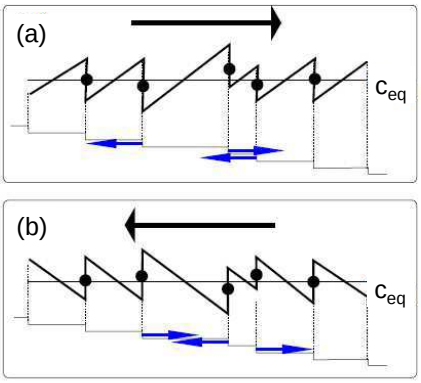

Figure II.6 *– Schéma d'une surface vicinale extraite de la référence [45]. Les traits en dents de scie représentent la densité d'ad-atomes sur les terrasses. Si la concentration en bord de marche est supérieure (inférieure) à la concentration d'équilibre c_{eq}, la marche avance (recule). Dans le cas où la force électrique est orientée dans le sens descendant des marches (a) la surface est instable. Dans le cas contraire (b) la surface est stable (voir texte).*

courant électrique) et du gradient de potentiel chimique μ lié à la morphologie de la surface.

$$j = \frac{Mc}{kT}\left(f - \frac{\partial \mu}{\partial x}\right) \tag{2.11}$$

où M, c et kT sont respectivement la mobilité des ad-atomes, leur concentration à la surface et l'énergie thermique.

(iii) l'expression du potentiel chimique, μ, d'Herring-Mullins [47, 48]. Pour cette grandeur suivons les étapes du calcul variationnel, proposé par Villain et Pimpinelli [49], pour un solide dont la hauteur de la surface, h, ne dépend que de la coordonnée x.

En modifiant localement le profil de la surface δh (voir figure II.7) le nombre d'atomes δN change et la variation δF d'énergie libre pour une transformation isotherme ($\delta F = -P\delta V + \mu\delta N$) s'écrit :

$$\delta F = \left(\frac{\mu_0}{v} - P\right)\int \delta h dx dy + \int \left(\frac{\partial \varphi}{\partial h'}\delta h'\right) dx dy \tag{2.12}$$

δF est la somme d'une contribution volumique liée à la variation du nombre total d'atomes et d'une contribution de surface. Dans l'équation

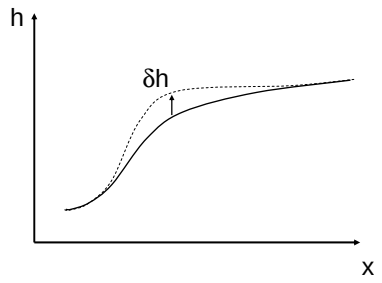

Figure II.7 *– Profil unidimensionnel de la morphologie de la surface et petite variation locale de hauteur δh.*

2.12, on note v le volume atomique et φ l'énergie de "surface projetée" sur l'axe x. Par exemple dans le cas d'un solide dont l'énergie de surface est isotrope, γ, et pour un profil unidimensionnel, φ s'écrit :

$$\varphi(h'(x)) = \gamma\sqrt{1 + h'(x)^2} \tag{2.13}$$

Dans le cas qui nous intéresse d'un solide cristallisé dont l'orientation est proche d'une face nominale, l'énergie de surface du solide peut s'exprimer sous la forme [50] :

$$\gamma = \gamma_0 + \gamma_1|h'(x)| + \gamma_3|h'(x)|^3 \tag{2.14}$$

où γ_0 est l'énergie de surface de la face nominale (sans marche). $\gamma_1|h'(x)|$ tient compte du surplus d'énergie associé aux marches atomiques (sans interaction). Ce terme est donc proportionnel à la densité linéique de marches, i.e. à la pente $|h'(x)|$. Le terme $\gamma_3|h'(x)|^3$ est quant à lui associé aux interactions élastiques répulsives entre les marches atomiques. En effet l'interaction entre deux marches étant inversement proportionnelle à leur distance au carré, $h'(x)^2$ [39, 51], on obtient le résultat précédent en tenant compte de la densité de marches.

Intégrons par parties le terme de surface, $\int(\frac{\partial\varphi}{\partial h'}\delta h')dx$, de l'équation

2.12 :

$$\int \left(\frac{\partial\varphi}{\partial h'}\delta h'\right) dx = \int \left(\frac{\partial\varphi}{\partial h'}\frac{\partial}{\partial x}(\delta h)\right) dx = \left[\frac{\partial\varphi}{\partial h'}(\delta h)\right] - \int \delta h \left(\frac{\partial}{\partial x}(\frac{\partial\varphi}{\partial h'})\right) dx \tag{2.15}$$

En ne considérant que des variations locales de hauteur δh (problème variationnel à extrémités liées) le terme entre crochet est nul et il vient que la variation d'énergie libre δF s'écrit :

$$\delta F = \int \delta h \left(\frac{\mu_0}{v} - P - \frac{\partial}{\partial x}(\frac{\partial\varphi}{\partial h'})\right) dxdy \tag{2.16}$$

Nous en déduisons donc l'expression du potentiel chimique d'Herring-Mullins [47–49] :

$$\mu = \mu_0 - v\left(\frac{\partial}{\partial x}(\frac{\partial\varphi}{\partial h'})\right) \tag{2.17}$$

et en tenant compte de l'expression de φ pour une surface vicinale (voir eq. 2.14) on obtient finalement :

$$\mu = \mu_0 - 6\gamma_3 v\left(\frac{\partial h}{\partial x}\right)\left(\frac{\partial^2 h}{\partial x^2}\right) \tag{2.18}$$

Combinant cette expression du potentiel chimique (eq. 2.18) avec l'équation de conservation de la masse (eq. 2.10) et l'équation de Fick (eq. 2.11) pour de petites perturbations autour de la pente moyenne $\overline{h'}$ de la face vicinale ($h = \overline{h'}x + \delta h$) on obtient l'équation spatio-temporelle linéarisée d'évolution de la hauteur δh :

$$\frac{\partial\delta h}{\partial t} = -\frac{\partial}{\partial h'}\left[\frac{Mcf}{kT}\right]_{\overline{h'}}\frac{\partial^2\delta h}{\partial x^2} - 6\gamma_3 v\left[\frac{Mc}{kT}\right]_{\overline{h'}}\frac{\partial^4\delta h}{\partial x^4} \tag{2.19}$$

Cette équation d'évolution de la hauteur δh étant linéarisée on peut faire une analyse linéaire de stabilité en cherchant des solutions sinusoïdales de la forme :

$$\delta h \sim e^{(\sigma t + ikx)} \tag{2.20}$$

où σ est le facteur d'amplification et k est le nombre d 'onde. On obtient

la relation suivante :

$$\sigma = \frac{\partial}{\partial h'}\left[\frac{Mcf}{kT}\right]_{\overline{h'}} k^2 - 6\gamma_3 v \left[\frac{Mc}{kT}\right]_{\overline{h'}} k^4 \tag{2.21}$$

Le terme en k^2 est un terme qui est déstabilisant si $f > 0$. Il provient du biais introduit par le courant électrique sur le mouvement des ad-atomes. Le terme en k^4 est quant à lui stabilisant. Il a pour origine la répulsion élastique entre les marches qui tend à les maintenir à une distance égale. Si le facteur d'amplification σ est positif il se développe une instabilité de mise en paquet des marches atomiques conduisant aux temps courts à une onde de densité de marches. Ce facteur d'amplification est maximum pour la longueur d'onde λ :

$$\lambda = 2\pi\sqrt{\left(\frac{12\gamma_3 v\,[Mc]_{\overline{h'}}}{\frac{\partial}{\partial h'}\,[Mcf]_{\overline{h'}}}\right)} \tag{2.22}$$

On peut obtenir une estimation de la valeur de cette longueur d'onde en faisant l'hypothèse que la mobilité M des ad-atomes, leur concentration c et la force électrique f qu'ils subissent sont des fonctions qui varient peu avec la vicinalité de la surface d'où :

$$\lambda \sim 2\pi\sqrt{\frac{12v\gamma_3}{f_0}} \tag{2.23}$$

où $f_0 \sim zeE_m$ est la force électrique exercée sur les ad-atomes de Si. z est leur charge effective ($0.01 > z > 0.1$ [52, 53]), e la charge élémentaire de l'électron et E_m le champ électrique appliqué ($E_m \sim 400V/m$). On peut évaluer qualitativement le coefficient γ_3 d'interaction entre marches à partir d'une analyse dimensionnelle $\gamma_3 \sim E \times a_0 \sim 10$ J/m^2 où E est le paramètre élastique élémentaire, i.e. le module d'Young, et a_0 est la distance inter-atomique caractéristique du Si. De ces considérations on en déduit une estimation haute de la longueur d'onde : $\lambda \sim 100$ μm. Même si ce calcul surestime la valeur expérimentale elle permet de valider l'approche choisie. En extraire des informations plus précises, nécessite de modéliser plus en détails l'interaction élastique et/ou la force électrique (voir notre article [40]).

2.2.2 Facettage induit par électromigration

Examinons désormais le régime aux temps longs de l'instabilité sous électromigration, i.e. quand la surface, initialement vicinale, s'est décomposée en deux facettes. Dans le tableau 2.1 sont notées les facettes que nous avons observées aux temps asymptotiques et qui diffèrent selon l'orientation initiale de la surface.

Face vicinale	(118)	(223)	(443)	(105)
Facette "1"	(001)	(111)	(111)	(001)
Facette "2"	(113)	(113)	(110)	(101)

Tableau 2.1 – *Décomposition des faces vicinales par électromigration en deux facettes "1" et "2".*

Nous interprétons la formation d'une surface facettée par le fait qu'un courant électrique change les énergies effectives des faces cristallographiques et favorise une décomposition de la face vicinale en deux facettes stables malgré l'augmentation d'aire de la surface libre (voir discussion complète dans [40]). Toutefois, minimiser l'énergie de surface en formant des facettes ne signifie pas pour autant déterminer la longueur d'onde du facettage. Pour comprendre l'origine de cette longueur d'onde nous avons proposé dans l'article [40] un modèle où la forte densité de marches atomiques et donc les relaxations élastiques induites jouent un rôle central. Ce modèle théorique s'appuie sur les résultats de Marchenko [54] et Alerhand et al. [55] démontrant que si la surface d'un cristal se décompose en deux domaines (e.g. deux facettes ou deux reconstructions de surface) il doit se développer spontanément en surface une structure périodique qui a pour origine l'équilibre entre le coût énergétique local due à la présence de lisères entre les domaines (β) et les relaxations élastiques provenant des forces $\vec{F}$ induites par la différence de contraintes de surface entre les deux domaines (voir Fig. II.8(a)). Afin de ne pas décrire uniquement l'état facetté final mais aussi les états intermédiaires nous avons entrepris de comparer le modèle macroscopique de Marchenko et Parshin avec un modèle qui tient compte des détails microscopiques des facettes et donc de toutes les interactions élastiques entre marches atomiques (voir Fig. II.8(b)).

A l'échelle de la marche atomique, et pour un réseau de Bravais, on

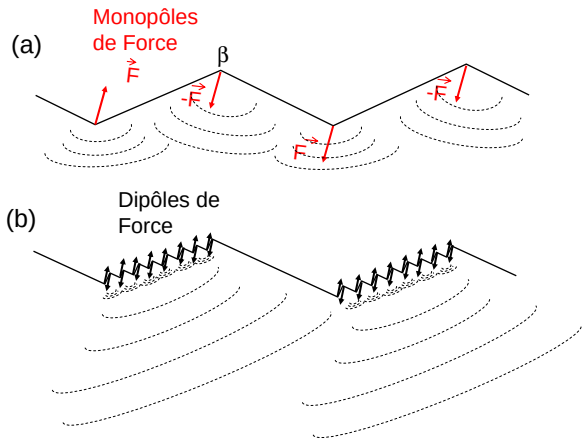

Figure II.8 – *Modélisation d'une surface facettée. Descriptions macroscopique et microscopique (voir texte).*

peut montrer en suivant le raisonnement de Marchenko et Parshin [51], qu'une marche brise localement la symétrie de la surface et se comporte comme une densité linéique de dipôles de force le long de la marche. Les équations linéaires de l'élasticité montrent qu'il en résulte une interaction élastique entre marches à longue portée ($1/r^2$). Marchenko et Parshin ont été capable, dans une certaine mesure, de préciser le coefficient de proportionnalité même si sa valeur exacte dépend de détails microscopiques qui échappent à la théorie de l'élasticité. Remarquons que si deux marches voisines ne sont pas équivalentes il en résulte que l'approximation dipolaire n'est pas valable et que la marche se comporte comme une densité linéique de monopoles de force [3]. On peut tout de même retrouver une description en terme de densité linéique de dipôles en considérant un nombre suffisant de marches pour annihiler l'effet du motif de la maille. En s'appuyant sur ces résultats nous avons calculé (voir article [40]) le bilan énergétique des interactions élastiques d'une surface formée de paquets de marches réguliers (voir figure II.8).

Le calcul énergétique de la relaxation élastique pour un ensemble périodique de paquets de marches se fait de la façon suivante :

3. e.g. dans le cas des faces vicinales de Si(100) les terrasses sont alternativement reconstruites (2×1) et (1×2). Un monopole de force apparaît donc à la lisière

(i) Considérons des paquets de marches formés de N marches atomiques séparées d'une distance a. La relaxation élastique au sein du paquet de marches s'écrit :

$$W_{intra} = \frac{A_{dip}}{a^2} \sum_{i<j,j}^{N} \frac{1}{(i-j)^2} \sim \frac{A_{dip}}{a^2} \left[N\frac{\pi^2}{6} - 1 - \ln(N) \right] \tag{2.24}$$

où A_{dip} est un terme proportionnel au carrée de l'amplitude du dipôle de force de la marche [4].

(ii) Ces paquets de marches sont périodiquement espacés d'une distance $M \times a$, où $M > N$. Il en résulte une relaxation d'origine élastique entre les paquets de marches :

$$W_{inter} = \frac{A_{dip}}{a^2} \sum_{k,-\infty}^{+\infty} \sum_{i,j=1}^{N} \frac{1}{\left(kM + (i-j)\right)^2} \sim -\frac{A_{dip}}{a^2} \ln \left[\frac{\sin\left(\frac{\pi N}{M}\right)}{\left(\frac{\pi N}{M}\right)} \right] \tag{2.25}$$

D'où l'expression du bilan énergétique par unité de longueur L :

$$\frac{W}{L} = \frac{\tau}{L} + \frac{1}{L}\frac{A_{dip}}{a^2} \ln\left(\frac{L}{\pi a} \sin(\pi p) \right) \tag{2.26}$$

où p est la fraction de l'aire occupée par les paquets de marches ($p = N/M$)

Le terme $\frac{\tau}{L}$ a été rajouté pour tenir compte du coût énergétique de la lisère entre les domaines. Cette expression est remarquable car elle rappelle exactement la formulation à l'échelle macroscopique obtenue par Marchenko [54] pour une relaxation élastique par monopoles alternés (voir fig.II.8(a)). Toutefois contrairement au calcul de Marchenko, les ingrédients physiques sont ici d'origine microscopique, e.g. le dipôle de force élastique au lieu de la différence de contraintes de surface ou encore la distance inter-marche a au lieu d'un cut-off indéterminé de quelques distances atomiques.

Le bilan énergétique de l'eq. 2.26 admet un minimum pour une longueur d'onde λ donnée. A partir des mesures expérimentales, de longueur d'onde (λ), et de fraction de surface couverte par les facettes (p) nous avons

4. Selon [44], en élasticité linéaire et isotrope, $A_{dip} = \frac{1-\nu^2}{\pi E} A^2$ avec ν le coefficient de Poisson, E le module d'Young et A l'amplitude du dipole de force élastique.

pu en déduire le rapport de l'énergie de lisière τ avec l'amplitude du dipôle élastique des marches pour toutes les orientations des faces vicinales (voir tableau 2.2).

	λ (μm)	p	$\tau a^2/A$
(118)	6.6	0.39	6.5
(223)	12	0.38	7.1
(443)	13	0.19	6.3
(105)	8	0.23	5.9

Tableau 2.2 – *valeurs expérimentales de la longueur d'onde λ, de la fraction d'aire couverte par les paquets de marches p et du rapport de l'énergie linéique de lisière avec le préfacteur de l'énergie linéique de relaxation élastique $\tau a^2/A$.*

La comparaison de ce modèle microscopique avec le modèle de Marchenko et Parshin nous a aussi permis de montrer que les contraintes de surface d'une face vicinale décroissent linéairement avec l'angle de la face vicinale θ. Ce résultat est analogue à celui obtenu par Salanon et Hecquet [56] :

$$\sigma(\theta) - \sigma(0) \sim -\frac{A_{dip}}{h}|\theta| \tag{2.27}$$

où h est la hauteur d'une marche atomique.

2.3 Transition abrupte méandrage / mise en paquet de marches atomiques (voir article joint [7])

La richesse du pseudo-diagramme de phase des instabilités morphologiques des faces vicinales de Si en fonction de la température (voir tableau 2.3) n'a pas été interprétée totalement dans le cadre d'un modèle unifié. Nous avons donc entrepris de décrire certaines de ces transitions morphologiques expérimentalement et théoriquement.

En particulier nous nous sommes intéressés à la transition en température méandrage/mise en paquets des marches (domaines II/III) quand le courant électrique est orienté dans le sens descendant des marches.

La figure II.9 montre des morphologies de méandrage et de mise en paquets des marches observées en microscopie optique ainsi que des illustra-

	Domaine I	Domaine II
Sens montant	vicinale	paquet de marches
Sens descendant	paquet de marches	méandrage des marches
Latyshev [57,58]	–	$1050 - 1250°$ C
Gibbons [59]	$850 - 950°$ C	$1040 - 1190°$ C
Métois [60]	$900 - 1050°$ C	$1150 - 1250°$ C
Homma [61], Yang [62]	$\sim 945°$ C	$\sim 1190°$ C
	Domaine III	Domaine IV
Sens montant	vicinale	paquet de marches
Sens descendant	paquet de marches	–
Latyshev [57,58]	$1250 - 1350°$ C	$> 1350°$ C
Gibbons [59]	$1200 - 1300°$ C	$> 1300°$ C
Métois [60]	$1250 - 1300°$ C	–
Homma [61], Yang [62]	$\sim 1245°$ C	–

Tableau 2.3 – *Instabilités et domaines de température pour lesquelles les différentes morphologies de surface des faces vicinales de Si on été observées.*

tions schématiques. Le méandrage (en phase) des marches donne naissance à une microstructure perpendiculaire à la direction moyenne des marches tandis que la mise en paquet des marches laisse apparaître une microstructure parallèle aux marches.

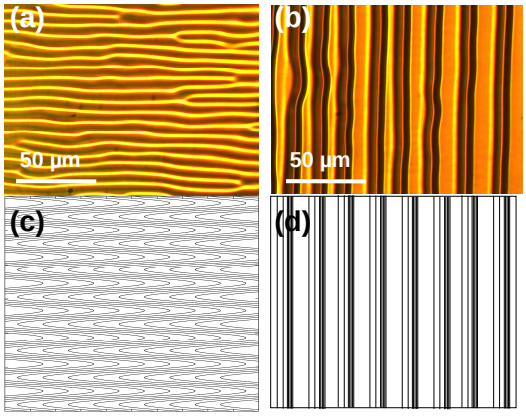

Figure II.9 – *Images expérimentales et représentation schématique de surfaces instables formant du méandrage de marches (a)-(c), et de la mise en paquets de marches (b)-(d).*

Pour observer la transition entre ces deux instabilités nous avons sou-

mis l'échantillon à un gradient de température en différenciant les échanges thermiques aux deux extrémités de l'échantillon (par un contact mécanique différent grâce à une vis de serrage). Sur la figure II.10 sont représentées des images de la surface de Si obtenues par microscopie optique après six heures sous électromigration. Grâce au gradient thermique nous pouvons observer des zones, plus froides, où l'instabilité de méandrage s'est développée et des zones, plus chaudes, où l'instabilité de mise en paquet des marches a pris le dessus. Connaissant le gradient thermique par des mesures locales de température par pyrométrie (résolution 0.5 mm), nous avons estimé la largeur de la transition à 4 K autour de 1224° C. La transition abrupte entre ces deux modes instables se produit par nucléation de domaines en paquets de marches au milieu d'un large domaine de méandrage.

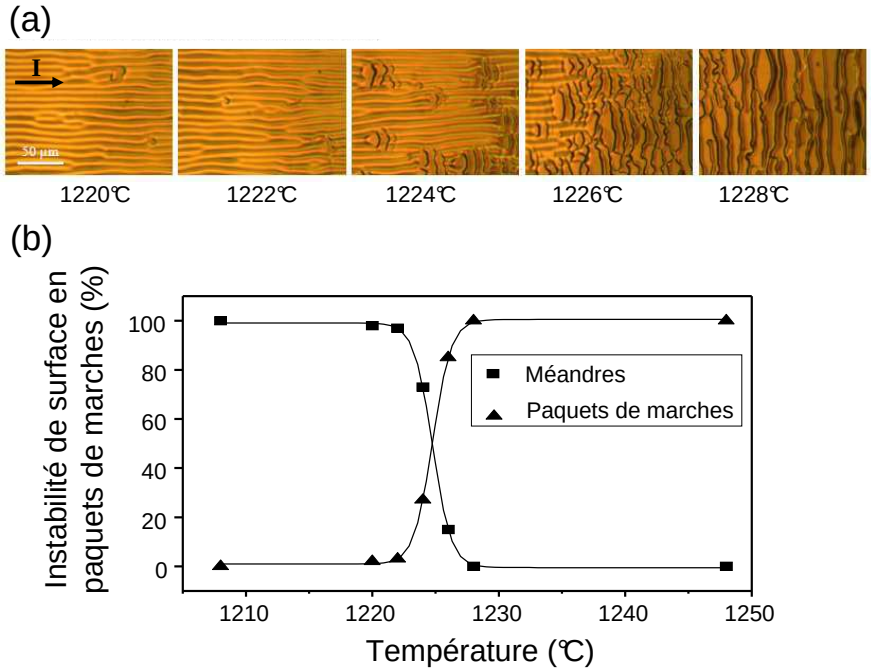

Figure II.10 *– (a) Images optiques ex situ de la surface de Si après 6 heures sous électromigration. On observe, en suivant le gradient de température, la transition morphologique depuis le méandrage des marches jusqu'à la mise en paquets des marches. (b) Evolution de la fraction de surface couverte par l'instabilité de mise en paquets des marches atomiques.*

Nous avons entrepris en collaboration avec l'équipe de théoriciens de l'IM2NP (Jean-Marc Debierre, Thomas Frisch et Mathieu Dufay) d'inter-

préter la transition entre ces deux instabilités morphologiques. A partir de deux modèles spatio-temporels de dynamique de marches (méandrage et mise en paquet des marches), issus des principes posés par Burton, Cabrera et Franck [38], nous avons procédé à des analyses linéaires de stabilité. L'idée principale était d'évaluer quantitativement l'évolution en température des facteurs d'amplification maximum des instabilités de méandrage σ_M et de mise en paquet des marches σ_B. Comme le rapport des amplitudes évolue avec le temps selon $exp\left[(\sigma_M - \sigma_B)t\right]$ rapidement l'une des instabilités domine l'autre. Les figures II.11(a)-(b) illustrent les principaux résultats de cette analyse théorique. Les deux instabilités sont présentes simultanément pour des nombres d'onde différents. Il y a un croisement de ces deux facteurs d'amplification autour de T$=1500$ K en accord avec l'expérience. Les paramètres d'ajustement du modèle nous ont montré que le processus atomistique limitant les transferts de matière était l'attachement/détachement des ad-atomes en bord de marches.

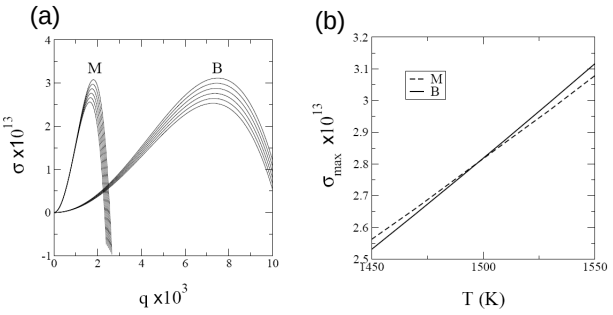

Figure II.11 *– (a) Evolution des facteurs d'amplification du méandrage σ_M et de la mise en paquets de marches σ_B en fonction de nombre d'onde k. Les différentes courbes sont obtenues pour des températures croissantes (en augmentant de bas en haut par pas de 20 K). (b) Evolution des maxima des facteurs d'amplification avec la température. Il y a un croisement autour de T$=1500$ K.*

Toutefois si notre modélisation nous a permis d'expliquer la transition en température entre les domaines II/III elle reste insuffisante pour expliquer les transitions I/II et III/IV. Plusieurs raisons à cela : dans le régime haute température le rôle des ad-lacunes et de l'évaporation dans les transferts de matière ne peuvent plus être négligés. En outre la prise en compte

du phénomène d'advection [63] provenant de la vitesse finie des marches par rapport aux déplacement des ad-atomes influe sur les effets de l'électromigration. Enfin, et concernant le régime basse température, une description plus fidèle des processus microscopiques d'attachement/détachement semble nécessaire pour expliquer le basculement du méandrage vers la mise en paquets des marches.

2.4 Conclusion

L'étude de l'électromigration a donné lieu à de nombreux résultats, tant au niveau théorique qu'expérimental. Le système expérimental modèle est la surface vicinale de Si(111). Il est connu depuis la fin des années 80 que le passage d'un courant électrique dans un cristal de Si induit une instabilité de mise en paquets des marches atomiques qui mène à la formation de paquets de marches. Nous avons contribué à une meilleure compréhension du phénomène à travers :

(i) Une étude complète de la dynamique de transformation d'une face vicinale vers une surface facettée en passant par le développement d'une onde de densité de marches atomiques.

(ii) L'observation expérimentale de l'onde de densité de marches sur des surfaces vicinales de désorientations différentes a permis de mettre evidence un phénomène étonnant : la longueur d'onde de l'instabilité ne dépend pas de l'orientation de la surface. Cette observation a été expliquée par un modèle microscopique faisant intervenir un terme déstabilisant, la force électrique qui agit sur les ad-atomes de silicium, et un terme stabilisant provenant des interactions répulsives entre marches atomiques.

(iii) La description du stade final de l'instabilité qui présente une morphologie facettée. Nous avons proposé que la longueur d'onde de cet état était contrôlée par les contraintes élastiques de surface. Nous avons fait un lien entre ces contraintes de surface, qui résulte d'une vision "macroscopique" de la surface, et les interactions entre marches atomiques qui correspondent à une description "microscopique" de la surface.

(iv) Enfin nous avons pu mesurer expérimentalement et décrire théoriquement une transition en température entre deux instabilités morpholo-

giques, le méandrage et la mise en paquets des marches.

Jusqu'à une période récente la difficulté majeure dans les études expérimentales des phénomènes d'électromigration restait liée au couplage entre le courant électrique et la température (le courant induit par effet Joule une augmentation de la température). Récemment l'équipe de Shvets (Trinity College, Dublin) a réussi à partir de la fabrication d'un porte-échantillon original, à découpler les effets de la température et de l'intensité du courant [64–66]. Ils ont pu mettre en évidence des effets nouveaux en particulier l'existence d'un champ électrique critique nécessaire pour la mise en paquet des marches. Toutefois ces études ont été menées avec des outils de caractérisation *ex situ* et il nous semblerait intéressant de les reprendre *in situ* en LEEM.

ARTICLES SÉLECTIONNÉS : INSTABILITÉS DES SURFACES DE SILICIUM INDUITES PAR ÉLECTROMIGRATION

[6] : Onde de densité de marches et facettage sur les faces vicinales de silicium
Leroy *et al.*, Phys. Rev. B (2007)

Vicinal silicon surfaces: From step density wave to faceting

F. Leroy,[1,*] P. Müller,[1,*] J. J. Métois,[1] and O. Pierre-Louis[2]
[1]*Centre de Recherche sur la Matière Condensée et les Nanosciences, UPR CNRS associé aux universités Aix Marseille II et III, Aix-Marseille University, Campus de Luminy, case 913, F-13288 Marseille Cedex 9, France*
[2]*CNRS/The Rudolf Peierls Centre for Theoretical Physics, 1 Keble Road, Oxford OX1 3NP, United Kingdom*
(Received 16 February 2007; revised manuscript received 18 April 2007; published 5 July 2007)

We investigate faceting mechanisms induced by electromigration in the regime where atomic steps are transparent. For this purpose we study several vicinal orientations by means of *in situ* (optical diffraction, electronic microscopy) as well as *ex situ* (atomic force microscopy, microprofilometry) visualization techniques. The data show that faceting proceeds in two stages. The first stage is short and leads to the appearance of a step density wave, with a wavelength roughly independent of the surface orientation. The second stage is much slower and leads to the formation of a hill-and-valley structure, the period of which depends on the initial surface orientation. A simple continuum model enables us to point out why the wavelength of the step density wave does not depend on the microscale details of the surface. The final wavelength is controlled by the competition between elastic step-step interaction and facet edge energy cost. Finally, the surface stress angular dependence is shown to emerge as a coarsed-grained picture from the step model.

DOI: 10.1103/PhysRevB.76.045402 PACS number(s): 66.30.Qa, 68.35.Md, 68.35.Bs, 68.35.Gy

I. INTRODUCTION

Due to its scientific and technological interest, faceting of stepped surfaces has been a long standing subject of intensive research.[1–25] Indeed, from a fundamental viewpoint the underlying mechanisms are still a matter of debate. Furthermore, faceted systems appear to be promising templates for the "bottom-up" design of nanostructures.

One of the most important mechanisms for faceting is current-induced step bunching. While the instability of the surface is driven by electromigration,[5,13–16] the resulting pattern arises from the interplay between electromigration-induced mass transport and the minimization of the elastic energy variations resulting from the changes in the surface morphology. As we shall see in the following, step bunching also appears as a promising way to study fundamental aspects of step-step elastic interactions as well as to control the surface morphology at the microscale or nanoscale. At the nanoscale, a considerable amount of research has been devoted to understanding the role of surface steps in the morphological evolution of vicinal Si(111) surfaces during sublimation.[1–25] These phenomena depend both on temperature and on the direction of the heating current. Stoyanov[16] was the first to propose a step model based on the Burton-Cabrera-Frank (BCF) model,[26] in which electromigration is introduced as a bias in the Brownian motion of the adatoms on the surface.[14–16] At the microscale, Marchenko[27,28] and then Alerhand *et al.*[29] proposed a simple theory, based on elastic minimization, to explain the micrometric periods which appear by annealing unstable surfaces.

In this paper we study the influence of the surface orientation on the instability, as well as the link between nanoscopic and microscale models. To do so, we have performed a systematic study of the surface morphology from the first stages (where the vicinal surface is described as a step pattern) to the microscale state (where the faceted surface is described as a hill-and-valley structure formed by microscale facets) for various vicinal orientations. In all cases the morphological evolution proceeds in two stages: a short one based on the formation of a step density wave (the period of which, roughly, does not depend upon the surface orientation) followed by a much slower one, where periodic microscale facets form via a step bunching mechanism. The final faceting period seems to depend on the elastic properties of the so-formed microscale facets.

The paper is divided into four parts. Section II is devoted to a description of the vicinal faces under study and then to a description of the experimental procedure. The experimental results are reported in Sec. III. In Sec. IV we analyze the final state (Sec. IV A) and the first stages of faceting (Sec. IV B). The last part (Sec. V) consists of a short conclusion.

II. DESCRIPTION OF THE SAMPLES AND EXPERIMENTS

A. Morphological and elastic description of the vicinal faces under study

Vicinal surfaces can be described as stairlike surfaces, where monoatomic steps separate microscopically flat terraces. Since the atoms belonging to the step edges have a different number of nearest neighbors than the atoms in the underlying bulk, steps give rise to a lattice distortion that mediates an elastic interaction between them. The elastic description of the steps depends upon the state of the surface (surface of a stress-free body or surface of a stressed body, for example[30]) as well as upon its structure. As a preamble, we thus would like to provide the reader with a detailed description of the geometry and the elastic properties of the surfaces that will be analyzed in the subsequent sections.

As shown in Fig. 1(a), the selected vicinal orientations (118), (223), (443), and (105) surfaces—form a closed cycle in the stereographic projection. More precisely, in Fig. 1(a) are shown in red the normal to the selected vicinal faces and in blue the normal to the (001), (113), (111), (110), and (100) surfaces which appear on the Si equilibrium shape.[31] In Fig.

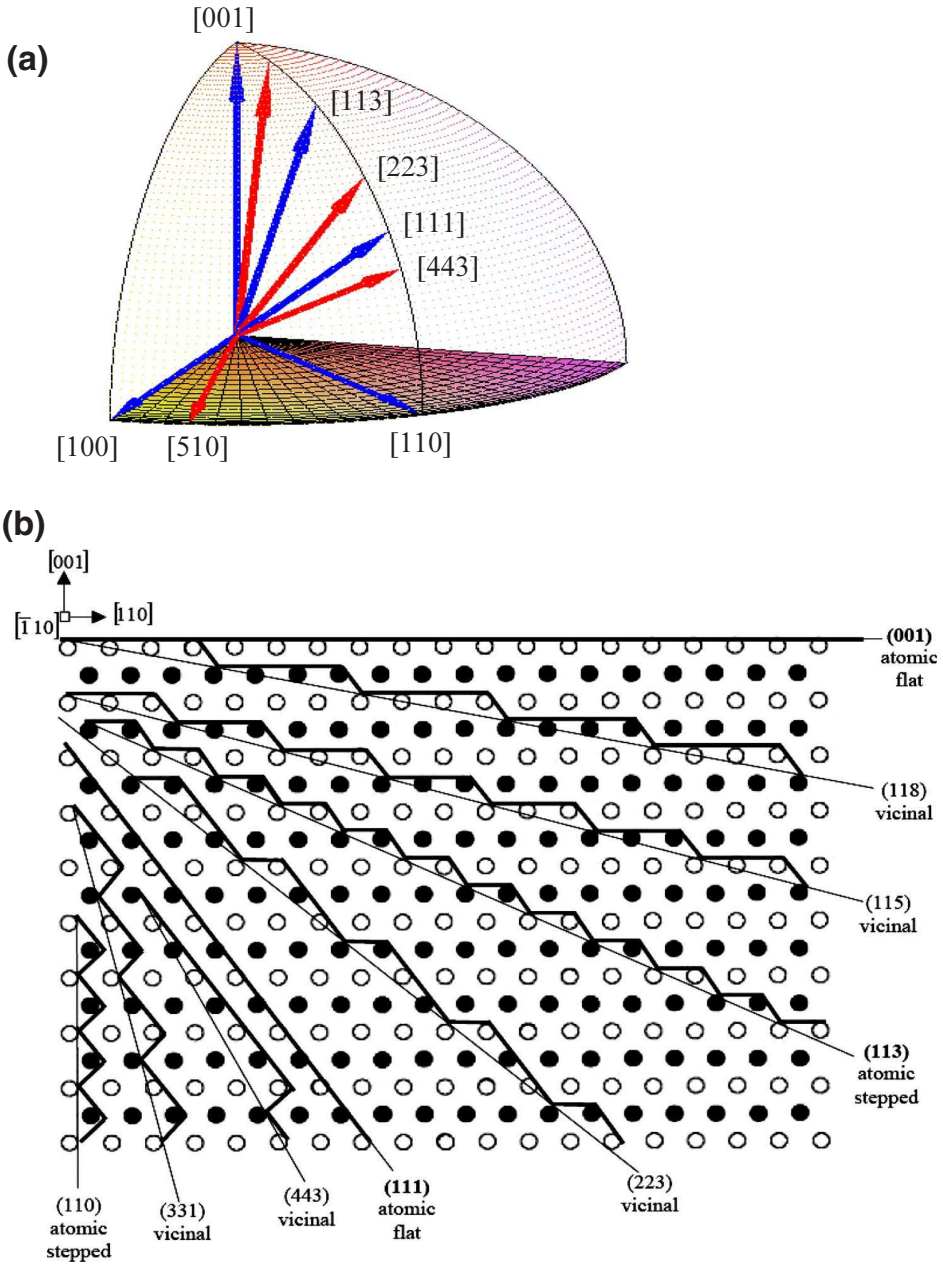

FIG. 1. (Color online) (a) Stereographic representation of the vicinal surfaces under study. The arrows represent the normal to the vicinal surfaces. Notice that the (001), (113), (111), (110), and (100) surfaces belong to the silicon equilibrium shape (Refs. 31 and 39) (b) Projection along the [$\bar{1}$10] direction of some of the studied vicinal surfaces of a face centered cubic material. Notice that the (111) and (001) surfaces are flat at the atomic level and that the (113) and (101) surfaces are flat at the second neighbor (atomic stepped surfaces). For the sake of simplicity we only consider in Fig. 2(b) the simple case of a face centered cubic crystal and not the true diamond structure of the silicon. It is enough for our purposes.

1(b) are also reported the morphologies of some crystal surfaces with zone axis [$\bar{1}$10]. We may see, e.g., that the (118) surface is a vicinal of the (001) surface and thus is constituted of (001) terraces separated by monoatomic steps forming (111) microfacets while (223) and (443) surfaces are vicinals of the (111) surface and thus are composed of (111) terraces separated by monoatomic steps forming (001) microfacets. Furthermore, notice that the (001) and (111) surfaces are flat at the atomic scale (*F* surfaces) while the (113) and (101) surfaces can be considered to be flat at the second-neighbor scale (at least for the fcc model).

In such a terrace-step model, important differences exist between the different vicinal surfaces under study. Let us thus consider separately vicinals of Si(111) and vicinals of Si(001).

(i) Since the (111) surface is isotropic, vicinals of Si(111) exhibit equivalent (111) terraces characterized by isotropic surface stresses [see Fig. 2(a)] In other words, the surface

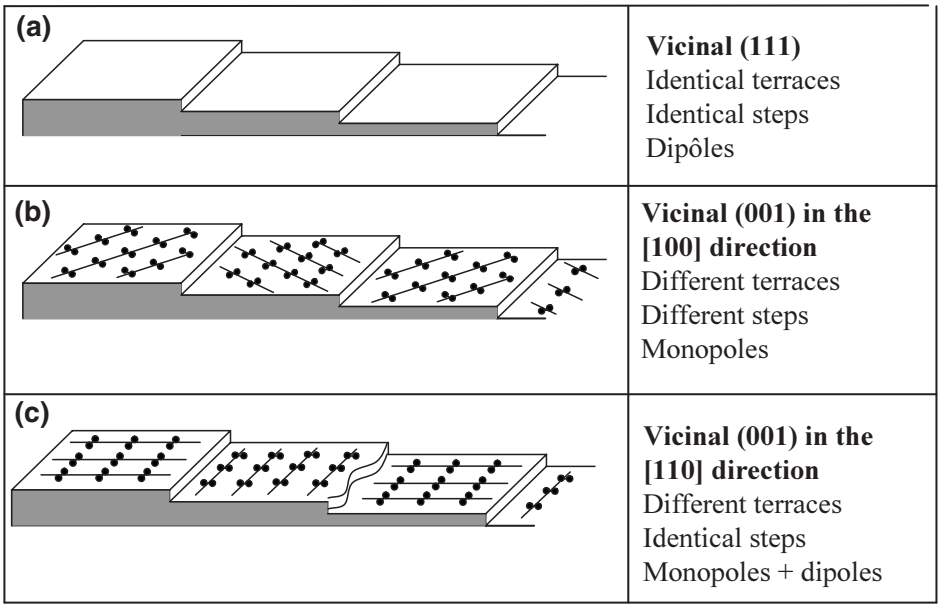

FIG. 2. Schematic representation of the various kinds of vicinal surfaces under study. According to the terrace structure, the steps can be described as rows of elastic dipoles or by the sum of elastic monopoles and elastic dipoles. Furthermore, for the vicinal of the (001) surface one step is rougher than the other (Ref. 32) as drawn in (b). The couples of dots represent the dimers and the lines on the terraces represent the rows of dimmers.

stress is a scalar. From an elastic viewpoint, steps, separating the (111) terraces, can be modeled by rows of elastic dipoles distributed along the step edge.[30] The elastic interaction between steps per unit length then scales as ℓ^{-2} where ℓ is the inter step distance (see the Appendix).

(ii) Si(001) is not an isotropic surface. Indeed, its number of dangling bonds is reduced by the formation of dimer pairs aligned along the $\langle \bar{1}10 \rangle$ direction.[32] Thus, due to the diamond structure of silicon, two neighboring terraces separated by an atomic step do not have the same surface termination: one terrace exhibits a (1×2) reconstructed surface with dimers parallel to the $[\bar{1}10]$ direction, while the other terrace exhibits a (2×1) reconstructed surface with dimers parallel to the [110] direction. In other words, two neighboring terraces exhibit two equivalent surface reconstructions rotated by 90° with respect to each other. Since the surface stress component parallel to the dimer axis is more tensile than the surface stress component perpendicular to the dimer axis,[29] the surface stress of the (001) terraces is a second-rank tensor which reads $\begin{pmatrix} s_{xx} & 0 \\ 0 & s_{yy} \end{pmatrix}$ for one terrace and $\begin{pmatrix} s_{yy} & 0 \\ 0 & s_{xx} \end{pmatrix}$ for the other (when written in the [110], $[\bar{1}10]$ surface axis). As a consequence, the elastic description of the vicinal surfaces of Si(001) depends upon the azimuthal disorientation angle.

More precisely, (i) ideal vicinal surfaces with [110] zone axis [case of (113) and (118) ideal surfaces] are formed by steps parallel to the [110] direction [see Fig. 2(b)], so that the surface stress difference $\pm|s_{xx}-s_{yy}|$ in the direction normal to the step gives birth to a net force across the step. The action of these steps on the underlying crystal can be modeled by a line of elastic monopoles perpendicular to the steps and distributed along the step edge.[30] The elastic interaction between steps thus scales as $\ln \ell$ where ℓ is the interstep distance (see Ref. 30 and the Appendix).

(ii) For vicinal faces with $\langle 100 \rangle$ zone axis [case of (510) surface], the steps are parallel to the $\langle 100 \rangle$ direction [see Fig. 2(c)], and the surface stress tensor reads $\frac{1}{2}\begin{pmatrix} s_{xx}+s_{yy} & s_{xx}-s_{yy} \\ s_{xx}-s_{yy} & s_{xx}+s_{yy} \end{pmatrix}$ for one terrace and $\frac{1}{2}\begin{pmatrix} s_{yy}+s_{xx} & s_{yy}-s_{xx} \\ s_{yy}-s_{xx} & s_{yy}+s_{xx} \end{pmatrix}$ for the other one (when written in the [100], [010] surface axis). Thus adjacent terraces have opposite surface shear stresses $\pm(s_{xx}-s_{yy})$, giving rise to a shear stress discontinuity at the step edge. This discontinuity can be described by a row of monopoles parallel to the step edge. (Think about a piece of surface submitted to a shear stress that means to forces acting on each side of the elemental area and parallel to the side. When removing the half plane to form the step, only remains a net force along the step.) The monopoles of two neighboring steps are antiparallel. We show in the Appendix that the elastic interaction between such monopoles also scales as $\ln \ell$. As a partial conclusion, from an elastic viewpoint, the action of the steps of such vicinal faces on the underlying crystal can be modeled by a line of elastic monopoles parallel to the step and distributed along the step edges added to the usual dipolar contribution.

In Table I are reported the structural and elastic descriptions of the vicinal surfaces under study as well as the direction of the dc current (in the direction of ascending steps).

For completeness, notice that our description of (001) vicinal surfaces only concerns ideal surfaces. Real vicinal Si(001) surfaces misoriented towards the [110] direction may exhibit a transition from single-height step to double-height step (for an other zone axis, double steps have not been reported). The critical angle at which the transition occurs depends upon the sample temperature.[33] At 1150 K biatomic height steps have been found for misorientation of more than 4°.[34] Extrapolating Fig. 8 of Ref. 33, Si(113) and Si(118) surfaces should not exhibit double steps for the temperature we use.

TABLE I. Description of the vicinal faces under study. The dc current is in the ascending direction for step bunching to occur in the temperature range under study.

Vicinal surfaces	Terraces orientation	Interstep distance a (Å)	Zone step direction	dc direction (perpendicular to the step)	Elastic description (orientation with respect to the step)
(118)	(001)	7.7	$[\bar{1}10]$	$[44\bar{1}]$	Monopoles ($\perp$) +Dipoles ($\perp$)
(223)	(111)	15.6	$[\bar{1}10]$	$[33\bar{4}]$	Dipoles ($\perp$)
(443)	(111)	24	$[\bar{1}10]$	$[33\bar{8}]$	Dipoles ($\perp$)
(510)	(100)	6.75	[001]	$[\bar{1}50]$	Monopoles ($\parallel$) +Dipoles ($\perp$)

B. Experimental procedure

The Si single crystals of size $20\times2\times0.3$ mm^3 were first chemically cleaned and then clamped between two electrodes of the sample holder in the UHV chamber. After a few flashes heating up to 1300 °C during 2 min to clean the surface, the dc current was set to heat the sample at the chosen temperature (1100 °C, 1200 °C). The heating current direction is parallel to the longer side of the samples and perpendicular to the steps of the vicinal surfaces. The experiments have been performed with an ascending step current direction (regime II of Ref. 35), for which a surface instability occurs. The current direction used for the various vicinal surfaces is reported in Table I. Heating duration varies from 15 min to more than 100 h in order to observe the whole kinetic behavior of the faceting process. The residual pressure during heating was less than 1×10^{-9} mbar. Notice that thanks to the evaporation regime, a clean surface is periodically regenerated so that the surface remains clean during the process. The samples are observed *in situ* by optical diffraction [see the experimental setup in Fig. 3(a)], transmission electron microscopy (TEM), and *ex situ* by atomic force microscopy (AFM) and optical microscopy. The TEM apparatus is a JEOL 100C microscope modified for UHV *in situ* experiments;[36] the AFM is a Nanoscope III from Digital Instruments used in the noncontact mode. Optical diffraction experiments were performed with a laser beam ($\lambda=0.53$ nm) at an incident angle close to the normal incidence. The scattered light is observed with a charge-coupled-device (CCD) camera [see Fig. 3(a)].

III. EXPERIMENTAL RESULTS

A. *In situ* experiments

1. Optical diffraction

We record the light scattered by the sample as a function of time. A few minutes are enough to obtain the diffracted pattern of Fig. 3(b) in the case of a Si(105) surface heated at 1200 °C. The diffracted pattern reveals a periodic surface structure with a wavelength roughly around $\lambda\approx4$ μm. We do not observe any pattern with a smaller period. Moreover, during the earlier stages of annealing (a few hours), the period remains roughly fixed while the intensities of the diffracted spots change. It can thus be concluded that as soon as the sample is annealed, a surface undulation with a period $\lambda\approx4$ μm appears, while the amplitude increases with time. For longer annealing duration (several hours), the period slowly grows toward an asymptotic state and the diffracted pattern is slowly blurred because of the appearance of numerous defects.

2. TEM experiments

TEM has been used to follow the early stages of the instability. More precisely the silicon surface is illuminated in grazing incidence, so that the shadow of the edge of the sample can be observed. The amplitude of the surface corrugation is enhanced by rotating the screen in the microscope and observing the image also in grazing conditions (as described in Ref. 36). The results, given in Fig. 4, show that the surface morphology exhibits a sinusoidal shape at the early

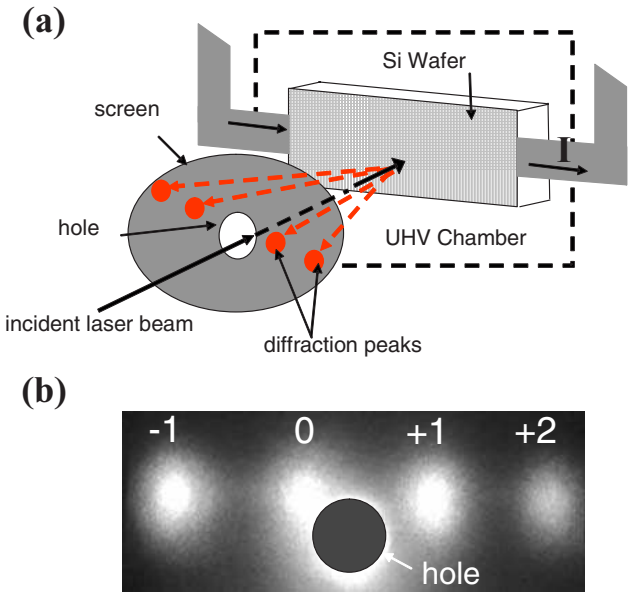

FIG. 3. (Color online) (a) Sketch of the optical diffraction equipment, (b) optical diffraction pattern recorded for Si(105) after 1 h at 1200 °C. Labels 0, +1, +2, and −1 correspond to the different orders of diffraction.

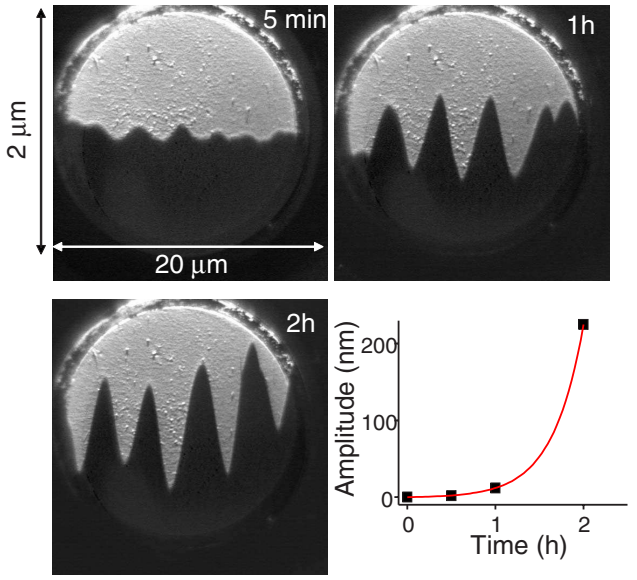

FIG. 4. (Color online) TEM observation of the first stages of the roughening of the Si (105) surface. The images correspond to 5 min, 1 h, then 2 h of annealing (notice the two different perpendicular scales due to the grazing incidence). In the bottom right part of the figure is also reported the time evolution of the amplitude of the oscillation (T=1250 °C).

beginning of the process. The time evolution of the amplitude of the corrugation is also reported in Fig. 4. This evolution can be perfectly fitted by an exponential law.

In other words, *in situ* experiments point out that the early stages of annealing are characterized by the appearance of a characteristic wavelength with an exponential "explosion" of the amplitude, which is the characteristic feature of linear instability with a unique unstable mode.

B. *Ex situ* experiments

Ex situ experiments essentially consist in "post-mortem" examination of the samples. More precisely, the vicinal surfaces are heated in UHV, then taken out of the chamber and observed by AFM, optical microscopy, and mechanical microprofilometry (Dektak 6M stylus profiler from Veeco). A set of AFM images measured from the Si(105) annealed at 1250 °C during different heating duration (1, 4.5, 24, 64 h) is reported in Fig. 5. For each picture the profiles recorded along the dotted lines are also reported. Finally, in Fig. 5(e) a three-dimensional (3D) picture of the surface after 64 h of annealing is shown. For the shortest annealing duration [Fig. 5(a)], we observe some local inhomogeneities on the surface, which locally disturb the surface morphology. These points do not behave as nucleation sites since the surface also exhibits a regular wavy pattern underneath. As the heating duration increases, the one-dimensional array of bunches gets more pronounced as the size of the bunches increases. At the longest duration the bunches look more asymmetric and form microscale facets. An increase of surface disorder is also observed.

The crystallographic angles formed by the facets have been measured directly on the profiles.

C. Summary of the experimental data

All the results are summarized in Fig. 6. For the Si(105) annealed at 1250 °C, we have shown the time evolution of

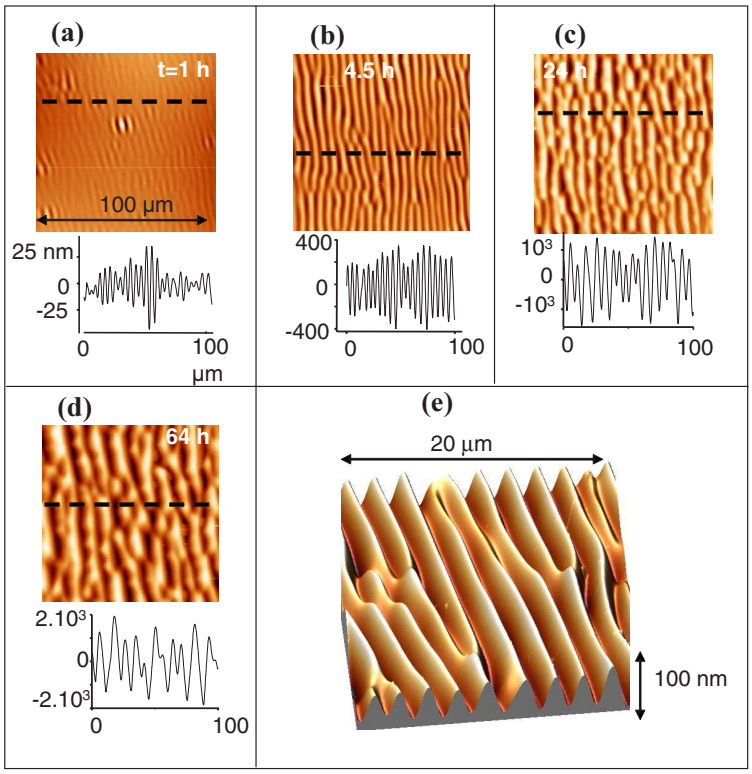

FIG. 5. (Color online) AFM images of the Si (105) surface evolution versus time. (a), (b), (c), (d), and (e), respectively, correspond to 1, 4.5, 24, and 64 h of annealing at 1250 °C. The corresponding profiles (obtained along the dotted lines) are reported just below. In (e) the 3D picture obtained after 64 h of annealing is reported.

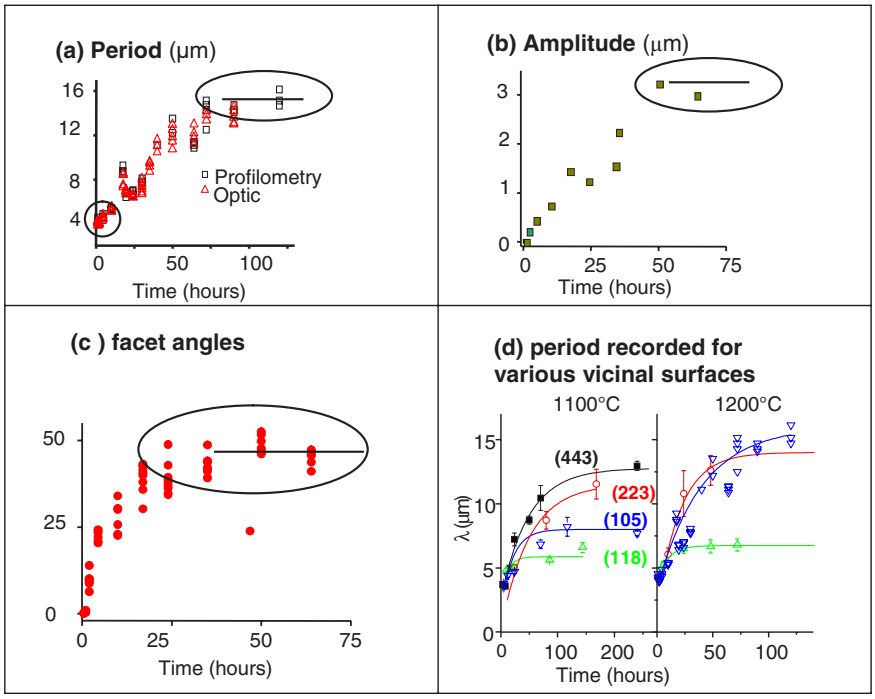

FIG. 6. (Color online) Summary of the experimental results obtained at 1250 °C. For the Si (105) surface the time evolution of the period (a), of the amplitude, (b) then of the angles formed by the facet (c) are reported. In Fig. 7(d) the results obtained for a set of vicinal surfaces at two different temperatures are synthesized. Sections IV A and IV B of the discussion will be devoted to the initial and final part of the curves surrounded in (a), (b), and (c).

the period [Fig. 6(a)], the amplitude [Fig. 6(b)], and the angle [Fig. 6(c)] of the facets. The angles are measured by AFM, mechanical microprofilometry, and optical microscopy. In Fig. 6(d), the results obtained for the various vicinals faces for two different temperatures are also reported. Notice that the initial wavelength [encircled in Fig. 6(a)] is roughly the same (≈ 4 μm) whatever the initial vicinality angle while the asymptotic value [surrounded by an ellipse in Fig. 6(a)] depends upon the vicinal angle. Moreover, three different regimes, with peculiar characteristics, are clearly observed.

(i) In the early stages, a surface instability develops exponentially with time (see also Fig. 4). The corresponding wavelength is roughly equal to $\lambda \approx 4$ μm. *In situ* optical diffraction measurements as well as TEM measurements clearly show that no smaller periodicity is observed at shorter times. This result highlights the fact that simple mechanisms based on step pairing, then double-step pairing, and so on (e.g., zipping mechanisms), as described in Refs. 8 and 37, are not appropriate to describe the underlying mechanism. Our opinion, reinforced by *ex situ* AFM images, is that the instability proceeds by a collective motion of the steps, giving birth to a step density wave. Curiously the value of the wavelength is roughly the same whatever the initial vicinal surface (see Fig. 7). In other words, at first order, this value does not depend upon the initial distance between the monoatomic steps on the initial vicinal surface. Some other authors have yet noticed that the initial wavelength roughly does not change with the vicinality angles.[19,20] In Fig. 7 we report our results (stars). We can thus define a domain (the upper dotted segment in Fig. 7) in which the wavelength roughly does not depend upon the vicinality. Some authors have also studied the wavelength change versus the vicinality, so that we can report in Fig. 7 two other domains where the wavelength seems to be constant whatever the initial interstep distance. These domains are also drawn as dotted segments in Fig. 7. The three dotted segments do not merge into a single dotted line because the experiments have not been performed at the same temperature while the wavelength depends on the sample temperature.[19–25] For completeness we also report some other values "gleaned" in the literature[21–25] but for which the experimental conditions (temperature, annealing duration, vicinal angle) are not well known. In any event, all these values belong to the range 1.5 μm$\leqslant\lambda\leqslant 5$ μm while the vicinality angle varies by two orders of magnitude. For completeness, notice that some authors have reported some weak angle dependence.[19,20,38]

(ii) At later stages, the kinetics of faceting becomes slow and a hill-and-valley structure forms. The bunches then start to form facets, the crystallographic orientation of which can

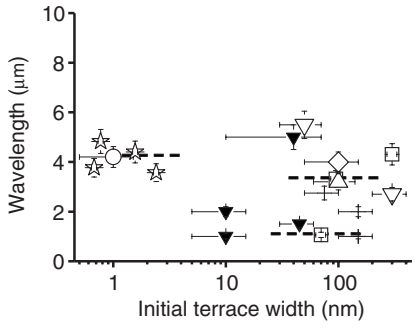

FIG. 7. Wavelengths that appear at the very beginning of the process. More precisely we report our results (stars) as well as the results obtained by other authors in other contexts. The dotted lines correspond to domains in which the wavelength does not change (see text for more details). White circle (Ref. 21), black down-triangles (Ref. 25), white squares (Refs. 19 and 20), diamonds (Ref. 60), white up-triangle (Ref. 23), white down-triangles (Ref. 22), and black cross (Ref. 24).

TABLE II. Decomposition of the vicinal faces in F_1 and F_2 facets for the stationary state. The interstep distance calculated in the (113) and (110) surfaces are estimated (from a projection of the interplane distance) to 2.88 Å and 4.46 Å, respectively.

Vicinal face	(118)	(223)	(443)	(510)
F_1 (flat at the atomic scale)	(001)	(111)	(111)	(100)
F_2 (exhibit monoatomic steps)	(113)	(113)	(110)	(110)

be easily obtained from angle measurements. It is found that the angle (α) of one of the microscale facets remains constant while the other (β) increases with time.

(iii) After a long time, a stationary state is reached. It is formed by the F_1 and F_2 facets the crystallographic indexes of which are reported in Table II for each initial vicinal face. The crystallographic nature of the facets shows that the bunches evolve towards the closest densely packed crystallographic planes surrounding the initial vicinal surface in the equilibrium crystal shape.[31] Notice that the F_2 facets are not flat at the atomic scale because it is easier to reach a stepped face than a flat one for which supplementary activation energy is needed for step coalescence. At the end of the first regime there is a unique wavelength but the step density still depends upon the initial vicinality. Notice further that annealing by an alternative current of the so-faceted structure restores the flatness of the nominal vicinal surface as it should for electromigration-induced faceting.

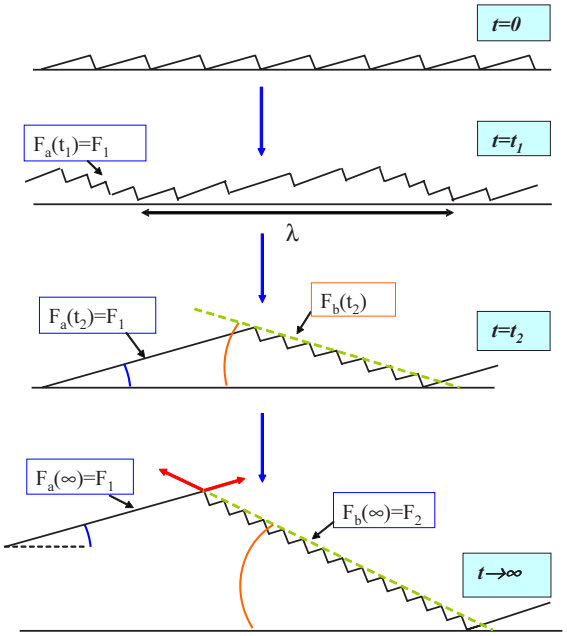

FIG. 8. (Color online) Sketch of the faceting mechanisms. At $t=0$ is the initial vicinal surface. At $t=t_1$, a step wave density forms by collective motion of the steps. At $t=t_2$ the step bunching mechanism starts so that the initial terrace (F_a) grows at constant angle (α) while a facet (F_b) forms with the angle $\beta(t_2)$. At the end of the process ($t=\infty$) there is a stationary state formed by the flat facet F_1 and the stepped facet F_2 characterized by their own surface stress tensors. The surface stress component perpendicular to the edge are $\vec{s}_1$ and $\vec{s}_2$.

IV. DISCUSSION

To sum up, all these experimental results are compatible with a quick-step density-wave mechanism followed by a much slower step-bunching mechanism as mentioned in a previous paper,[39] and as proposed in the case of nontransparent steps in Ref. 40. During step bunching, the angle β (defined in Fig. 8) of the microscale facet increases with time while the terraces of the initial vicinal surface remain flat (α is constant). The final state is a stationary state formed with the two closest facets in the equilibrium shape surrounding the initial vicinal face [see Fig. 1(a)] and thus is fixed by crystallography. A sketch of the mechanism of kinetic faceting (with t the time) is reported in Fig. 8.

In the following, we will focus on the final and initial stages of the process.

A. Analysis of the final state: Towards a Marchenko-Alerhand description

Let us consider the usual faceting transition: an unstable surface (thus with negative surface stiffness) decomposes into a periodic sequence of facets with orientations θ_1 and θ_2 having different surface stresses.[41] The instability originates in the decrease of the total surface energy from the planar to the faceted state. The slopes of the facets are given, but the period of the sequence is fixed by elasticity.[27,29] The surface stress discontinuities at the boundaries can be modeled by rows of monopoles perpendicular to the discontinuities.[27,29] The elastic relaxation induced by these forces diverges logarithmically[27,29] so that the elastic relaxation overcomes the energy of the domain boundaries. This results in the spontaneous formation of periodic facets with period L.[27,29] More precisely, the total energy change from the flat towards the faceted state classically reads[30]

$$\Delta E = \Delta E_{surf} + \Delta E_{bound} + \Delta W_{elast},$$

where ΔE_{surf} is the surface energy change (negative since the initial surface is unstable), ΔE_{bound} the boundary energy (positive), and ΔW_{elast} the elastic relaxation (negative).

Notice that while ΔE_{bound} and ΔW_{elast} depend upon L, this is not the case of ΔE_{surf} which only depends upon the crystallographic orientation of the facets. The equilibrium period fixed by the condition $\partial \Delta E / \partial L = 0$ thus does not depend on ΔE_{surf}.[30] Other mechanisms can also lead to a selection of an average distance between bunches.[42]

In the case under study, annealing the faceted structure without electromigration restores the nominal flat surface. In other words, in the absence of electromigration, the final state is unstable (ΔE_{surf} is positive). The faceting is thus no longer caused by the surface energy reduction but by a driving force due to the electrical field. Here we assume, as in Refs. 8, 11, and 43, that the selection of the period remains based on the elastic relaxation whatever the origin of the destabilization (thermodynamic or kinetics). It should mean

that the electromigration field role is equivalent to defining an effective surface energy change ΔE_{surf}^{eff} in the expression of ΔE. Furthermore, since the electric field does not depend upon L, ΔE_{surf}^{eff} does not play a role in the selection of the period.

Furthermore, in order to have a general picture—based on atomic steps—which applies at all times, we describe the final state as an elastic interaction between steps characterized by dipoles or monopoles rather than an interaction between microscale facets characterized by their own surface stress tensor.

The usual approach to calculate step-induced elastic field is (i) to describe the step in terms of localized forces distributions applied at the step edge, (ii) to model the action of these forces on the underlying crystal by point forces acting on a semi-infinite flat crystal, and (iii) to use the Green function to calculate the strain field and then the stored elastic energy.[44] The result is well known for the surface of a stress-free (stressed) body (for a review see Ref. 30) modeling the vicinal surface as a periodic array of 1D rows of elastic dipoles (monopoles) perpendicular to the step edge. In our case, the description of the elastic interactions between the steps is more complex for two reasons: (i) as shown in Sec. II the vicinal initial surfaces may be described by various configurations (alternated monopoles and/or dipoles), and (ii) in the final state these rows rearrange to form a hill-and-valley structure characterized by two lengths: the step-step distance in a bunch and the distance in between two neighboring bunches. Thus the elastic description of the final state depends on the type of monoatomic steps (which means upon the initial vicinal surface) and on the characteristic lengths. However, even if electromigration is known to induce kinetics instability, the elastic energy we calculate is that one of the final faceted structure consisting in large terraces separated by step bunches. This final state, reached for a maximum of the step density, is driven by energetic and not kinetics. Electromigration thus does not modify the interstep distance in a dense bunch.

To estimate the stored elastic energy modification arising from the faceting we will proceed in three steps: (i) calculation of the elastic interaction between two steps, (ii) calculation of the elastic energy of the faceted state, and (iii) calculation of the elastic energy difference between the initial vicinal face and the faceted final state. Finally, we will compare our results to the usual Alerhand-Marchenko microscale approach.[27,29] We will see that the comparison will give access to the surface stress change close to a high-index surface.

Notice that in the following, we will use isotropic linear elasticity. Indeed, while isotropic elasticity fails to reproduce the displacement field induced by the steps, it is now well known that isotropic elasticity can be used for determining the elastic energy with good accuracy.[45]

1. Elastic interaction between steps

As recalled in the Appendix, the elastic interaction energy per unit length between two parallel steps separated by a distance ℓ is well known (for a review see Ref. 30). For elastic dipoles perpendicular to the step edge it scales as ℓ^{-2}, while for elastic monopoles perpendicular to the step it scales as $\ln(\ell/a_0)$ where a_0 is a cutoff length of the order of a few atomic units. We show in the Appendix that the elastic energy between two rows of antiparallel elastic monopoles also scales as $\ln(\ell/a_0)$ but with a different prefactor.

2. Elastic energy of the faceted surface

The elastic energy in the faceted final configuration can be easily obtained by adequate summations of the elastic energy interactions between two parallel rows. For the sake of simplicity we will calculate separately the elastic energy due to the interaction of steps in a bunch (containing N steps) and the elastic interaction between the bunches (see Fig. 9 for the geometrical definitions). The first term will be called intrabunch energy, the second the interbunch energy. The analytical expressions of these energies are reported in Table III where for the sake of simplicity we separate the dipolar and the monopolar contributions. Thus in the following we consider the step-step interaction as described by the dipole-dipole interaction or monopole-monopole interaction but never consider the dipole-monopole interaction.

The exact expressions can be expressed as a summation of the elastic energy between two steps over the considered configuration (intra or interbunch). Approximated analytical expressions are obtained by (i) transforming the summation to an integral then by (ii) considering $N,M \gg 1$. In Table III the expressions for elastic dipoles [Table III(a)] and for elastic alternated monopoles [Table III(b)] are reported.

In Fig. 10, the elastic interactions calculated numerically by performing the exact summations but without any monopole-dipole interaction are plotted. They are in good agreement with the approximated analytical expressions calculated by integration so that in the following we will use the approximated expressions. The main results are that (i) the intrabunch contributions depend linearly on the number of steps in a bunch (for monopoles or dipoles), (ii) for monopoles the intrabunch elastic energy is smaller for N even than for N odd so that bunches prefer to be formed by an even number of steps, (iii) the interbunch analytical expressions are similar to the expressions given by Marchenko[27] and Alerhand *et al.*[29] who modeled a faceted surface as a periodic pattern (period L) of 1D rows of elastic monopoles perpendicular to the edges (see bottom of Fig. 9), and (iv) for bunches of monopoles the nature of the interaction (attraction or repulsion) depends upon the parity of N [see the $\mp$ sign in Table III(b)]. However, in the following we will only consider the stablest situation with even N [see point (ii)]. Point (iii) can be easily understood in the case of elastic dipoles perpendicular to the steps. Indeed, as in electrostatics, a ribbon of dipoles creates in the far field the same displacements as two rows of antiparallel monopoles located at the ribbon edges. For alternated monopoles it is quite similar since they behave as the ℓ-apart components of a dipole. The main difference with the Marchenko-Alerhand microscale approach is that in our expressions the prefactor of the $\ln\left[1-\left(\frac{N}{M}\right)^2\right]$ term is proportional to the amplitude of the dipole or monopole prefactor while in the Marchenko-Alerhand approach it is proportional to the difference between the surface stress of the adjacent facets.[27,29] We will

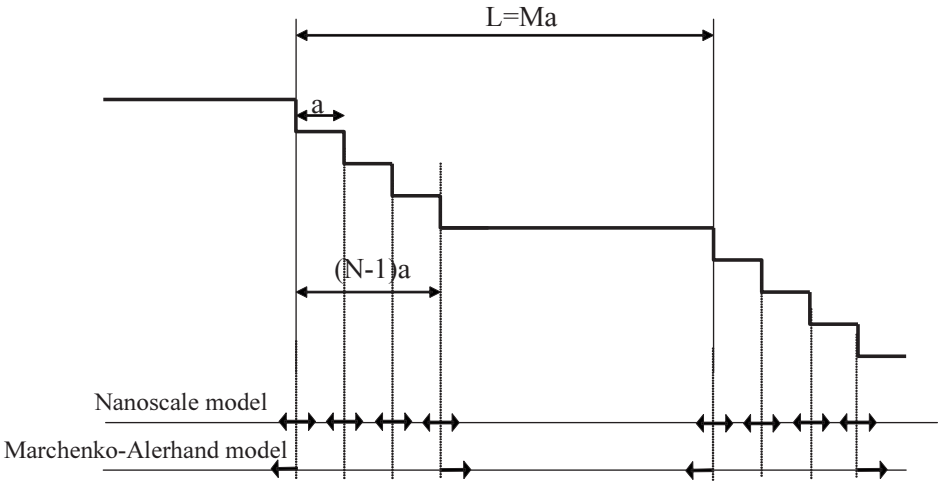

FIG. 9. Elastic model used for the calculations. The period $L=Ma$ consists in a flat terrace and a step bunch (interstep distance a) formed by $(N\text{-}1)$ steps. In the bottom part of the figure, the corresponding nanoscale and Marchenko-Alerhand models are reported. In the nanoscale model, steps (in the bunch) are modeled by rows of point forces (in the figure are only sketched the elastic dipoles perpendicular to the steps, at which could be added elastic monopoles according to the description of the vicinal faces under consideration as shown in Fig. 2). In the Marchenko-Alerhand model, the bunch itself is considered as a microscale facet modeled by rows of elastic monopoles located (and perpendicular) to the facet edges.

TABLE III. (a) Elastic energy W/L for dipoles. Moreover the expressions are given per unit step-length, thus the unity is an energy over surface area. (b) Elastic energy W/L for alternated monopoles. Notice that $A_{dip}=+\frac{1-\nu^2}{\pi E}A^2$ but $A_{monop}=\frac{(1+\nu)(1-2\nu)}{\pi E}F_y^2$ (see the Appendix). The $+$ and $-$ signs arise, respectively, for N even and N odd. Moreover, the expressions are given per unit step length; thus, the unity is an energy over surface area.

(a)	Intrabunch	Interaction between two bunches (interbunch)	Interaction energy for an infinite periodic surface
Exact expression	$\frac{A_{dip}}{a^2}\sum_{i<j,j}\frac{1}{(i-j)^2}$	$\frac{A_{dip}}{a^2}\sum_{i,j=1}^{N}\frac{1}{[M+(i-j)]^2}$	$\frac{A_{dip}}{a^2}\sum_{k}\sum_{i,j=1}^{N}\frac{1}{[kM+(i-j)]^2}$
Approximated expression	$\frac{A_{dip}}{a^2}\left[N\frac{\pi^2}{6}-1-\ln N\right]$	$-\frac{A_{dip}}{a^2}\ln\left[1-\left(\frac{N}{M}\right)^2\right]$	$-\frac{A_{dip}}{a^2}\ln\left[\frac{\sin\left(\frac{\pi N}{M}\right)}{\left(\frac{\pi N}{M}\right)}\right]$
(b)	Intrabunch	Between two bunches (interbunch)	For an infinite pattern of bunches
Exact expression	$\frac{A_{mon}}{a_0^2}\sum_{i<j,j=1}^{N}(-1)^{j-i}\ln\left((j-i)\frac{a}{a_0}\right)$	$\frac{A_{mon}}{a_0^2}\sum_{i,j=1}^{N}(-1)^{j-i}\ln\left((M+j-i)\frac{a}{a_0}\right)$	$\frac{A_{mon}}{4a_0^2}\sum_{k}\sum_{i,j=1}^{N}(-1)^{j-i}\ln\left[\left((kM+j-i)\frac{a}{a_0}\right)\right]$
Approximated expression	$\frac{A_{mon}}{4a_0^2}\left[2N\ln\left(\frac{\pi a_0}{2a}\right)-1\pm\ln N\right]$	$\pm\frac{A_{mon}}{4a_0^2}\ln\left[1-\left(\frac{N}{M}\right)^2\right]$	$\pm\frac{A_{mon}}{4a_0^2}\ln\left(\frac{\sin\left(\frac{\pi N}{M}\right)}{\left(\frac{\pi N}{M}\right)}\right)$

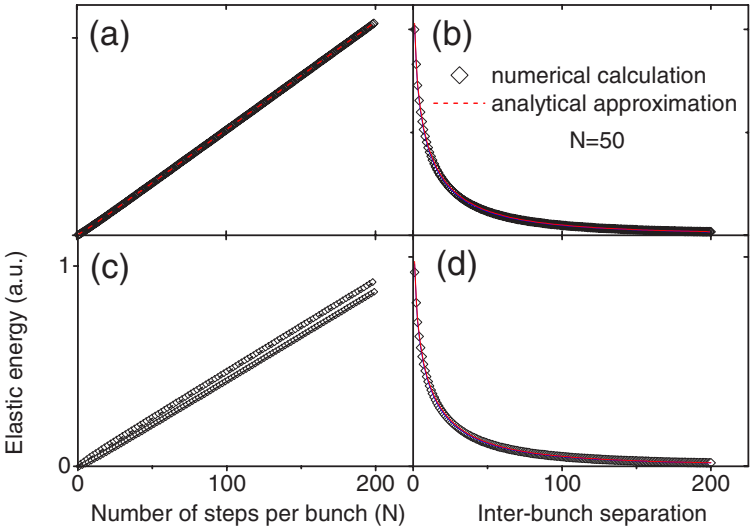

FIG. 10. (Color online) Graph of the elastic energies reported in Table III: (a) intrabunch term calculated for dipoles, (b) interbunch term calculated for dipoles, (c) intrabunch term calculated for monopoles (the upper curve is for N odd, the lower curve for N even), and (d) interbunch term calculated for monopoles with even N.

see in Sec. IV B that the comparison between the nanoscale and the microscale models enables us to propose an analytical expression of the surface stress angular dependence close to a high-index facet.

3. Elastic energy change due to faceting

Let us consider the energy change due to the faceting process that means the energy change due to the transformation from a vicinal surface towards a faceted system. This energy change per unit length reads

$$\frac{\Delta W}{L} = \Delta f(p) + \frac{\tau}{L} - \frac{\bar{A}}{L}\ln\left(\frac{L}{\pi a}\sin(\pi p)\right), \tag{1}$$

where $\bar{A}=A_{dip}/a^2$ and $\bar{A}=A_{monop}/4$ for dipoles or monopoles, respectively.

The first term in Eq. (1) is the elastic energy change due to the step coalescence. It can be written as a simple function $\Delta f(p)=f(p)-f(p_0)(1-p)+f(p_1)p$, where $p=N/M$ is the relative coverage of one phase with respect to the other (see Fig. 9) and p_0 and p_1, are the slopes of the facets F_1 and F_2. The exact analytical form of $f(p)$ depends upon the monopolar or dipolar nature of the step but this is not essential. More important is the fact that $f(p)$ does not depend on the period $L=Ma$. The term τ has been introduced to take into account the boundary energy between both domains. It does not appear naturally in the simple sketch given in Fig. 8 but should appear when considering that because of the symmetry breaking, the steps located at the edges of the bunch cannot have the same energy as the steps inside the bunch. Finally, the last term describes the interbunch elastic interaction. It does not depend upon the nature of the step interaction except the prefactor.

When considering that the surface occupation of each domain is, at least for the final state, fixed by crystallography (since the facets in the final state correspond to cusps of the γ plot[31]), the energy change per unit length is a simple function of L, so that its minimum value is reached for $\frac{\partial \Delta W/L}{\partial L}|_p=0$. The equilibrium period thus reads

$$\lambda = \frac{\pi a}{\sin(\pi p)}\exp\left(\frac{\tau}{\bar{A}}\right). \tag{2}$$

This expression can be compared to that obtained by Marchenko[27] and Alerhand *et al.*[29] They considered the final state as formed by microscale facets characterized by their own surface stress which components perpendicular to the facet edges are drawn in Fig. 8 at $t=t_\infty$:

$$\lambda = \frac{\pi a_0 e}{\sin(\pi p)}\exp\left(\frac{\pi E\tau}{2(1-\nu^2)|\vec{s}_1-\vec{s}_2|^2}\right). \tag{3}$$

The fit of the experimental results give the ratio τ/A for the vicinal surfaces under study (see Table IV where the value of a has been estimated from Table II).

Thus, within the experimental error bars, we find at $T=1150\ ^\circ\mathrm{C}$, $\langle\tau/\bar{A}\rangle\approx 6.5\pm 0.5$ whatever the initial surface. More precisely, for the (223) and (443) surfaces (for which the steps only bear elastic dipoles) one obtains, when using $A_{dip}\approx 10^{-30}$ J m (see Sec. IV A), $\tau\approx 8.6\times 10^{-11}$ J m^{-1} for the (223) surface and $\tau\approx 3.1\times 10^{-11}$ J m^{-1} for the (443) surface. For the (118) and (510) surfaces the steps bear elastic dipoles and monopoles (see Table I) so that we cannot simply extract τ from Table IV. Indeed as reported at the beginning of Sec. IV A 2 the dipolar and monopolar contributions do not simply add so $\bar{A}$ is an unknown composition of A_{dip} and A_{mon}. However, if the amplitude of the monopoles can be neglected with respect to the amplitude of the dipole, we get

TABLE IV. Experimental values of the period, the relative occupation, and the so-deduced ratio $\tau/\bar{A}$ values for $T=1150\ ^\circ\mathrm{C}$.

	λ (Å)	$p=\tan\theta_1/(\tan\theta_1+\tan\theta_2)$	$\tau/\bar{A}$
(118)	6.6×10^3	0.39	6.50
(223)	12×10^3	0.38	7.10
(443)	13×10^3	0.19	6.25
(510)	8×10^3	0.23	5.93

$\tau \approx 7.9 \times 10^{-11}$ J m^{-1} for the (118) surface and $\tau \approx 3.0 \times 10^{-11}$ J m^{-1} for the (510) surface. On the contrary if we only consider the monopolar contribution, with $A_{monop}/a_0^2 \approx 3 \times 10^{-12}$ J m^{-1} (see Sec. III A), there is $\tau \approx 2 \times 10^{-11}$ J m^{-1} whatever the vicinal surface under consideration. Notice that in both cases (monopoles or dipoles) (i) the order of magnitude of τ is comparable to the step energy reported for the Si(111) surface (3×10^{-11} J m^{-1}) (Ref. 46) and that (ii) when considering only the dipolar contribution we obtain two set of values, one around $\tau \approx 8 \times 10^{-11}$ J m^{-1} when the facet edges separate a (001) or (111) from a (113) facet, the other around $\tau \approx 3.0 \times 10^{-11}$ J m^{-1} when the facet edges separate a (001) or (111) from a (110) facet (see Table II).

4. Link between the nanoscale and the microscale model: The surface stress angular dependence

The nanoscale and microscale models are equivalent if the cutoff length a_0 of the microscale model (Marchenko, Alerhand) depends upon the initial interstep distance a (more precisely $a_0 e = a$) and if from Eqs. (2) and (3) we can write the equality

$$\bar{A} = 2\frac{1-\nu^2}{\pi E}(\vec{s}_1 - \vec{s}_2)^2, \tag{4}$$

with again $\bar{A} = A_{dip}/a^2$ and $\bar{A} = A_{monop}/4$ for dipoles and monopoles, respectively.

For dipoles, introducing the step height h (so that $a = h/\tan\theta$ where θ is the angle of the vicinal facet) and using $A_{dip} = 2\frac{1-\nu^2}{\pi E}A^2$ [compare Eqs. (A2) and (A3) in the Appendix], Eq. (4) reads

$$\frac{A^2}{h^2}\tan^2\theta = s_1^2 + s_2^2 - 2s_1 s_2 \cos\theta. \tag{5}$$

However, in the Appendix we show that [see Eq. (A2)]

$$A^2 = A_1^2 + (hs_1)^2, \tag{6}$$

where $s_1 = s_{xx}$ is the surface stress component perpendicular to the step.

For weak values of θ one obtains from comparison of the two previous relations

$$s_2 = s_1 - \frac{|\theta|}{h}A_1. \tag{7}$$

This expression is analogous to the one found by Salanon and Hecquet for stressed solids[47] where the steps are described by the sum of rows of dipoles and monopoles (both perpendicular to the step) and the surface stress expression is developed up to second order in θ.

Equation (7) means that since the presence of steps leads to surface stress relaxation, the surface stress is maximum for a low-index surface and thus decreases with $|\theta|$. On the contrary, the energy cost to create surface steps implies that the surface energy increases with $|\theta|$. In other words, local minima (cusps) of the surface energy plot (γ plot) correspond to local maxima (anticusps) of the surface stress plots.[30,39,47]

Beyond this approach it is also possible to use our experimental results to obtain absolute values of surface stress. Indeed, using the microscale model of Marchenko[27] and Alerhand *et al.*[29], the measurement of the final period gives the difference $(s_1 - s_2)$ between the surface stress components (normal to the step) of the facets F_1 and F_2. Using a set of vicinal surfaces (labeled k) chosen to form a closed cycle on the stereographic projection, we measure $\lambda^k(s_1^k, s_2^k)$ and thus obtain a set of values $s_1^k - s_2^k$ corresponding to the surface stress differences between the facets F_1 and F_2 that appear on the vicinal faces k. Since we are working on a closed cycle, the measurement of the periods λ^k is enough to obtain the absolute values s_1^k and s_2^k. The method has been extended to all intermediate faceted stages obtained after a time t smaller than the duration needed to reach the final state. In this case it is necessary to measure the period $\lambda^k(s_1^k, s_2^k)$ as well as the angles α_t^k, β_t^k formed by the facets obtained at t and then to solve the systems of equations $\lambda_t^k(s_{1,t}^k, s_{2,t}^k, \alpha_t^k, \beta_t^k)$ to obtain the values $s_{i,t}^k$ of the facets α and β appearing at time t and characterized by the angles α_t^k and β_t^k. Many numerical solutions exist but only one set of s_i^k values verifies the fact that all the facets that belong to the equilibrium shape exhibit a maximum of surface stress. This procedure has been used to obtain, for the first time, the complete surface-stress plot of Si.[39]

B. Analysis of the initial-step density waves: Towards a unique wavelength $\lambda \approx 4$ μm

In this section, we discuss the origin of the robustness of the wavelength of the initial step density waves with respect to the vicinality of the original surface. Most of the previous models concerning the step bunching instability are based on the Stoyanov approach of the step bunching instability induced by the electromigration.[16] More precisely, different regimes have been studied to calculate the most unstable mode in the linear regime. For slow attachment kinetics the main period of the instability depends upon the transparency parameters at the steps and reads $\lambda = 2\pi a_0^{-1}(6A\xi)^{1/2}\left(\frac{a_0}{l}\right)$ for opaque or moderately transparent steps[18] and $\lambda = 2\pi a_0^{-1}(6A\xi)^{1/2}\left(\frac{a_0}{Q^{1/2}}\right)$ for very transparent steps.[40] In both expressions a_0 is an atomic distance unit, A an elastic quantity describing the dipolar forces at the steps, ξ the reduced electromigration force, and Q a characteristic length varying from a tenth of an atomic distance up to some atomic distances.[40] Both expressions can be put in the generic form of a characteristic lengthscale $\lambda = 2\pi a_0^{-1}(6A\xi)^{1/2}$ times a "geometric factor," which is a dimensionless combination of atomic scales. Indeed, the interstep distance ℓ is of the order of some atomic distances in the experiments presented above. We show here that this generic form can be derived within the frame of a continuous model, which does not refer to microscale details.

For this purpose, we consider a model in which the initial surface is rough since the vicinal surfaces under study have high slopes. We write a continuum model based on macroscopic quantities having smooth orientation dependence. We use a 1D model, along the variable x, and we neglect sublimation or growth.

From the mass conservation equation,

$$\frac{\partial h}{\partial t} = -\frac{\partial j}{\partial x}, \tag{8}$$

with h the local height and j the surface flux.

We then consider the diffusion process driven by the variations of the chemical potential μ and the electromigration force:

$$j = \frac{M}{kT} c \left(f - \frac{\partial \mu}{\partial x} \right), \tag{9}$$

where M, f, and c are, respectively, the orientation-dependent mobility, migration force, and concentration of adatoms at the surface.

We write the free energy of the surface as

$$F = \int \varphi(p) dx = \int \left(\gamma_0 + \gamma_1 \left| \frac{\partial h}{\partial x} \right| + \gamma_3 \left| \frac{\partial h}{\partial x} \right| \right) dx, \tag{10}$$

where γ_0 and γ_1 are constants and γ_3 is a function of the local slope $p = \partial h / \partial x$. More precisely, for the usual vicinal surfaces described as a 1D array of elastic dipoles γ_0 is the terrace energy, γ_1 is the step energy, and $\gamma_3 = \beta_3 (\partial h / \partial x)^2$ depends upon the step-step interaction energy β_3 and is proportional to the square of the local slope so that $\varphi(p)$ reads $\varphi(p) = \gamma_0 + \gamma_1 |p| + \beta_3 |p|^3$. In the following, we consider γ_3 as a simple unknown function of the local slope $p = \partial h / \partial x$ to take into account different types of vicinal surfaces.

The chemical potential is defined as

$$\mu = \frac{\delta F}{\delta h} \left(\frac{\delta N}{\delta h} \right)^{-1}, \tag{11}$$

where $N = \int h / a_0^2 dx$ is the number of atoms of the solid.

A variational calculation then leads to the usual Herring expression[48] of the surface energy variation:

$$\delta F = -\int \frac{\partial}{\partial x} \frac{\partial \varphi}{\partial p} \delta h, \tag{12}$$

so that for a positive slope one obtains

$$\mu = -a_0^2 \tilde{\gamma}_3 \left(\frac{\partial h}{\partial x} \right) \left(\frac{\partial^2 h}{\partial x^2} \right), \tag{13}$$

with $\tilde{\gamma}_3 = 2 \frac{\partial \gamma_3}{\partial p} + \frac{\partial^2 \gamma_3}{\partial p^2} p$.

Putting Eq. (13) into Eqs. (8) and (9), we obtain the time evolution equation of the surface height as

$$\frac{\partial h}{\partial t} = -\frac{\partial}{\partial x} \left\{ \frac{Mc}{kT} \left[f + \frac{\partial}{\partial x} \left(\tilde{\gamma}_3 a_0^2 \frac{\partial^2 h}{\partial x^2} \right) \right] \right\}. \tag{14}$$

For small height perturbations around the mean orientation of the vicinal surface of average slope $\bar{p}$, we have $h = \bar{p} x + \delta h$ which leads to

$$\partial_t h = -\partial_p \left[\frac{Mcf}{kT} \right]_{p=\bar{p}} \partial_{xx} \delta h - a_0^2 \left[\tilde{\gamma}_3 \frac{Mc}{kT} \right]_{p=\bar{p}} \partial_{xxxx} \delta h, \tag{15}$$

where the partial derivatives are denoted $\partial h / \partial i = \partial_i h$.

TABLE V. Expressions $\tilde{\gamma}_3$ and λ obtained for dipoles and monopoles. The interaction energies used for the calculations are given by Eqs. (A4) in the Appendix.

	$\tilde{\gamma}_3$	λ
Dipoles	$A_{dip} \pi^2 p / a_0^2$	$2\pi^2 \sqrt{\frac{2A_{dip}}{f_0}} \left[\frac{\bar{p} g_M(\bar{p})}{\partial_p (g_M g_f)\|_{p=\bar{p}}} \right]^{1/2}$
Monopoles	$A_{monop} / p a_0^2$	$2\pi \sqrt{\frac{2A_{monop}}{f_0}} \left[\frac{g_M(\bar{p})}{\bar{p} \partial_p (g_M g_f)\|_{p=\bar{p}}} \right]^{1/2}$

Considering in Eq. (15) a wavelike perturbation of the height $\delta h = \exp(i\omega t + ikx)$ leads to the following equation:

$$i\omega = \partial_p \left[\frac{Mcf}{kT} \right]_{p=\bar{p}} k^2 - a_0^2 \left[\frac{\tilde{\gamma}_3 Mc}{kT} \right]_{p=\bar{p}} k^4. \tag{16}$$

A criterion for the bunching instability to occur is that the prefactor of the term in k^2 should be positive. The maximum growth rate is reached for:

$$\lambda = 2\pi \sqrt{\left(\frac{2\tilde{\gamma}_3 a_0^2 [Mc]_{p=\bar{p}}}{\partial_p [Mcf]_{p=\bar{p}}} \right)}. \tag{17}$$

Let us now separate the amplitude from the angle dependence of M, c, and f. For this purpose we define

$$M = M_0 g_M(\rho), \quad c = c_0 g_c(p), \quad f = f_0 g_f(p), \tag{18}$$

where $g_i(p)$ are dimensionless functions of the order of 1.

The wavelength then reads

$$\lambda = 2\pi \sqrt{\frac{2\tilde{\gamma}_3 a_0^2}{f_0}} \sqrt{\frac{g_c g_M}{\partial_p (g_M g_c g_f)|_{p=\bar{p}}}}, \tag{19}$$

where we omit, for the sake of simplicity, the p dependence by writing $g_i(\bar{p}) = g_i$.

An inspection of Eq. (19) shows that the wavelength does not depend on the amplitude M_0 of the mobility or on the amplitude of the mobile concentration c_0.

It is important to note that since the vicinal surfaces at high slopes are far from singular facets, the orientation dependences $g_i(p)$ do not exhibit any singularities, so that the last term of the previous relation must have a weak slope dependence.

Let us discuss more precisely the different terms of Eq. (19). In the absence of growth or sublimation, the mobile adatom concentration should be at equilibrium, $c_0 = c_{eq}$, so that $g_c(p) = 1$. In this case there are two possible expressions of the wavelength according to the p dependence of γ_3 which means according to the monopolar or dipolar nature of the steps. The results are summarized in Table V.

Let us calculate the order of magnitude of the wavelength λ.

(i) For the dipolar case the value of the dipolar moment of Si is known to be roughly $A_{dip} \pi^2 / 6 \approx 10^{-30}$ J m.[49,50] Using the electromigration force expression $f_0 = zeE_m$ where z is the

effective charge $(0.01<z<0.1)$,[51,52] and e is the electronic charge and $E_m=400$ V m^{-1}, there is $8\mu<2\pi^2\sqrt{\frac{2A_{dip}}{f_0}}<20\mu$. This result is slightly larger than our experimental value $\lambda \approx 4$ μm so that there should be $\left[\frac{\bar{p}g_M(\bar{p})}{\partial_p(g_M g f)|_{p=\bar{p}}}\right]^{1/2}<1$.

(ii) For the monopolar case A_{monop} can be roughly estimated from the surface stress of the Si(001) surface. Since $s_1+s_2\approx 1$ N m^{-1},[29,53] and using formula (A2) of the Appendix one obtains $A_{monop}/a_0^2\approx 3\times 10^{-12}$ J m^{-1} so that $3\mu<2\pi\sqrt{\frac{2A_{monop}}{f_0}}<11\mu$.

The fact that the wavelengths are comparable for monopoles and dipoles can be easily understood, since in elasticity the only dimensional constant is the Young's modulus E and the only specific length scale is the atomic distance a_0. As A_{dip} and A_{monop} scale as Ea_0^4,[54] it is thus possible, from Eq.(12), to write for monopoles and for dipoles,

$$\lambda = 2\pi\sqrt{2}a_0^2\left(\frac{E}{f_0}\right)^{1/2}\left[\frac{\tilde{g}_3 g_c g_M|_{p=\bar{p}}}{\partial_p(g_M g_c g_f)|_{p=\bar{p}}}\right]^{1/2}, \qquad (20)$$

where we have defined $\tilde{\gamma}_3(p)=a_0^2 E\tilde{g}_3(p)$. Therefore, the order of magnitude of the wavelength has to be the same for dipoles or monopoles. Nevertheless, because of rough approximations, the orders of magnitude of the A_{dip} and A_{monop} values appear to be larger here than the experimental ones. Our experimental results are consistent with the fact that the brackets in Eq. (20) must be a very weak function of the slope, at least for the vicinal faces under study characterized by high vicinality angles.

V. CONCLUSION

The main characteristics of the faceting mechanism, in the transparency regime, of vicinal surfaces characterized by a high density of steps are the following.

(i) In the early stages, the instability takes the form of a step density wave, with a fixed wavelength and amplitude that increases exponentially with time. The corresponding wavelength is roughly equal to $\lambda\approx 4$ μm. Considering a continuum model based on macroscopic quantities having a weak orientation dependence, we have shown that the order of magnitude of the wavelength does not depend upon the details of the surface at the atomic level, such as step transparency and kinetic properties, elastic description of the initial vicinal surfaces (dipoles or monopoles), or the vicinality angle (at least to leading order).

(ii) At later stages, the kinetics of faceting becomes slow and a hill-and-valley structure forms by a process in which the terrace orientation is conserved but the facet orientation increases with time. We have not studied in detail the kinetics of the mechanism, which will be reported in a forthcoming paper.

(iii) Asymptotically, a stationary state is reached. The stationary facets are the closest densely packed crystallographic planes surrounding the initial vicinal surface in the equilibrium crystal shape. Because of the activation energy needed for step coalescence, the facets (F_2) are not flat at the atomic scale, while the terraces (F_1) remain flat at the atomic scale. For both situations (dipoles or monopoles), the final state was described in terms of energetic competitions between elastic relaxation and the cost needed to create the facet edges, as described by Marchenko[27] and then Alerhand *et al.*[29] by directly using a microscale model. The comparison between the analytical expressions issued from the two approaches: step models and the microscale approaches, gives access to the angular dependence of the surface stress. This can be used to study the surface stress anisotropy as first reported in Ref. 39.

Last but not least, our results show that it is possible to tune the period of the faceting in the micrometric range. The goal now is to be able to tune the faceting at the nanoscale. It could be possible by using growth instability[55] or externally applied stress.[56]

ACKNOWLEDGMENTS

This work has been supported by an ANR PNANO grant: Nano-morphogénèse. The authors would like to thank A. Kalifa for his help in using microprofilometry, F. Pailherey for his technical help, and B. Croset, A. Saùl, and R. Kern for helpful discussions.

APPENDIX: ELASTIC INTERACTION BETWEEN STEPS

The elastic energy stored in an elastic body is simply half the work done by the surface force distribution $\vec{P}(\vec{x})$ [characterized by its components $P_\alpha(\vec{x})$] against the surface displacement. It can be written (for a review see Ref. 30)

$$W=\frac{1}{2}\sum_{\alpha,\beta}\int\int P_\alpha(\vec{x})D_{\alpha\beta}(\vec{x},\vec{x}')P_\beta(\vec{x}')d^3x\,d^3x', \qquad (A1)$$

where $D_{\alpha\beta}(\vec{x},\vec{x}')$ (with $\alpha,\beta=x,y$) is the Green tensor that means the displacement field $\vec{u}(\vec{x})$ associated with a point force of amplitude unity located at $\vec{x}'$.[44]

For two (parallel or antiparallel) monopoles located in $(x_1,y_1,0)$ and $(x_2,y_2,0)$ the force distribution reads[30]

$$P_\alpha(\vec{x})=F_\alpha[\delta(x-x_1)\delta(x-y_1)\pm\delta(x-x_2)\delta(x-y_2)]\delta(z)$$

with the sign + for parallel monopoles and − for antiparallel monopoles [$\delta(x)$ is the Dirac "function"] where F_α has the dimension of a force $(\alpha=1,2,3)$.

For two (parallel or antiparallel) dipoles perpendicular to the y direction (parallel to the step), the force distribution reads[30]

$$P_\alpha(\vec{x})=A_\alpha\left[\left.\frac{\partial\delta(x)}{\partial x}\right|_{x-x_1}\delta(x-y_1)\pm\left.\frac{\partial\delta(x)}{\partial x}\right|_{x-x_2}\delta(x-y_2)\right]\delta(z)$$

where A_α has the dimensions of a mechanical torque. Here again, the sign + is for parallel dipoles and − for antiparallel dipoles. For a step dividing the surface in two equivalent terraces, the surface stresses s_{11} of the two neighboring terraces exert a mechanical torque per unit length of moment $s_{11}h\hat{y}$ (h being the step height) which has to be equilibrated by the torque of the force dipolar distribution so that[57,58,30] $A_3=s_{11}h$. On the contrary, the A_1 component can only be calculated by means of interatomic potentials (see, for example Ref. 59).

Let us now consider two ℓ-apart steps parallel to the $\vec{y}$ direction bearing identical dipoles parallel to the $\vec{x}$ direction or antiparallel monopoles in the $\vec{y}$ direction. Using the properties of the Dirac "function" there is for the monopoles

$$W_{monop} = F_y^2 \int_{-\infty}^{\infty} \int_{-\infty}^{\infty} [D_{yy}(0, y-y') - D_{yy}(\ell, y-y')] dy dy'$$

and for the dipoles

$$W_{dip} = A^2 \int_{-\infty}^{\infty} \int_{-\infty}^{\infty} \left[\left. \frac{\partial D_{x,x}}{\partial x} \right|_{0,y-y'} + \left. \frac{\partial D_{xx}}{\partial x} \right|_{\ell,y-y'} \right] dy dy',$$

where

$$D_{ii} = \frac{1-\nu^2}{\pi E} \left[\frac{1}{r} - \frac{\nu (i-i')^2}{(1-\nu)\, r^3} \right]$$

with $r = \sqrt{(x-x')^2 + (y-y')^2}$ for $i = x, y$ and now $A^2 = A_1^2 + A_3^2$.

Performing thus the integral there is, when defining the density of elastic energy of interaction per unit length of the step $w = \lim_{L \to \infty} \frac{W}{L}$,

$$w_{dip} = +2 \frac{1-\nu^2}{\pi E} A^2 \frac{1}{\ell^2} \quad \text{with } A^2 = A_1^2 + (s_{11} h)^2, \quad \text{(A2)}$$

$$w_{monop} = -2 \frac{(1+\nu)(1-2\nu)}{\pi E} F_y^2 \ln\left(\frac{\ell}{a_0} \right),$$

where the quantity a_0 is an atomic unit introduced as a cutoff in order to avoid local divergences in the calculation of the integrals. In both cases the rows repulse each other. Notice that w_{monop} diverges while w_{dip} converges.

Let us note that when performing the same summation for parallel monopoles in the $\vec{x}$ direction one recovers the well-known result $w_{monop} = +2 \frac{1-\nu^2}{\pi E} F_x^2 \ln\left(\frac{\ell}{a_0}\right)$.

In the following, Eq. (A2) will be written

$$w_{dip} = \frac{A_{dip}}{\ell^2}, \quad w_{monop} = -\frac{A_{monop}}{a_0^2} \ln\left(\frac{\ell}{a_0} \right). \quad \text{(A3)}$$

Notice that with these notations, A_{dip} and A_{monop} have the same units: energy times length.

The previous results (A3) can now easily be extended to the case of an infinite array of parallel rows. For this purpose it is enough to use the superposition principle and thus to do the corresponding summations. For vicinal surfaces formed by a periodic pattern of parallel rows, the results simply reads

$$w_{dip}^{vic} = \frac{\pi^2}{6} \frac{A_{dip}}{\ell^2}, \quad w_{monop}^{vic} = -\frac{A_{monop}}{2a_0^2} \ln\left(\frac{2\ell}{\pi a_0} \right). \quad \text{(A4)}$$

For faceted surfaces formed by step bunches separated by flat terraces the summations are less easy to perform. They are given in Table III where the approximated expressions obtained by substituting integrals to sums are also given. The exact and approximated expressions are compared in Fig. 10.

*Also at Université Paul Cézanne-Aix Marseille III.

[1] M. Sato, M. Uwaha, and Y. Saito, Phys. Rev. B **62**, 8452 (2000).
[2] J. Krug and H. T. Dobbs, Phys. Rev. Lett. **73**, 1947 (1994).
[3] D.-J. Liu and J. D. Weeks, Phys. Rev. B **57**, 14891 (1998).
[4] K. Sudoh and H. Iwasaki, Phys. Rev. Lett. **87**, 216103 (2001).
[5] S. Stoyanov and V. Tonchev, Phys. Rev. B **58**, 1590 (1998).
[6] O. Pierre-Louis, Phys. Rev. Lett. **87**, 106104 (2001).
[7] S. Filimonov and Y. Hervieu, Surf. Sci. **553**, 133 (2004).
[8] S. Song, M. Yoon, S. Mochrie, G. Stephenson, and S. Milner, Surf. Sci. **372**, 37 (1997).
[9] K. Kuhnke and K. Kern, J. Phys.: Condens. Matter **15**, S3311 (2003).
[10] Y. Yang, E. Fu, and E. Williams, Surf. Sci. **356**, 101 (1996).
[11] S. Song, M. Yoon, and S. Mochrie, Surf. Sci. **334**, 153 (1995).
[12] D. Kandel and E. Kaxiras, Phys. Rev. Lett. **76**, 1114 (1996).
[13] A. Latyshev, L. Litvin, and A. Aseev, Appl. Surf. Sci. **130-132**, 139 (1998).
[14] S. Stoyanov, Surf. Sci. **370**, 153 (1997).
[15] S. Stoyanov, Surf. Sci. **416**, 200 (1998).
[16] S. Stoyanov, Jpn. J. Appl. Phys., Part 2 **29**, L659 (1990).
[17] H. Minoda, Phys. Rev. B **64**, 233305 (2001).
[18] O. Pierre-Louis, Surf. Sci. **529**, 114 (2003).
[19] B. Gibbons, S. Schaepe, and J. Pelz, Surf. Sci. **600**, 2417 (2006).
[20] B. Gibbons, J. Naffsinger, and J. Pelz, Surf. Sci. **575**, L51 (2005).
[21] K. Yagi, H. Minoda, and M. Degawa, Surf. Sci. Rep. **43**, 45 (2001).
[22] J.-F. Nielsen, M. S. Pettersen, and J. P. Pelz, Surf. Sci. **480**, 84 (2001).
[23] A. V. Latyshev, L. V. Litvin, and A. L. Aseev, Appl. Surf. Sci. **130**, 139 (1998).
[24] Y.-N. Yang, Elain S. Fu, and Ellen D. Williams, Surf. Sci. **356**, 101 (1996).
[25] Y. Homma and N. Aizawa, Phys. Rev. B **62**, 8323 (2000).
[26] W. Burton, N. Cabrera, and F. Frank, Philos. Trans. R. Soc. London, Ser. B **243**, 299 (1951).
[27] V. I. Marchenko, Sov. Phys. JETP **54**, 605 (1981).
[28] V. I. Marchenko, JETP Lett. **33**, 381 (1981).
[29] O. L. Alerhand, D. Vanderbilt, R. D. Meade, and J. D. Joannopoulos, Phys. Rev. Lett. **61**, 1973 (1988).
[30] P. Müller and A. Saùl, Surf. Sci. Rep. **54**, 157 (2004).
[31] J. M. Bermond, J. J. Métois, X. Egea, and F. Floret, Surf. Sci. **330**, 48 (1995).
[32] M. Lagally, Y. W. Mo, R. Kariotis, B. Scwartzentruber, and M. B. Webb, in *Kinetic Ordering and Growth at Surfaces*, edited by M. G. Lagally (Plenum Press, New York, 1990).
[33] H. J. Zandvliet, Rev. Mod. Phys. **72**, 593 (2000).
[34] R. Kaplan, Surf. Sci. **93**, 145 (1980); P. E. Wierenga, J. A. Kubby, and J. E. Griffith, Phys. Rev. Lett. **59**, 2169 (1987); C. E. Aumann, D. E. Savage, R. Kariotis, and M. G. Lagally, J. Vac. Sci. Technol. A **6**, 1963 (1988).
[35] J. J. Métois and Y. Stoyanov, Surf. Sci. **440**, 419 (1999).
[36] P. Müller and J. J. Métois, Surf. Sci. **599**, 187 (2005).

[37] M. Uwaha and M. Sato, J. Phys. Soc. Jpn. **67**, 3675 (1998).
[38] F. K. Men, F. Liu, P. J. Wang, C. H. Chen, D. L. Cheng, J. L. Lin, and F. J. Himpsel, Phys. Rev. Lett. **88**, 096105 (2002).
[39] J. J. Métois, A. Saùl, and P. Müller, Nat. Mater. **4**, 238 (2005).
[40] O. Pierre-Louis, Phys. Rev. Lett. **96**, 135901 (2006).
[41] C. Herring, Phys. Rev. **82**, 87 (1951).
[42] M. Sato and M. Uwaha, Surf. Sci. **442**, 318 (1999).
[43] M. Yoon, S. Mochrie, M. Tate, S. Gruner, and E. Eikenberry, Surf. Sci. **411**, 70 (1998).
[44] A. Maradudin and R. Wallis, Surf. Sci. **91**, 423 (1980).
[45] G. Prévot, B. Croset, Y. Girard, A. Coati, Y. Garreau, M. Hohage, L. D. Sun, and P. Zeppenfeld, Surf. Sci. **549**, 52 (2004).
[46] J. J. Métois and P. Müller, Surf. Sci. **548**, 13 (2004).
[47] B. Salanon and P. Hecquet, Surf. Sci. **412/413**, 639 (1998).
[48] C. Herring, *The Physics of Powder Metallic* (McGraw-Hill, New York, 1951), Chap. 8, pp. 143–179.
[49] J. M. Bermond, J. J. Métois, J. C. Heyraud, and C. Alfonso, Surf. Sci. **331-333**, 855 (1995).
[50] H. C. Jeong and E. D. Williams, Surf. Sci. Rep. **34**, 171 (1999).
[51] E. D. Williams, E. Fu, Y. N. Yang, D. Kandel, and J. Weeks, Surf. Sci. Lett. **326**, L746 (1996).
[52] J. J. Métois and M. Audiffren, Int. J. Mod. Phys. B **11**, 3691 (1997).
[53] D. Sander and H. Ibach, in *Physics of Covered Surfaces*, edited by H. Bonzel, Landölt-Bornstein, New Series, Vol. III (Plenum, New York, 2002), p. 42.
[54] O. Pierre-Louis and C. Misbah, Phys. Rev. B **58**, 2259 (1998).
[55] A. Pascale, I. Berbezier, A. Ronda, A. Videcoq, and A. Pimpinelli, Appl. Phys. Lett. **89**, 104108 (2006).
[56] V. A. Shchukin, A. I. Borovkov, N. N. Ledentsov, and D. Bimberg, Phys. Rev. B **51**, 10104 (1995).
[57] V. Marchenko and A. Parshin, Sov. Phys. JETP **52**, 129 (1980).
[58] A. Andreev and Y. Kosevitch, Sov. Phys. JETP **54**, 761 (1981).
[59] R. Kern and M. Krohn, Phys. Status Solidi A **116**, 23 (1989).
[60] T. Yoshinobu, S. Matsukawa, K. Sudoh, and H. Iwasaki, Jpn. J. Appl. Phys., Part 2 **39**, L380 (2000).

[7] : Transition de méandrage et de mise en paquet de marches atomiques
Leroy *et al.*, Surf. Sci. (2009)

Surface Science 603 (2009) 507–512

Contents lists available at ScienceDirect

Surface Science

journal homepage: www.elsevier.com/locate/susc

Step bunching to step-meandering transition induced by electromigration on Si(1 1 1) vicinal surface

F. Leroy [a,*], D. Karashanova [a,b], M. Dufay [c,d], J.-M. Debierre [c], T. Frisch [c], J.-J. Métois [a], P. Müller [a]

[a] Centre Interdisciplinaire de Nanoscience de Marseille, CNRS - UPR 3118, Aix-Marseille Université Campus de Luminy Case 913, 13288 Marseille Cedex 09, France
[b] Central Laboratory of Photoprocesses "Acad. J.Malinowski" Bulgarian Academy of Sciences, Sofia 113, Bulgaria, Acad. G.Bonchev str., B1.109, Bulgaria
[c] Institut Matériaux Microélectronique Nanosciences de Provence, Aix-Marseille Université, Faculté des Sciences et Techniques de Saint-Jérôme, Case 151, 13397 Marseille Cedex 20, France
[d] CNRS/The Rudolf Peierls Centre for Theoretical Physics, 1 Keble Road, Oxford OX1 3NP, United Kingdom

ARTICLE INFO

Article history:
Received 8 October 2008
Accepted for publication 12 December 2008
Available online 25 December 2008

Keywords:
Vicinal single crystal surfaces
Surface diffusion
Step formation and bunching
Silicon

ABSTRACT

The step configuration of a vicinal Si surface is studied under electromigration and a gradient of temperature. An abrupt transition ($\Delta T = 4$ °C) from step-meandering to step bunching is found at 1225 °C for a step-down direct-current direction. This transition starts by random fluctuations which then extend on the whole surface. The transition is studied in the framework of a linear stability analysis of the usual Burton–Cabrera–Frank model by comparing the amplification factors of step-meandering and step bunching instabilities. Both compete at a given temperature, but since the amplification factors behave differently with temperature, bunching abruptly supersedes meandering above a critical temperature.

1. Introduction

Among the different kinetic instabilities occurring at vicinal Si surfaces [1–9], Latyshev and co-workers [1,2] have been the first to report that heating Si(1 1 1) vicinal surfaces by a direct-current modifies the surface morphology. More precisely it has been shown in Ref. [3–6] that the step configuration depends on the current direction (step-up or step-down direction) as well as on the temperature. In Table 1, are reported the four recognized temperature domains (labelled I, II, III and IV) and the corresponding surface morphologies (regular vicinal surface, step bunching, step-meandering) according to the direct-current direction (step-up or step-down). We also give in Table 1 the temperature ranges reported in the literature for these domains. Yagi and co-workers (see Ref. [7]) have extended these results to various vicinal faces and shown that the transition temperatures weakly depend on the initial inter-step distance. It has also been shown that these behaviors are modified in homoepitaxial growth conditions so that step bunching takes place for step-down direction whatever the temperature range [3] (see Tables 1 and 2).

Stoyanov [10–12] proposed a simple and attractive model to describe the DC current-induced step bunching. For this purpose, he considered that, owing to the electrical field, diffusing adatoms acquire a small effective charge which induces a directional bias in the Brownian motion of adatoms on the surface. Following this work, the multiple temperature-dependant reversals described in Table 1, were first assigned to a sign reversal of the effective charge of the adatoms [13]. However, later, it was shown that the effective charge remains positive whatever the temperature range [14]. It was thus proposed [15,16], that these temperature-dependent reversals could originate from a modification of the step transparency. In other words, depending on the temperature, the adatoms can more or less easily pass from one terrace to the adjacent one through the step: for non transparent steps the adatoms are trapped by steps whereas for perfectly transparent steps adatoms do not incorporate into the steps. This idea is supported by calculation of the transparency properties based on a statistical analysis of the various pathways an adatom can follow close to a step. The main result is that the kink density is responsible for the non-monotonous temperature dependence of the transparency properties [17]: at low and high temperatures (domains I and III), steps are impermeable due to the high density of kinks whereas at intermediate temperature (domain II), steps are transparent due to step smoothing induced by step edge diffusion.

The main goal of this article is to provide new insight into the meandering/bunching transition which occurs from domain II to domain III for a step-down current. For this purpose, a temperature gradient has been maintained between the two ends of a Si(1 1 1) vicinal sample in order that one end belongs to domain II, and the other to domain III. This enables to observe on the same sample the evolution of the surface morphology between domains II and III

* Corresponding author. Tel.: +33 660362824.
E-mail address: leroy@cinam.univ-mrs.fr (F. Leroy).

0039-6028/$ - see front matter © 2008 Elsevier B.V. All rights reserved.
doi:10.1016/j.susc.2008.12.016

Table 1
Temperature domains for different surface morphologies observed in absence of any external flux (sublimation regime).

	Domain I	Domain II	Domain III	Domain IV
Step-up direction	Regular vicinal surface	Step bunching	Regular vicinal surface	Step bunching
Step-down direction	Step bunching	Step-meandering	Step bunching	–
Latyshev [1,2]	–	1050–1250 °C	1250–1350 °C	Above 1350 °C
Gibbons [6]	850–950 °C	1040–1190 °C	1200–1300 °C	Above 1300 °C
Metois [3]	900–1050 °C	1150–1250 °C	1250–1300 °C	–
Homma [4], Yang [5]	~ 945 °C	~ 1190 °C	~ 1245 °C	–

via a buffer zone with a mixed morphology. We believe that a careful examination of such a zone can give access to the temperature range at which the transition occurs and to a better understanding of the underlying basic mechanisms.

2. Experimental results

We use a Si(443) surface which, in its initial state, exhibits (111) terraces separated by monoatomic steps (terrace width: 24 Å) parallel to $[1\bar{1}0]$ direction. The silicon sample ($20 \times 2 \times 0.3\ mm^3$) has been cut in a *p*-doped silicon wafer ($\rho \sim 1\ \Omega\ cm$). The Si sample is first chemically cleaned then clamped between two electrodes of the sample holder in a UHV chamber (residual pressure 10^{-10} mbar). The silicon sample is then cleaned by repeated flashes at 1300 °C obtained by an alternative current (40 Hz) passing through the sample (the alternative current preserves the initial single step morphology during the cleaning process). Once cleaned, the silicon sample is heated by switching from AC to DC current without lowering the temperature in order to keep the initial single step configuration. The DC current is perpendicular to the steps (current in the $[11\bar{2}]$ direction) and in the step-down direction.

Table 2
The different regimes of the surface morphology in presence of a deposition flux.

	Domain I	Domain II	Domain III
Metois [3]	900–1050 °C	1150–1250 °C	1250–1300 °C
Step-down direction	Step bunching	Step bunching	Step bunching

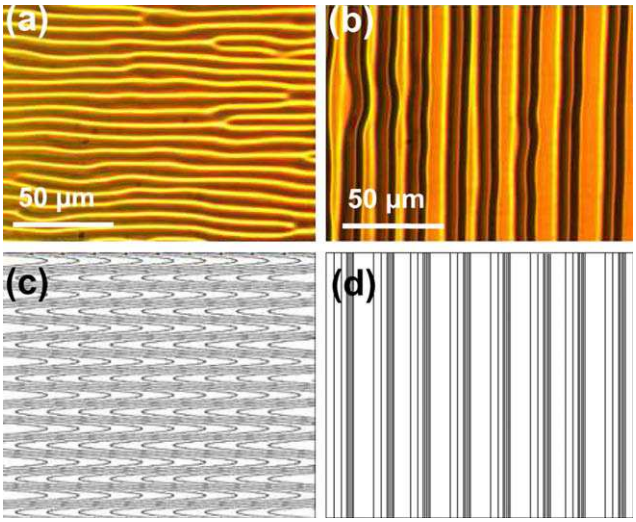

Fig. 1. (a and b) Optical micrographs of both extremities of the sample. One can see microscopic structures perpendicular (resp. parallel) to the initial step direction corresponding to step-meandering (resp. step bunching). (a) Meandering in zone 1 at $T < 1220$ °C. (b) Bunching in zone 2, at $T > 1230$ °C. (c and d) Sketches of the surface morphologies where in (c) can be easily recognized the horizontal microscopic structures seen in (a) due to the step-meanders and in (d) the vertical microscopic structures seen in (b) due to the step-bunches.

The temperature gradient is simply obtained by clamping differently both ends of the sample. It follows that the transfer of heat by conduction with the sample holder is different at each side giving rise to a temperature gradient. The temperature is locally measured by a thin filament pyrometer (TFP) using a tungsten filament with a diameter of 15 µm. When the filament and the wafer have the same thermal radiation intensity the filament disappears. Careful calibration of the temperature is obtained from the temperature of the $Si(111) - (7 \times 7) \leftrightarrow (1 \times 1)$ phase transition at 860 ± 10 °C. The thickness of the filament allows us to measure the temperature every 0.5 mm. We thus record a quasi-linear gradient over the sample size with a temperature difference of roughly 200 °C between the two extremities separated by 1.5 cm. The mean temperature of the sample (in its medium zone) is maintained at 1280 °C during 6 h (in order to reach stationary states).

At the end of the experiment the step configuration is abruptly frozen turning off the electric current to avoid any further modification of the morphology. The sample surface is observed *ex situ* by optical microscopy. In Fig. 1 are reported optical micrographs of two zones of the sample, respectively, maintained at 1200 °C (Fig. 1a) and 1280 °C (Fig. 1b). The micrometric structures correspond respectively to step-meandering and step bunching as sketched in Fig. 1c and d. In Fig. 2 is shown a sequence of optical micrographs of the intermediate zone for which the morphology continuously changes from step-meandering (low temperature zone) to step bunching (high temperature zone). The buffer zone is about 500 µm wide and spreads over a temperature range smaller than 8 °C (the temperature gradient is measured by IR pyrometry). Let us describe qualitatively the morphology change in this intermediate zone. For the lowest temperatures ($T < 1220$ °C) ridges and valleys are observed perpendicular to the initial step direction and correspond to the formation of step-meandering. At higher temperature some small ripples like defects appear parallel

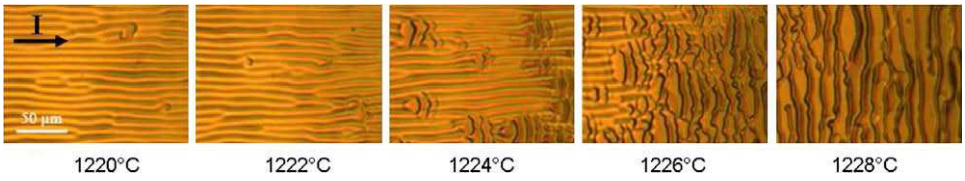

Fig. 2. Optical micrographs of the transition zone from step-meandering (left) to step bunching (right).

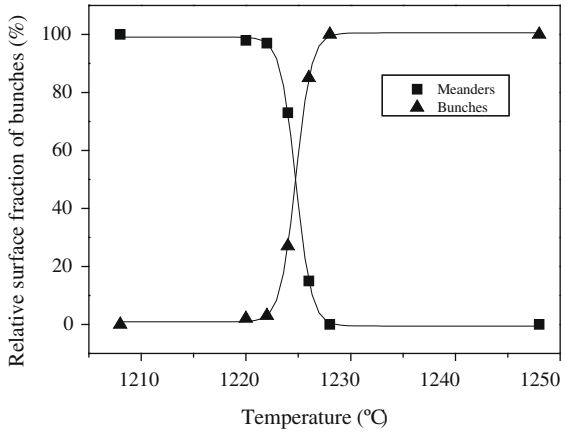

Fig. 3. Evolution of the meandering/bunching fraction of the surface as function of the temperature.

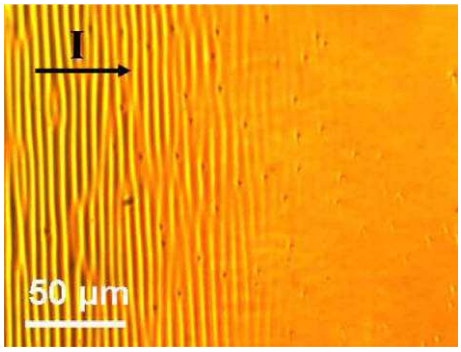

Fig. 4. Optical micrograph of the surface of Si(433) in the step-up current configuration and a temperature gradient ($\Delta T \simeq 2$ K between left and right sides of the image).

to the initial step configuration and thus perpendicular to the ridges and valleys. They correspond to step bunching and progressively cover the whole surface at $T > 1230$ °C. The co-existence of meandering and bunching of steps occurs on a narrow temperature range and the transition thus takes place by local inhomogeneities (see also Ref. [7]) that disturb the initial surface morphology. However, we believe that these local defects do not behave as nucleation sites since more generally we find (see Ref. [18]) that step bunching starts *via* a regular wavy pattern that simultaneously appears on the whole surface.

In order to get more quantitative information, the buffer area was divided into small vertical bands of identical width (roughly 150 µm). Then the relative fraction covered by ridges parallel to $[1\,1\,\bar{2}]$ and $[1\,\bar{1}\,0]$ directions (respectively, perpendicular and parallel to the initial steps) was measured in each band. The relative proportion of step-meandering and bunching versus the local temperature is reported in Fig. 3.

We observe that the meandering/bunching transition is abrupt. The transition temperature is 1225 °C in agreement with the values reported by Gibbons et al. (see Ref. [6]) and Métois et al. (see Ref. [3]). Beyond the absolute value of the transition, it must be noticed that the temperature width of the transition is very narrow (4 K). We will see in the next section that the abruptness of the transition arises from the competition between two unstable modes (bunching and meandering). At a given temperature the linear amplification factors of both instabilities cross, favoring one mode over the other. For completeness in Fig. 4 is reported the result of a similar experiment (Si sample under a temperature gradient) but now with a step-up current. In agreement with the results reported in Table 1, the low temperature zone is now bunched while the high temperature zone remains a regular vicinal surface with monoatomic steps which cannot be seen at the microscopic scale of the optical micrograph (see Fig. 4). Note that the temperature of the transition remains about $T = 1225$ °C.

3. Linear stability model

We now introduce a simple argument based on a linear stability analysis of the Burton–Cabrera–Franck (BCF) model [19] for a step-down current. The idea is to show that bunching may supersede meandering when temperature T is increased, as observed experimentally. The physical parameters of the model are: electrical field E, effective charge number Z^*, coefficient of repulsion between steps A, site area on Si(1 1 1) terraces Ω_s, step stiffness $\tilde{\beta}$, attachment kinetic coefficient ν, terrace width L_0, adatom concentration C_0, evaporation rate τ, and adatom diffusion coefficient D_s. Dividing all lengths by L_0 and times by L_0^2/D_s, one obtains dimensionless BCF equations. In its simplest formulation, our model makes use of six dimensionless parameters (see Ref. [20]):

$$\eta = \frac{L_0 Z^* eE}{k_B T} \tag{1}$$

is proportional to the electrical field,

$$\rho = \frac{\nu L_0}{D_s} \tag{2}$$

weighs attachment against diffusion,

$$\phi = \Omega_s C_0 \tag{3}$$

gives the proportion of occupied sites,

$$a = \frac{A\Omega_s}{k_B T L_0^3} \tag{4}$$

measures step-step repulsion,

$$b = \frac{\tilde{\beta}\Omega_s}{k_B T L_0} \tag{5}$$

is related to the step stiffness, and

$$s = \frac{L_0}{x_s} \tag{6}$$

gives the evaporation rate, with $x_s = \sqrt{D_s \tau}$. These six parameters are not independent in practice since most of them vary with temperature. It is the goal of the present model to mimic their variations in a realistic way and to determine how they affect the development of the basic instabilities.

Simple geometrical parameters are $L_0 = 24$ Å and $\Omega_s = 12.9$ Å^2. Experimentally, it is a serious challenge to measure accurately some of the physical parameters such as ν, and to determine their temperature dependence is even more difficult. When possible, we will use the most recent results available in the literature. The dimensionless parameter η cannot be given very accurately because the uncertainty on Z^* is large. A reasonable order of magnitude is $\eta = 10^{-6}$ [20] and we assume it constant. Both attachment/detachment at steps and diffusion on terraces involve interaction energies between an adatom and its neighbours at the atomic scale. For this reason, both are activated mechanisms. Altogether, we can thus expect that parameter ρ has a temperature dependence of the form

$$\rho = \rho_0 e\left(-\frac{T_0}{T}\right), \tag{7}$$

where ρ_0 and T_0 are two unknown parameters. ρ characterizes the relative importance of step attachment/detachment to surface dif-

fusion and k_BT_0 is related to the kink energy. Considering the adatom density close to equilibrium we take $\phi = 0.2$ [21]. The known estimate of the step interaction coefficient $A = 0.40$ eVÅ [22] gives

$$a(T) = a_0/T, \tag{8}$$

with $a_0 = 4.3$ K. The temperature dependence of parameter b (Eq. (5)) is governed by that of the step stiffness $\tilde{\beta}$. Recent experiments indicate a quasi-linear variation in a narrow range of temperatures, 850 °C < T < 975 °C [23]. For wider temperature ranges, a law of the form

$$\tilde{\beta} = KT\sinh^2\left(\frac{J_x}{2k_BT}\right) \tag{9}$$

was derived in a solid-on-solid statistical model from the kink density at temperature T [24]. Fitting this law to the experimental results of Ref. [23], we obtain $K = 8 \times 10^{-6}$ eV/(ÅK) and $J_x = 0.34$ eV for the kink energy, a value which is in good agreement with the experimental estimate $J_x = 0.32$ eV given in [22]. The last dimensionless parameter, s, weights the evaporation effects. In the present experiments, $x_s = 5 \times 10^{-6}$ m was estimated from step velocity measurements by Reflection Electron Microscopy [25] so that $s = 10^{-4}$. In a previous study, we showed that evaporation can be simply neglected for such low values of the parameter s [20].

We now turn to the evaluation of the linear amplification factor for the bunching instability. We use a one-dimensional description which assumes that the steps remain straight and parallel. This is roughly what is observed in the experiments. The linear stability analysis of this problem is well documented [26,22,27]. In our notations, the amplification factor for a perturbation of wavelength k reads [20]:

$$\sigma_B(k) = 4\phi[f(\eta,\rho) - ag(\eta,\rho)(1-\cos k)]\sin^2\frac{k}{2}, \tag{10}$$

with

$$f(\eta,\rho) = \frac{2\rho\eta^3 e^\eta}{[\eta(e^\eta+1)+\rho(e^\eta-1)]^2}, \tag{11}$$

and

$$g(\eta,\rho) = \frac{3\rho\eta(e^\eta+1)}{\eta(e^\eta+1)+\rho(e^\eta-1)}. \tag{12}$$

On the other hand, based on the experiments, we assume in-phase meandering. The corresponding amplification factor of the meandering instability is

$$\sigma_M(k) = \frac{A_1(k)\eta^2 + (a+b)k^2A_2(k)}{D_1D_2(k)}, \tag{13}$$

the exact expressions of $A_1(k)$, $A_2(k)$, D_1, and $D_2(k)$ being given in the appendix.

Fig. 5 shows the evolution of $\sigma_M(k)$ and $\sigma_B(k)$ with temperature. Although the two instabilities coexist, the ratio of their amplitudes varies in time as $\exp[(\sigma_M - \sigma_B)t]$, so that one of them ultimately governs the system dynamics. The maxima of the amplification factors are reported in Fig. 6 as function of temperature. The transition from step-meandering to step bunching occurs at $T_c = 1225$ °C, for which σ_B becomes larger than σ_M. This nice agreement with the experiments was obtained by setting the two free parameters in Eq. (7) to $\rho_0 = 1.45$ and $T_0 = 3800$ K[1]. Thus as already stated, $k_BT_0 = 0.33$ eV scales as the kink energy J_x.

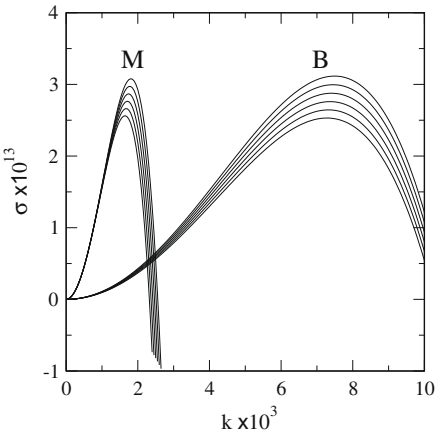

Fig. 5. Evolution of the amplification factors $\sigma_M(k)$ and $\sigma_B(k)$ with temperature (increasing from bottom to top by steps of 20 K).

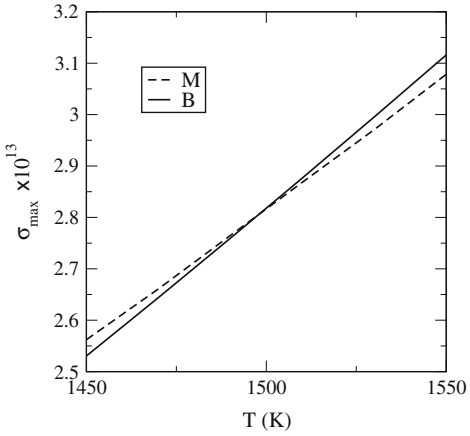

Fig. 6. Evolution of the maximum of the amplification factors M and B with temperature. The two curves cross at about 1225 °C.

We thus have $\rho \simeq 0.1$ which leads (with $L_0 = 24$ Å) to a kinetic length $d = \frac{D_s}{\nu} = 60a$ where $a = 3.86$ Å is the lattice constant. Let us recall that, kinetics regimes can be classified according to the ρ value that gives the relative importance of step attachment/detachment to surface diffusion. More precisely, two extreme cases can be distinguished: (i) the Diffusion Limited (DL) regime for which $\rho \to \infty$, so that the kinetics is determined by the time scale for an adatom to diffuse across a terrace and (ii) the Attachment/Detachment Limited (ADL) regime for which $\rho \to 0$, so that attachment/detachment takes place over a much longer time scale than adatom diffusion across a terrace[2]. In our case, $\rho \simeq 0.1$, thus the kinetics is limited by attachment–detachment.

Our value can be compared to already published results. At 890 °C, Man et al. [28] used 2D silicon island decay to measure $d = (75 \pm 25)a$ (see Fig. 1 in [28]) in quite good agreement with $d \sim 110a$ we find by extrapolation of Eq. (7) at 890 °C. On the basis of theoretical calculations of the area decay of 2D islands, Man et al. [28] proposed that the transition from DL to ADL regime takes place around $d = 240a$ so that they stated that the decay kinetic is governed by surface diffusion (see also Ref. [29]). At first sight,

[1] The transition temperature results from the intersection of two curves with two different slopes. There is only one couple of slopes which give the correct transition temperature.

[2] In the general case without desorption and without flux, the adatom current on a terrace reads $J = \frac{D_sC_0}{kT}\frac{\Delta\mu}{2d+L_0}$ where C_0 is the equilibrium adatom concentration at an isolated step and $\Delta\mu$ is the chemical potential difference between the two steps forming the terrace.

these results seem to be in contradiction with ours since we find ADL regime even though we have similar values of the kinetic length d. However, one has to compare all the different characteristic lengths at the surface to conclude. These are the inter-step distance L_0, the kinetic length d, and the diffusion length x_s. In our case, since the diffusion length is in the micrometric range [25] evaporation does not play any role, thus only two characteristic lengths remain, L_0 and d. Thus the relevant parameter to deduce the prevalent mechanism is $\rho = L_0/d$ and not only d. Man and coworkers [28] studied the decay kinetics of 2D islands, measuring the size evolution of an island of radius r located at the center of a larger island of radius R with the condition $R \gg r$ [28,29]. The characteristic size $L_0 = R - r$ thus is micrometric so that $\rho \sim 10^4 a/75a \sim 130$ which characterizes a DL regime as the authors stated. Obviously, for high vicinal faces for which L_0 becomes small, the same value of the kinetic length $d = (75 \pm 25)a$ leads to the ADL regime.

At last let us briefly comment on the sensitivity of the physical parameters ρ_0 and T_0 with the transition temperature T_c then let us comment on the SM and SB wavelengths.

- The fitting parameters ρ_0 and T_0 deviate by $\Delta\rho_0 = 0.004$ and $\Delta T_0 = 7$ K if the transition temperature varies by $\Delta T_c = 10$ K. Thus the parameters ρ_0 and T_0 are very well-defined. On the other hand, a variation of the physical parameters by say ten percents has dramatic effects, since the transition is shifted by several hundred degrees or even completely suppressed.
- In the framework of linear analysis, characteristic length scales at which SM and SB instabilities start are related to the wave vectors of the maximum of the amplification factors (see Fig. 5). However, due to non linear effects, the temporal evolution of the initial surface differs for SM and SB instabilities. More precisely, due to coarsening effects the SB wavelength increases as $\sqrt{t}$ (see Ref. [30]) while the SM wavelength remains more or less constant (see Ref. [20]). Thus the experimental SM wavelength is similar to the one calculated in Fig. 5, while the experimental SB wavelength is larger.

4. Summary and discussion

Experimental results based on a silicon sample under electromigration and a temperature gradient unambiguously show that a transition from step-meandering to step bunching occurs on a narrow temperature range around a well-defined temperature. This transition starts by local inhomogeneities or random fluctuations which then extend on the whole surface. This behavior can be easily explained in the framework of a simple linear analysis approach in which both instabilities can coexist at a given temperature but with different temperature dependence of the amplification factor. Thus at a critical temperature $T = 1225$ °C step bunching takes place to the detriment of step-meandering for step-down DC current. The experimental results can be recovered using a two-parameter model compatible with attachment/detachment limited kinetics.

These parameters ρ_0 and T_0 allow to define the temperature-behavior of the attachment–detachment and diffusion coefficients ratio (see Eq. (7)). Note that all available models describing the temperature-reversals depicted in Table 1 (see introduction) invoke temperature-dependent step properties such as step transparency [15,16], adatom mobility close to step edges [31,32] or attachment kinetics at the step edge [33]. In our simple model, all these ingredients may be, from a phenomenological viewpoint, incorporated in the temperature dependence assumed in Eq. (7) *via* the attachment coefficient ν and the step stiffness $\tilde{\beta}$ related to the kink density.

Let us now discuss the main assumptions of our model as well as the neglected ingredients (ad-vacancies, evaporation). Even though the II/III transition can be explained with our model, the I/II and III/IV transitions (step-down current) (see Table 1) cannot be strictly recovered. The low temperature transition (I/II) is not reproduced due to the vanishing of $\rho(T)$ in Eq. (7). However such a vanishing behavior at low temperature cannot be valid. The first improvement of Eq. (7) consists in adding a constant term. That way we can recover the I/II transition preserving the II/III transition since the additional constant is negligible at higher temperature. Concerning the III/IV high temperature transition, holes nucleation must be accounted for. Misbah et al. [34] have shown that the ad-vacancies created at this temperature can be at the origin of the III/IV transition (see Table 1) but this effect could not be included within our BCF-based approach. At last, evaporation may also play a role at II/III and III/IV transitions as depicted by Dufay et al. (see Ref. [20]). It has been shown that advection induced by the retraction of steps can either reinforce the effect of electromigration in case of step-down current or counterbalance it if the current is in the step-up direction.

For completeness, let us mention that other temperature-dependent mechanisms have been studied in the literature as the adatom diffusivity close to a step edge [35,31,32], the energy barrier for attachment/detachment or the diffusion coefficient on a terrace [13,33,36]. We believe that most of these mechanisms could be incorporated in our phenomenological approach of $\rho(T)$. The leading mechanisms could be identified by an accurate comparison between experiments and Kinetic-Monte-Carlo simulations [35,37] which are under current development.

Acknowledgement

This work has been supported by ANR PNANO Nanomorphogenese.

Appendix

We now give the exact expressions of the functions involved in Eq. (13). Defining

$$\Lambda = \sqrt{\eta^2 + 4k^2},$$

we have

$$D_1 = \eta \cosh\left(\frac{\eta}{2}\right) + \rho \sinh\left(\frac{\eta}{2}\right),$$

$$D_2(k) = \Lambda\rho \cosh\left(\frac{\Lambda}{2}\right) + (k^2 + \rho^2) \sinh\left(\frac{\Lambda}{2}\right),$$

$$A_1(k) = \phi\rho\left[\Lambda\rho\left(\cosh\left(\frac{\eta}{2}\right)\cosh\left(\frac{\Lambda}{2}\right) - 1\right) + \sinh\left(\frac{\Lambda}{2}\right)\left(2k^2\cosh\left(\frac{\eta}{2}\right) - \eta\rho\sinh\left(\frac{\eta}{2}\right)\right)\right],$$

$$A_2(k) = \phi\rho D_1\left[\Lambda\rho\left(\cosh\left(\frac{\eta}{2}\right) - \cosh\left(\frac{\Lambda}{2}\right)\right) - 2k^2\sinh\left(\frac{\Lambda}{2}\right)\right].$$

References

[1] A. Latyshev, A. Aseev, A. Krasilnikov, S. Stenin, Surf. Sci. 213 (1989) 157.
[2] A. Latyshev, A. Aseev, A. Krasilnikov, S. Stenin, Surf. Sci. 227 (1990) 24.
[3] J.J. Métois, S. Stoyanov, Surf. Sci. 440 (1999) 407.
[4] Y. Homma, R. McClelland, H. Ibino, Jpn. J. Appl. Phys. 29 (1990) L2254.
[5] Y. Yang, E. Fu, E. Williams, Surf. Sci. 356 (1996) 101.
[6] B. Gibbons, S. Schaepe, J. Pelz, Surf. Sci. 600 (2006) 2417.
[7] K. Yagi, H. Minoda, M. Degawa, Surf. Sci. Rep. 43 (2001) 45.
[8] H. Omi, Y. Homma, V. Tonchev, A. Pimpinelli, Phys. Rev. Lett. 95 (2005) 216101.
[9] J. Kallunki, J. Krug, M. Kotrla, Phys. Rev. B 65 (2002) 205411.
[10] S. Stoyanov, Jpn. J. Appl. Phys. 30 (1991) 1.
[11] S. Stoyanov, M. Ichikawa, T. Doi, Jpn. J. App. Phys. 32 (1993) 2047.

[12] S. Stoyanov, H. Nakahara, M. Ichikawa, Jpn. J. App. Phys. 33 (1997) 254.
[13] D. Kandel, J. Weeks, Phys. Rev. Lett. 74 (1995) 3632.
[14] M. Degawa, H. Minoda, Y. Tanishiro, K. Yagi, Surf. Sci. 461 (2000) L528.
[15] S. Stoyanov, Surf. Sci. 370 (1997) 345.
[16] S. Stoyanov, Surf. Sci. 416 (1998) 200.
[17] S. Filimonov, Y. Hervieu, Surf. Sci. 553 (2004) 133.
[18] F. Leroy, P. Müller, J.J. Metois, O. Pierre-Louis, Phys. Rev. B 76 (4) (2007) 045402.
[19] W. Burton, N. Cabrera, F. Frank, Phil. Trans. Roy. Soc. 243 (1951) 299.
[20] M. Dufay, T. Frisch, J.-M. Debierre, Phys. Rev. B 75 (24) (2007) 241304.
[21] Y.-N. Yang, E.D. Williams, Phys. Rev. Lett. 72 (12) (1994) 1862.
[22] H.C. Jeong, E.D. Williams, Surf. Sci. Rep. 34 (1999) 171.
[23] A.B. Pang, K.L. Man, M.S. Altman, T.J. Stasevich, F. Szalma, T.L. Einstein, Phys. Rev. B 77 (11) (2008) 115424.
[24] Y. Saito, Statistical Physics of Crystal Growth, World Scientific, Singapore, 1996.
[25] J.J. Métois, Unpublished results.
[26] O. Pierre-Louis, Surf. Sci. 529 (2003) 114.
[27] C. Misbah, O. Pierre-Louis, Y. Saito, Rev. Mod. Phys. (in press).
[28] K.L. Man, A.B. Pang, L.S. Altman, Surf. Sci. 601 (2007) 4669.
[29] H. Hibino, C.-W. Hu, T. Ogino, I.S.T. Tsong, Phys. Rev. B 63 (2001) 245402.
[30] D. Liu, J. Weeks, Phys. Rev. B 57 (1998) 14891.
[31] T. Zhao, J. Weeks, Surf. Sci. 580 (2005) 107.
[32] T. Zhao, J. Weeks, D. Kandel, Phys. Rev. B 71 (2005) 155326.
[33] B. Gibbons, PhD Dissertation, Electromigration Induced Step Instabilities on Silicon Surfaces, Ohio State University, 2006, p. 165.
[34] C. Misbah, O. Pierre-Louis, A. Pimpinelli, Phys. Rev. B 51 (1995) 17283.
[35] N. Suga, J. Kimpara, N. Wu, H. Yasunaga, A. Natori, Jpn. J. Appl. Phys. 39 (7B) (2000) 4412.
[36] O. Pierre-Louis, Phys. Rev. Lett. 96 (13) (2006) 135901.
[37] M. Sato, M. Uwaha, Y. Saito, Phys. Rev. B 62 (12) (2000) 8452.

Troisième partie

Croissance auto-organisée de nanostructures

MISE EN PERSPECTIVE

La réalisation d'objets de tailles nanométriques sur une surface offre des perspectives nouvelles en physique fondamentale et en termes d'applications. A cette échelle, les propriétés physiques de la matière peuvent différer notablement de celles du matériau massif.

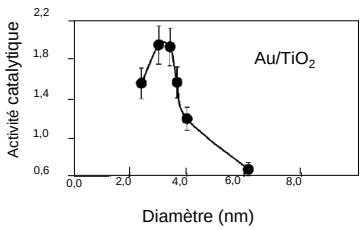

Figure III.1 *– Activité catalytique de nanoparticules d'or, déposées sur une surface de TiO_2(110), en fonction de leurs diamètres. La réaction est l'oxydation du monoxyde de carbone à 350 K. Figure extraite de la référence [67].*

Par exemple, le confinement électronique tridimensionnel dans les nanostructures semiconductrices conduit à des états électroniques discrets et donc à des propriétés optiques spécifiques [68]. Si les avancées dans les domaines de l'opto- ou de la micro-électronique sont les plus spectaculaires, d'autres domaines d'activité tels que la catalyse utilisent par nature des processus physiques à l'échelle nanométrique. La compréhension des paramètres clés qui pilotent l'activité catalytique des matériaux permet d'envisager d'améliorer le rendement et la sélectivité réactionnelle. Par exemple, la taille des nanoparticules joue un rôle prépondérant en catalyse hétéro-

gène. Ainsi l'or, lorsqu'il est sous forme de particules de 3 nm de diamètre catalyse activement l'oxydation du monoxyde de carbone tandis qu'il est complètement inactif si les particules sont de taille supérieure à 10 nm (figure III.1). Les propriétés physiques de ces nouveaux matériaux sont donc très sensibles à leur structure cristallographique, leur forme, leur taille ainsi qu'à l'arrangement spatial des nano-objets. Pour étudier leurs propriétés par des sondes non-locales il est par conséquent nécessaire de réaliser une assemblée d'objets identiques qui présentent les mêmes caractéristiques physiques (figure III.2).

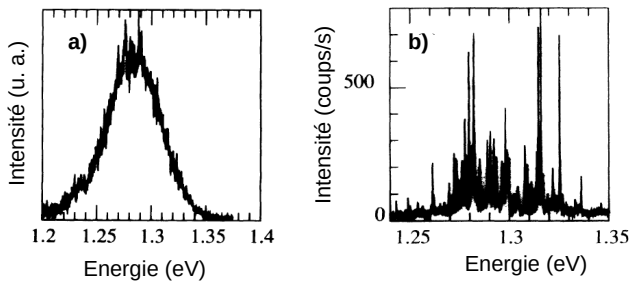

Figure III.2 *– Spectres de photoluminescence de boîtes quantiques InAs dans GaAs sur un même échantillon mais sur une superficie sondée différente. a) 5000×5000 nm^2. b) 500×500 nm^2. Dans ce dernier cas les raies d'émission de chacune des boîtes sont résolues mettant en évidence la disparité de leurs propriétés physiques et donc de leurs tailles. Figure extraite de la référence [69].*

Toutefois la fabrication contrôlée de nano-structures reste un défi. Si les techniques de lithographie électronique atteignent aujourd'hui les dimensions nanométriques, la qualité des nano-structures réalisées n'est pas optimale à cause des défauts (en particulier cristallins) générés lors de l'élaboration. En outre le temps de fabrication est long car les objets sont réalisés un par un. Le développement des techniques de dépôt telles que l'épitaxie par jet moléculaire permet aujourd'hui d'élaborer simultanément un nombre macroscopique de nano-objets, de qualité cristalline remarquable. Cependant l'évaporation des matériaux conduit en général à une assemblée désordonnée d'objets et à une large dispersion de tailles ($\geq$20%) du fait même des processus gouvernant la croissance : nucléation homogène ou hétérogène, compétition entre nanostructures voisines durant la crois-

sance, mûrissement partiel vers une forme d'équilibre.... Depuis le début des années 90, une voie prometteuse a émergé. L'étude des surfaces à l'échelle nanométrique a révélé, dans certains cas, l'existence d'une structuration spontanée et ordonnée de la surface (reconstruction, facettage), avec des périodes allant de 1 à 100 nm. Ce phénomène d'auto-organisation des surfaces [70–72] peut servir de gabarit pour la croissance ordonnée de nanostructures, en répliquant le motif de la surface.

Différents types de nanostructuration de surfaces ont été explorés. La croissance ordonnée de nanostructures a été réalisée sur les marches d'une surface vicinale (figure III.3a), en utilisant les contraintes élastiques induites par des agrégats enterrés (figure III.3b), sur des surfaces nanostructurées grâce à un adsorbat (figure III.3c), sur des reconstructions de surface (figure III.3d), ou encore en mettant à profit la déformation de surface induite par un réseau de dislocations enterrées (figure III.3e-f).

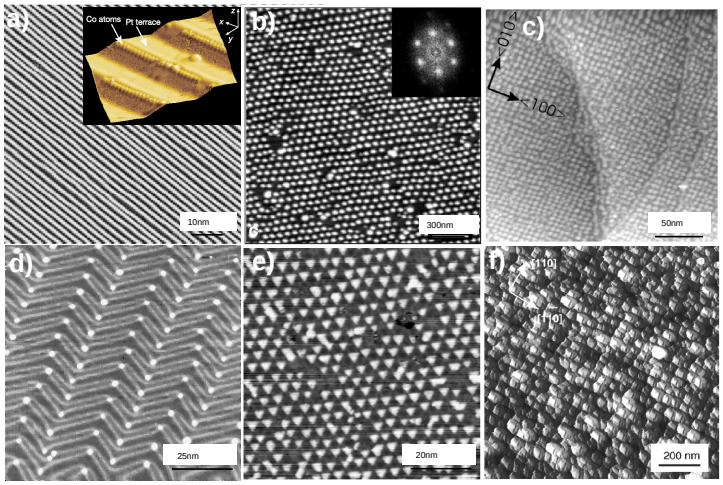

Figure III.3 *– Différents cas d'auto-organisation de nano-structures sur une surface. a) Fils monoatomiques de cobalt sur la surface vicinale de Pt(997) [73]. b) Dernier plan d'un super-réseau de 60 périodes de boîtes quantiques de PbSe encapsulées dans* $Pb_{(1-x)}Eu_xTe$ *[74]. c) Plots d'or (0,67 monocouche déposée) sur une surface d'N/Cu(100) [75]. d) Plots de cobalt sur une surface d'Au(111) [76]. e) Plots de fer sur un réseau de dislocations formé par une bicouche de cuivre sur une surface de Pt(111) [77]. f) Plots de germanium sur une surface de Si(001) nanostructurée par un réseau de dislocations enterrées [78]. Figures extraites des références citées.*

Les grandeurs à caractériser sont la structure cristallographique des nanostructures, leurs tailles, leurs formes et leur répartition spatiale ce qui nécessite une grande dynamique de mesure spatiale. La microscopie en champs proche est l'outil le plus souvent utilisé, toutefois il est extrêmement difficile de sonder la structure atomique d'agrégats. La microscopie électronique à transmission n'a pas cet inconvénient mais les études *in situ* sont délicates. Au contraire, les techniques de diffusion des rayons X peuvent être mises en œuvre, dans des conditions expérimentales très diverses (ultra-vide, haute pression, température...). En outre la combinaison de la diffraction pour caractériser la structure à l'échelle atomique [79], et de la diffusion centrale [80,81] pour étudier la morphologie à l'échelle nanométrique confère aux techniques de rayons X une grande dynamique de mesure spatiale. Nous avons donc combiné les deux techniques en condition d'incidence rasante pour caractériser la croissance auto-organisée de nanostructures. Dans la suite j'aborderai un exemple d'étude où nous avons mis à profit ces techniques pour caractériser la croissance auto-organisée d'agrégats de Pd sur une surface nanostructurée d'Al_2O_3 obtenue par oxydation d'un monocristal de Ni_3Al. Ces études de croissance ont été menées en collaboration avec l'équipe "agrégats et catalyse" du CINaM. Elles ont servi de base aux études de réactivité de CO sur des agrégats de Pd de tailles parfaitement contrôlées (voir article [82]).

PRINCIPAUX RÉSULTATS

2.1 État de l'art

Dans un agrégat les états électroniques des atomes sont couplés entre eux donnant naissance à des états électroniques "moléculaires" quand le nombre d'atomes est faible et à une structure de bandes à mesure qu'on se rapproche du cristal infini. On distingue de ce fait généralement deux régimes dans l'activité catalytique des particules métalliques en fonction de leurs tailles : (i) le régime "moléculaire" au-dessous d'une certaine taille critique et (ii) le régime "volumique" pour les grandes particules. Les grandes variations de réactivité attendues théoriquement dans le régime moléculaire sont un révélateur de l'évolution rapide de la structure électronique avec la taille de la nanoparticule. Toutefois jusqu'à aujourd'hui, la mise en évidence expérimentale de ces variations par une mesure précise de la réactivité de nanoparticules métalliques est quasi-inexistante. Il a donc été entrepris, par l'équipe "agrégats et catalyse" du CINaM, de mesurer la réactivité vis-à-vis de l'adsorption de CO de nanoparticules de Pd sur Al_2O_3 en travaillant sur une large gamme de tailles pour recouvrir les régimes "moléculaire" et "volumique". La difficulté expérimentale essentielle tient dans la fabrication contrôlée d'une assemblée de nanoparticules de Pd de tailles et de structures très homogènes pour éviter de moyenner sur des réactivités de particules très différentes. Il est aussi nécessaire de contrôler la disposition spatiale des agrégats pour faire en sorte que les aires de cap-

ture du CO par les nanoparticules de Pd soient identiques entre elles. Ces contraintes sont fortes sans compter que toute contamination des nanoparticules modifie brutalement les propriétés électroniques. Il a donc été fait le choix de croître sous ultra-vide des nanoparticules de Pd par épitaxie par jet moléculaire sur un substrat nanostructuré d'Al_2O_3 fabriqué par oxydation d'un cristal de $Ni_3Al(111)$. S'il a été montré [83, 84] que la surface oxydée de $Ni_3Al(111)$ produit une structuration de surface héxagonale de période 4.1 nm permettant d'obtenir la croissance auto-organisée d'agrégats de Pd, une étude quantitative de la qualité de ce réseau restait à réaliser. En effet les études locales qui ont été faites par microscopie à effet tunnel ne permettent pas d'avoir une vue d'ensemble et de quantifier le degré d'ordre à longue distance. Par ailleurs les effets de convolution avec la pointe du STM mais aussi les effets provenant du couplage entre les états électroniques des agrégats et ceux de la pointe du STM limitent notre capacité à évaluer quantitativement la taille des agrégats et donc aussi la distribution de tailles. Nous avons donc entrepris de caractériser *in situ*, par GISAXS la croissance d'agrégats de Pd sur $Al_2O_3/Ni_3Al(111)$. Ces expériences ont été menées sur l'instrument Surface Ultra-Vide de la ligne de lumière BM32 de l'ESRF (European Synchrotron Radiation Facility).

2.2 Croissance de nanostructures de Pd auto-organisées sur Al_2O_3 par GISAXS (voir article joint [8])

La technique de diffusion centrale des rayons X en incidence rasante (GISAXS) consiste à mesurer le signal de diffusion des rayons X par un échantillon aux petits angles, i.e. à proximité du faisceau incident. De cette façon le transfert de vecteur d'onde est petit par rapport au vecteur d'onde incident et donc les longueurs caractéristiques mesurées sur l'échantillon sont très supérieures à la longueur d'onde utilisée ($\lambda \sim$0.1 nm). Pour exacerber le signal diffusé provenant de la surface, le faisceau de rayons X est collimaté en condition d'incidence rasante avec un angle proche de l'angle critique de réflexion totale externe du matériau ($\alpha_c \sim$0.1-0.5°). Cette configuration présente le double avantage d'étaler le faisceau X incident sur la

surface et donc d'augmenter le signal diffusé et d'autre part de réduire la pénétration du faisceau dans le volume du matériau qui pourrait générer un signal diffus parasite (voir figure III.4).

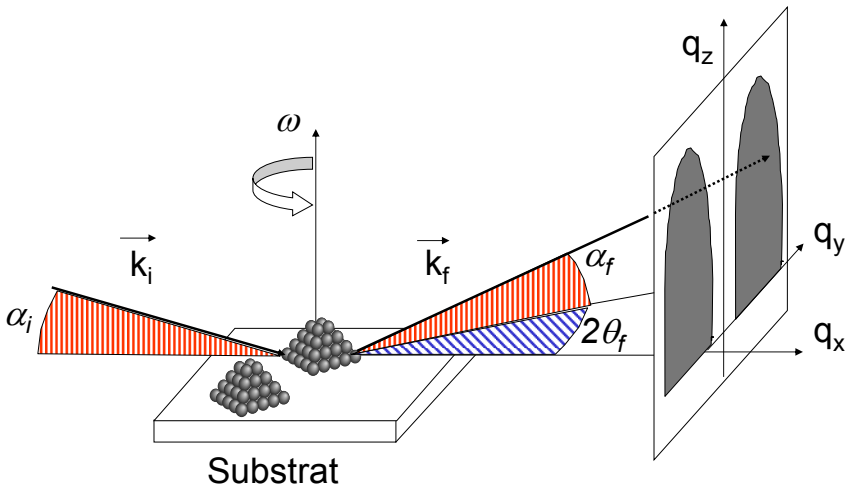

Figure III.4 *– Principe de la mesure par GISAXS. Les angles d'incidence et d'émergence par rapport au plan de la surface sont notés α_i et α_f. L'angle d'émergence hors du plan d'incidence est noté θ_f. L'azimuth de l'échantillon est noté ω.*

La technique de GISAXS complète donc avantageusement la technique plus classique de réflectivité des rayons X, en mesurant l'intensité hors spéculaire. Des informations sur les corrélations latérales, les formes et les tailles des agrégats peuvent être extraites des données expérimentales. Dans le cas qui nous intéresse, d'agrégats ordonnés de Pd sur un substrat nanostructuré, le technique de GISAXS nous a permis de caractériser *in situ* l'ordre à longue distance ainsi que d'évaluer la taille et la forme des agrégats de Pd.

La figure III.5a présente un cliché expérimental d'un dépôt à température ambiante équivalent à 0.5 monocouche atomique de Pd sur un substrat d'Al_2O_3/ $Ni_3Al(111)$. Deux tiges fines apparaissent sur chaque côté de la tige spéculaire, elles correspondent à la diffusion des rayons X aux petits angles par un réseau bidimensionnel d'agrégats de Pd. De façon similaire

aux pics de Bragg d'un cristal tridimensionnel, l'étroitesse de ces tiges parallèlement à la surface provient des interferences constructives entre les ondes diffusées par un réseau périodique d'agrégats.

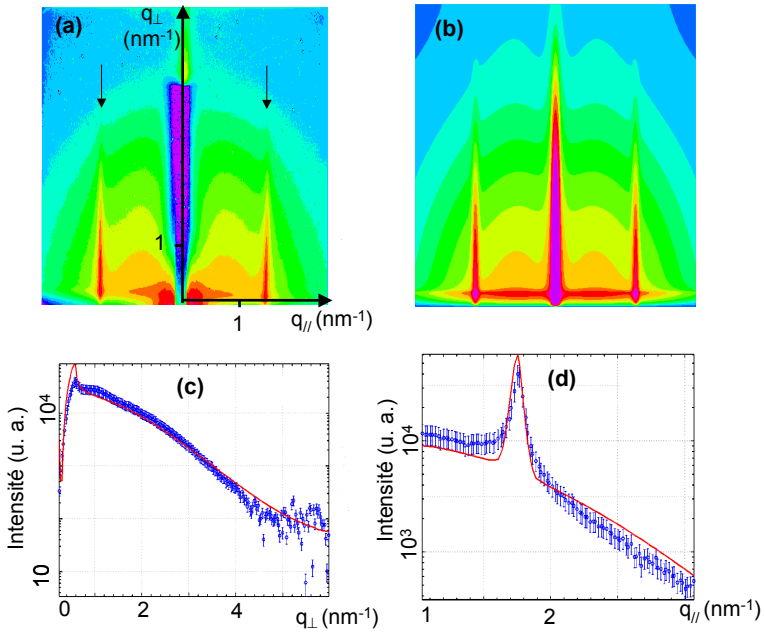

Figure III.5 *– (a) cliché GISAXS experimental d'agrégats de Pd sur Al_2O_3 (0.5 monocouche atomique). Les flèches noires montrent les tiges de diffusion du réseau d'agrégats de Pd. (b) Simulation d'un cliché GISAXS à partir des paramètres ajustés du pas du réseau, de la taille et de la forme des agrégats. (c) et (d) Coupes unidimensionnelles d'intensité extraites des données GISAXS, respectivement parallèle et perpendiculaire au plan de la surface : données (carré) et ajustements (ligne pleine).*

L'ordre à longue distance est confirmé par la cartographie complète de l'espace réciproque projeté dans le plan de la surface. Cette carte est réalisée en mesurant l'intensité GISAXS à différents azimuths tournant l'échantillon par pas de $1°$ sur une gamme angulaire totale de $60°$. Cette carte montre la présence de deux variants équivalents de réseaux d'agrégats tournés de $24.5°$ (voir figure III.6).

Pour pleinement caractériser l'organisation des agrégats, une étude quantitative des tiges de diffusion a été faite sur la base d'un modèle géométrique de réseau d'agrégats de formes et tailles données. L'ajustement des mesures à été fait grâce au logiciel IsGISAXS [85] développé par Rémi Lazzari (INSP, Paris). Les ingrédients du modèle sont les suivants : Les agré-

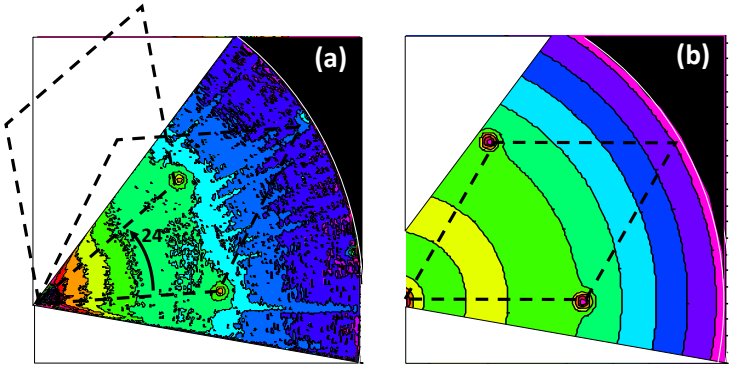

Figure III.6 *– Cartes de l'espace réciproque des agrégats de Pd dans le plan de la surface : (a) et (b) cartes expérimentale et simulée. Les losanges montrent la cellule hexagonale du réseau d'agrégats. Sur la carte expérimentale deux variants sont visibles tournés de 24.54°.*

gats ont une forme de sphère tronquée dont le rayon moyen et le degré de troncature sont des paramètres ajustables. Concernant le réseau, la taille moyenne des domaines ainsi que le paramètre de maille du réseau sont ajustables. On a ajouté aussi un paramètre de désordre local de type "Debye Waller" qui tient compte des variations locales du paramètre de réseau tout en préservant l'ordre à longue distance. Les ajustements des courbes expérimentales (Fig. III.5(c)-(d)) ainsi que la simulation GISAXS correspondante (Fig. III.5(b)) valident les hypothèses de la modélisation. L'analyse montre que pour une dépôt de 0.5 monocouche atomique de Pd, les agrégats sont des sphères tronquées de rayon 0.95±0.25 nm et de hauteur 1.2±0.3 nm. La périodicité du réseau est de 4.14±0.05 nm et la taille moyenne des domaines est de l'ordre de 200±20 nm.

Nous avons plus particulièrement utilisé la technique de GISAXS pour étudier des dépôts de Pd beaucoup plus faibles, inférieurs au dixième de monocouche atomique. Sur la figure III.7, nous pouvons voir que le signal GISAXS est visible jusqu'au troisième ordre de diffraction par le réseau d'agrégats démontrant que l'ordre est à longue distance même pour les plus petites quantités déposées.

Sur la base de ces études, indiquant un haut degré d'ordre et une ho-

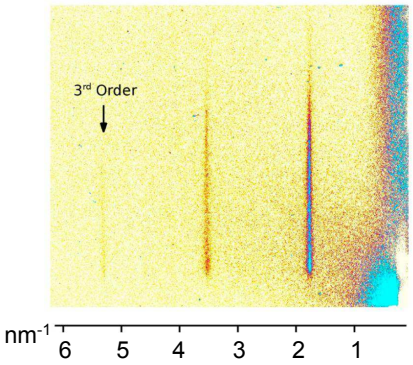

Figure III.7 *– (a) cliché GISAXS experimental d'agrégats de Pd sur Al_2O_3 (<0.1 monocouche atomique). On observe la présence d'une tige de diffraction par le réseau d'agrégat d'ordre trois.*

mogénéité en taille et en forme des agrégats nous avons pu réaliser des expériences systématiques d'adsorption de CO pour différents dépôts et à différentes températures. Les mesures d'adsorption de CO sur Pd sont détaillées dans l'article [82]. Elles nous ont permis d'estimer l'évolution, en fonction de la taille des agrégats de Pd, de l'énergie d'adsorption de CO (voir fig. III.8).

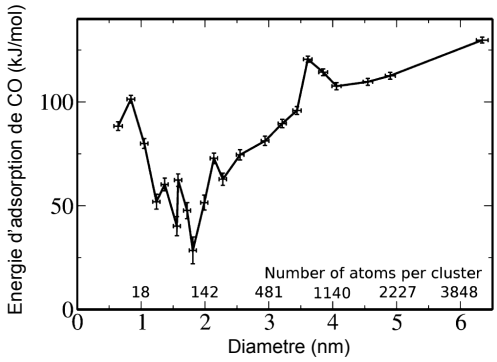

Figure III.8 *– Evolution de l'énergie d'adsorption de CO en fonction de la taille des agrégats de Pd. Notons en particulier aux plus petites tailles (diamètre inférieur à 1.5 nm, i.e. 150 atomes) une évolution non monotone de l'énergie. Elle est caractéristique du caractère "moléculaire" de la structure électronique des agrégats.*

ARTICLES SÉLECTIONNÉS : CROISSANCE AUTO-ORGANISÉE DE NANOSTRUCTURES

[8] : De la molecule au cristal : reactivité d'agrégats métalliques supportés
Sitja *et al.*, Nano Lett. (2013)

NANO LETTERS

Letter

pubs.acs.org/NanoLett

Transition from Molecule to Solid State: Reactivity of Supported Metal Clusters

Georges Sitja,*[,†] Séverine Le Moal,[†,‡,§] Maxence Marsault,[†] Guido Hamm,[†,∥] Frédéric Leroy,[†] and Claude R. Henry[†]

[†]Centre Interdisciplinaire de Nanoscience de Marseille, Aix-Marseille Université/CNRS, UMR 7325, Campus de Luminy, Case 913, F-13288 Marseille cedex 09, France

[‡]Chair of Physical Chemistry, Catalysis Research Center, Technische Universität München, Lichtenbergstraße 4, D-85748 Garching, Germany

Supporting Information

ABSTRACT: The evolution of the adsorption energy of carbon monoxide (CO) molecules on palladium (Pd) clusters as function of Pd particle size from the molecular regime (less than ∼100 atoms per particle) to the bulk regime has been revealed. This adsorption energy is retrieved from the residence time of CO molecules on the Pd clusters, measured by a pulsed molecular beam technique, versus temperature. Unprecedented accuracy on the determination of the particle size has been achieved here by using a regular array of metal clusters exhibiting a size dispersion down to the ultimate limit of a Poisson distribution. This allows getting rid of the convolution effects that generally occur when considering particles grown through other techniques.

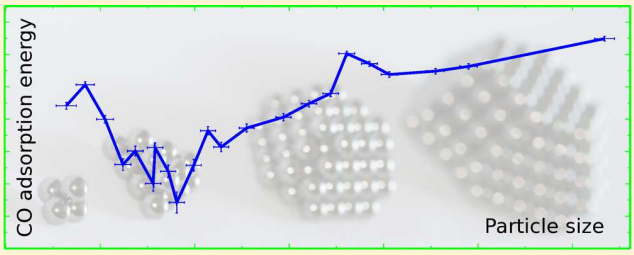

KEYWORDS: *Nanostructured alumina film, particles arrays, CO adsorption energy, pulsed molecular beam technique (MBRS), size dependence*

Metal clusters exhibit physical and chemical properties that dramatically differ from those of bulk metals. This has been put in evidence for optical,[1,2] magnetic,[3] catalytic,[4−7] thermodynamics[8,9] as well as electrochemical[10] and electric transport properties.[11,12] It is known for a long time that the catalytic activity of metal particles is size dependent.[5] Two regimes are usually observed, namely the bulk regime for the largest particle sizes and the molecular regime for particle sizes smaller than a critical number of atoms. In a cluster, electronic states of each interacting atom are modified by the coupling to the other atoms. This implies the shift of electronic energy levels that leads to electronic molecular states when number of atoms is low, or to energy bands (of solid state materials) when the number of levels is high. The fluctuation of the reactivity of clusters as a function of exact number of atoms reveals the molecular characteristics of very small clusters. In order to investigate the reactivity versus size relationship, two main approaches have been used:

(i) The first one ("cluster science" approach) is based on the study of the reactivity of size-selected clusters grown by atom condensation in an inert carrier gas and deposited on an inert oxide or carbon surface.[4,6,13−25] These studies have shown that up to 30 atoms, the reactivity fluctuates as a function of the exact number of atoms in the clusters. However this technique has two main drawbacks. First the size-selected particles are randomly distributed on the surface, leading to different particle environments (except for very low coverages but the corresponding signal-to-noise ratio is insufficient for these studies). Secondly this technique using laser evaporation sources and RF-quadrupole mass spectrometers only allows obtaining small clusters (typically smaller than 40 atoms) in reasonable experimental time. More recently, new types of cluster sources using magnetron sputtering combined with electrostatic quadrupole deviator or magnetic sector allowed production and separation of clusters up to 10 nm in size.[26−30] However, with these large sizes, the size selection is no longer atomic and size dispersion of 10% is typically obtained.

(ii) The second approach ("surface science" approach) is based on metal clusters grown by atom condensation on oxide or ionic single crystals under ultrahigh vacuum (UHV) conditions. This allows an investigation of the catalytic properties over larger cluster sizes.[31−33] With these model catalysts, size and shape effects have been evidenced for metal nanoparticles during simple catalytic reaction like CO oxidation and NO reduction by

Received: December 23, 2012
Revised: March 10, 2013

   dx.doi.org/10.1021/nl304741t | *Nano Lett.* XXXX, XXX, XXX−XXX

CO.[34−36] However the metal clusters usually nucleate on substrate defects, which are randomly distributed on the surface, leading to two main difficulties: the particle size distribution is rather large and the distance between clusters can vary a lot. The first point is a severe limitation on the study of the reactivity versus clusters size. The second point hampers accurate measurements of the catalytic reaction kinetics because of the reverse spillover effect (unequal reactants capture area of the clusters).[35] Hence to overcome the limitations of both previous approaches and to achieve a precise reactivity versus size relationship there is a crucial need for a new model system with both homogeneous particle size and regular spacing (namely a regular array).

As the catalytic activity of metallic particles heavily depends on the presence of contaminants, it is mandatory to control both the chemical composition of clusters and substrates. Several elaboration methods of particles arrays already exist. The methods using chemical processes at any stage of elaboration (i.e., colloidal synthesis,[37] lithography techniques,[38] and masks-based technique[1]) do not guarantee the absence of impurities. A better way is to elaborate under UHV conditions nanostructured templates for the growth of metal clusters by atom condensation. These substrates can be obtained either by sequential procedure (focused ion beam (FIB),[39] atomic force microscopy (AFM)[40] or by massively parallel methods.[41,42] The latter way has the advantage that it yields extended arrays of defects within a relatively short procedure. In particular, it has been shown that nucleation centers for the ordered growth of nanoparticles can arise from judicious surface preparation (for example, ordered growth of Au nanoparticles on N/Cu(001)[41] or of Co nanoparticles on Au(677)[42]). For the purpose of growing ordered Pd nanoparticles, we have used a thin nanostructured alumina film grown on a Ni_3Al single crystal as template.[43,44]

This nanostructured template, two Al−O layers in thickness, is obtained by oxidation ($p(O_2) = 5 \times 10^{-8}$ mbar, 45 L O_2) at 1000 K of a $Ni_3Al(111)$ single crystal. Prior to oxidation, the substrate surface is cleaned by cycles of Ar ion sputtering (I = 15 μA, V = 2 keV, 30 min) and annealing (1100 K, 20 min). It is characterized by low energy electron diffraction (LEED) and STM. As the unit cell parameters of the substrate and the alumina film slightly differ, the system relaxes toward a state of constraints where a regular hexagonal array of defects spontaneously appears.[44] This array of defects acts as a geometric ensemble of nucleation centers for Pd atoms, provided that the growth parameters (deposition flux and substrate temperature) are accurately tuned. On the basis of systematic STM studies, we determined the optimal growth parameters and checked the arrangement and the size homogeneity of the clusters as well as their stability upon temperature variations.[45] Moreover, we conducted nucleation and growth simulations (Monte Carlo kinetics) that indicate that the growth parameters can be chosen to achieve a size distribution that follows a Poisson distribution,[46] which is the narrowest size-distribution achievable by random processes (standard deviation in the number of atoms per particle (N) is equal to $\sqrt{N}$ when N is large enough; more details are available in the Supporting Information). STM images reveal a perfect hexagonal local order.[47] Figure 1, which shows clusters of mean size (35 ± 6) atoms, depicts the crucial role played by the nanostructured alumina film: from the very beginning of growth, the clusters are well centered on the nodes of a regular hexagonal lattice of unit cell parameter 4.1 nm.

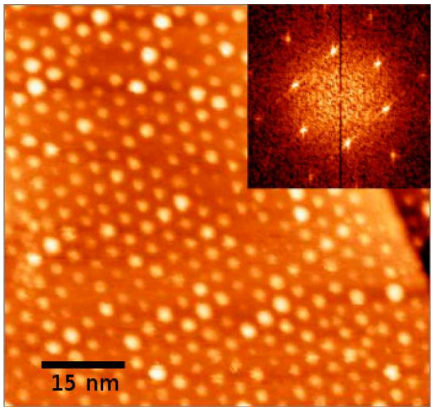

Figure 1. STM image (U = 1.19 V, I = 19 pA) of 0.15 Pd ML (clusters of about (35 ± 6) atoms, that is (1.24 ± 0.07) nm diameter) deposited at RT on a nanostructured alumina film on $Ni_3Al(111)$, highlighting the quasi-perfect long-range order of the Pd clusters array. Inset: the corresponding Fourier transform shows very sharp peaks even for high orders.

Retrieving the particle size distribution from STM images is difficult due to tip−sample convolution effects. Moreover the narrow scanning frame of the STM hampers any long-range analysis of this distribution. Therefore we conducted further investigations by grazing incidence small-angle X-ray scattering (GISAXS), a valuable tool that gives access to a much more sensitive and larger scale analysis of the long-range organization and the mean cluster size[48−50] (see more details in Supporting Information). The sharp scattering peak in the GISAXS pattern of Figure 2 denotes the presence of large domain sizes of regularly distributed nanoparticles (240 × 240 nm^2). The quasi absence of diffuse scattering besides the sharp peak confirms that the size distribution is narrow and that the order spreads over the whole sample surface (0.5 cm^2). For very low coverage (<0.1 ML) X-ray scattering is extended enough to reveal up to the third order peak (Figure 2b). In the present work, we have chosen not to rely on STM or GISAXS measurements to determine the size distribution of clusters, and we have retrieved the mean size and standard deviation from the amount of deposited Pd by assuming a Poisson distribution (as demonstrated by Monte Carlo calculations[46]).

Studying the catalytic activity of these arrays requires that the organization of the clusters remains the same during the reaction at elevated temperature. We have checked by systematic STM measurements after annealing under UHV at various temperatures that the hexagonal lattice of particles is stable until 600 K (see Figure S1 in Supporting Information). Additionally, GISAXS experiments have shown that these particle arrays exhibit stability upon oxygen exposure ($P(O_2) = 10^{-6}$ mbar) at room temperature.[51]

To evaluate the adsorption energy of CO, we implemented the molecular beam relaxation spectroscopy (MBRS) technique, which allows time-resolved monitoring of the residence time of CO molecules at the surface.[52] Adsorption energies can be retrieved through this technique by analyzing the residence time versus temperature.

By employing a multichannel analyzer, we measured the adsorption energy of CO molecules on Pd clusters with ±2 kJ/mol accuracy. Figure 3 displays a typical adsorption−desorption

dx.doi.org/10.1021/nl304741t | Nano Lett. XXXX, XXX, XXX−XXX

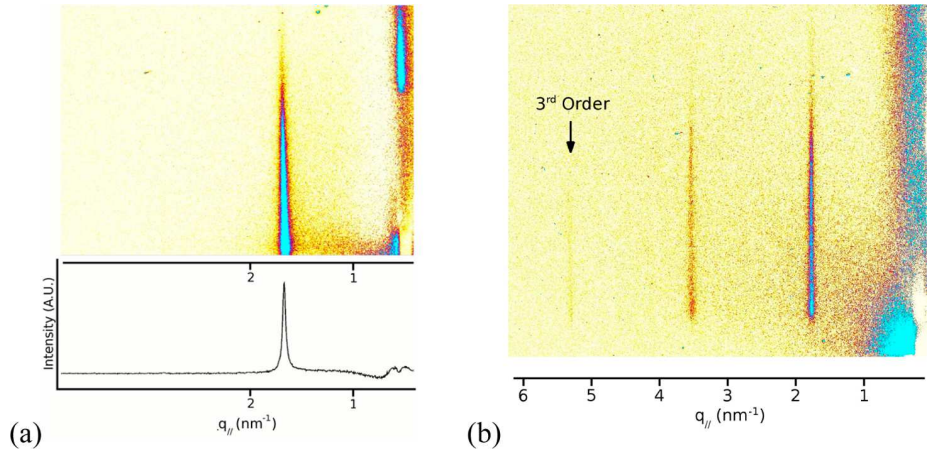

Figure 2. (a) Experimental GISAXS pattern of 0.1 Pd ML (clusters of (23 ± 5) atoms, that is, (1.08 ± 0.08) nm diameter) deposited at RT on a nanostructured alumina film on $Ni_3Al(111)$. The quasi-absence of diffuse scattering demonstrates both the very good organization of the obtained array and the very good homogeneity in size of the Pd clusters. (b) GISAXS pattern for a Pd coverage smaller than 0.1 ML where up to third order rod is visible.

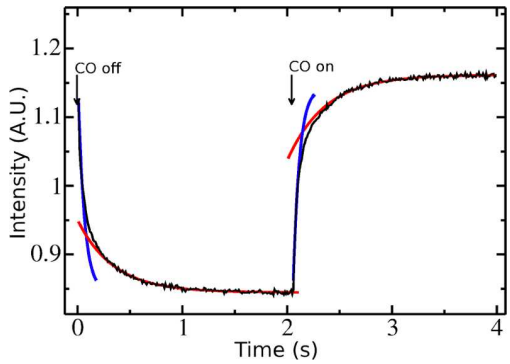

Figure 3. CO adsorption−desorption signal (averaged over 60 consecutive cycles) on 0.02 Pd ML (clusters of mean size of (4.7 ± 2) atoms and (0.64 ± 0.10) nm diameter) deposited at 373 K on a nanostructured alumina film on $Ni_3Al(111)$. A rapid component and not resolved with our experimental setup (blue curve, with time constant of 30 ms corresponding to the fastest response of our experimental setup) due to CO adsorption on the alumina film, and a slow exponential component (red curve) due to CO adsorption on Pd clusters are clearly visible.

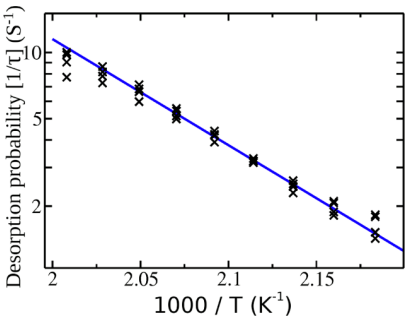

Figure 4. Arrhenius plot of CO desorption probabilities (inversely proportional to residence times) on 0.02 Pd ML (clusters mean size of (4.7 ± 2) atoms). The slope allows directly determining the CO adsorption energy. The good linearity of the curve ensures that the measurement was done far from saturation coverage even for the smallest studied clusters (the maximum coverage is 0.37 CO molecules per Pd surface atom) where the adsorption decreases due to the interaction between CO molecules. The low dispersion around the straight line gives information on the reliability of the measurements carried out.

pulse of CO from a Pd clusters array of mean particle size (4.7 ± 2) atoms (0.02 ML Pd). The rapid increase/fall of the signal (not resolved with our experimental setup), when the beam is ON/OFF, corresponds to CO adsorption/desorption from the alumina film while the slow increase/decrease of the signal corresponds to CO adsorption/desorption from the Pd clusters. These slow variations follow an exponential law with a time constant that equals the mean residence time of CO molecules on the clusters. An Arrhenius plot of the CO residence time versus temperature can be seen in Figure 4 for a collection of clusters of (4.7 ± 2) atoms mean size. The corresponding adsorption energy deduced from this graph is equal to 88.2 kJ/mol. For the smallest clusters (which corresponds to the Arrhenius plot of Figure 4), as the ratio [(surface of capture for CO molecules)/(number of Pd surface atoms)] is maximum, CO coverage reaches its maximum value for all measurements, which is equal to 0.37 CO molecules per Pd surface atom. This value is low enough to ensure that we were out of the region of high coverage where non linearity arises for all studied sizes. Furthermore, no changes in the value of CO adsorption energy have been measured during experiments (time scale 40 min to 1 h), that is, when performing several temperature ramps to extract the CO adsorption energy, each ramp gives the same value. This gives an indirect evidence for the absence of particle sintering upon CO exposure.

We took the highest care in the clusters elaboration in order to ensure similar nucleation and growth conditions for each studied size. Namely, the substrate temperature was monitored with 1 °C accuracy and the amount of deposited Pd was controlled by means of quartz microbalance that had been calibrated in an absolute way by Rutherford backscattering spectrometry (RBS). Uncertainties on the amount of deposited Pd are smaller than 3%. Deposition rate was kept constant throughout the whole set of experiments to 3×10^{13} atoms·cm^{-2}·s^{-1}.

In Figure 5, CO adsorption energy is plotted versus the size of the Pd clusters. Two different size regimes clearly appear: for particles of size typically larger than 2.3 nm, CO adsorption

dx.doi.org/10.1021/nl304741t | *Nano Lett.* XXXX, XXX, XXX−XXX

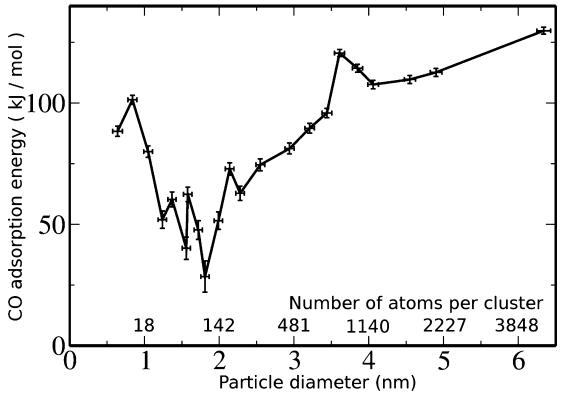

Figure 5. Evolution of CO adsorption energy with Pd clusters size. The nonmonotonous variations of the adsorption energy observed in the smallest size regime (i.e., diameter below 1.5 nm or below 100 atoms per cluster) are attributed to the molecular nature of clusters on that scale. An asymptotic trend tending to the previously reported value of bulk palladium is observed for the highest coverage. The evolution of the adsorption energy for particle size above 2 nm diameter (about 150 atoms per cluster) reveals the size effect on the electronic structure of the solid. (Detailed explanations about the origin of error bars can be found in Supporting Information).

energy increases quasi-monotonically with particle size, while for particle size typically smaller than 1.8 nm, a strongly irregular variation is found. The CO adsorption energy for the largest particle size (130.0 kJ/mol) is very close to the expected value for bulk Pd (138.2 kJ/mol),[53] which validates our experimental approach. This result was expected because the largest particle sizes in Figure 5 correspond to Pd deposits that exceed the coalescence threshold of the particles array. It is also worth to note that Figure 5 features a bump in the 3.5−4 nm size range that had already been reported for Pd clusters in the 2−4 nm size range on MgO (001).[54]

Between 3.5 and 2.3 nm the adsorption energy of CO decreases with shrinking cluster size. The tendency of the adsorption energy to decrease when downsizing the particles has already been observed in a recent study by Freund et al.,[55] for Pd clusters in the 2−8 nm size range grown on Fe_3O_4/Pt(111) with however much lower amplitude (relative variation of less than 20%). Freund et al.[55] have attributed this general trend to both the decreasing of the polarizability and the lattice parameter contraction when shrinking cluster size. This effect is not compensated in Pd clusters by low coordinated sites as it would be in other metals like Pt.[56] Conversely, narrow particle size distribution together with homogeneous particle environment allowed in our case the achievement of unmatched accuracy, which reveals important variations in energy. Adsorption energies down to 30 kJ/mol have been obtained, which is four times as low as the measured value for bulk Pd. At this point, it is worth to consider that the growth technique yields a size distribution that is at best as narrow as the Poisson distribution. This probably results in an overvaluation of the adsorption energy for particles of 1.8 nm mean size, due to convolution with those of slightly different size. One can hence presume that precise particle sizes within this narrow range could even exhibit lower values of adsorption energy than 30 kJ/mol. Though the nonmonotonous part of the curve in the small particle size regime might seem erroneous at first glance, this is obviously not the case. In fact, in this size range (5 to about 150 atoms) we are in the molecular regime for which the reactivity strongly depends on the number of atoms, which reveals their molecular nature within this size range. This has already been explored by reactivity experiments on mass-selected soft-landed clusters.[13−19]

A critical particle size cannot be precisely determined from the curve (Figure 5) to define the threshold of the small size regime within which the behavior of the particles is governed by their molecular nature. On the one hand, we observed that the adsorption starts varying in an irregular way for particle size smaller than 2.4 nm, namely particles of 250 atoms in average, which seems already quite large. On the other hand, it is tempting to identify this threshold with the particle size at which we measured the lowest adsorption energy, namely 1.8 nm, corresponding to about 100 atoms. Probably the transition between the nonscalable regime and the scalable regime is not abrupt and we can conclude that it lies between 150 and 200 atoms, region where molecular orbitals start to merge to bulk electronic bands, which are characteristic of solid state matter.

One important point to notice is the inherent limit to the quality of the size histogram one can reach using our growth method. The number of different size classes that can be found with enough high probability is given by a Poisson distribution and is at least equal to the square root of the mean number of atoms per cluster. Even if this number is low for small sizes, it becomes difficult to speak about monodisperse sets of clusters when the mean number of atoms per cluster is for example 100, where at least 20 different classes of size are present. Nevertheless, we measured for each Pd coverage only one adsorption energy and the corresponding signals have always been fitted nicely by only one single exponential function. This seems to be an oddity as each different size class has to contribute to the adsorption−desorption signal in a specific way. In fact, when measuring adsorption and desorption rates with our technique, we set a typical period of shutter operation from 2 to 4 s per cycle that impedes to measure long residence times, and our experimental setup is not able to measure residence times under 30 ms. In these conditions, observation is generally locked on the size that leads to the most compatible CO residence time in our time scale and temperature window of measurements.

Finally, one important aspect to consider in our experimental approach is the stability in shape of the clusters upon reaction with CO. At the operating temperatures (420−520 K), atom mobility is not weak enough to consider that the smallest particles remain totally stable during adsorption/desorption cycles. Important changes in the particle shape could thus happen and alter the measurement of the adsorption energy. Precisely, the adsorption energy would vary during the adsorption/desorption cycles, given that the particle morphology would evolve during the variations in coverage. As a result, the adsorption/desorption signal would not exhibit a purely monoexponential shape. However, we never observed significant deviations of the adsorption/desorption signal from its canonical monoexponential shape, even at the smallest particle sizes. This can have two possible origins: either CO adsorption energy does not significantly depend on the cluster shape or changes in morphology occur at a time scale that is too different from the temporal frame of measurement (i.e., much faster or much slower than the adsorption/desorption cycle) to yield an observable signature within this frame. Extending in time the adsorption/desorption cycle would allow to observe a hypothetical slow evolution of cluster structure if this one has a significant effect on adsorption energy. To investigate the effect

dx.doi.org/10.1021/nl304741t | Nano Lett. XXXX, XXX, XXX−XXX

of much faster modifications in the cluster shape, more sophisticated experiments need to be conducted, involving for instance the monitoring by GISAXS of the cluster morphology upon CO adsorption.

In conclusion, we have reported the original combination of a model system of supported metal clusters that exhibits a very low dispersion in cluster size and high environment homogeneity with a powerful experimental technique that allows retrieving reliable adsorption energies. By this combination, we succeeded in experimentally monitoring the evolution of a physicochemical property (adsorption energy in the present case) of a material from its molecular state (a few-atom clusters) to its solid state (bulklike clusters tending to form a complete metal layer). This study clearly shows that a cluster made of less than about one hundred atoms exhibits molecular properties. Importantly, this aspect has to be considered when conducting experiments on samples with such low particle sizes. In particular, the determination of cluster size from STM images may be unreliable for cluster in this size range if the tip-cluster interaction depends on the cluster size in a strongly non regular fashion, like adsorption energy does.

■ ASSOCIATED CONTENT

Supporting Information

Additional information and figures. This material is available free of charge via the Internet at http://pubs.acs.org.

■ AUTHOR INFORMATION

Corresponding Author

*E-mail: sitja@cinam.univ-mrs.fr.

Present Addresses

[§](S.L.M.) Institut de Chimie Moléculaire et des Matériaux d'Orsay, Université Paris Sud, UMR 8182, F-91405 Orsay cedex, France.

[∥](G.H.) Steinerstrasse 38, 53225 Bonn, Germany

Notes

The authors declare no competing financial interest.

■ ACKNOWLEDGMENTS

The authors would like to thank Gilles Renaud and the staff of the BM32 beamline of the European Synchrotron Radiation Facility (Grenoble, France) as well as the DFH-UFA (French-German University) organization for financial support. S.L.M. also thanks Marie D'Angelo and Emrick Briand (Institut des NanoSciences de Paris, France) for their help during RBS experiments.

■ REFERENCES

(1) Haynes, C. L.; Van Duyne, R. P. *J. Phys. Chem. B* **2001**, *105*, 5599−5611.

(2) Mulvaney, P. *Langmuir* **1996**, *12*, 788−800.

(3) New, R. M. H.; Pease, R. F. W.; White, R. L. *J. Vac. Sci. Technol., B* **1995**, *13*, 1089.

(4) *Nanocatalysis*; Heiz, U., Landman, U., Eds.; Springer-Verlag: Berlin Heidelberg, 2007.

(5) Che, M.; Bennett, C. O. *Adv. Catal.* **1989**, *36*, 55−172.

(6) Heiz, U.; Vanolli, F.; Sanchez, A.; Schneider, W.-D. *J. Am. Chem. Soc.* **1998**, *120*, 9668−9671.

(7) Yang, M. X.; Gracias, D. H.; Jacobs, P. W.; Somorjai, G. A. *Langmuir* **1998**, *14*, 1458−1464.

(8) Volokitin, Y.; Sinzig, J.; de Jongh, L. J.; Schmid, G.; Vargaftik, M. N.; Moiseev, I. I. *Nature* **1996**, *384*, 621−623.

(9) Wang, Z. L.; Petroski, J. M.; Green, T. C.; El-Sayed, M. A. *J. Phys. Chem. B* **1998**, *102*, 6145−6151.

(10) Gorer, S.; Ganske, J. A.; Hemminger, J. C.; Penner, R. M. *J. Am. Chem. Soc.* **1998**, *120*, 9584−9593.

(11) Klein, D. L.; Roth, R.; Lim, A. K. L.; Alivisatos, A. P.; McEuen, P. L. *Nature* **1997**, *389*, 699−701.

(12) Bezryadin, A.; Dekker, C.; Schmid, G. *Appl. Phys. Lett.* **1997**, *71*, 1273−1275.

(13) Eberhardt, W.; Fayet, P.; Cox, D. M.; Fu, Z.; Kaldor, A.; Sherwood, R.; Sondericker, D. *Phys. Rev. Lett.* **1990**, *64*, 780−783.

(14) Heiz, U.; Sanchez, A.; Abbet, S.; Schneider, W.-D. *J. Am. Chem. Soc.* **1999**, *121*, 3214−3217.

(15) Sanchez, A.; Abbet, S.; Heiz, U.; Schneider, W.-D.; Häkkinen, H.; Barnett, R. N.; Landman, U. *J. Phys. Chem. A* **1999**, *103*, 9573−9578.

(16) Judai, K.; Abbet, S.; Wörz, A. S.; Heiz, U.; Henry, C. R. *J. Am. Chem. Soc.* **2004**, *126*, 2732−2737.

(17) Tong, X.; Benz, L.; Kemper, P.; Metiu, H.; Bowers, M. T.; Buratto, S. K. *J. Am. Chem. Soc.* **2005**, *127*, 13516−13518.

(18) Kaden, W. E.; Wu, T.; Kunkel, W. A.; Anderson, S. L. *Science* **2009**, *326*, 826−829.

(19) Kaden, W. E.; Kunkel, W. A.; Sloan Roberts, F.; Kane, M.; Anderson, S. L. *J. Chem. Phys.* **2012**, *136*, 204705.

(20) Hayakawa, T.; Yasumatsu, H.; Kondow, T. *Eur. Phys. J. D.* **2009**, *52*, 95−98.

(21) Vajda, S.; Pellin, M. J.; Greeley, J. P.; Marshall, C. L.; Curtiss, L. A.; Balletine, G. A.; Elam, J. W.; Catillon-Mucherie, S.; Redfern, P. C.; Mehmood, F.; Zapol, P. *Nat. Mater.* **2009**, *8*, 213−216.

(22) Lee, S.; Lee, B.; Mehmood, F.; Seifert, S.; Libera, J. A.; Elam, J. W.; Greeley, J.; Zapol, P.; Curtiss, L. A.; Pellin, M. J.; Stair, P. C.; Winans, R. E.; Vajda, S. *J. Phys. Chem. C* **2010**, *114*, 10342−10348.

(23) Lim, D.-C.; Hwang, C.-C.; Ganteför, G.; Kim, D. K. *Phys. Chem. Chem. Phys.* **2010**, *12*, 15172−15180.

(24) Bonanni, S.; Aït-Mansour, K.; Harbich, W.; Brune, H. *J. Am. Chem. Soc.* **2012**, *134*, 3445−3450.

(25) Peters, S.; Peredkov, S.; Neeb, M.; Eberhardt, W.; Al-Hada, M. *Surf. Sci.* **2013**, *608*, 129−134.

(26) Young, N. P.; Li, Z. Y.; Chen, Y.; Palomba, S.; Di Vece, M.; Palmer, R. E. *Phys. Rev. Lett.* **2008**, *101*, 246103.

(27) Wortmann, B.; Mende, K.; Duffe, S.; Grönhagen, N.; von Issendorff, B.; Hövel, H. *Phys. Status Solidi B* **2010**, *247*, 1116−1121.

(28) Wepasnick, K. A.; Li, X.; Mangler, T.; Noessner, S.; Wolke, C.; Grossmann, M.; Ganteför, G.; Fairbrother, D. H.; Bowen, K. H. *J. Phys. Chem. C* **2011**, *115*, 12299−12307.

(29) Bardotti, L.; Tournus, F.; Pellarin, M.; Broyer, M.; Melinon, P.; Dupuis, V. *Surf. Sci.* **2012**, *606*, 110−114.

(30) Hartmann, H.; Popok, V. N.; Barke, I.; von Oeynhausen, V.; Meiwes-Broer, K.-H. *Rev. Sci. Instrum.* **2012**, *83*, 073304.

(31) Campbell, C. T. *Surf. Sci. Rep.* **1997**, *27*, 1−111.

(32) Henry, C. R. *Surf. Sci. Rep.* **1998**, *31*, 231−325.

(33) Libuda, J.; Freund, H. J. *Surf. Sci. Rep.* **2005**, *57*, 157−198.

(34) Valden, M.; Lai, X.; Goodman, D. W. *Science* **1998**, *281*, 1647−1650.

(35) Piccolo, L.; Henry, C. R. *J. Mol. Catal. A: Chem.* **2001**, *167*, 181−190.

(36) Johánek, V.; Laurin, M.; Grant, A. W.; Kasemo, B.; Henry, C. R.; Libuda. *Science* **2004**, *34*, 1639−1644.

(37) Boyen, H.-G.; Kästle, G.; Weigl, F.; Koslowski, B.; Dietrich, C.; Ziemann, P.; Spatz, J. P.; Riethmüller, S.; Hartmann, C.; Möller, M.; Schmid, G.; Garnier, M. G.; Oelhafen, P. *Science* **2002**, *297*, 1533−1536.

(38) Somorjai, G. A.; Rioux, R. M. *Catal. Today* **2005**, *100*, 201−215.

(39) Melinon, P.; Hannour, A.; Bardotti, L.; Prével, B.; Gierak, J.; Bourhis, E.; Faini, G.; Canut, B. *Nanotechnology* **2008**, *19*, 235305.

(40) Xie, X. N.; Chung, H. J.; Sow, C. H.; Wee, A. T. S. *Mater. Sci. Eng. R* **2006**, *5*, 1−48.

(41) Prévot, G.; Guesmi, H.; Croset, B. *Surf. Sci.* **2007**, *601*, 2017−2025.

(42) Leroy, F.; Renaud, G.; Létoublon, A.; Rohart, S.; Girard, Y.; Repain, V.; Rousset, S.; Coati, A.; Garreau, Y. *Phys. Rev. B* **2008**, *77*, 045430.
(43) Degen, S.; Krupski, A. K.; Kralj, M.; Langner, A.; Becker, C.; Solokowski, M.; Wandelt, K. *Surf. Sci.* **2005**, *576*, L57−L64.
(44) Hamm, G.; Barth, C.; Becker, C.; Wandelt, K.; Henry, C. R. *Phys. Rev. Lett.* **2006**, *97*, 126106.
(45) Marsault, M. Ph.D. Thesis, Université Aix-Marseille 2, France, 2010.
(46) Sitja, G.; Omar Uñac, R.; Henry, C. R. *Surf. Sci.* **2010**, *604*, 404−408.
(47) Hamm, G.; Becker, C.; Henry, C. R. *Nanotechnology* **2006**, *17*, 1943−1947.
(48) Renaud, G.; Lazzari, R.; Revenant, C.; Barbier, A.; Noblet, M.; Ulrich, O.; Leroy, F.; Jupille, J.; Borensztein, Y.; Henry, C. R.; Deville, J.-P.; Scheurer, F.; Mane-Mane, J.; Fruchart, O. *Science* **2003**, *300*, 1416−1419.
(49) Leroy, F.; Renaud, G.; Létoublon, A.; Lazzari, R. *Phys. Rev. B* **2008**, *77*, 235429.
(50) Renaud, G.; Lazzari, R.; Leroy, F. *Surf. Sci. Rep.* **2009**, *64* (8), 255−380.
(51) Sitja, G.; Marsault, M.; Leroy, F.; Le Moal, S.; Henry, C. R. *Int. J. Nanotechnol.* **2012**, *9*, 569−575.
(52) Henry, C. R. Surface Dynamics. In *The Chemical Physics of Solid Surfaces*; Woodruff, D. P., Ed.; Elsevier: Amsterdam, 2003; Vol. *11*, p 247.
(53) Engel, T.; Ertl, G. *J. Chem. Phys.* **1978**, *69* (3), 1267−1281.
(54) Henry, C. R.; Chapon, C.; Goyhenex, C.; Monot, R. *Surf. Sci.* **1992**, *272*, 283−288.
(55) Flores-Camacho, J. M.; Fischer-Wolfarth, J.-H.; Peter, M.; Campbell, C. T.; Schauermann, S.; Freund, H.-J. *Phys. Chem. Chem. Phys.* **2011**, *13*, 16800−16810.
(56) Ramsier, R. D.; Lee, K. W.; Yates, J. T. *Surf. Sci.* **1995**, *322*, 243−255.

dx.doi.org/10.1021/nl304741t | *Nano Lett.* XXXX, XXX, XXX−XXX

Supplementary information

(1) Thermal stability of Pd clusters arrays

The stability of Pd clusters arrays, grown at RT on a ultrathin alumina film on $Ni_3Al(111)$, has been studied *in situ* by STM under UHV by annealing at increasing temperature. Figure S1 displays two typical images of a 0.15 ML Pd deposit after subsequent annealing at 470 K and 670 K. At 470 K (Fig. S1(a)) the ordering of the particles is still perfect and equivalent to the original RT deposit. On the contrary, after annealing at 670 K (Fig. S1(b)), the particles organization is no more perfectly hexagonal and some particle sites seem empty. Indeed the measurement of the clusters density as a function of annealing temperature (Fig. S1(c)) shows that up to 600 K the clusters density is constant and equal to the defects density of the dot structure of the alumina film while at temperatures higher than 600 K the clusters density decreases. This means that clusters can "escape" from the trapping sites and coalesce with neighbouring clusters.

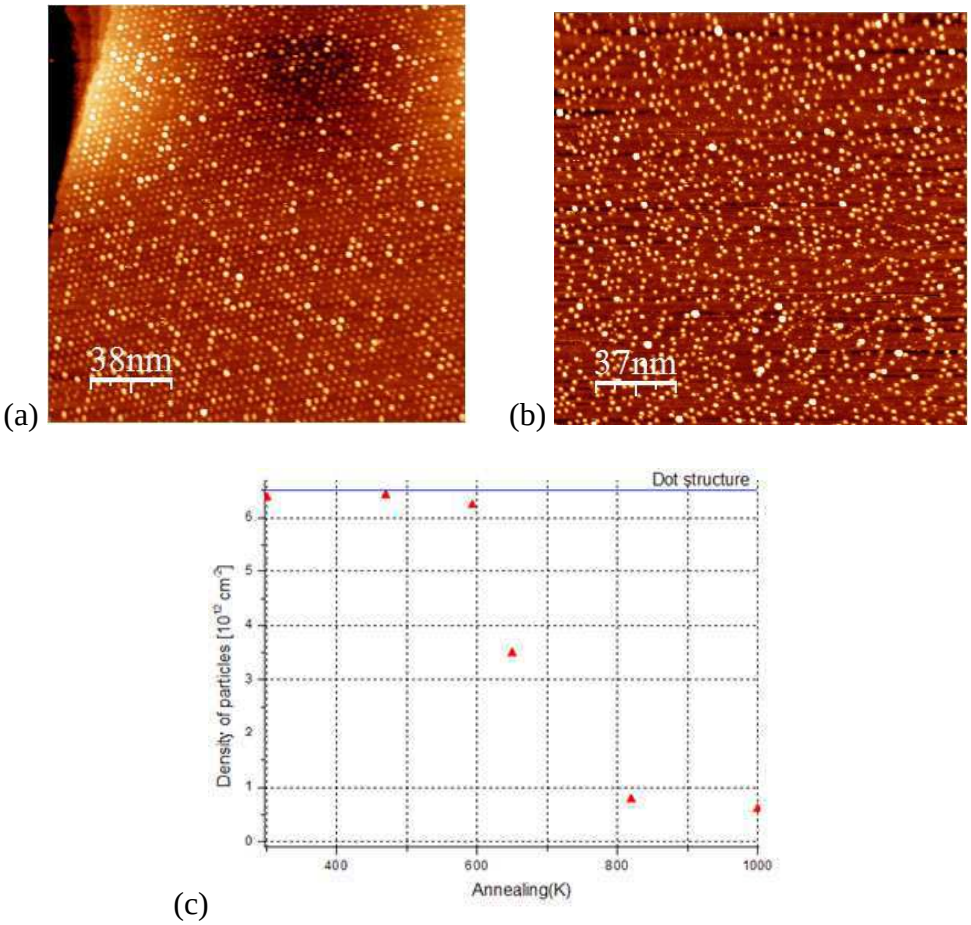

Figure S1: STM image of a RT Pd deposit (0.15 ML) after annealing (a) at 470 K and (b) at 670 K . In (c) the density of clusters is plotted as a function of annealing temperature. Above 600K clusters are mobile and coalesce.

(2) Analysis of GISAXS measurements

GISAXS is a very sensitive method to check the long range organisation of metal clusters on a flat surface[1]. Figure S2(a) presents an experimental GISAXS pattern of 0.5 ML of Pd deposited at RT on the ultrathin alumina film. The two fine rods appearing on each side of the central specular rod correspond to the small angle X-ray scattering by a regular array of clusters. Similarly to Bragg peaks for conventional bulk X-ray diffraction, the in-plane narrowness of these scattering rods is coming from the constructive interferences between X-ray waves scattered by a lattice of clusters. The long-range order is confirmed mapping the reciprocal space in the surface plane[2-4] by rotating the sample azimuth by steps of 1° over 60° (see fig. S3(a)). This map shows the presence of two equivalent variants of clusters arrays rotated by 24.54° in agreement with nc-AFM observations[6]. To fully characterize the organization of clusters, cuts of intensity parallel and perpendicular to the scattering rods have been extracted from the GISAXS patterns and analysed[3-5]. The fit performed with the IsGISAXS software[7] is based on a model of truncated spheres for the clusters shape and on tuneable lattice parameter and domain size for the array. The quality of the fit and the overall agreement of the experimental pattern with the GISAXS simulation is clearly evident (see Fig.2 (b)-(d)). In this example for a Pd coverage of 0.5 ML (i.e. cluster mean size of (118$\pm$11) atoms) the GISAXS analysis shows that Pd clusters are slightly truncated spheres with mean size 1.9±0.5 nm diameter and 1.2±0.3 nm height. The height-to-radius ratio of the clusters is stable as function of the coverage and is equal to 1.26±0.46. The deduced periodicity of the array is 4.14±0.05 nm in perfect agreement with STM data. Additionally the domain size is estimated to be 240±20 nm. The best fit shows that the remaining small diffuse scattering measured in between the scattering rods does not arise from the width of the size distribution but from a “Debye Waller” like contribution of the Pd clusters which are randomly displaced away from the array nodes by a gyration radius of 0.32±0.05 nm.

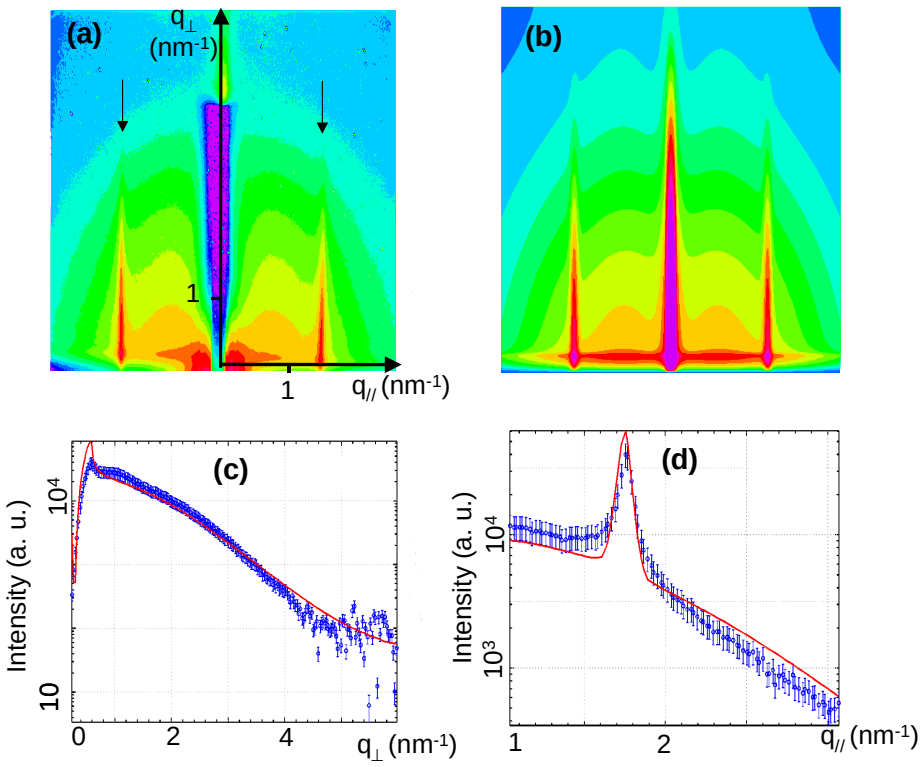

Figure S2: (a) GISAXS experimental pattern of Pd clusters on alumina thin film (0.5 ML). The black arrows show the scattering rods from the clusters array. (b) Best GISAXS simulation based on the deduced parameters of the fit. (c) and (d) GISAXS cuts of the X-ray scattering rods parallel and perpendicular to the surface plane: data (square) and fit (solid line).

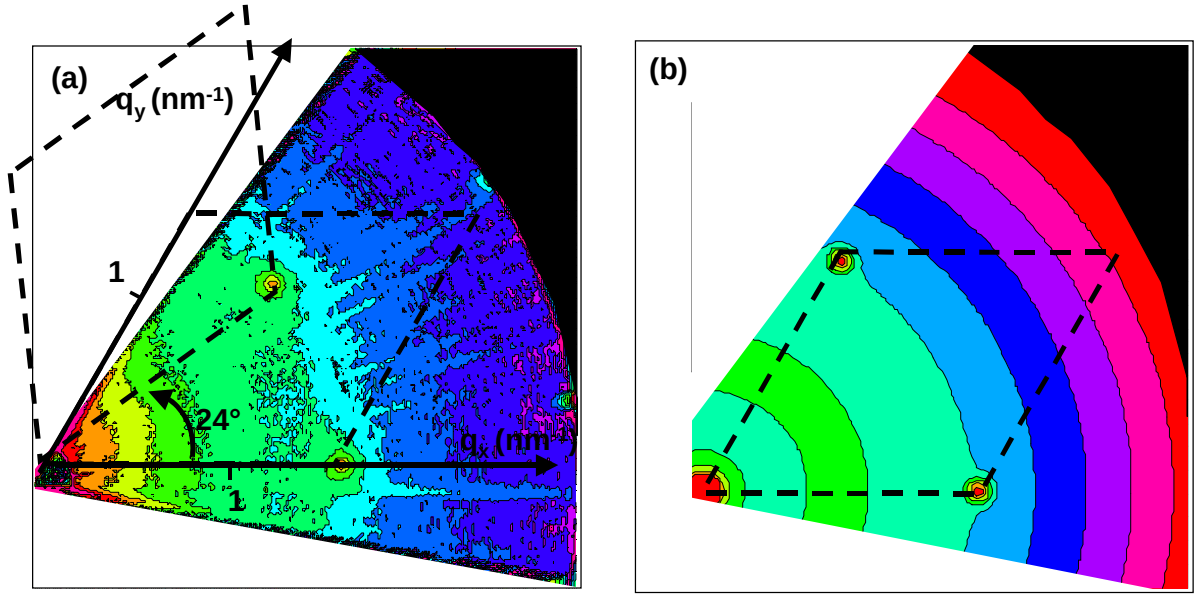

Figure S3: (a) Experimental and (b) simulated in-plane maps of the reciprocal space of Pd clusters arrays. The lozenges show the elementary hexagonal unit cells of the array of Pd clusters. In the experimental map two variants are clearly visible rotated by 24.54°.

(3) Error bars for nanoparticle size and CO adsorption energy values

Figure 5 gives results of our study with error bars for the size and for the measured energy. It is important to explain how these bars have been obtained.

(a) Error bars for nanoparticle size

Several hints give us the certitude that we get a Poisson distribution despite the bad quality of size histogram we can expect from STM images like Figure 1 of the article.

First, the quasi-absence of diffusion in GISAXS patterns (Figure 2 of the article) is incompatible with wide distribution. This apparent discrepancy arises from the following reason: X-rays probe core electronic orbitals whereas STM is only sensitive to valence levels. These valence levels are affected by mutual interaction of the atoms in the cluster. As a result, apparent size in STM can dramatically change by adding or removing one single atom or even by changing the place of one atom.

Secondly, our Monte Carlo simulations[8] show that Poisson distribution can be achieved even with very weak trapping wells.

Third, GISAXS patterns at very early state of nucleation (Figure 2b) and STM images for very small deposits demonstrate that these wells are not so weak. Thus, we expect to have a Poisson distribution as consequence of these 3 hints coupled to the very well ordered array of wells at the surface.

Another indirect proof that nucleation occurs everywhere from the beginning is that even for the smallest deposit (ie. 4.7 atoms per cluster) a significant signal has been measured by MBRS (Figures 3 and 4 of the article). This would not be possible with mainly empty sites and quite big clusters.

For perfect random process (the probability for an atom to condense at surface and arrive to one cluster does not depend on the cluster), the probability to have a cluster with N atoms when the mean size is x is given by the Poisson distribution $P_x(N)$: $P_x(N) = \frac{e^{-x} x^N}{N!}$

It can be proved that for X >> 1, which corresponds to the Normal distribution (also known as Gaussian distribution), $G_x(y) = \frac{1}{\sqrt{2\pi x}} e^{\frac{(y-x)^2}{2x}}$ is an approximation of Poisson distribution.

For more clarity Figure S4 displays for various particles mean sizes (x) both Poisson and Gaussian distributions. In each figure, red histograms correspond to the Poisson distribution and solid black lines are related to the Gaussian distribution. For each mean size, the left graph displays the probability as a function of the number of atoms in particles, and the right graph displays the probability as a function of the effective diameter of particles $\left(\sqrt[3]{\frac{12N}{\pi}}\right)$ (in case of clusters with a hemispherical shape and an occupied volume per atom of 1.)

Even for the smallest clusters sizes we have (i.e. 4.7 atoms per particle), the Gaussian distribution is not very far from the Poisson distribution that we expect to actually have on our sample. The width of the Gaussian distribution is proportional to $\sigma = \sqrt{x}$. The full width at half maximum (FWHM) is given by the formula: $FWHM = 2\sqrt{2\ln 2} \times \sigma \approx 2.355\sigma$.

For clusters large enough (i.e. when $1/\sigma << 1$) FWHM can be easily worked out as a function of the cluster effective diameter. If α is the proportional coefficient that links $\left(\sqrt[3]{N}\right)$ with the diameter D of a cluster (i.e. $D = \alpha\sqrt[3]{N}$) then the standard deviation is $\Delta D = \alpha\frac{\sqrt{\alpha}}{3}\frac{1}{\sqrt{D}}$ and $FWHM \approx 2.355\frac{\alpha\sqrt{\alpha}}{3}\frac{1}{\sqrt{D}}$. For palladium hemispheric clusters, α = 0.383 when D is expressed in nm.

In figure 5, error bars are calculated by adding the systematic error of 3% on the amount of deposited Pd (as determined from calibration by Rutherford Backscattering Spectrometry) to 2σ (it means one standard deviation). For large particles, the 3% error is the preponderant term, while for smaller particles the intrinsic quality of the Poisson distribution is the limitation. As for Poisson distribution, relative error varies inversely to the square root of the mean numbers of atoms per particle, the frontier where σ = 3 is for particles of 1111 atoms.

(b) Error bars on the CO adsorption energy

Error bars for the adsorption energy are measured directly from the quality of Arrhenius fit. After having obtained the pre-exponential factor and the adsorption energy, we fix to different values the adsorption energy and fit again the pre-exponential factor until the fit is obviously out of experimental points. This procedure gives the estimated error for a given size.

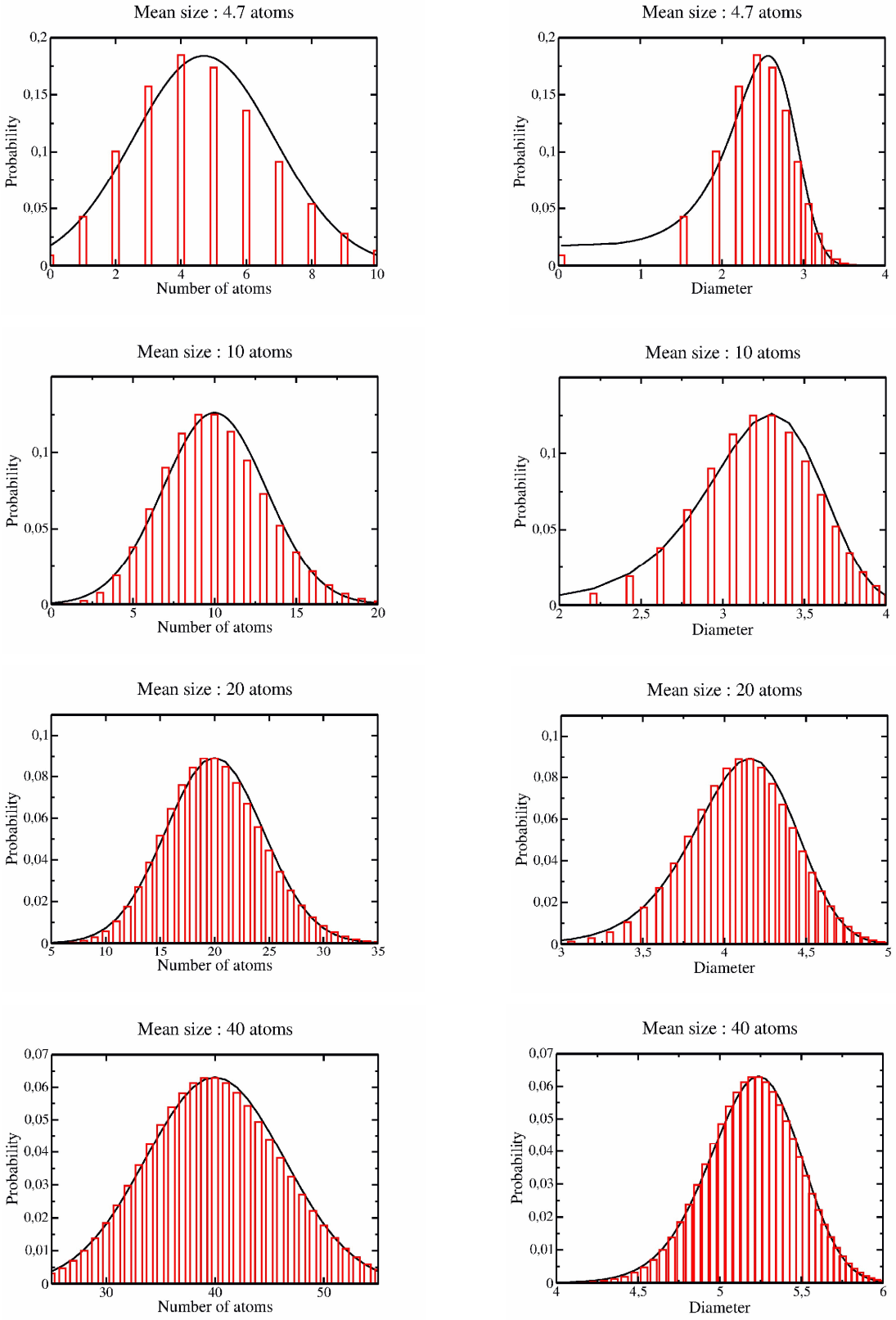

Figure S4: Poisson (histogram) and Gaussian (solid line) distributions for different particle mean sizes as a function of atoms number and effective diameter.

References

(1) Renaud, G.; Lazzari, R.; Revenant, C.; Barbier, A.; Noblet, M.; Ulrich, O.; Leroy, F.; Jupille, J.; Borensztein, Y.; Henry, C. R.; Deville, J.-P.; Scheurer, F.; Mane-Mane, J. ; Fruchart, O. *Science* **2003**, *300***,** 1416-1419.

(2) Stein, G.E.; Kramer, E.J.; Li, X.; Wang, J. *Phys. Rev. Lett*., **2007**, *98*, 086101.

(3) Leroy, F.; Renaud, G.; Létoublon, A. ; Rohart, S. ; Girard, Y. ; Repain, V. ; Rousset, S. ; Coati, A. ; Garreau, Y. *Phys. Rev. B* **2008**, ***77***, 045430.

(4) Leroy, F.; Renaud, G.; Létoublon, A.; Lazzari, R. *Phys. Rev. B* **2008**, *77*, 235429.

(5) Renaud, G.; Lazzari, R. and Leroy, F. *Surface Science Report*. **2009**, *64(8)*, 255-380.

(6) Hamm, G.; Barth, C.; Becker, C.; Wandelt, K.; Henry, C.R. *Phys. Rev. Lett.* **2006**, *97*, 126106.

(7) Lazzari, R., *J. Appl. Crystallography*, **2002**, *35*, 406-421.

(8) Sitja, G.; Omar Uñac, R.; Henry, C. R. *Surf. Sci.* **2010**, *604*, 404-408.

Conclusion et perspectives

DAns ce mémoire j'ai mis l'accent sur mes activités de recherches les plus récentes dédiées à l'étude de la dynamique des surfaces hors-équilibre : le démouillage de films solides et les instabilités morphologiques induites par électromigration. Pour être complet, durant ces années passées à Marseille, j'ai aussi conduit des études *in situ* de croissance de nanomatériaux par des techniques de diffusion/diffraction des rayons X qui ont notamment été synthétisées dans un article de revue [26]. Cette expérience acquise dans l'utilisation des rayons X a été largement mise à profit au CINaM pour répondre à des questions précises telles que le facettage des fronts de démouillage des films solides (voir chapitre correspondant et articles [18–20]). Les expériences de diffraction de rayons X nous ont aussi permis de mettre en évidence que les films de Si/SiO_2 sous contraintes planaires bi-axiales ($\sim 1\%$ par rapport au paramètre de maille nominal) relaxent complètement pendant le démouillage. Cette relaxation élastique modifie la dynamique de démouillage par une légère augmentation de la densité de nanocristaux formés comme cela est attendu théoriquement [86]. En plus des études menées sur le démouillage solide et les phénomènes d'électromigration, nous avons aussi étudié, par diffraction X de surface, les déformations élastiques induites par les "défauts de surface" que sont les marches atomiques [87] en collaboration avec Bernard Croset et Geoffroy Prévot de l'INSP (Paris VI) ainsi qu'Alessandro Coati du synchrotron SOLEIL et Yves Garreau de MPQ (Paris VII). Ces études structurales nous ont permis d'accéder au monopole/dipole de force que constitue une marche atomique. Elles complètent donc les études que nous avons menées sur la dynamique des instabilités de mise en paquet et de méandrage des marches atomiques par électromigration. Sur un plan plus théorique, et toujours en lien avec les marches atomiques, nous avons étudié la forme d'équilibre d'un cristal dans un champ de force en particulier le comportement universel de la partie arrondie qui jouxte une facette cristallographique [88]. Enfin avec l'équipe "agrégats et catalyse" du CINaM mon expérience des rayons X a été utile pour étudier la croissance auto-organisée d'agrégats de Pd comme cela est détaillé dans la dernière partie de ce manuscrit [82].

Dans la continuité de ce travail je souhaite, pour les trois prochaines années, approfondir les questions relatives à la dynamique des surfaces en

abordant un point clé : la dynamique de la ligne triple. En effet il a été reconnu depuis longtemps que la ligne triple joue un rôle essentiel dans les processus physiques de transfert de matière. C'est un sujet qui a largement été abordé pour les liquides, mais relativement peu pour les solides malgré l'importance technologique des films minces dans les composants actuels.

Historiquement, la classification des modes de croissance des solides s'est largement inspirée des concepts de mouillage des liquides. Dans le livre de De Gennes, Brochard et Quéré "*Capillary and Wetting Phenomena*", le mouillage des liquides est classé en trois catégories : le mouillage total qui correspond au mode de croissance couche/couche atomique pour les solides (mode dit Van der Merwe). Le mouillage partiel qui a son équivalent pour les solides dans le mode de croissance dit Volmer-Weber et enfin le pseudo-mouillage partiel auquel on peut associer le mode de croissance Stranski-Krastanov pour les solides (présence d'un film précurseur mouillant puis formation d'agrégats tridimensionnels). Notons que l'un des articles les plus importants en science des surfaces, celui de Mullins [2] sur les processus de gravure aux joints de grain, propose de considérer que les angles à la ligne triple entre les grains et la surface libre sont pilotés par les angles de contact d'équilibre de Young. Cette condition est aujourd'hui toujours utilisée dans des problèmes variés d'évolution morphologique de surface impliquant la ligne triple. On peut citer en 1986, les travaux de Srolovitz et Safran qui l'ont utilisée pour décrire l'ouverture circulaire d'un trou dans un film mince supporté en condition de mouillage partiel [89]. Les travaux de Wong *et al.* en 2000 se sont appuyés sur la même approche pour traiter un problème similaire impliquant le retrait d'un film formant un front droit [3]. Citons encore Schmid *et al.* [90] qui ont interprété le mouvement non-brownien de nanocristaux sur un substrat par une réaction asymétrique à la ligne triple conduisant à des conditions d'angles de contact de Young différentes devant et derrière les nanocristaux. A aucun moment n'est remise en cause la question de la validité des angles de contact à la ligne triple de Young, alors même que ces études sont menées hors-équilibre. Ce point est d'autant plus étonnant qu'il est connu depuis longtemps que dans les liquides, selon qu'un front avance ou recule, l'angle de contact avec le substrat n'est pas le même. Cette question mérite donc

qu'on s'y intéresse.

Les différences fondamentales entre les solides et les liquides vis-à-vis de la dynamique de la ligne triple sont : (i) un mécanisme de transport de matière par diffusion de surface au lieu d'un écoulement piloté par les propriétés hydrodynamiques des liquides, (ii) l'anisotropie des énergies de surfaces (facettes) et celle des énergies de diffusion de surface et (iii) les contraintes élastiques présentes en cas d'hétéro-épitaxie. Ces différences entre les liquides et le solides posent trois questions fondamentales que nous souhaitons aborder :

- Comment la condition de Young d'équilibre à la ligne triple est elle modifiée hors-équilibre, par exemple pendant le mouillage ou le démouillage d'un film solide ?
- Comment une réaction à la ligne triple modifie sa dynamique ?
- Quelles sont les conséquences d'hétérogénéités de surface (chimique/topographique) sur le comportement de la ligne triple ?

Dans la continuité des études que nous avons menées sur le démouillage des films solides, notamment dans le cadre de l'ANR P-NANO "DEFIS", je souhaiterai donc traiter ces questions relatives aux propriétés locales, hors-équilibre, de la ligne triple solide-solide-vide (ou solide-solide-vapeur). Ce projet de recherche est financé dans le cadre d'un projet ANR-Blanc pour les années 2014-2018. Nous combinerons la microscopie LEEM, qui permettra de suivre *in situ* le déplacement de la ligne triple et donc de connaître sa dynamique, et la microscopie en champ proche qui nous permettra de caractériser avec une haute résolution sa morphologie. Pour ce, nous avons récemment couplé au LEEM, sous ultravide, un microscope STM/AFM de chez Omicron (voir figure III.9). Cela a nécessité de fabriquer au CINaM un porte-échantillon compatible entre les deux instruments. Cette combinaison unique en France entre ces deux instruments devrait nous permettre d'aborder cette problématique scientifique. Notre collaboration avec les théoriciens Olivier Pierre-Louis (ILM, Lyon) et Yukio Saito (Keio University, Tokyo) est aussi un atout indéniable.

Sur le plan des systèmes physiques, nous nous appuierons sur notre connaissance du couple Si/SiO_2 pour étudier la dynamique de la ligne triple pendant le démouillage. Ce système présente aussi l'intérêt d'être ré-

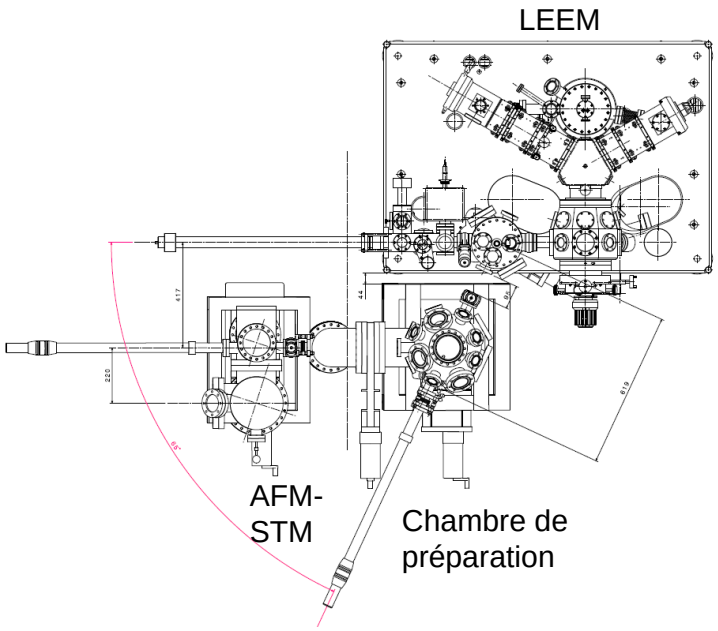

Figure III.9 *– Plan de l'ensemble expérimental actuel comprenant le LEEM, une chambre de préparation de surface et un microscope AFM-STM de chez Omicron.*

actif à haute température selon la réaction $Si_{(s)} + SiO_2 \rightarrow 2\,SiO_{(g)}$ ce qui devrait nous permettre de mettre en lumière le rôle de la réaction sur l'angle de contact et sur la dynamique de la ligne triple. Trois approches sont envisagées pour ces études réactionnelles qui s'appuient sur quelques résultats préliminaires (voir figure III.10) :

- La réaction à haute température $Si_{(s)} + SiO_2 \rightarrow 2\,SiO_{(g)}$ concomitante au démouillage d'un film mince de Si produit une gravure dans le substrat de SiO_2. Comment la dynamique de la ligne triple du film démouillant est modifiée par la cinétique de la réaction et la gravure du substrat ?
- A l'inverse pour un film de SiO_2 sur un substrat de Si, un recuit haute température conduit à la décomposition de l'oxyde par nucléation et croissance de domaines désoxydés de forme circulaire (voir figure III.10(a)). Comment le recul de la ligne triple SiO_2/Si/vide est-il piloté par la cinétique de réaction ?

– Pour des nanocristaux de Si sur SiO_2 obtenus par démouillage, la réaction $Si_{(s)} + SiO_2 \rightarrow 2\ SiO_{(g)}$ semble provoquer un mouvement désordonné de ces nanocristaux et simultanément la formation de trous dans le substrat de SiO_2 (voir figure III.10(b)-(c)). Quel est le rôle de la ligne triple dans ce processus ?

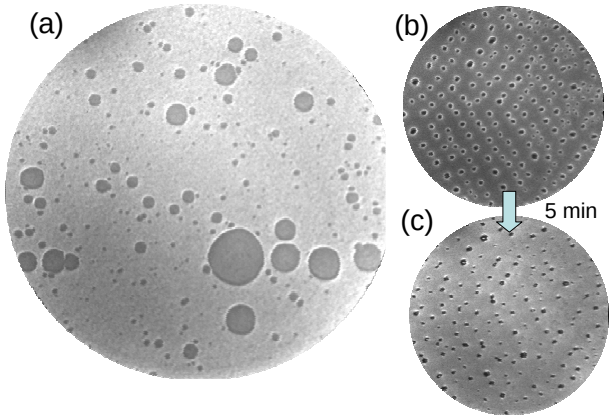

Figure III.10 *– (a) Image LEEM de la décomposition partielle de SiO_2 sur un substrat de Si (l'oxyde apparaît en gris clair et le silicium nu en gris foncé). Champ de vue 25 μm. (b)-(c) Images LEEM, à 5 min d'intervalle, de la réaction à 1000°C de nanocristaux de Si (obtenus par démouillage) avec le substrat de SiO_2. Les nanocristaux de Si ont disparu et ont laissé place à des trous dans la couche de SiO_2. Champ de vue 15 μm.*

Pour terminer sur le rôle des hétérogénéités du substrat sur la dynamique de la ligne triple d'un film supporté, nous envisageons, en collaboration avec le CEA-Léti, de fabriquer des substrats SOI dont la couche de SiO_2 sous-jacente au film de Si est nanostructurée. L'objectif est d'étudier dans quelle mesure la topographie du substrat peut conduire à un phénomène d'ancrage local de la ligne triple lors du démouillage solide.

La compréhension précise de l'influence de ces paramètres doit nous permettre de proposer des méthodes pour piloter les processus de transfert de matière et ainsi contrôler par exemple la formation par démouillage de nanocristaux ordonnés de taille calibrée.

A plus long terme, et dans le cadre d'un projet instrumental, je souhaiterai apporter des développements à la microscopie LEEM au laboratoire. Le fonctionnement de ce microscope suit les mêmes principes généraux

que ceux utilisés en microscopie électronique en transmission ou en microscopie optique, i.e. basés sur la nature ondulatoire de l'onde électromagnétique. De ce fait il est possible, en principe, d'utiliser toute la panoplie des phénomènes interférentiels pour améliorer le contraste des images et accéder à de nouveaux modes d'imagerie. En particulier l'holographie électronique a connu un fort développement ces dix dernières années en s'appuyant sur la microscopie électronique à transmission. A l'aide des déphasages résultant de la présence de champs dans un matériau il a été possible d'obtenir un contraste magnétique ou électrique. Cette technique a aussi permis d'augmenter considérablement le pouvoir de résolution spatial en particulier en mettant en évidence localement des déformations élastiques de quelques millièmes de paramètre de maille. Aujourd'hui ces développements pourraient aussi être apportés à un microscope LEEM. Ils permettraient d'accéder à de nouveaux champs d'études. En particulier cartographier *in situ* les champs magnétiques ou électriques à la surface d'un matériau avec une résolution nanométrique aurait de très nombreuses applications soutenant la comparaison avec les meilleurs microscopes LEEM ayant un canon à électrons polarisés en spin.

Quatrième partie

Curriculum Vitae et vie scientifique

CURRICULUM VITAE

Frédéric Leroy

Maitre de conférence - Aix-Marseille Université

96 Chemin de Palama, Villa 42
13013 Marseille
06 60 36 28 24
leroy@cinam.univ-mrs.fr
http://www.cinam.univ-mrs.fr/cinam/index.php

Formations/Diplômes

2013 **Habilitation à diriger des recherches de l'Université Aix-Marseille**, "*Dynamique hors équilibre : Quelques exemples en physique des surfaces*".

Composition du jury :
- Luc Barbier (CEA-Saclay) : Rapporteur
- Nick Barrett(CEA-Saclay) : Examinateur
- Nicolas Eustathopoulos (CNRS) : Membre invité
- Claude Henry (CNRS) : Examinateur
- Martin Hÿtch (CNRS) : Rapporteur
- Jean-Marc Layet (Aix-Marseille Université) : Président
- Pierre Müller (Aix-Marseille Université) : Examinateur
- Sylvie Rousset (CNRS) : Rapporteur

2001 – 2004 **Thèse de doctorat de l'Université Joseph Fourier**, *Grenoble*, Spécialité : Physique, "*Diffusion centrale des rayons X en incidence rasante appliquée à l'étude in situ de la croissance de nanostructures : Vers la croissance auto-organisée*".

Composition du jury :
- Harald Brune (EPFL) : Examinateur
- Joël Chevrier (Université Joseph Fourier, Grenoble) : Examinateur
- Bernard Croset (CNRS) : Rapporteur
- Jean-René Régnard (Université Joseph Fourier, Grenoble)
- Gilles Renaud (CEA-Grenoble)
- Ian Robinson (University College of London) : Président et Rapporteur

2000 – 2001 **DEA de physique des matériaux : des nanostructures aux grands instruments**, *Université Joseph Fourier*, Grenoble.

Classement : 1er

1999 – 2000 **Agrégation de Sciences physiques (option physique)**.

Classement national : 62ème

1996 – 1999 **École Nationale Supérieure de Physique de Grenoble**.

Spécialité : Matériaux Fonctionnels

Expériences de recherche

2005 à Aujourd'hui **Maître de conférence à Aix-Marseille Université**.
- Démouillage solide de films minces de silicium et germanium sur silice
- Electromigration sur les faces vicinales de silicium
- Croissance auto-organisée et caractérisation par GISAXS *in situ* d'agrégats de Pd sur $Al_2O_3/Ni_3Al(111)$
- Mesures par diffraction des rayons X des déformations induites par les marches atomiques

2004 – 2005 **Post-doctorant à l'institut Max-Planck de physique du solide**, Stuttgart, Allemagne.
- Etude par microscopie à effet tunnel et spectroscopie d'absorption X de la croissance d'architectures 2D organométallique sur des surfaces métalliques.

2001 – 2004 **Thèse de doctorat au CEA-Grenoble**.

Diffusion centrale des rayons X en incidence rasante appliquée à l'étude *in situ* de la croissance de nanostructures : Vers la croissance auto-organisée

Expériences d'enseignement

2005 à Aujourd'hui **Maître de conférence à Aix-Marseille Université**, UFR Sciences.
Département de rattachement : Physique
- Formation principale : "Sciences Physique-Chimie"
- Formations secondaires : "Sciences pour l'ingénieur" ; "Sciences de la Vie et de la Terre" ; "Math-Info"

2001 – 2004 **Moniteur à l'Université Joseph Fourier**, Grenoble.
IUT Mesures Physiques
- Enseignements de physique des matériaux

Responsabilités administratives

2013 – 2017 **Membre du projet ANR Blanc *LOTUS***.
Dynamique de la ligne triple solide-solide-vide

2009 – **Membre du comité de programme du synchrotron SOLEIL**.
Propriétés électroniques et magnétiques de la matière/ surfaces et interfaces

2009 – 2011 **Coordinateur national du projet ANR P-NANO *DEFIS***.
Démouillage de Films Solides

2009 – 2011 **En délégation au CNRS**, *Projet de recherche : Démouillage solide de films minces par LEEM.*

2008 – 2011 **Membre élu du département "sciences de la matière"**, *Université Paul-Cézanne*, Marseille.

2008 – 2011 **Membre élu du conseil de laboratoire**, *CINaM*, UMR 7325.

2011 **Membre du comité de sélection**, *Maître de Conférence N°0342 publié en 33/35 ème section*, Université Paul Cézanne (Aix-Marseille 3).

2005 – 2008 **Membre du projet ANR P-NANO *Nanomorphogénèse***.

Juillet 2008 **Co-organisateur de l'école d'été NanoSteps**, *Centre CNRS, Cargese, Corse.*

2008 **Membre du comité de sélection**, *Maître de Conférence N°0568S publié en 28 ème section*, Université Paul Cézanne (Aix-Marseille 2).

2008 **Membre du comité de sélection**, *Maître de Conférence N°0335 publié en 28 ème section*, Université Paul Cézanne (Aix-Marseille 3).

Responsabilités d'encadrement

2009 – **Thèse : Thibault Passanante**.
Démouillage de films solides de Ge et Si sur SiO_2

2012 – 2013 **ATER : Oualid Ourdjini**.
Désoxydation de films chimiques minces de silice sur silicium par LEEM

2009 – 2011 **Post-doc : Ezra Bussmann**.
Démouillage de films solides dans le système "Silicon-On-Insulator"

2009 **Stage M2 : Thibault Passanante**.
Démouillage de films solides de Si sur SiO_2

2007 – 2008 **Post-doc : Daniela Karashanova**.
Electromigration sur les surfaces vicinales de Si

2008 **Stage M2 : Xu Feng**.
Surface Strain Anisotropy of Monocrystalline Surfaces

2005 **Diploma thesis : Robin Ohmann**.
Rastertunnelmikroskopie und -spektroskopie an molekularen Nanostrukturen

ARTICLE DE REVUE :

G. Renaud, R. Lazzari and **F. Leroy**

"*Probing surfaces and interfaces morphology with Grazing Incidence Small Angle X-Ray Scattering*" Surface Science Report. 64(8), 255-380 (2009)

ARTICLES

Démouillage de films solides :

[1] E. Bussmann, F. Cheynis, **F. Leroy**, and P. Müller
"*Thermal instability of silicon oxide and silicon on insulator thin films measured by low energy electron microscopy*" IOP Conf. Ser. : Mater. Sci. Eng., 12-012016 (2010)

[2] E. Bussmann, F. Cheynis, **F. Leroy**, P. Müller, O. Pierre-Louis
"*Dynamics of solid thin-film dewetting in the silicon-on-insulator system*" New Journal of Physics 13, 043017 (2011)

[3] F. Cheynis, E. Bussmann, **F. Leroy**, T. Passanante, P. Müller
"*Dewetting Dynamics of silicon-on-insulator thin-film*" Phys. Rev. B 84, 245439 (2011)

[4] **F. Leroy**, F. Cheynis, T. Passanante, P. Müller
"*Dynamics, anisotropy, and stability of silicon-on-insulator dewetting fronts*" Phys. Rev. B 85, 185414 (2012)

[5] F. Cheynis, E. Bussmann, **F. Leroy**, T. Passanante, P. Müller
"*Stress effects on solid-state dewetting of nano-thin films*" Int. J. Nanotechnol., Vol.9 (3-7) 396, (2012)

[6] F. Cheynis, **F. Leroy**, T. Passanante, and P. Müller
"*Agglomeration dynamics of germanium islands on a silicon oxide substrate : A grazing incidence small-angle x-ray scattering study*" Appl. Phys.

Lett. 102, 161603 (2013)

[7] **F. Leroy**, F. Cheynis, T. Passanante, and P. Müller
"*Influence of facets on solid state dewetting mechanisms : Comparison between Ge and Si on SiO_2*" Phys. Rev. B 88, 035306 (2013)

[8] F. Cheynis, **F. Leroy**, and P. Müller
"*Dynamics and instability of solid-state dewetting*" C.R. Physique 14, 578-589 (2013)

Electromigration sur les surfaces vicinales de silicium :

[1] **F. Leroy**, P. Müller, J. J. Métois, and O. Pierre-Louis
"*Vicinal silicon surfaces : From step density wave to faceting*" Phys. Rev. B 76, 045402 (2007).

[2] D. Karashanova, JJ. Métois, **F. Leroy**, P. Müller
"*Is it possible to use external stress to tune silicon surface morphology ?*" Mat. Sci. Semi. Process. 12, 12-15 (2009)

[3] **F. Leroy**, D. Karashanova, M. Dufay, J.-M. Debierre, T. Frisch, J.-J. Métois, P. Müller
"*Step bunching to step meandering transition induced by electromigration on Si(111) vicinal surface*" Surf. Sci. 603 507-512 (2009).

Diffusion centrale des rayons X en incidence rasante appliquée à la croissance de nanostructures :

[1] G. Renaud, R. Lazzari, C. Revenant, A. Barbier, M. Noblet, O. Ulrich, **F. Leroy**, J. Jupille, Y. Borensztein, C. R. Henry, J. P. Deville, F. Scheurer, J. Mane-Mane and O. Fruchart
"*Real-time monitoring of growing nano-particles*" Science 300, 1416 (2003).

[2] **F. Leroy**, C. Revenant, G. Renaud, R. Lazzari
"*In situ GISAXS study of the growth of Pd on MgO(001)*" Appl. Surf. Sci. 238, 233-237 (2004)

[3] C. Revenant, **F. Leroy**, R. Lazzari, G. Renaud and C. R. Henry
"*Quantitative analysis of grazing incidence small angle X-ray scattering Pd/MgO(001) growth*" Phys. Rev. B 69, 035411 (2004).

[4] **F. Leroy**, R. Lazzari and G. Renaud
"*Effects of near-neighbor correlations on the diffuse scattering from a one-dimensional paracrystal*". Acta Cryst. A 60, 565-581 (2004).

[5] **F. Leroy**, G. Renaud, A. Letoublon, R. Lazzari, C. Mottet, J. Goniakowski
"*Self-Organized Growth of Nanoparticles on a Surface Patterned by a Buried Dislocation Network*" Phys. Rev. Lett. 95, 185501 (2005).

[6] **F. Leroy**, R. Lazzari and G. Renaud
"*X-ray scattering from stepped and kinked surfaces : an approach with the paracrystal model*" Surf. Sci. 601, 1915-1929 (2007).

[7] C. Revenant, **F. Leroy**, G. Renaud, R. Lazzari, A. Létoublon, T. Madey
"*Structural and morphological evolution of Co on faceted Pt/W(111) surface upon thermal annealing*" Surf. Sci. 601, 3431 (2007).

[8] R. Lazzari, **F. Leroy** and G. Renaud
"*Grazing-incidence small-angle x-ray scattering from dense packing of islands on surfaces : Development of distorted wave Born approximation and correlation between particle sizes and spacing*" Phys. Rev. B 76, 125411 (2007).

[9] R. Lazzari, G. Renaud J. Jupille and **F. Leroy**
"*Self-similarity during growth of the Au/TiO2 (110) model catalyst as seen by the scattering of x-rays at grazing-angle incidence*" Phys. Rev. B 76, 125412 (2007).

[10] **F. Leroy**, G. Renaud, A. Létoublon, S. Rohart, Y. Girard, V. Repain, S. Rousset, A. Coati, and Y. Garreau
"*Kink ordering and organized growth of Co clusters on a stepped Au(111) surface : A combined grazing-incidence x-ray scattering and STM study*" Phys. Rev. B 77, 045430 (2008).

[11] **F. Leroy**, G. Renaud, A. Létoublon, R. Lazzari
"*Growth of Co on Au(111) studied by multiwavelength anomalous grazing-*

incidence small-angle x-ray scattering : From ordered nanostructures to percolated thin films and nanopillars" Phys. Rev. B 77, 235429 (2008).

[12] G. Renaud, R. Lazzari and **F. Leroy**
"*Probing surfaces and interfaces morphology with Grazing Incidence Small Angle X-Ray Scattering*" Surface Science Report. 64(8), 255-380 (2009)

[13] G. Sitja, M. Marsault, **F. Leroy**, S. Le Moal, C. R. Henry
"*Regular arrays of palladium and palladium-gold clusters supported on ultrathin alumina films : stability under oxygen*" Int. J. Nanotechnol., Vol.9 (3-7) 567-575, (2012)

[14] G. Sitja, S. Le Moal, M. Marsault, G. Hamm, **F. Leroy**, C. R. Henry
"*Transition from Molecule to Solid State : Reactivity of Supported Metal Clusters*" Nanoletters 13 (5), 1977-1982 (2013)

Autres :

[1] **F. Leroy**, P. Müller
"*External field as a tool for measuring absolute values of step-step interaction*" Surf. Sci. 602 126-132 (2008).

[2] S. Stepanow, R. Ohmann, **F. Leroy**, N. Lin, T. Strunskus, C. Wäll and K. Kern
"*Rational Design of Two-Dimensional Nanoscale Networks by Electrostatic Interactions at Surfaces*" ACS Nano. 4, 1813-1820 (2010)

[3] G. Prévot, **F. Leroy**, B. Croset, Y. Garreau, A. Coati, P. Müller
"*Step-induced elastic relaxation and surface structure of the Si(7710) surface*" Surf. Sci. 606 209-216 (2012)

[4] J. Boulenguez, S Berthier, **F. Leroy**
"*Multiple scaled disorder in the photonic structure of Morpho Rhetenor butterfly*" Appl. Phys. A 106, 1005-1011 (2012)

[5] A. Michon, L. Largeau, A. Tiberj, J. R. Huntzinger, O. Mauguin, S. Vézian, D. Lefebvre, F. Cheynis, **F. Leroy**, P. Müller, T. Chassagne, M. Zielinski, M. Portail
"*X-Ray Diffraction and Raman Spectroscopy Study of Strain in Graphene*

Films Grown on 6H-SiC(0001) Using Propane-Hydrogen-Argon CVD" Material Science Forum 740/742 (2013) 117

BIBLIOGRAPHIE

[1] R. Brandon and F. J. Bradshaw. The mobility of the surface atoms of copper and silver. *Royal Aircraft Establishment*, Report 660, 1966.

[2] W. W. Mullins. Theory of thermal grooving. *J. Appl. Phys.*, 28 :333, 1957.

[3] H. Wong, P. W. Voorhees, M. J. Miksis, and S. H. Davis. Periodic mass shedding of a retracting solid film step. *Acta Mater.*, 48(8) :1719–1728, May 2000.

[4] D. J. Srolovitz and C. V. Thompson. Beading instabilities in thin film lines with bamboo microstructures. *Thin Solid Films*, 139 :133–141, 1986.

[5] E. Jiran and C. V. Thompson. Capillary Instabilities in Thin Films film. *J. Electron. Mater.*, 19(11), 1990.

[6] E. Jiran and C. V. Thompson. Capillary instabilities in thin, continuous films. *Thin Solid Films*, 208(1) :23–28, February 1992.

[7] W. Kan and H. Wong. Fingering instability of a retracting solid film edge. *J. Appl. Phys.*, 97(4) :043515, 2005.

[8] O. Pierre-Louis, a. Chame, and Y. Saito. Dewetting of Ultrathin Solid Films. *Phys. Rev. Lett.*, 103(19) :195501, November 2009.

[9] M. Dufay and O. Pierre-Louis. Anisotropy and Coarsening in the Instability of Solid Dewetting Fronts. *Phys. Rev. Lett.*, 106(10) :105506, March 2011.

[10] Y. Fan, R. Nuryadi, Z. A. Burhanudin, and M. Tabe. Thermal agglomeration of ultrathin silicon-on-insulator layers : Crystalline orientation dependence. *Jap. J. Appl. Phys.*, 47(3) :1461–1464, 2008.

[11] Y. Ono, M. Nagase, M. Tabe, and Takahashi Y. Thermal Agglomeration of Thin Single Crystal Si on SiO2 in Vacuum. *Jpn. J. Appl. Phys.*, 34(4) :1728–1735, 1995.

[12] R. Nuryadi, Y. Ishikawa, and M. Tabe. Formation and ordering of self-assembled Si islands by ultrahigh vacuum annealing of ultrathin bonded silicon-on-insulator structure. *Appl. Surf. Sci.*, 159-160 :121–126, June 2000.

[13] R. Nuryadi, Y. Ishikawa, Y. Ono, and M. Tabe. Thermal agglomeration of single-crystalline Si layer on buried SiO[sub 2] in ultrahigh vacuum. *J. Vac. Sci. Technol., B*, 20(1) :167, 2002.

[14] B. Legrand, V. Agache, J. P. Nys, V. Senez, and D. Stiévenard. Formation of silicon islands on a silicon on insulator substrate upon thermal annealing. *Appl. Phys. Lett.*, 76(22) :3271, 2000.

[15] E. Dornel, J-C. Barbé, F. de Crécy, G. Lacolle, and J. Eymery. Surface diffusion dewetting of thin solid films : Numerical method and application to Si/SiO_2. *Phys. Rev. B*, 73(11) :115427, March 2006.

[16] D. T. Danielson, D. K. Sparacin, J. Michel, and L. C. Kimerling. Surface-energy-driven dewetting theory of silicon-on-insulator agglomeration. *J. Appl. Phys.*, 100(8) :083507, 2006.

[17] E. Bussmann, F. Cheynis, F. Leroy, P. Müller, and O. Pierre-Louis. Dynamics of solid thin-film dewetting in the silicon-on-insulator system. *New J. Phys.*, 13(4) :043017, April 2011.

[18] F. Cheynis, E. Bussmann, F. Leroy, T. Passanante, and P. Müller. Dewetting dynamics of silicon-on-insulator thin films. *Phys. Rev. B*, 84(24) :245439, December 2011.

[19] F. Cheynis, F. Leroy, T. Passanante, and P. Müller. *Appl. Phys. Lett.*

[20] F. Leroy, F. Cheynis, T. Passanante, and P. Müller. *Phys. Rev. B*.

[21] F. Leroy, F. Cheynis, T. Passanante, and P. Müller. Dynamics, anisotropy, and stability of silicon-on-insulator dewetting fronts. *Phys. Rev. B*, 85(19) :195414, May 2012.

[22] E. Bauer, M. Mundschau, W. Swiech, and W. Telieps. Surface studies by Low Energy Electron Microscopy (LEEM) and conventional UV PhotoEmission Electron Microscopy (PEEM). *Ultramicroscopy*, 31 :49–57, 1989.

[23] R. M. Tromp and M.C. Reuter. Imaging with a low-energy electron microscope. *Ultramicroscopy*, 50(2) :171–178, July 1993.

[24] M. E. Keeffe, C. C. Umbach, and J. M. Blakely. *J. Phys. Chem. Solids*, 55.

[25] W. W. Mullins. Flattening of nearly plane solid surface due to capillarity. *J. Appl. Phys.*, 30 :77, 1959.

[26] G. Renaud, R. Lazzari, and F. Leroy. Probing surface and interface morphology with Grazing Incidence Small Angle X-Ray Scattering. *Surf. Sci. Rep.*, 64(8) :255–380, August 2009.

[27] E. van Vroonhoven, H. J. W. Zandvliet, and B. Poelsema. $(2\times1)-(1\times1)$ Phase Transition on Ge(001) : Dimer Breakup and Surface Roughening. *Phys. Rev. Lett.*, 91(11) :116102, September 2003.

[28] F. Liu, J. Tersoff, and M. G. Lagally. Self-organization of steps in growth of strained films on vicinal substrates. *Phys. Rev. Lett.*, 80(6) :1268–1271, FEB 9 1998.

[29] S. P. Garcia, H. L. Bao, and M. A. Hines. Etchant anisotropy controls the step bunching instability in KOH etching of silicon. *Phys. Rev. Lett.*, 93(16), OCT 15 2004.

[30] M. H. Xie, S. H. Cheung, L. X. Zheng, Y. F. Ng, H. S. Wu, N. Ohtani, and S. Y. Tong. Step bunching of vicinal GaN(0001) surfaces during molecular beam epitaxy. *Phys. Rev. B*, 61(15) :9983–9985, APR 15 2000.

[31] I. Berbezier, B. Gallas, A. Ronda, and J. Derrien. Dependence of SiGe growth instability on Si substrate orientation. *Surf. Sci.*, 412-13 :415–429, SEP 3 1998.

[32] A. V. Latyshev, H. Minoda, Y. Tanishiro, and K. Yagi. Electromigration and gold-induced step bunching on the Si(111) surface. *Surf. Sci.*, 401(1) :22–33, MAR 20 1998.

[33] Y. N. Yang and E. D. Williams. Carbon-induced faceting of Si(112). *Surf. Sci.*, 215(1-2) :102–110, MAY 1989.

[34] D. Kandel and J. D. Weeks. Theroy of impurity-induced step bunching. *Phys. Rev. B*, 49(8) :5554–5564, FEB 15 1994.

[35] A. Latyshev, A. Aseey, A. Krasilnikov, and S. Stenin. *Surf. Sci.*, 213 :157, 1989.

[36] K. N. Tu. Recent advances on electromigration in very-large-scale-integration of interconnects. *J. Appl. Phys.*, 94(9) :5451–5473, NOV 1 2003.

[37] P. S. Ho and T. Kwok. Electromigration in metals. *Rep. Prog. Phys.*, 52(3) :301–348, MAR 1989.

[38] W. Burton, N. Cabrera, and F. Frank. *Phil. Trans. Roy. Soc.*, 243 :299, 1951.

[39] H.-C. Jeong and E. D. Williams. Steps on surfaces : experiment and theory. *Surf. Sci. Rep.*, 34(6-8) :171–294, September 1999.

[40] F. Leroy, P. Müller, J. J. Métois, and O. Pierre-Louis. Vicinal silicon surfaces : From step density wave to faceting. *Phys. Rev. B*, 76(4) :045402, 2007.

[41] F. Leroy, D. Karashanova, M. Dufay, J.-M. Debierre, T. Frisch, J.-J. Métois, and P. Müller. Step bunching to step-meandering transition induced by electromigration on Si(111) vicinal surface. *Surf. Sci.*, 603(3) :507–512, February 2009.

[42] T. Frisch. Dynamique dans les systèmes hors équilibre : Quelques exemples en croissance cristalline et en matière molle. *Habilitation à Diriger des Recherches de l'Université de Provence*, 2005.

[43] K. Yagi, H. Minoda, and M. Degawa. *Surf. Sci.Rep.*, 43 :45, 2001.

[44] P. Müller and A. Saúl. Elastic effects in surface physics. *Surf. Sci. Reports*, 54 :157–258, 2004.

[45] C. Misbah, O. Pierre-Louis, and Y. Saito. Crystal surfaces in and out of equilibrium : A modern view. Rev. Mod. Phys., 2010.

[46] S. Stoyanov. *Jpn. J. Appl. Phys.*, 30 :1, 1991.

[47] C. Herring. In R. Gomer and C. S. Smith, editors, *Structure and Properties of Solid Surfaces*, page 5. Univ. Chicago, Press, 1953.

[48] W. Mullins. In *Metal surfaces : structure energetics and kinetics*, page 17. American Society for Metals, Park Ohio, 1963.

[49] J. Villain and A. Pimpinelli. *Physique de la croissance cristalline*. Aléa Saclay Eyrolles, 1995.

[50] H. C. Jeong and E. D. Williams. Steps on surfaces : experiment and theory. *Surf. Sci. Report*, 34 :171–294, 1999.

[51] V. I. Marchenko and A. Y. Parshin. Elastic properties of crystal surfaces. *JETP*, 52 :129, 1980.

[52] Ellen D. Williams, Elain Fu, Y.-N. Yang, D. Kandel, and J.D. Weeks. Measurement of the anisotropy ratio during current-induced step bunching. *Surface Science*, 336(1–2) :L746 – L752, 1995.

[53] J.-J. Metois and M. Audiffren. An experimental study of step dynamics under the influence of electromigration : Si(111). *Int. J. Mod. Phys. B*, 11(31) :3691–3702, DEC 20 1997. Colloquium on Surface Dynamics and Crystal Growth - Villain Festschrift, Grenoble, France, Mar 15, 1996.

[54] V. Marchenko. Theory of the equilibrium shape of crystal. *JETP*, 54 :605, 1981.

[55] O. Alerhand, D. Vanderbilt, R. Meade, and J. Joannopoulos. Spontaneous formation of stress domains on crystal-surfaces. *Phys. Rev. Lett.*, 61 :1973, 1988.

[56] B. Salanon and P. Hecquet. *Surf. Sci.*, 412-413 :639, 1998.

[57] A. Latyshev, A. Aseev, A. Krasilnikov, and S. Stenin. *Surf. Sci.*, 213 :157, 1989.

[58] A. Latyshev, A. Aseev, A. Krasilnikov, and S. Stenin. *Surf. Sci.*, 227 :24, 1990.

[59] B. Gibbons, S. Schaepe, and J. Pelz. *Surf. Sci.*, 600 :2417, 2006.

[60] J. J. Métois and S. Stoyanov. *Surf. Sci.*, 440 :407, 1999.

[61] Y. Homma, R. McClelland, and H. Ibino. *Jpn. J. Appl. Phys.*, 29 :L 2254, 1990.

[62] Y. Yang, E. Fu, and E. D. Williams. *Surf. Sci.*, 356 :101, 1996.

[63] M. Dufay, T. Frisch, and J.-M. Debierre. Role of step-flow advection during electromigration-induced step bunching. *Physical Review B (Condensed Matter and Materials Physics)*, 75(24) :241304, 2007.

[64] C. O. Coileain, V. Usov, I. V. Shvets, and S. Stoyanov. Critical field behavior and antiband instability under controlled surface electromigration on Si(111). *Phys. Rev. B*, 84(7), AUG 9 2011.

[65] V. Usov, C. O. Coileain, and I. V. Shvets. Influence of electromigration field on the step bunching process on Si(111). *Phys. Rev. B*, 82(15), OCT 6 2010.

[66] V. Usov, C. O. Coileain, and I. V. Shvets. Experimental quantitative study into the effects of electromigration field moderation on step bunching instability development on Si(111). *Phys. Rev. B*, 83(15), APR 25 2011.

[67] M. Valden, X. Lai, and D. W. Goodman. Onset of catalytic activity of gold clusters on titania with the appearance on nonmetallic properties. *Science*, 281 :1647–1650, 1998.

[68] M. Bruchez, M. Moronne, P. Gin, S. Weiss, and A. P. Alivisatos. Semiconductor nanocrystals as fluorescent biological labels. *Science*, 281(5385) :2013–2016, SEP 25 1998.

[69] J. Y. Marzin, J. M. Gerard, A. Izrael, D. Barrier, and G. Bastard. Photoluminescence of single InAs Quantum dots obtained by self-organized growth of GaAs. *PHYSICAL REVIEW LETTERS*, 73(5) :716–719, AUG 1 1994.

[70] H. Ibach. The role of surface stress in reconstruction, epitaxial growth and stabilization of mesoscopic structures. *Surf. Sci. Reports*, 29 :193, 1997.

[71] V. A. Shchukin and D. Bimberg. *Rev. of Mod. Phys.*, 71 :1125, 1999.

[72] S. Rousset, V. Repain, G.Baudot, H. Ellmer, Y. Garreau, V. Etgens, J. Berroir, B. Croset, M.Sotto, P. Zeppenfeld, J. Ferre, J.P. Jamet, C. Chappert, and J. Lecoeur. *Mat. Science and Eng.*, B96 :169, 2002.

[73] P. Gambardella, A. Dallmeyer, K. Maiti, M. C. Malagoli, W. Eberhardt, K. Kern, and C. Carbone. Ferromagnetism on one-dimensional monatomic metal chains. *Nature*, 416 :301, 2001.

[74] G. Springholz, V. Holy, M. Pinczolits, and G. Bauer. Self-organized growth of three-dimensional quantum-dot crystals with fcc-like stacking and a tunable lattice constant. *Science*, 282(5389) :734–737, OCT 23 1998.

[75] H. Ellmer, V. Repain, M. Sotto, and S. Rousset. *Surf. Sci.*, 183-189 :511, 2002.

[76] B. Voigtländer, G. Meyer, and N. M. Amer. Epitaxial growth of thin magnetic cobalt films on au(111) studied by scanning tunneling microscopy. *Phys. Rev. B*, 44(18) :10354–10357, Nov 1991.

[77] H. Brune, M. Giovannini, K. Bromann, and K. Kern. *Nature*, 394 :451, 1998.

[78] F. Leroy, J. Eymery, P. Gentile, and F. Fournel. Controlled surface nanopatterning with buried dislocation arrays. *Surf. Sci.*, 545(3) :211–219, NOV 10 2003.

[79] B. E. Warren. *X-ray diffraction*. Dover Publication , Inc, New York, 1969.

[80] A. Guinier and G. Fournet. *Small-angle scattering of X-rays*. Jonh Wiley & Sons, New York, 1955.

[81] G. Glatter and O. Kratky. *Small angle X-ray scattering*. Academic Press, 1982.

[82] G. Sitja, S. Le Moal, M. Marsault, G. Hamm, F. Leroy, and C. R. Henry. Transition from molecule to solid state : Reactivity of supported metal clusters. *Nano Letters*, 0(0) :null, 0.

[83] S. Degen, A. Krupski, M. Kralj, A. Langner, C. Becker, M. Sokolowski, and K. Wandelt. Determination of the coincidence lattice of an ultra thin Al2O3 film on Ni3Al(111). *Surf. Sci.*, 576(1-3) :L57–L64, FEB 10 2005.

[84] G. Hamm, C. Barth, C. Becker, K. Wandelt, and C. R. Henry. Surface structure of an ultrathin alumina film on Ni3Al(111) : A dynamic scanning force microscopy study. *Phys. Rev. Lett.*, 97(12), SEP 22 2006.

[85] R. Lazzari. IsGISAXS : a program for grazing-incidence small-angle X-ray scattering analysis of supported islands. *J. Appl. Phys.*, 35(4) :406–421, AUG 2002.

[86] F. Cheynis, E. Bussmann, F. Leroy, T. Passanante, and P. Müller. Stress effects on solid-state dewetting of nano-thin films. *Int. J. Nanotechnol.*, 9(3-7) :396–411, 2012.

[87] G. Prévot, F. Leroy, B. Croset, Y. Garreau, a. Coati, and P. Müller. Step-induced elastic relaxation and surface structure of the Si(7710) surface. *Surf. Sci.*, 606(3-4) :209–216, February 2012.

[88] F. Leroy and P. Müller. External field as a tool for measuring absolute values of step-step interaction. *Surf. Sci.*, 602(1) :126–132, JAN 1 2008.

[89] D. J. Srolovitz and S. A. Safran. Capillary instabilities in thin films. I. Energetics. *J. Appl. Phys.*, 60(1) :247, 1986.

[90] A. K. Schmid. Alloying at Surfaces by the Migration of Reactive Two-Dimensional Islands. *Science*, 290(5496) :1561–1564, November 2000.

Résumé

Dans ce mémoire sont abordées quelques études sur la dynamique hors-équilibre des surfaces cristallines. L'accent est porté sur le démouillage de films minces monocristallins et sur les instabilités morphologiques induites par électromigration. Sur le plan instrumental, la Microscopie à Electrons Lents et la Diffusion Centrale des Rayons X en Incidence Rasante nous ont permis d'accéder à la dynamique des phénomènes *in situ* et en temps réel. Nous montrons que le démouillage à l'état solide des films minces de Silicium et de Germanium sur Silice conduit à des instabilités dendritiques du front de démouillage pilotées par le gain d'énergie de surface/interface et cinétiquement contrôlées par la diffusion de surface des adatomes. Le rôle central du facettage sur les instabilités morphologiques du front de démouillage est étudié en détails, en particulier certaines orientations cristallines limitent la vitesse de recul du front de démouillage et favorisent le développement de fronts droits stables.

Les instabilités morphologiques induites par électromigration sur les faces vicinales de Silicium sont un moyen d'étudier les interactions élastiques entre marches atomiques. Nous montrons que ces interactions favorisent le développement successif d'une onde de densité de marches puis d'un facettage périodique de la surface aux temps longs.

Enfin est abordée l'étude de la croissance auto-organisée de nanostructures de Pd sur une surface oxydée de Ni_3Al et nous terminons par quelques perspectives concernant l'étude de la dynamique de la ligne triple solide-solide-vapeur ainsi que sur la technique de Microscopie à Electrons Lents.

Summary

In this dissertation, the out-of-equilibrium dynamics of crystalline surfaces have been studied. We have emphasized on solid state dewetting of single crystalline thin films and morphological instabilities induced by electromigration. On an experimental viewpoint, Low Energy Electron Microscopy and Grazing Incidence Small Angle X-ray Scattering provide real time and *in situ* information. In particular we show that solid state dewetting of Silicon and Germanium thin films onto Silica give rise to dendritic like instabilities driven by the gain of surface/interface energies and kinetically limited by ad-atoms surface diffusion mechanisms. The central role of dewetting front faceting on morphological instabilities is highlighted ; in particular some crystallographic orientations reduce the dewetting front speed and favour stable and straight fronts.

The morphological instabilities induced by electromigration on vicinal surfaces of Silicon provide the opportunity to study mono-atomic step-step interactions. We show that these repulsive interactions favour the successive development of a step density wave then a faceting of the whole surface at long times.

At last, the self-organized growth of Pd nanostructures onto an oxidized surface of Ni_3Al is presented. We end up with some perspectives concerning the dynamics of the solid-solid-vapor triple line as well as the technique of Low Energy Electron Microscopy.